CORRELATION BETWEEN ENGLISH PERMO-TRIASSIC SANDSTONE LITHOFACIES AND PERMEABILITY AND ITS IMPORTANCE FOR GROUNDWATER

by

BAN XUAN TO

A thesis submitted to

The University of Birmingham

for the degree of

DOCTOR OF PHILOSOPHY

School of Geography, Earth and

Environmental Sciences

The University of Birmingham

January 2016

ABSTRACT

Predicting contaminant movement in aquifers is essential for the protection of groundwater resources. Contaminant movement is strongly influenced by hydraulic property heterogeneity. The aim of this project has been to determine if hydraulic property values are correlated with geological structures, even if the aquifer is a cemented sandstone: if they are, the correlations could be used in gaining insight into, and quantitatively estimating, solute transport.

Example Permo-Triassic sandstone lithofacies associations across England were examined in order to determine common lithofacies geometries. Several thousand measurements of permeability and several hundred measurements of porosity were determined on a core from northern England and two outcrops from the Midlands in order to examine correlations with lithofacies. Two types of synthetic fluvial multiple channel systems with flow along and across channels were then numerically simulated to determine the significance of the correlations found.

Results indicate that the Permo-Triassic sandstones have a wide range of lithologies and permeabilities, varying between and within sequences and regions. Permeability is generally greater for aeolian sandstone than for fluvial sandstone. The borehole core study shows that lithofacies correlate with porosity, permeability, and permeability to porosity ratio, though some significant overlaps occur for permeabilities of the three coarser lithofacies. Mudclasts can reduce sandstone permeability of the two coarser lithofacies by up to 6 % and 8% respectively. Markov chain analysis indicates that the sequences of lithofacies are structured, and hence the permeability is also similarly structured. The two outcrop studies confirm that permeability structures vary more between than within beds. Solute transport modelling indicates that differing solute breakthrough patterns will occur with different types of hydraulic property distributions based on lithofacies geometry. Thus lithofacies correlations can be used to help predict solute movement, but transverse dispersion, not explicitly studied here, also appears particularly important. Generally, the heterogeneous porous medium can be reasonably represented by an equivalent homogeneous medium for prediction purposes, however determining appropriate properties for the equivalent homogeneous medium is challenging.

ACKNOWLEDGMENTS

I would like to express my special thanks to my supervisor John Tellam for offering me a challenging project, and his guidance, care, support, and encouragement throughout the PhD programme. Sincere thanks to my co-supervisors Alan Herbert and James Wheeley for feeding my project with brilliant ideas, supporting and encouraging me throughout the PhD.

My grateful to the Vietnam Ministry of Education and Training for funding my PhD programme, and to the University of Birmingham for partly funding for the PhD. Special thanks to the British Geological Survey and its members of staff for providing the BritPit data and lending me the mini-permeameter equipment, especially to Dr. Andrew Butcher for training me how to use the equipment and supporting for the field work and Dr. John Bloomfield for kindly allowing me to access his personal data.

Many thanks to mining companies including Tarmac Quarry Products Ltd., Grinshill Stone Quarries Ltd., and the Queen Head Pub owner and local people for kindly allowing me to access their properties.

Thanks to Richard Greswell and Mark Cuthbert for their encouragement and help with setting up the experiments. Thanks to Paul Hands for helping with my thin-section samples. Thanks to my fellow PhD Hydrogeology students at the Hydrogeology Research Group, Water Sciences, School of Geography, Earth and Environmental Sciences, particularly Bryony Anderson, Mahmoud Jaweesh, Omar Al Azzo, Simiao Sun, Lindsay MacMillan, Christopher Barry, and Benjamin Harvey for help with moving many boxes of cores, and giving useful advice.

Thanks to my family, my wife and kids, for being with me not only in my time in Birmingham, but probably in my whole life.

TABLE OF CONTENTS

LIST OF FIGURES

LIST OF TABLES

CHAPTER 1

INTRODUCTION

1.1 The general concept

Heterogeneity has been recognized for a long time as a problem in the development of accurate predictions of groundwater flow and solute transport in aquifers. More information on heterogeneity is required for solute transport predictions in particular, as flow can often be represented successfully by an equivalent porous medium approach (Tellam and Barker, 2006). In solute movement, the presence of fast pathways can lead breakthrough fronts to occur much earlier than would be estimated from average groundwater velocity over the whole length and or depth of the sequence. Information on heterogeneity on a useful scale is not easy to obtain, especially when there are often only measurements of hydraulic properties taken at scales greater than the scale of heterogeneity of the deposit (e.g. from a borehole of 100 m deep drilled through a sequence with bed thicknesses of 0.5 m).

Heterogeneity of hydraulic properties is expected to result from variation in depositional environments, compaction, and diagenesis (Strong and Milodowski, 1987, Strong, 1993, Bloomfield et al., 2001, Bloomfield et al., 2006, Newell, 2006, Bouch et al., 2006, McKinley et al., 2011). Thus, hydraulic properties are likely to be correlated with depositional environments, compaction, and diagenetic processes. For a given degree of compaction, provided diagenesis is not dominating, a correlation might be expected between hydraulic properties and depositional environments. Depositional environments can be represented by lithofacies, a lithofacies being a distinct rock unit identifiable using key features such as colour, grain size, grain shape and packing, and sedimentary structures, and usually formed in a

particular, recognizable, regime reflecting specific sedimentary processes and environmental conditions (Selley, 1988, Reading, 1996).

Lithofacies may be identified by using borehole geophysics by using a range of standard tools including natural gamma radiation, resistivity, and optical televiewer. Moreover, if the geometry of each identified lithofacies can be interpreted from its deposition and palaeoenvironment, then the lateral distribution of hydraulic properties might be estimated.

The hypotheses investigated in this thesis are therefore:

1. that hydraulic property distributions can be quantitatively predicted from knowledge of lithofacies distributions, i.e. that hydraulic property values and lithofacies are correlated;
2. that such distributions have a significant effect on solute transport.

The sequence that will be used to investigate these hypotheses is the Triassic sandstone of England, as explained in Section 1.3.

In the next section, previous work on a range of aquifer types is described, including the small amount of previous work completed on the English Permo-Triassic sandstones. Finally, the aims and the approaches used are outlined.

1.2 A summary of previous work on correlations between lithofacies and permeability

1.2.1 Introduction

Much work has been done to search for correlations between sedimentary facies and permeability in hydrocarbon reservoir systems. However, usually hydrocarbon reservoirs are much deeper and have suffered less flushing and therefore less dissolution of authigenic minerals than shallow fresh-water aquifer systems. It might be expected therefore that correlations would be stronger in shallower systems than in deeper sequences that may be affected more by diagenesis. In addition, petroleum studies are done in the context of oil recovery rather than solute transport.

For hydrogeology, various attempts to study the relationship between sedimentary characteristics and hydraulic properties have been undertaken for unconsolidated deposits, and two studies prior to and overlapping with the current study have found encouraging results for the Permo-Triassic sandstone sequences. The following sub-sections briefly describe these studies and their findings.

1.2.2 Correlations in hydrocarbon reservoir sandstones

In hydrocarbon reservoir sandstones, correlations between lithofacies and petrophysical properties, such as porosity and permeability, have been found in a range of palaeoenvironments (e.g. Jacobsen and Rendall, 1990, Dreyer et al., 1990, Gibbons et al., 1993, Doyle and Sweet, 1995, Byrnes, 1997, Ehrenberg, 1997, Bahar and Kelkar, 2000, Tye and Hickey, 2001, Büyükutku and Bağcı, 2005). These studies are summarised in Table 1-1. In general, they all find that there is a relationship between sedimentological structure and

hydraulic property structure, despite the effects of cementation, but that there is also overlap between properties.

Table 1-2 summarises some successful applications of the work on correlations in context of simulation for flow and transport and enhanced recovery in hydrocarbon reservoir sandstones (e.g. Aigner et al., 1996, Anderson et al., 1999, Hornung and Aigner, 1999, Willis and White, 2000). In general the applications use the following approaches: 1) determine lithofacies sequence in the reservoir rocks; 2) assign a permeability distribution for each lithofacies or each part of the sequence from measurements or from general knowledge; 3) establish model volume with permeability distribution to undertake the prediction of flow and transport.

Although successful application of correlation between facies and permeability has been confirmed for hydrocarbon systems, and the results are of potentially great use in groundwater application, it would be inappropriate to transfer directly and uncritically the hydrocarbon research to hydrogeology. This is due to some important differences between the geological systems relevant to the hydrocarbon and groundwater industries. Firstly, hydrogeological systems and hydrocarbon systems are often associated with sequences with different diagenetic and stress histories (Strong and Milodowski, 1987) with the former often much shallower, hence having undergone greater cement and framework grain dissolution, and decompression than the deeper hydrocarbon systems (e.g. Lambert et al., 1997). Hence it may be that palaeoenvironmental / hydraulic property correlations are stronger than are seen in work undertaken on core plugs from deep oil wells. Secondly, scales of interest to groundwater problems at site scale (e.g. bed by bed) are smaller than those often associated with hydrocarbon problems where formation scale may be more important, thus meaning that ‘sub’-facies (e.g. types of fluvial channel deposit) rather than facies (e.g. fluvial v. lagoonal) may have greater

importance in hydrogeology. In addition, the main interest of groundwater systems is in terms of solute transport (i.e. dispersion), but that of oil industry is enhanced oil recovery, and the work in the oil industry has not therefore considered solute transport implications.

1.2.3 Correlations in unconsolidated clastic aquifers

For unconsolidated sediments and other rock types, the correlation between sedimentological characteristics and hydraulic properties have also been investigated in some studies worldwide (e.g. Davis et al., 1993, Davis et al., 1997, Jussel, 1989, Davis et al., 2006, Huysmans et al., 2008, Possemiers et al., 2012) (Table 1-3).

The approaches used for these studies on unconsolidated deposits are similar to the ones applied in the studies of hydrocarbon reservoirs. They were first identifying lithofacies, sedimentological units, then obtaining their hydraulic properties such as permeability and porosity by measurements using various techniques including conventional methods (pumping, laboratory tests), air mini-permeametry. Correlations were found in these uncemented deposits as they were for deeper, oil reservoir systems. This suggests that it is likely that correlations will be found in the English Permo-Triassic sandstone sequence, and that they are worth searching for.

Table 1-1. A summary of literature on lithofacies / hydraulic property correlations in the context of hydrocarbon development

Paper	Rock	Approach	Location	Findings
Jacobsen and Rendall (1990)	Middle Jurassic fluvial-deltaic sandstones	Outcrops	North Sea	Found good correlation between sandstones lithofacies and permeability
Dreyer et al. (1990)	Middle Jurassic fluvial-deltaic sandstones	Outcrops	North Sea	Found good correlation between sandstones lithofacies and permeability from outcrops
Ehernberg (1997)	Middle Jurassic fluvial-deltaic sandstones	6 boreholes (2.3-2.6 km and 3.6-3.9 km below see floor)	Northern North Sea	Strong relationships between sandstone lithofacies and permeability and porosity though some significant overlap values of permeability and porosity for different lithofacies. Also recognized significant decline trend of average values of porosity and permeability with depth.
Gibbon et al. (1993)	Sandstones of shallow marine environment	Boreholes 120 and 140 m deep	North Sea	Reported nine lithofacies, ranging from massive homogeneous sandstone to fine-grained, micaceous sandstones of variable bioturbation, that are strongly correlated with permeabilities although overlap in average permeability seen for some lithofacies; permeability is controlled by grain size with greater permeability for coarser-grained sandstones.
Doyle and Sweet (1995)	fluvial sandstone, Gypsy Sandstone	Outcrop and shallow borehole cores	Northern Oklahoma,USA	Good relationships between porosity and permeability
Lambert et al. (1997)	shallow marine sandstones of the Tocito Sandstone, Upper Cretaceous	Outcrops, 2 shallow & 4 deep boreholes	Northwest New Mexico, USA	Nine lithofacies were identified and have a major control on permeability. Permeabilities and porosities measured at the outcrops and shallow borehole cores are significantly greater than those measured at the deep borehole cores this is due to the dissolution of calcite cement and framework grain and effects of weathering and decompression at shallow depth. Highest permeability was related to the large- and medium-scale cross-bedded sandstone facies; intermediate permeability were measured for the interbedded sandstone and shale facies; lowest permeabilities were corresponding to the ripple cross-laminated sandstone and the muddy bioturbated sandstone facies. The mudstones can spatially act barrier and baffles to flows and compartmentalise the reservoir.
Bahar and Kelkar (2000)		Geostatistical simulation to translate geological information from borehole cores and logs into porosity and permeability		Good correlation between sandstone lithofacies and permeability
Büyükutku and Bağcı (2005)	Shallow marine sandstone, Kuzgun Fm, Middle-Upper Miocene	Outcrop	Adana Basin, Southern Turkey	Recorgnised three lithofacies which each has distinct permeability and porosity distribution. Grain size exert a strong controlls on permeability with coarser-grained sandstone are more permeable. Coarser-grained, cross-bedding sandstone which is free of clay or cement on pore throat has highest permeability and porosity.

Table 1-2. A summary of literature on applications of lithofacies/hydraulic property correlations in the context of hydrocarbon development

Paper	Rock	Approach	Location	Findings
Aigner et al. (1996)	Upper Triassic aged sandstones	Outcrop: related hierarchy of sedimentary cycles into hierarchy of reservoir heterogeneity	South Germany	The importance of sedimentary facies and different types of fluvial multiple cycles within large-scale depositional cylces in cotrolling the fluid-flow behavior of the sandstones reservoir.
Hornung and Aigner (1999)	Sandstone of the Stubensandstein aged Upper Triassic		South Germany	Recognized 9 architectural elements with 14 facies. Elements and facies have distinctive porosity and permeability. Based on relationship between architectural elements and facies with porosity and permeability, suggestions for reservoir compartments were made, good reservoir compartments relating to bedload channel sandstones in the medial position of a cycle, highly cemented sandstones forming aquitards, and extensive floodplain mudstones, lacustrine deposits, palaeosols, and suspended-load sediments acting as aquicludes.
Anderson et al. (1999)	Braided river deposits	Sand and gravel pit outcrop; simulation of solute transport	Stoughton, Wisconsin, USA	Seven 'hydrofacies', groups of sedimentary units having similar hydrogeological characteristics, were formed from 11 lithofacies. Results from the Stoughton Pit and the synthetic braided river system highlight the importance of the high permeability units forming connected hydrofacies for hydrogeological study concerning solute transport and remediation.
Willis and White (2000)	Tide-influenced deltaic sandstones, Frewens Sandstone of the Frontier Formation	Outcrops. Simulations.	central Wyoming, USA	Five lithofacies, higher number indicating larger grain size, thicker bedding, and more permeable deposits. Simulations of water flow using different scales, various grid resolutions, and assignment of permeability to lithofacies were undertaken for the sandstones at outcrop. Flow models suggest that coarser-grained units tend to push water upwards; thin shales draping sandstone beds exert a control on flow pattern, depending direction of flow; cement, where present, can cause considerable reduction in relative permeability and this is important because of their presence in the coarsest-grained sediments towards the top of the sandstone unit; effects of shales drapes and methods for prediction of intrafacies/permeability correlation depend on the model grid scale.

Table 1-3. A summary of literature on lithofacies / hydraulic property correlations in unconsolidated deposits

Paper	Rock	Approach	Location	Findings
Davis et al. (1993)	1.6 km^2 of Pliocene-Pleistocene aged fluvial deposits, Sierra Ladrones Formation	Outcrop study; minipermeametry	Central New Mexico, USA	Four architecture elements were mapped, including a high-energy channel element, a low-energy channel element, an overbank-fine element, and palaeosol elements. In situ permeabilities were measured using a gas mini-permeameter. It indicated a good correlation between architecture element types and mean log permeability values. Geostatistical analysis from six directions ($N30^0E$, $N60^0E$, $N90^0E$, $N30^0W$, and $N60^0W$) showed that the horizontal variograms of mean log-permeability showed a non-perpendicular anisotropy, with greatest correlation at $N30^0W$ and smallest correlation at $N90^0E$. The $N30^0W$ direction reflects the orientation of average directions of scours of lower-energy channel elements (directions of the tributary system), whereas the $N90^0E$ direction corresponds to directions of progressing dominance with the overbank-fine element (directions of the ancestral Rio Grande flood plain). For vertical variograms, the correlation structure was controlled by average-element thicknesses.
Davis et al. (1997)	Ditto	3, metre-scale studies	Ditto	Three deposits (high-energy channel, a low-energy channel, & palaeosol) were mapped for their bounding surfaces. In situ mini-permeameter measurements were undertaken. Each of the 3 outcrop studies had distinct permeability correlation structures. Concluded that between facies variation dominated over within facies variation.
Jussel (1989)	Fluvial gravel deposits	Properties measured on samples from outcrops.	Zurich, Switzerland	Six depositional elements (grey gravel, brown gravel, sand lenses, open framework gravel, open framework/bimodal-couples, and silt lenses). Found that K values were relatively similar over short horizontal extents (decimetres to few metres) and these regions of similar values dipped. These trends were also seen with porosity.

Table 1-3. A summary of literature on lithofacies / hydraulic property correlations in unconsolidated deposits (continues)

Paper	Rock	Approach	Location	Findings
Davis et al. (2006)	Channel sand deposits in the Plio-Pleistocene Sierra Ladrones Formation	Outcrop	Albuquerque Basin, New Mexico, USA	Found that cementation varied spatially and was weakly correlated with lithofacies. Cementation was negatively correlated to permeability, causing permeability to be locally reduced by up to three orders of magnitude. The permeability correlation structure was strongly controlled by the spatial distribution of cementation and this caused an increase the variance of log-permeability by an order of magnitude.
Huysmans et al. (2008)	Brussels Sand Formation: shallow marine sand deposits of early Middle-Eocene	Quarry outcrop; 2750 cm-scale measurements using a gas mini-permeameter were made and then compared with permeability data from pumping and piezometer tests at different locations	Bierbeek quarry, Central Belgium	Two sedimentary zones were defined: a sand-rich zone consisting of a cross-stratified sand facies; and a clay-rich zone containing clay-rich bottomsets and mud drapes within the cross-stratification. 4 lithofacies were identified (cross-stratified sands, clay-rich bottomsets, mud drapes, and cemented concretions). Heterogeneity and anisotropy of permeability were caused by small scale sedimentary heterogeneity. Spatial distributions of permeability were mainly controlled by geometry of the sedimentary structures. Bottomsets and mud drapes, distinct units of the clay-rich zone, were less permeable, and were associated with a more continuous spatial permeability distribution than other facies in the cross-stratified sands, suggesting that clay-rich layers can act as baffles to flows, separating the aquifer into parts. Geostatistical analysis on permeability data showed that the orientation of the foreset laminae controlled permeability anisotropy of the cross-stratified facies.
Possemiers et al. (2012)	Ditto	Outcrops. A further 3800 cm-scale gas permeability measurements were obtained at the 3 outcrops	Bierbeek, Mon-Saint-Guibert, Chumount-Gistoux, central Belgium	The complicated sedimentological heterogeneity of the Brussels Sands led to a highly heterogeneous spatial distribution of permeability at different scales. At large scale, significant variation in permeability occurred. At a small scale, in all 3 outcrops, sedimentology strongly controlled heterogeneity and anisotropy of permeability. Confirmed Huysmans et al. (2008) that bottomsets and mud drapes had distinct permeability distributions compared with the cross-stratified sand lithofacies with relatively lower permeability for the former. In the cross-stratified sands, the orientation of the foresets controlled permeability anisotropy.

1.3 The English Permo-Triassic sandstones

1.3.1 Introduction

In following subsections, the reasons for choosing the English Permo-Triassic sandstone sequences are given (Section 1.3.2), an overview of their sedimentological characteristics is provided (Section 1.3.3) and their general hydrogeological features are described (Section 1.3.4). Finally, previous studies on the correlation between Permo-Triassic sandstone lithofacies and sedimentary characteristics and permeability (and porosity) are briefly described (Section 1.3.5).

1.3.2 Choice of the English Permo- Triassic system

The Permo-Triassic sandstone is the second most used aquifer in the UK after the (Cretaceous) chalk, contributing to 25% of the England and Wales licensed groundwater abstraction and supplying water for a number of large cities such as Manchester and Liverpool, Birmingham, Leeds, Doncaster, and Nottingham (Allen et al., 1997, Tellam and Barker, 2006, Bloomfield et al., 2006).

The Permo-Triassic sandstones have similar matrix hydraulic characteristics to many other sandstone deposits (Jensen et al., 1996) i.e. hydraulic conductivity varying widely, bed-scale layered heterogeneity, and hydraulic anisotropy within single beds. The permeability of the Permo-Triassic sandstone is dual permeability with contributions from both matrix and fractures (Price et al., 1982, Allen et al., 1997, Allen et al., 1998, Tellam and Barker, 2006). Relative contributions of matrix and fracture porosity change over basins, at depths, and at different scales (Allen et al., 1998).

Allen et al. (1997), Bloomfield et al. (2006) and Tellam and Barker (2006) suggest that the Permo-Triassic sandstone aquifer in England is spatially heterogeneous and anisotropic due to variations in depositional environments and diagenetic processes.

Hence, because of its importance in England, its importance as an example of a class of aquifer found worldwide, and because it has been claimed that its hydraulic properties are related to its sedimentological character, the English Triassic sequence has been chosen as the study system. In order to limit the scope to something possible within the time limits available, only intergranular properties will be examined. However, it is clear from tracer experiments (Ward et al., 1998, Streetly et al., 2002, Greswell et al., 2014) that intergranular solute movement is very important even over site-scale distances, and there is also limited evidence that intergranular solute movement is even more important over larger scales (Carlyle et al., 2004, Tellam and Barker, 2006).

1.3.3 A brief overview of relevant geological characteristics of the English Permo-Triassic sandstones

The English Permo-Triassic sandstones are typically continental fluvial and aeolian red-bed sequences and broadly similar sandstones are widespread internationally.

There are parts of the English Permo-Triassic sequence that are at least predominantly fluvial in origin, parts that are at least predominantly aeolian in origin, and parts that are mixed fluvial-aeolian. The fluvial sequences often show cyclic sedimentation (e.g. Fitch et al., 1966, Thompson, 1970, Wills, 1970, 1976), and Wills (1970) has suggested scale hierarchy of cycles in the Permo-Triassic sandstones from metre to hundreds of metre scale (Section 3.3). Sedimentary cyclicity interpretation has been widely and successfully applied in hydrocarbon reservoir sandstones, but rarely in the context of the hydrogeology of aquifer sandstones.

Aeolian sequences include dune and sandsheet deposits (Benton et al., (2002). Mixed sequences result from aeolian re-distribution of sediments between fluvial events.

Further details are provided in Chapter 3.

1.3.4 A brief overview of the hydraulic properties of the English Permo-Triassic sandstone

The hydraulic conductivity of the matrix of the Permo-Triassic sandstone sequence varies over about seven orders of magnitude, from about 10^{-6} to 20 m/d, with a median value of 0.56 m/d: it usually follows an approximately log normal distribution (Allen et al., 1997). No systematic variation in matrix permeability has been found with depth (Allen et al., 1997). Anisotropy in hydraulic conductivity (i.e. horizontal to vertical ratio) is reported up to 50, but is often much closer to 1 and can be less than 1 in some cases (Allen et al., 1997, Tellam and Barker, 2006). Limited data suggest permeability to be sensitive to water chemistry (Tellam and Barker, 2006). Porosity values vary from 2 to 35% with a median value of 26%, and often there is an approximately linear relationship between log hydraulic conductivity and porosity (Allen et al., 1997).

1.3.5 Previous work on correlations between hydraulic properties and lithofacies in the English Permo-Triassic sandstone

In the English Permo-Triassic sandstone sequences, correlations between sandstone lithofacies and their hydraulic properties has been sought mainly qualitatively but also sometimes quantitatively (e.g. Bouch et al., 2006, Newell, 2006, Bloomfield et al., 2006, Moran, 2008, McKinley et al., 2011). The following paragraphs are brief descriptions of these studies.

Bouch et al. (2006) examined borehole cores from three boreholes drilled at the Birmingham University campus, Birmingham, UK. The cores were taken from the Wildmoor Sandstone Formation, Sherwood Sandstone Group. They recorded five lithofacies, including three braided-river lithofacies (channel-lag, channel-fill, and abandoned channel), an aeolian sandsheet lithofacies, and a palaeosol. Although no attempt was made to correlate lithofacies with permeability, some observations were made from the study: 1) abandoned channel mudstones and palaeosol could act as barriers to vertical flow at scale of tens of metres; 2) the sandstones which have fairly high porosity show locally variable extent of cementation, and a highly-cemented, thin-layered unit would be by-passed by horizontal flow, but would inhibit vertical flow; 3) granulation seams that had permeability of 2 to 3 orders of magnitude less than the permeability of the sandstones could act locally as baffles to lateral fluid flow; 4) grain size and dolomite cements were factors controlling the matrix permeability.

Newell (2006) studied sandstones in outcrops in south Devon, southwest England. The sandstones were from the Triassic Otter Sandstone Formation (Sherwood Sandstone Group), aged Lower-Middle Triassic. Calcrete is common in the Formation. Four lithofacies associations were identified: aeolian sandstone association; calcrete-rich, multistorey channel association; calcrete-poor, multistorey channel association; and solitary channel sandstone and mudstone association. A total 36 core plugs were made from samples taken at Ladram Bay coastal cliffs, and from the Harpford Borehole. The core plugs appear to be one of three facies forms: sandstone of free-calcrete or minor calcrete development; sandstone with extensive calcrete development; and calcrete conglomerate. Hydraulic properties were derived from the core plugs with porosity values range from 7 to 34%, and gas permeability varying over five orders of magnitude from about 4×10^{-17} to 7×10^{-12} m^2. Calcretes in core plugs can cause a reduction in permeability and porosity to less than 10^{-15} m^2 and less than 12% respectively.

Calcretes can become locally abundant in the aquifer, causing porosity reduction by up to 30%. Calcretes and non-calcrete sandstone core plugs showed clearly contrasting porosity and permeability. The calcrete sandstone samples have permeability from $5x10^{-17}$ - $8x10^{-14}$ m^2 and porosity from 7-15 %, whereas the non-calcrete sandstones have permeability ranging from $8x10^{-14}$ - $9x10^{-12}$ and porosity from 15-34 %. Laterally extensive (up to 1 km) calcrete conglomerates an act as barriers to vertical flow.

Bloomfield et al. (2006) investigated sandstones of the Helsby Sandstone and Wilmslow Sandstone Formations of the Sherwood Sandstone Group, at the Abbey Wood borehole in Cheshire, UK. Six sandstone and one mudstone lithofacies were identified. The six sandstone lithofacies include two fluvial sandstones (coarse and fine-grained channel fill facies), three aeolian sandstones (sabkha deposit, dunes and sandsheets facies) and a massive sandstone which was believed to be of either fluvial or aeolian origin. Permeabilities were determined from core plugs using nitrogen as the permeant and the whole core was investigated at intervals of approximately 0.4m using a mini-permeameter that was also used to test the core plugs. It was impossible to sample the mudstone or fine-grained channel fills because they were too friable. Statistical analysis on the permeability data showed that the lithofacies have distinct permeability distributions. In particular, the two fluvial sandstones and massive sandstone facies generally had lower permeability than the aeolian sandstone facies, and within the aeolian sandstones, the sandsheet and dune facies were more permeable than the sabkha sandstone facies. Core plug derived permeabilities varied over five orders of magnitude from 1.4×10^{-16} to 7.8×10^{-12} m^2, with a geometric mean of about 1.9×10^{-13} m^2, and showed weak anisotropy, horizontal permeability being about three times greater than vertical permeability. Porosity ranges from 5.9 to 26.6%, with a mean of 20.3% and follows approximately a normal

distribution. There was a weak correlation between porosity and permeability and "unclear" correlations between porosity and lithofacies.

Just as the current study commenced, McKinley et al. (2011) published a study of outcrops at Styrrup Quarry, South Yorkshire, UK. The study outcrops are fluvial sandstones of the Sherwood Sandstone Group of Triassic age. Statistical analysis of global regression show weak correlation between both porosity and permeability and diagenetic and primary sedimentary structures such as grain size and sorting for the entire outcrop. Further dividing the outcrop dataset into seven bedding units (upper pebbly bed, trough-fill sandstone, lower pebbly bed, laminated sandstone, and the main channel body which was subdivided into 3 units: upper channel sandstone, lower channel sandstone, and cross-bedded sandstone) along with use of the geographically weighted regression method emerges important controls of primary depositional structures and diagenetic processes on permeability and porosity. Permeabilities are locally moderately-highly inversely correlated to grain sorting for the cross-stratified units. Inverse relationships between permeability and cements were seen in the main channel body. Inverse correlations between porosity and cements appears in the trough-fill sandstone, the main channel body and the lower pebbly bed. For the relationship between permeability and grain size, positive correlations were seen in the trough-fill sandstone, but inverse correlations at the upper pebbly bed, lower pebbly bed, and the main channel body (the cross-bedded sandstone). Inverse correlations between porosity and grain size were seen at the trough-fill sandstone and main channel body. Maximum permeability was found in the direction of erosion and dissection of earlier bedsets of channel-fill sandstone.

As a preliminary study prior to the one reported in this thesis, Moran (2008) examined a core from the Preston Laundry Borehole, Preston, Cheshire, UK – the core on which much of the

present work was performed. She identified five lithofacies, including a channel-lag sandstone, three channel-fill sandstones, and a mudstone. Permeabilities of the sandstones were measured both with a falling head test permeameter on core plugs and by use of a mini-permeameter on the unprepared surface of the borehole core. No samples were made for the mudstone facies. Porosity and log permeability from the core plugs were found to be strongly correlated. Statistical tests on porosity and permeability data indicated each lithofacies has distinct porosity and permeability distribution: however, there was some uncertainty given that the cores were partially saturated when tested using the mini-permeameter.

Although the preliminary results are encouraging in finding a relationship between lithofacies and permeability in the English Permo-Triassic sandstone sequence, there are only a few studies available, two of the most detailed studies being one dimensional in that they are on borehole cores, and the strengths of the correlations especially for fluvial lithofacies, the dominant lithofacies group in much of the sequence, remain poorly quantified.

1.4 Research aims and approach

1.4.1 Project aims

The project has two aims:

1. to determine the strength of correlation between lithofacies and permeability in example English Permo-Triassic sandstone sequences, and;
2. to determine whether the permeability distributions discovered can be used to improve prediction of solute transport.

1.4.2 Approach

The following approach was undertaken to achieve the aims:

1. examine variation of some examples of sandstone lithofacies associations across England, extending from Cumbria (northwest) through Midlands, to Devon (southwest) in order to determine likely architectures for later work on modelling solute transport;
2. statistically analyse existing borehole core permeability datasets;
3. determining petrographic and hydraulic property distributions in a borehole core and at outcrop;
4. statistically analyse data collected in 3 to determine strength of hydraulic property / lithofacies correlations;
5. undertake numerical modelling using the correlations between hydraulic property values and lithofacies collected in 3 and the architectural data collected in 1 to determine the effect of permeability distributions on solute transport in groundwater.

1.5 The structure of the thesis

Chapter 2 introduces the methods used for this study. Chapter 3 describes the work done on determining the sedimentological architecture and qualitative hydrogeology of a range of Permo-Triassic sandstone outcrops across England. Chapter 4 describes work done to determine the correlation between fluvial sandstones and permeability at a borehole core drilled at Preston Laundry, Cheshire, England. Chapter 5 describes the field work investigations on permeability configurations at two sites. Chapter 6 uses the architectural data collected in the field survey described in Chapter 3 and the correlations between lithofacies and permeability determined in Chapter 4 to construct numerical models of solute transport, these models then

being used to determine the importance of the correlations for solute transport. Finally all findings of the thesis are summarized in Chapter 7 along with recommendations for future work.

CHAPTER 2

METHODOLOGY

2.1 Introduction

The methods used to achieve the aims of the project (Chapter 1) fall mainly into two categories: field investigation methods and laboratory methods. Variation in depositional environments and heterogeneity of sandstone hydraulic properties were studied at outcrop. Lithofacies identification, sedimentary structure interpretation, hydraulic property determination of samples taken during field work and from borehole cores were determined in the laboratory. The following sections describe the methods used with their principles and background, but some important detail are also included in the relevant subsequent chapters.

2.2 Field site investigations

2.2.1 Lithological features and sedimentary structure mapping

The English Permo-Triassic sandstones appear with a wide range of depositional environments and significant heterogeneity. Study of outcrops is one effective approach to determine the heterogeneity of the sandstones. Some example sandstone outcrops across England, extending from Cumbria in northwest to Devon in southwest, were studied.

Lithological features and sedimentary features at outcrop were mapped based on photographs taken at study sites and from available literature. Lithofacies were defined on the basis of sedimentary features such as grain size, sorting, and sedimentary structures including horizontal and cross bedding and lamination, and the presence of pebbles. Lithofacies were also defined

from laboratory borehole cores by a simple approach of logging of sedimentary features: colour; grain size; lamination style (massive, plane, low angle, and high angle); presence of pebbles, mudclasts, and mica. The geometry of lithofacies or sedimentary units were measured using a tape and compass. Photographs taken at outcrops were used as a background map on which lithofacies, sedimentary units and features were redrawn and interpreted using what was observed from the field and obtained from the literature.

2.2.2 Sample collections and in situ measurements

At the study sites, where possible, samples were taken for thin-section analysis and to determine hydraulic properties. Of the study sites, the Wolverley sandstone outcrop in Worcestershire and the Bridgnorth sandstone outcrop Shropshire were studied in more detail (Chapter 5). The sedimentary structures of these two outcrops were mapped in detail. A probe/mini-permeameter, detailed below, was used to do in situ measurement of permeability.

2.3 Laboratory measurements

2.3.1 Sample preparation

2.3.1.1 Core plug samples

Core plug samples for hydraulic property determination were drilled from sandstone samples taken from the field (Chapter 3) and from a borehole core from Preston ('Preston Laundry borehole') (Chapter 4) (Fig.2-1a) using a conventional water-flush pillar drill rig with coring bit of 31 mm diameter. Both horizontal and vertical core plugs were obtained. The core plugs were drilled to have lengths from 54 mm to 72 mm, and were then cut right angles at both ends using a circular saw. The core plugs were then labelled (Fig.2-1b).

A total of 63 core plug samples were available from the study by Moran (2008) on the Preston Laundry borehole core. These core plugs were stripped of their heat-shrink wrapping in order to perform mini-permeameter measurements.

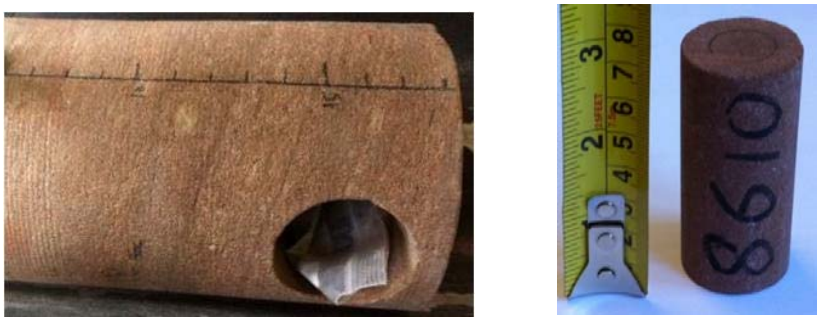

a) b)

Fig.2-1. Preston Laundry borehole core: a) borehole core from which a core was obtained, b) a core plug.

In preparing samples for the measurements of permeability using a falling head permeameter (detailed below), the core plugs which had already been measured for their dimensions and porosities were wrapped in at least two layers of polytetrafluoroethylene (PTFE) tape over their curved surfaces to prevent flow from their sides. The core plugs were then covered (constrained) with a heat-shrink plastic tube with about 4-5 cm of plastic tube left at each end. The plastic tube then was shrunk tightly against the side of the core plug using a heat gun, the ends being used to connect to the apparatus to measure hydraulic conductivity (Fig.2-2).

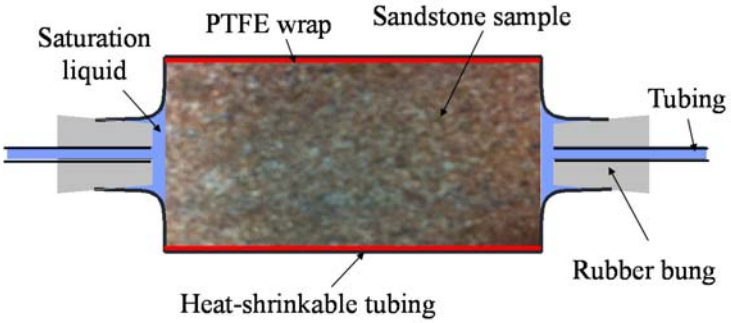

Fig.2-2. Diagram of a core plug ready for use in a falling head permeameter.

2.3.1.2 Samples for measurement of moisture content

Because of its possible effect on permeability measurement, the moisture content of the Preston Laundry borehole core needed to be determined. Samples 1.0- 2.0 cm long by 1.5 – 2.0 cm wide by 1.0-1.5 cm high were extracted from the core at different depths using a chisel and hammer. Almost all of these depths had already been measured for permeability using the mini-permeameter (Chapter 4). The sizes of sample were chosen to cover the effective penetration depth of the mini-permeameter (0.7 – 1.27 cm).

2.3.1.3 Thin-section analysis

Samples taken from the field sites and core samples were used to make thin-section samples. Thin-sections were analysed using a microscope to determine features such as mineral types, grain size and shape, grain sorting, and cementation. This information supported the lithofacies identification. Some of thin-sections were impregnated with blue-dyed resin to study porosity.

2.3.1.4 Water chemistry

The saturating fluid used for experiments was produced so as to have similar ionic strength and cation composition as the natural groundwater. This is to minimise any clay swelling or dispersion of colloids which may modify the permeability (Braney et al. 2001 and Michener 2003 in Tellam and Barker, 2006).

Table 2-1 shows an example of synthetic groundwater made for the Bridgnorth Sandstone Formation in the Bridgnorth area. Chemical analyses of groundwater were obtained from

Smedley et al. (2005). A solution of tenfold concentration was made up and then diluted to be used for experimental measurements of hydraulic conductivity.

Table 2-1. Chemistry analysis of the artificial groundwater for Bridgnorth Sandstone Formation (ionic strength in mol/l; mw = molecular weight).

	Natural groundwater					**Artificial water**		
	charge (z)	mw	mg/l	mol/kg	mz^2	mol/kg	mz^2	g/litre needed
Ca	2	40.08	77.7	0.0019	0.00775	0.0019	0.0078	0.285
Mg	2	24.31	13.1	0.0005	0.00216	0.0005	0.0022	0.133
Na	1	22.99	20.1	0.0009	0.00087	0.0009	0.0009	0.051
K	1	39.1	3.2	0.0001	0.00008			
Cl	-1	35.45	41.7	0.0012	0.00118	0.0048	0.0048	
SO_4	-2	96	39.1	0.0004	0.00163	0.0005	0.0022	
HCO_3	-1	61	204	0.0033	0.00334			
NO_3	-1	62	8.2	0.0001	0.00013			
H		1	**ionic strength = 0.0086**			**ionic strength= 0.0088**		
S		32.07						
O		16	**ionic strength**					
$MgSO_4.7H20$		246.38	**I = 0.5 Sum (mz^2)**					
NaCl		58.44						
$CaCl_2.2H20$		146.98						

2.3.2 Hydraulic property determination

2.3.2.1 Porosity

Porosity was determined based on a resaturation technique (Monicard, 1980). All unwrapped core plugs and moisture content chipped samples were measured for porosity. The samples were oven-dried at 60^0 C for at least 24 hours and then weighed with calibrated balance of accuracy of 0.01 g to obtain a fully dried mass (W_d). In Moran (2008), a temperature of 110^0 C (Greswell, 1995) was used for at least 24 hours, but in the current study 60^0C was used as suggested by Andrew Butcher, Wallingford British Geological Survey (BGS), to prevent any potential damage to the samples. The samples were then placed under a vacuum (~6 mm Hg (about 0.8 millibar)) for 1 – 2 hours (Greswell, 1995). The saturating fluid then was introduced

into the vacuum chamber though a valve to roughly 2 cm above sample level. The samples were left for at least 24 hours to become fully saturated. For the core plug samples, bulk volumes were calculated by measurement of the core plugs' cylindrical dimensions, whereas, the bulk volumes of the chipped samples were measured by water displacement (see below).

After saturation, excess water was wiped off the samples and they were weighed with the same balance used for the dry samples to obtain the fully saturated mass (W_f). The saturated chipped samples were then submerged in graduated cylinder containing a known volume of water to estimate bulk volume of the samples. The bulk volumes of the core plugs were calculated before the oven-drying stage by measurement of the core plugs' cylindrical dimensions.

Porosity, n, was calculated from the following equation

$$n = \frac{W_f - W_d}{V\rho_w} \tag{2-1}$$

where

n is porosity with unit of fraction [-] or percentage

W_f is saturated mass [M]

W_d is dry mass [M]

ρ_w is water density [ML^{-3}]

V is bulk volume of sample

For the core plugs, $V = \pi r^2 l$

where r is the radius of the core plug [L]

l is length of the core plug [L]

For the chip samples, V is estimated as described above.

2.3.2.2 Moisture content

A laboratory experiment was set up to investigate effect of moisture content on measurement of mini-permeameter-determined permeability. The selected plugs were fully saturated with water, left to dry and finally fully dried in an oven at 60^0 C for at least 24 hours. At each drying stage both moisture content and permeability were measured.

Samples selected for measurement of moisture contents were fully saturated and then dried in steps. Firstly the selected samples were fully oven-dried and then were saturated. The corresponding fully dried and saturated masses were weighed with a balance of an accuracy of 0.01 g. The saturated samples were then oven-dried (about 40^0 C) in steps. After a certain times, the samples were taken out of the oven and reweighed to obtain their partly wetted masses (W_{wet}). The moisture content for each drying step was calculated using equation (2-2).

$$\theta = \frac{W_{wet} - W_d}{V_b \rho_w} 100 \qquad (2\text{-}2)$$

where:

θ is moisture content [%]

W_d is fully dried mass [M]

W_{wet} is partly wetted mass [M]

ρ_w is the density of water; and

V_b is the bulk volume of the sample [L^3].

For core plugs (cylindrical) samples: $V_b = \pi r^2 l$.

For the irregular shaped samples, as similar method was undertaken.

2.3.2.3 Hydraulic conductivity measured with a falling head permeameter

In this study some heat-shrink wrapped samples were measured using falling head permeametry. The falling head permeameter (Fig.2-3) consists of a 4-mm internal diameter standpipe attached to a wall-mounted chart marked with mm graduations. A water tank, which has an overflow pipe to maintain water at a constant level, was located below the standpipe. A wrapped core plug was submerged in the constant-head water tank and connected to the graduated standpipe. Synthetic groundwater was pumped into the system up into the standpipe. The fall in head in the standpipe through time was recorded and based on Darcy's Law, the hydraulic conductivity, K, is calculated using equation (2-3).

$$K = \frac{aL}{At} \ln\left(\frac{h_1}{h_2}\right) \qquad (2\text{-}3)$$

where:

a is cross sectional area of standpipe [L^2]

A is cross sectional area of sample [L^2]

L is length of sample [L]

h_1 is head at t1 of measurement [L]

h_2 is head at a time $t2$ of measurement [L]

t is elapsed time between time t1 and t2 of measurement [T]

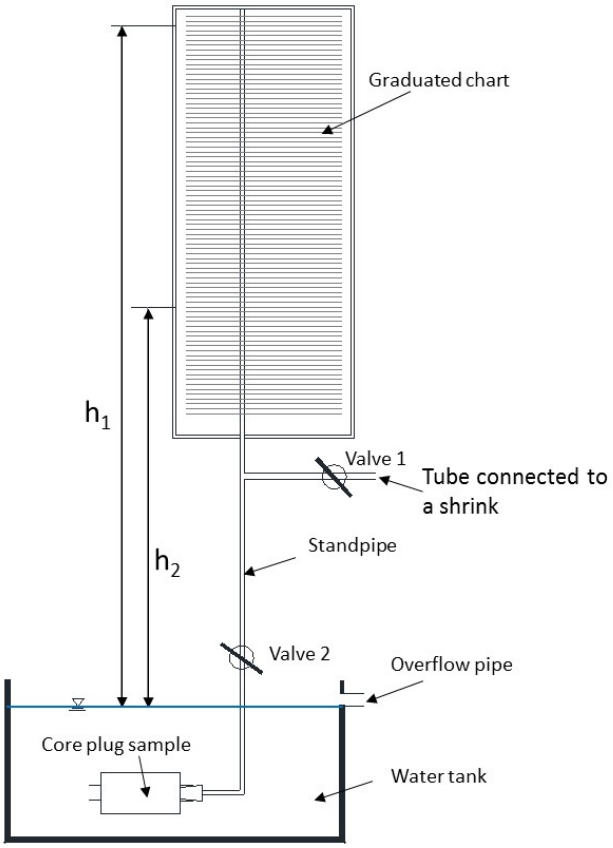

Fig.2-3. Diagram of a set up for falling head permeameter measurement.

Detail of the experimental procedures is provided by Greswell (2010).

It is important to ensure no air bubbles are trapped inside the sample because this may reduce permeability of the samples.

Hydraulic conductivity was calculated in a Microsoft Excel spreadsheet made by Richard Greswell using Darcy's Law. All spreadsheets can be found in Appendix 1.

An example of a measurement is shown in Fig.2-4. It is clear that the measurement follows the theory well, equation (2-3) being a linear relationship between log(h) and t.

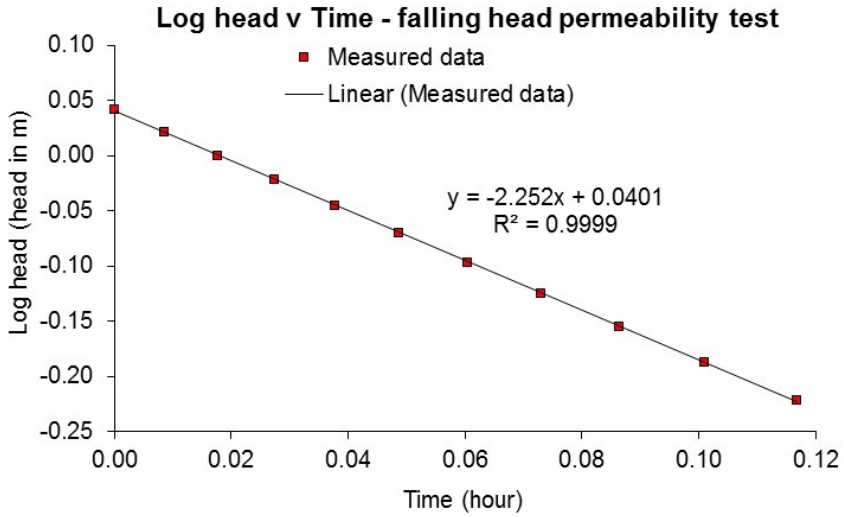

Fig.2-4. Falling head test for plug sample C1-3 from Cumbria, northwest England.

For each sample, the test was performed up to three times in the same flow direction immediately after each other, then with flow in the opposite direction. Almost all tests give similar results, but a few showed small differences. A geometric mean of the results was calculated and then taken as the representative value of hydraulic conductivity of the sample.

2.3.3 Permeability measurement using a probe/mini-permeameter

2.3.3.1 General description of probe/mini-permeameters

Probe or mini-permeameters have been widely used to quantify heterogeneity of media at different scales (e.g. Goggin et al., 1988a, Goggin, 1993, Davis et al., 1994, Bloomfield and Williams, 1995, Bloomfield et al., 2006, McKinley et al., 2011). Dykstra and Parsons (1950) introduced "probe" permeability measurements that were the first form of mini-permeameters. Eijpe and Weber (1971) developed a "mini" permeameter to measure permeability for rock and unconsolidated sands. Goggin (1988a) used a mini-permeameter to study heterogeneity of aeolian Jurassic aged Page Sandstone outcrop in Northern Arizona. Kittridge et al. (1990)

examined the permeability of outcrop and subsurface Permian aged carbonates in south-eastern New Mexico, America. Dreyer et al. (1990) used a similar instrument to study the correlation between lithofacies and permeability in the delta-plain distributary channels of the Jurassic aged Ravensar Group in Yorkshire, England. Davis et al. (1994) modified the gas mini-permeameter to a lightweight, syringe-based air mini-permeameter (LSAMP) to facilitate permeability at outcrops. Bloomfield et al. (2006) employed a mini-permeameter to characterize permeability distributions and correlations between sandstone lithofacies and permeability in the Abbey Wood borehole near Delamere, Cheshire, England. McKinley et al. (2011) used a mini-permeameter to study the relationship between depositional characteristics and permeability at an outcrop in Styrrup Quarry, South Yorkshire, England. Many other works relating to use of mini-permeameter can be found in both hydrocarbon and hydrogeology research.

Mini-permeameters are capable of quickly obtaining a large number of accurate, inexpensive, non-destructive measurements of permeability on flat sample surfaces. Mini-permeameters have been preferred in studying heterogeneity as they are able to investigate at much greater sampling densities and on much smaller scales than is possible with traditional techniques (Dinwiddie et al., 2003). Mini-permeameters can be operated either in steady-state conditions as preferred by many of the above authors or in unsteady-state conditions (e.g. Jones, 1992), the latter being effective in providing rapid estimations on low-permeability samples. Theoretical and recommended practices are described in Halvosen and Hurst (1990) and Sutherland et al. (1993).

Mini-permeameters allow compressed gas, normally nitrogen, to be forced into a dry, clean surface of a porous medium via a tip which is topped by rubber to ensure a good seal (Fig.2-5).

Gas forced into the porous surface under pressure flows freely in a radial pattern and exits through the free surface. Inflow gas flow rate and pressure are measured by an electronic mass-flow meter and an absolute pressure transducer respectively. Intrinsic permeability is calculated using a modified version of Darcy's Law (e.g. Goggin et al. (1988b) (Equation 2-4).

$$k = \frac{2\mu P_1 Q}{aG_o(P_1^2 - P_0^2)} \tag{2-4}$$

where:

k: intrinsic gas permeability (L^2)

P_1: injection pressure ($ML^{-1}T^{-2}$)

P_0: outflow atmosphere pressure ($ML^{-1}T^{-2}$)

Q: volumetric flow rate at injection pressure P1 (L^3T^{-1})

μ: gas viscosity ($ML^{-1}T^{-1}$)

a: internal tip-seal radius (L)

G_0: geometrical factor (-). This factor depends on relative dimensions of the tip seal and sample size.

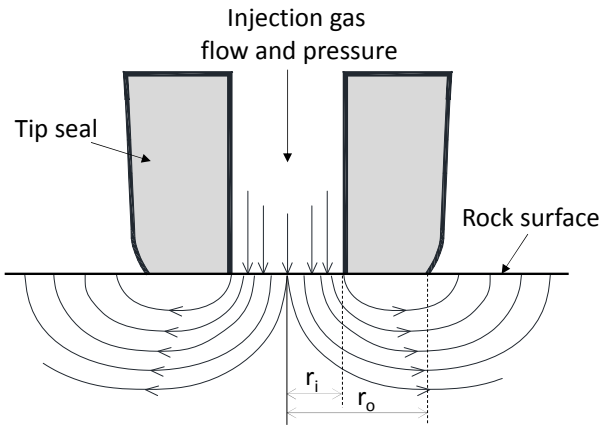

Fig.2-5. Diagram of tip seal and the gas flow pattern in homogeneous porous rock (adjusted from Goggin, 1993).

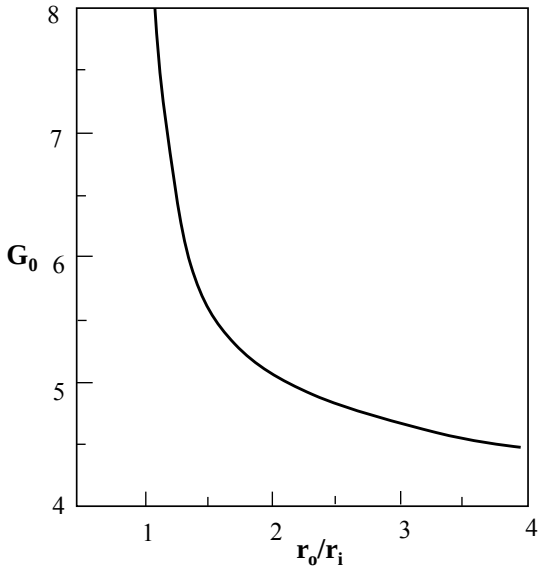

Fig.2-6. Geometric factor as function of outer to inner ratio of tip seals (adjusted from Goggin et al., 1988b).

The geometric factor G_0 should be estimated from the relative ratio of outer radius (r_o) and inner radius (r_i) of the tip seal (Fig.2-5). (Goggin et al., 1988b) developed a model to predict G_0 (Fig.2-6). Although this prediction is only valid for isotropic and homogenous samples, both Goggin et al. (1988b) and Halvorsen and Hurst (1990) found good agreement between theoretically derived and empirically derived G_0 from core plug of known tip seal dimension.

Sutherland et al. (1993) listed primary factors affecting gas flow response entering the sealed area in steady-state measurements, including: 1) gas sample permeability; 2) gas injection pressure; 3) viscosity of gas at injection pressure and temperature; 4) gas slippage (Klinkenberg effect); 5) high velocity flow effect; 6) sealing quality between the probe tip and the sample surface; 7) geometry of flow gas flow in sample; and 8) tip seal quality. Of those, factor 2-5 can be estimated, and if the geometry of gas flow can be defined, permeability at the injection point can be calculated using a modified form of Darcy's Law (Equation 2-4). The geometry of

gas flow around the measured point is only easily-defined for homogeneous and isotropic samples (Sutherland et al., 1993).

In this study, a steady-state Temco Mini-perm/probe permeameter MP-402 (Fig.2-7) was used to perform measurements of permeability for the Preston Laundry Borehole core, core plugs drilled from the Preston Laundry Borehole core, and for two sandstone outcrops at Wolverly, Worcestershire and at Bridgnorth, Shropshire (Chapter 5). The device was kindly lent by the British Geological Survey (Dr Andrew Butcher). The apparatus used a software package named "SmartPerm for MP-402" to run it. A reading is recorded once the software has determined that a reading is stable (Fig.2-9), the latter being defined by pre-set limits. The Temco mini-permeameter is designed to measure permeability ranging from 0.1 milliDarcy (9.87 x 10^{-17} m^2 or 8.33 x 10^{-5} m/d at 20^0C) to 5 Darcy (4.93 x 10^{-12} m^2 or 4.17 m/d at 20^0C) with an accuracy of ±2% (www.temco.com).

Fig.2-7. A photo of the air probe /mini-permeameter apparatus set up: The Temco Mini-permeameter control box including a compressed gas cylinder (left), a core stand (right), and a computer connect to the system (middle).

Fig.2-8. Close view of the tip sealing against a core sample.

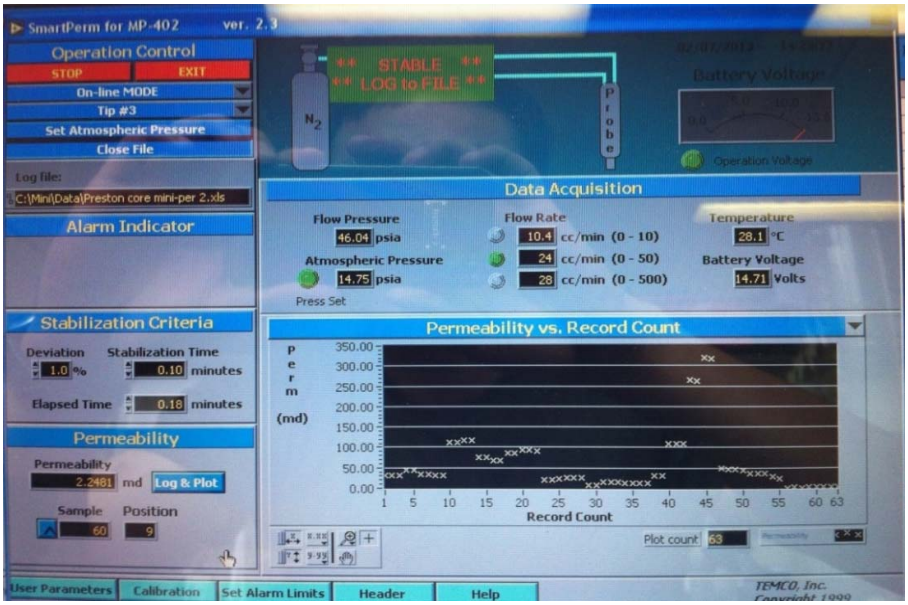

Fig.2-9. A photo of the SmartPerm software interactive screen showing that the system is stable to record a reading (message at top centre).

2.3.3.2 Calibration

Mini-permeameters can be calibrated either empirically or theoretically, provided they have a good tip seal and there is a symmetrical flow geometry into a homogeneous, isotropic porous medium (Halvorsen and Hurst, 1990, Goggin, 1993). Both methods provide good results (Eijpe and Weber, 1971, Goggin et al., 1988b, Halvorsen and Hurst, 1990, Sutherland et al., 1993,

Jones, 1992). Halvorsen and Hurst (1990) converted mini-permeameter flow rate into permeabilitiess by correlating mini-permeability flow rate to core plugs of known gas permeabilities, and by an analytical solution. The core plugs can be at the same interval as mini-permeameter measurement or from set of "homogeneous" core plug with conventional Hassler-sleeve permeability measurements.

Comparison with core plug permeability at the same intervals involves operation of mini-permeameter either at the position before core plugs are taken, or on core plugs themselves. Mini-permeameter flow rate measurements on both ends of the core plugs or at the position where later core plugs were taken were plotted by Halvorsen and Hurst (1990) against known permeabilities, at given fixed pressure rates and a given tip seal. The relationship between flow rate and permeability was then used to compute permeability for all subsequent mini-permeameter measurements, provided the pressure and tip seal size remain the same as in the calibration experiments. Halvorsen and Hurst (1990) performed calibration experiments for mini-permeameter flow rates against Hassler-sleeve core plug permeabilities and found that heterogeneous core plugs result in a weak correlation between flow rate and permeability (Fig.2-10a), whilst reasonably homogeneous core plus give a better correlation (Fig.2-10b).

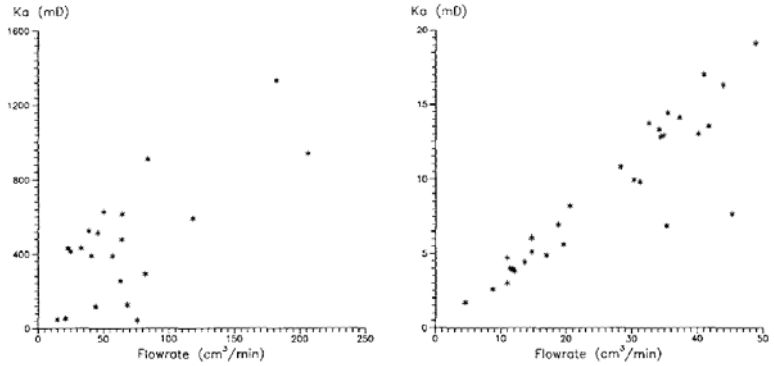

.a) b)

Fig.2-10. Plots of mini-permeameter flow rates versus Hassler-sleeve core plug permeabilities (Ka) from: a) heterogeneous reservoir, and b) homogeneous reservoir (from Halvorsen and Hurst, 1990).

For a set of "homogeneous" core plugs of a wide range of permeabilities, the core plugs can be examined for heterogeneity by visual examination, repeated measurement and with computer tomography (CT)-scanning (Halvorsen and Hurst, 1990, Goggin, 1993). Fig.2-11 shows a good correlation between flow rates and permeability for a calibration using homogeneous core plugs.

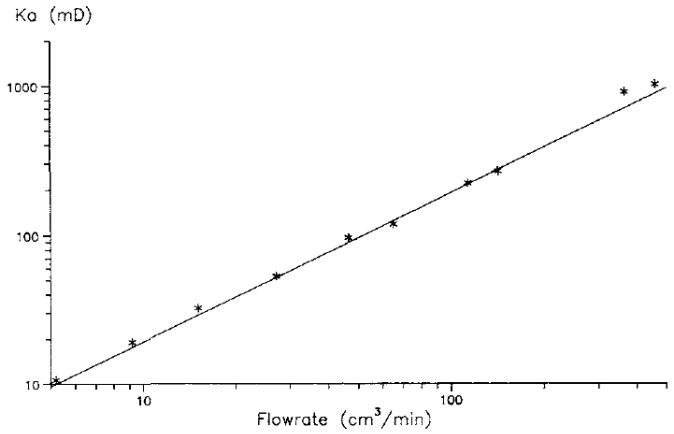

Fig.2-11. Plot of averaged mini-permeameter flow rate versus Hassler-sleeve homogeneous core plug permeabilities (Ka) (from Halvorsen and Hurst, 1990).

The analytical solution was introduced by Goggin et al. (1988b) that employs solution of G_0 (in Equation 2-4) with the assumption of neglecting gas slippage (Klinkenberg) and high-velocity flow effects. Goggin et al. (1988b) used a numerical solution to estimate the geometric factor G_0 that is a function of ratio of outer radius to inner radius of tip seal and sample geometry. Halvorsen and Hurst (1990) employed empirical calibration to estimate G_0 values from mini-permeameter measurements on a set of homogeneous core plugs of known permeabilities (K_g).

From Equation 2-4, they plotted K_g versus the term $\frac{2\mu P_1 Q}{(P_1^2 - P_0^2)}$. G_0 can be calculated from linear regression analysis (y = cx) with slope of best fit c = 1/(aG_0) (Fig.2-12).

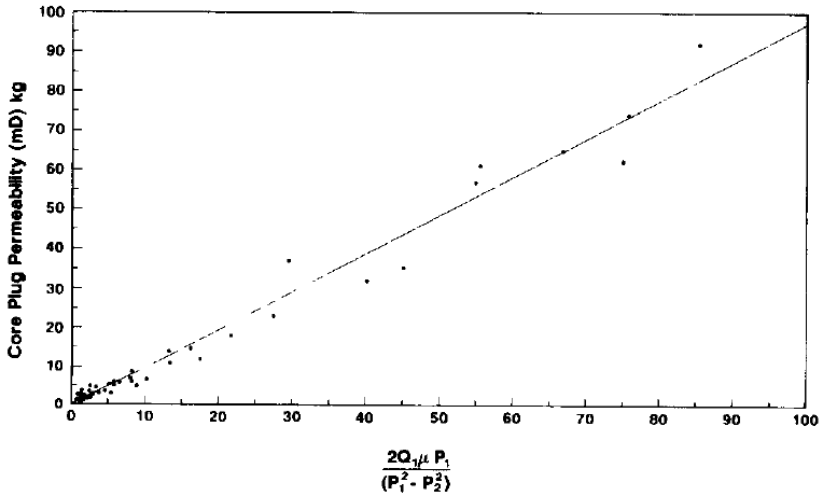

Fig.2-12. Plot of core plug permeabilities versus flow and pressure rate combination from Equation 2-4. The best fit trend line has slope of 0.9715 and R^2 = 0.989, giving G_0 = 5.15 (from Sutherland et al., 1993).

In this work, since a set of standard "homogeneous" core plugs is unavailable, the mini-pemeameter flow rate correlating to permeability was not performed, but the accuracy of mini-pemeameter flow rate measurement was calibrated using a soap film flow equipment was performed in the laboratory base at British Geological Survey Wallingford prior to subsequent mini-permeameter measurements.

The mini-pemeameter was evaluated by operating permeability measurement using the mini-permeameter on the known-permeability core plugs samples of the Preston Laundry Borehole core (Chapter 4). At the ends of each core plug, four to five points were measured with the mini-permeameter, and at each point, up to five repeated measurements were made. The correction for mini-permeameter derived permeability then will be adjusted.

2.3.3.3 Factors affecting mini-permeameter measurements

Although relatively simple devices, precautions must be taken when operating mini-permeamters. These include effects of slippage (Klinkenberg), high flow velocity, tip seal and sealing quality, and drying. The following subsections describe these effects and how to address them.

a) Slippage (Klinkenberg) effect

Permeability measured with gas as the permeant tends to be greater than permeability measured with liquid as permeant (e.g. Klinkenberg, 1941; Monicard, 1980). This is caused by the "slippage" effect along the pore wall of samples that is in contrast to fluid flow where flow velocities are zero at the pore wall. Gas molecules are moving at high speed and collide with each other after travelling a distance which is called as the "mean free path". The mean free path depends inversely on both mean pressure and molecular mass: the mean free path is greater for low pressure and shorter for higher pressure. At the pore wall, there will be some periods where there is no contact between gas molecules and pore wall, i.e. there is a gas 'slip' velocity at the pore wall, and gases move through the porous media faster, leading higher permeability measurement compared to fluid flow which is stationary at the pore wall.

Klinkenberg (1941) experimented on porous media and suggested a relationship, equation (2-6) between gas intrinsic permeability, a slippage factor and liquid intrinsic permeability.

$$k_g = K_L\left(1+\frac{b}{P_m}\right) \qquad (2\text{-}6)$$

where:

k_g is gas intrinsic permeability [L^2]

k_L is liquid intrinsic permeability [L^2]

P_m is mean pressure [$ML^{-1}T^{-2}$]

b is a gas slippage (Klinkenberg) factor which is constant for particular gas in a particular porous medium.

The gas slippage factor, b, can be estimated either from empirical slippage factor - gas permeability relationships or from multiple rate/pressure measurements on the same sample (Sutherland et al., 1993).

Note that the term $(1 + b/P_m)$ is always greater than or equal to 1.0, thus the apparent gas permeability is always greater than or equal to the liquid permeability of the porous medium. As the mean pressure increases, the term $(1 + b/P_m)$ approaches 1.0, and the apparent gas permeability approaches the liquid permeability. The Klinkenberg effect reduces with increasing mean pressure. The Klinkenberg effect is only noticeable with low gas pressure or for low permeability materials with permeability of less than 20 mD (about $2.0x10^{-14}$ m^2 or 0.02m/d) according to Goggin et al. (1988b).

In this study, the gas slippage may not cause significant problems for the mini-permeameter measurement on the borehole core (Chapter 4) and in situ permeameter measurements (Chapter 5) because their permeabilities are almost all greater than 20mD.

b) High velocity flow

High velocity flow effects (or inertial effects) occur where viscous flow no longer dominates. To deal with this effect, permeability is measured at several different pressures and the injection

pressures lying in the linear region of the mass flux / pressure gradient curves are selected. The high velocity flow effect can be eliminated with a mini-permeameter operating with pressure decay measurement (e.g. Jones, 1992). Goggin et al. (1988b) found that high velocity flow effect is significant for samples having permeability of greater than 1000 mD (about $9.9x10^{-13}$ m^2 or 0.83 m/d at 20^0 C).

In operating the mini-permeameter in this study, the injecting pressure was gradually increased to achieve sufficient pressure gradient. These pressures were monitored by transducers. The SmartPerm software used for the mini-permeameter shows flow rate and pressure on a Windows user-interface (Fig.2-9) on which pressure gradient can be controlled and low input pressure adjusted to achieved steady-state conditions necessary before a reading can be recorded (Fig.2-9). Some measurements on very low permeability units (e.g. mudstone-bearing units) where it took a very long time to achieve a stable flow and on other lithofacies where a nearby fracture caused exceptionally high permeability values were excluded from the permeability results.

The high velocity flow effect could not affect the mini-permeameter measurements for borehole cores (Chapter 4) since their permeability are less than 1000 mD, but may be problem for field measurements (Chapter 5). However, because of the unknown drying conditions at the sites and the necessary of relative values of permeabilities to correlate lithofacies to permeability within an outcrop, the mini-permeameter measurement are reasonably accepted, and, ideally, high velocity flow effects at these sites could be interesting for further study.

c) Tip seal geometry and penetration depths

The gas is injected into the sample surfaces via a tip seal (Fig.2-5). The tip seal allows gas to travel freely into sample surface and prevents gas leakage between the tip seal and the sample surface. The tip seals are made of compressible, impermeable silicon rubber, and are small enough compared with the sample size to efficiently seal without damaging the sample surface. The gas leakage through tip seal has been checked by applying tip seal against impermeable surface to ensure no gas leakage through the tip seal, and avoided by using good tip seals, and by repeating measurements for points where gas leakage is suspected. The tip seals are also designed to have appropriate dimensions to examine heterogeneity of the sample. Table 2-2 shows a range of tip seal sizes with different outer and inner radii designed for the Temco minipermeameter.

The penetration depths of mini-permeameter permeability measurements depend on the tip seal size and the hydraulic properties of the sample. Goggin (1988b) used a numerical solution technique to model homogeneous media and found that the penetration depth of mini-permeameter measurement was about four times the inner tip seal radius. On the other hand, Jensen et al. (1994) found that 90% extent of the probe response came from within 2.2 times the inner radius. Given the list of inner radii of the tip seals supplied for the mini-permeamter (Table 2-2), penetration depths were estimated. For practical purposes, tip seal #3 was suggested to be the most convenient to use (Andrew Butcher at BGS Wallingford), thus it was employed throughout the laboratory and in situ measurement of mini-permeameter in the project though the other tip seals were also used as comparisons during method development.

Tip seal 3 has outer and inner radii of 9.5 mm and 3.2 mm respectively, giving estimated penetration depths from 7.0 mm to 12.7 mm (Table 2-2).

Table 2-2. Tip seal used for a mini-pemeameter and estimated effective measurement depths

Tip ID	Tip radius (mm)		Effective penetration depth (mm)	
	outer	inner	2.2 times inner radius*	4 times inner radius**
1	2.4	0.8	1.8	3.2
2	4.8	1.6	3.5	6.4
3	9.5	3.2	7.0	12.8
4	12.7	6.4	14.1	25.6
5	25.4	9.5	20.9	38.0

* According to Jonsen et al. (1994)
** According to Goggin et al. (1988b)

d) Drying effect

Mini-permeametry measurement can be adversely affected by moisture contents of samples. Halvorsen and Hurst (1990) and Sutherland et al. (1993) indicated that the effect of saturation on permeability is only noticeable for materials of low permeability (2-20 mD, about 2×10^{-15} - 2×10^{-14} m^2), and is insignificant on materials with permeability of greater than 100 mD (about 9.9×10^{-14} m^2). Davis et al. (1994) found that saturation has an effect on mini-permeameter measurements, samples with moisture contents of 5 % causing errors of 5%.

In this work, mini-permeameter measurements were performed on core and core plug samples from Preston Laundry Borehole cores with various levels of saturation (see Chapter 4). To test the effect of this, a group of samples were oven-dried, resaturated, then dried in steps. Permeabilities were then measured using the mini-permeameter for each drying and wetting state of the samples. Full report on effect of the moisture content can be found in Chapter 4.

e) Laboratory operation of the mini-permeameter

The Temco mini-permeameter has a probe mounted on a frame when used in the laboratory (Fig.2-7). The frame can be moved up and down so that the probe can form a seal on a sample which is placed in the core holder (Fig.2-8a,b). During operation, a constant force is applied by the probe on the sample, controlled by a pneumatic cylinder and pressure regulator.

f) In situ operation of the mini-permeameter

For in situ measurements, a hand-held probe is employed: this includes a shoulder butt, as on a rifle. This may result in longer times for the mini-permeameter to obtain stable conditions. Differing application pressures by the operator can cause problems (Sutherland et al., 1993). To maintain approximately constant application force against outcrop surface, the probe can be spring mounted, thus controlling the maximum application force to be equal to the compressibility of the spring (Sutherland et al., 1993). However, a pneumatic cylinder is better choice over spring mounted probe for in situ field mini-permeametry (Sutherland et al., 1993).

In this work, a field-portable hand-held probe supplied as part of the Temco mini-permeameter package was applied normal to outcrop faces while maintaining constant flow pressure to reach a steady state where a measurement is recorded (as shown Fig.2-9). At each point, up to ten measurements were made, then averaged to obtain a representative value.

Since hand-held tool application is less consistent than the mechanical application of the probe in the laboratory rig, it might be expected that field results are less repeatable. However, calibration experiments for homogeneous core plugs show that there is only slightly less accurate measurements for the hand-held instrument than for probe core-holder frame (Goggin,

1993). In practice, after some experimentation in the present study, field measurements were taken by applying the maximum possible pressure by the operator, thus obtaining some consistency.

There are several sampling schemes for mini-permeametry in situ, including: a) random or facies based sampling; b) regular grids; c) horizontal and vertical transects; d) lateral series of vertical transects within a single parasequence; e) pads- group of measurements around points in a large scale transect or grid (Goggin, 1993). The sampling depends on scale of heterogeneity of formation and scale of interest, and is unlike the conventional core sample or core plug samples which are normally regular. In this study, sampling was chosen based on variation of lithofacies/sublithofacies.

CHAPTER 3

THE ENGLISH PERMO-TRIASSIC SANDSTONE SEQUENCE

3.1 Introduction

The English Permo-Triassic sandstone sequences are heterogeneous having been formed in a range of sedimentary environments. Understanding the heterogeneity, sedimentary structures and palaeo-environments is essential if the influences of lithology on hydraulic properties are to be understood. Within the sequence, there are two dominant, 'macro'-lithofacies – fluvial and aeolian. In addition, there are many '(sub)lithofacies', or simply 'lithofacies', that represent, for example, channel base or channel fill deposits. There is little collated information on the range of geometries of, in particular, these lithofacies in the English sequence, something that would be useful if correlations between lithofacies and hydraulic properties are established and they are to be used in helping predict solute movement. It would also be helpful to get idea of how hydraulic property values vary regionally compared with how they vary locally.

The aims of this chapter are therefore:

1. to provide an indication of the range of lithofacies seen in the Permo-Triassic Sandstone sequence across England;
2. to gather evidence on the geometries of various lithofacies seen within the sequence;
3. to provide a first pass idea of the hydraulic property variability within units, within outcrops, between outcrops, between palaeoenvironmental conditions and between regions.

However, achieving aims 1-3 will allow the results of the more detailed work on lithofacies/hydraulic property correlations described in Chapters 4 and 5 to be placed in context, will provide evidence for later construction of computer representations described in Chapter 6, will provide an indication of the current state of knowledge, and finally will indicate (qualitatively) the correlation between hydraulic properties and 'macro-lithofacies', i.e. fluvial v. aeolian lithofacies.

Sandstone sequences from sixteen outcrops and quarries across the country were examined, and a review of previous work undertaken. The outcrops were from five regions: the northwest, Cheshire, Shropshire, West Midlands, and the southwest (Fig.3-1). Sites were chosen to attempt to cover a range of possible basins and sedimentary environments, based on the use of the literature, and particularly Benton et al. (2002), and the BGS Britpit software kindly loaned by BGS. However, the survey is not comprehensive, with only a few of the very numerous exposures having been visited and hydraulic property measurements made only on small numbers of samples. A more detailed version of this chapter, including extensive literature summaries for the sites visited, is included as Appendix 6.

Sections 3.2 and 3.3 provide geological history and sedimentological overviews, and subsequent subsections describe each of the sites visited. A final section concludes.

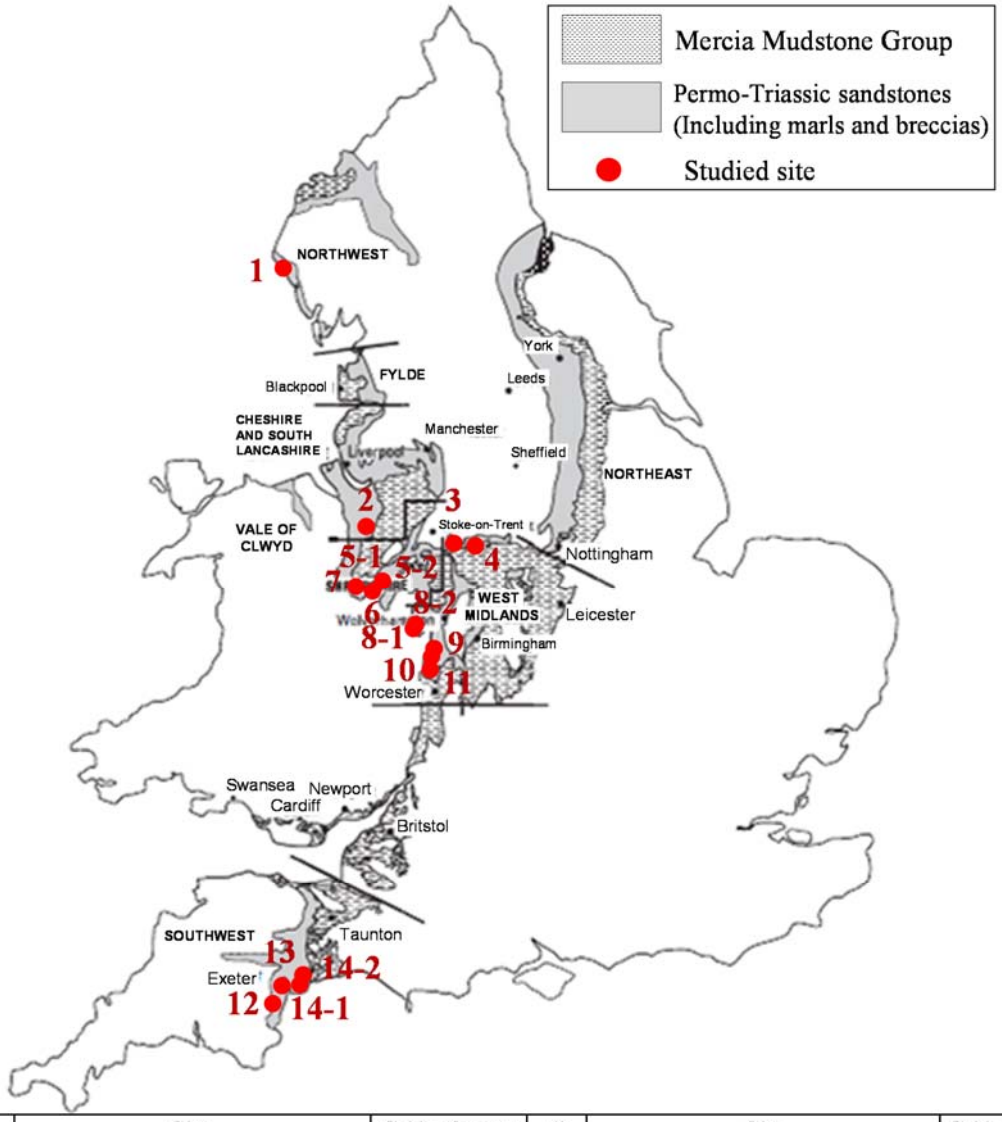

#	Site	Grid reference	#	Site	Grid reference
1	St Bees Head, west Cumbria	NX950123	8-1	Brignorth Town, Shropshire	SO717928
2	Rawhead, Cheshire	SJ510540	8-2	Bridgnorth Hermitage, Shropshire	SO727934
3	Hulme Quarry, Staffordshire	SJ 926445	9	Kinvern Edge, Staffordshire	SO836835
4	Croxden Quarry, Staffordshire	SK016413	10	Kingsford, Worcestershire	SO829818
5-1	Grinshill Old Quarries, Shropshire	SJ522238	11	Wolverley, Worcestershire	SO827794
5-2	Grinshill Working Quarries, Shropshire	SJ525238	12	Dawlish, Devon	SX971774
6	Nesscliffe, Shropshire	SJ385194	13	Ladram Bay, Devon	SY095849
7	Leaton Shropshire	SJ472181	14-1	Sidmouth-western side , Devon	SY105861
			14-2	Sidmouth-eastern side, Devon	SY129873

Fig.3-1. Visited English Permo-Triassic Sandstone outcrops (adjusted from Allen et al., 1997).

3.2 Outline geological history

During the Variscan Orogeny (late Carboniferous time), the areas are now southern England and Wales, northern France and Germany, eastern Europe, to North America were folded and faulted because of the tectonic collision of the Gondwana and Laurussian and together with other microplates to form the supercontinent Pangaea (Woodcock and Strachan, 2000).

In early Permian time, thermal relaxation led to the formation of depression basins across England and Wales, and Ireland. Northward flowing rivers across Britain drained the Variscan highland to the south (Woodcock and Strachan, 2000). Deposits of breccia and coarse sandstones eroded from highlands gradually filled the basins as alluvial flood and fan deposits (Allen et al. 1997). In England, often the basins were fault-hinged on one side. The breccias were overlain by well-sorted, cross-stratified sandstones such as those of the Bridgnorth Sandstones, Penrith Sandstones, and Collyhust Sandstones. These sandstones have been interpreted as aeolian deposits which laterally merged with fluvial silts and sands (Allen et al., 1997).

In the mid-Permian, the highlands of the Variscan Orogeny were smoothed out by aeolian and fluvial deposits. This enabled marine transgressions in late Permian times, and these deposited limestones, dolomites and evaporates with continental mudstones and sandstones around basin edges (Allen et al., 1997).

From the late Permian to early Triassic time, the basins were filled with continental fluvial and aeolian sediments. The Permian sequence was covered gradually and diachronously by thick clastic deposits that now form the Sherwood Sandstone Group. They were mainly fluvial deposits and formed by a major braided river system. The deposits generally had basal channel lags, fining-upward channel sands, and covered with overbank silts or floodplain muds. Aeolian

units, marls and breccias are also locally found in the Sherwood Sandstone Group (Allen et al., 1997).

The Triassic Sherwood Sandstone Group is overlain by the Mercia Mudstone Group which was partly marine and was probably deposited in shallow sea, or lakes connected with the sea, consisting of calcareous and evaporate-bearing mudstones and dolomitic siltstones, with some sandstones and anhydrite units (Woodcock and Strachan, 2000; Hounslow and Ruffell, 2006).

3.3 A Brief outline of the sedimentological background of the English Triassic sandstone sequence

The English Permo-Triassic sandstones are typically continental fluvial and aeolian red-bed sequences and broadly similar sandstones are widespread internationally.

Sedimentological cycles are defined as a repetition of a series of lithological materials through a sequence (Duff et al., 1967). Sedimentary cycles have long been recognised for the British Devonian Old Red sandstone (e.g. Allen, 1964; Selley, 1988), and for the Permo-Triassic sandstones in which cycles of different scales varying from about 1 to over 100 m thick occur in the fluvial deposits (e.g. Fitch et al., 1966; Thompson, 1970; Wills, 1970; 1976). Wills (1970) recorded scale hierarchy of cycles in the Permo-Triassic sandstones: micro-cycles at beds scale; mio-cycles formed by groups of micro-cycles and having thicknesses of up to 100 m; and magna-cycles consisting of groups of mio-cycles, normally equivalent to formations. There is an upward transition from wet (fluvial) to dry (aeolian) conditions in micro-cycles. Thompson (1970) and Wills (1970) defined full micro-cycles in upward sequence as: coarse-grained, pebbly sandstone resting on erosion surface at base; medium-grained followed by cross-laminated sandstone; fine-grained, up into flat-laminated sandstone; mudstone, covered with aeolian sandstone at the top. According to Wills (1976), cycles appear in boreholes penetrated

in almost all parts of the Triassic sandstones in the Midlands. Sedimentary cyclicity interpretation has been widely and successfully applied in hydrocarbon reservoir sandstones, but rarely in aquifer sandstones. Bloomfield et al. (2006) recognised metre-scale fining-up cycles in the Helsby sandstone and drying-up cycles in the Wilmslow sandstone (Sherwood Sandstone Group) in a borehole drilled in Cheshire, England.

The aeolian depositional environments produce a variety of sedimentary structures for the English Permo-Triassic sandstones, including plane bedding, planar tabular and trough cross-bedding, plane lamination, cross-lamination, ripples stratification, and irregular wavy (e.g. Thompson, 1970; Karpeta, 1990; Benton et al., 2002). Benton et al. (2002) summarized characteristics of aelian sandstones into three groups: 1) Dunes and draas comprise texturally mature sand grains. The sedimentary structures include large-scale cross-starification, high-angle (up to 30^0) foresets with sets separated by sharp, generally plannar, bounding surfaces; 2) sandsheets characterize with mm-scale bi-modal laminae, scours, granule lags, thin cross-laminated sandstones; 3) damp interdune consists of silty sandstones. The sedimentary structures include irregular wavy or lenticular lamination, slump structure, dominated with adhesion ripples.

3.4 West Cumbria, northwest England

3.4.1 Geological setting

The Permo-Triassic sandstones crop out along coastal cliffs of West Cumbria and in adjoining areas on the eastern margin of the East Irish Sea Basin (Fig.3-2 and Fig.3-3). The sandstones dip and thicken towards the coast (Allen et al., 1997). A large amount of research has been undertaken in the area by UK Nirex Limited (Nirex) and many others (e.g. Strong et al., 1994; Michie, 1996; Chaplow, 1996; Milodowski et al., 1998; Bowden et al., 1998) in relation to

characterization of bedrock in the Sellafield area for storage of radioactive waste. Though the Permo-Triassic sequence is composed of several units here (Fig. 3-4), field work concentrated on the St Bees Sandstone Formation exposures at St Bees Head. Details of the sequence and its geological context are given in Appendix 6.

The St Bees Sandstone is excellently exposed at St Bees Head and consists of very fine- to medium-grained, well cemented sandstones changing from sheetflood sandstone in the lower part to multi-channel sandstones at the top. The St Bees Sandstone Formation is laterally equivalent to the Chester Pebble Beds Formation in Cheshire Basin, but is finer in grain size and free of pebbles (Allen et al., 1997; Hounslow and Ruffell, 2006). The thickness of the St Bees Sandstone is up to 600 m onshore (Michie, 1996; Benton et al., 2002) and up to 1000 m offshore (Michie, 1996). The St Bees Sandstone is interpreted to have been deposited in low sinuosity braided rivers flowing to the north-north-west (Jones and Ambrose, 1994; Michie, 1996; Benton et al., 2002).

Fig. 3-2. Sandstone cliff at South Head, looking St Bees Head, West Cumbria, northwest England.

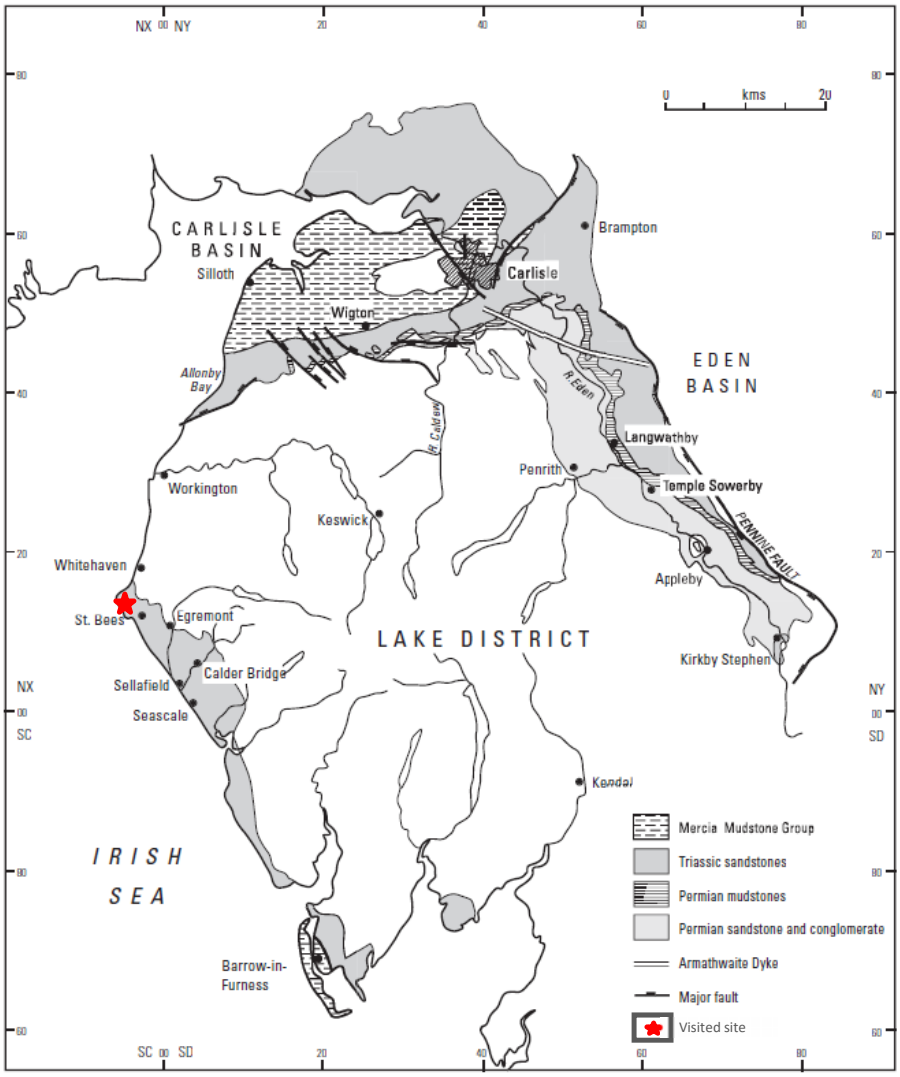

Fig.3-3. Geology of Permo-Triassic sandstones in northwest England (after Allen et al., 1997).

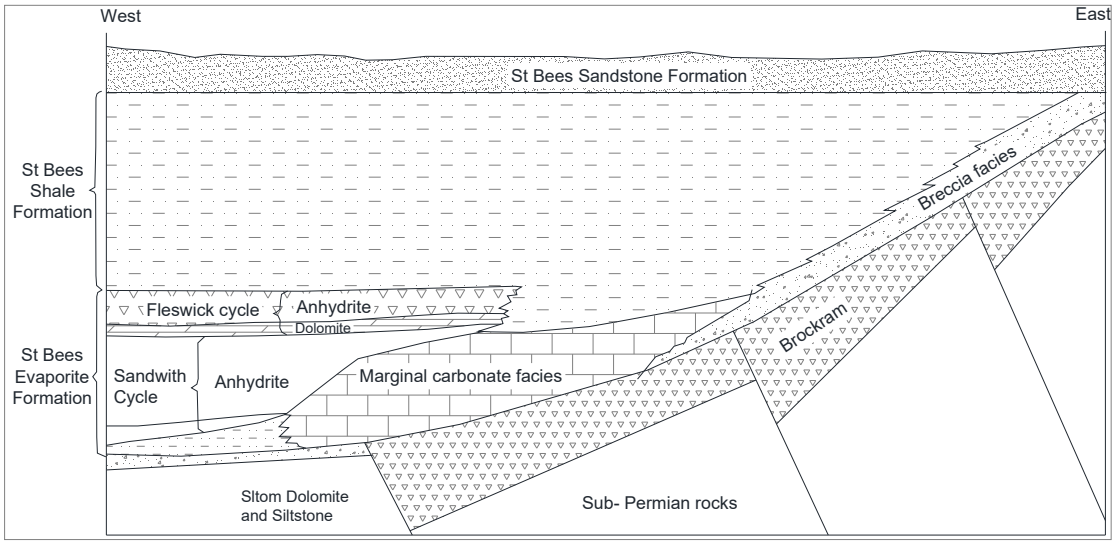

Fig.3-4. Schematic vertical cross-section showing relationships of Permian rocks in Appleby and the Cumbrian Coast group, West Cumbria (adjusted from Akhurst et al., 1997).

3.4.2 Studied site: St Bees Head, West Cumbria, northwest England (NX 950123)

The field site is located along the coast line at South Head, West Cumbria, northwest England (Fig.3-2 and Fig.3-3). The site shows spectacular sea cliffs of the St Bees Sandstone Formation (Fig.3-2) which is the lowest unit of the Sherwood Sandstone Group. The coastal cliffs expose 3D outcrops of up to 90 m high and several hundred metres long of dominantly fluvial systems. The St Bees Sandstone Formation consists of fine-to medium-grained, micaceous sandstone, and some thin beds of siltstone and mudstone without pebbles (Chaplow, 1996; Allen et al., 1997; Benton et al., 2002). The St Bees Sandstone Formation in the area rests gradationally on the St Bees Shale Formation, that crops out at Saltom Bay, and is covered sharply by the Calder Sandstone Formation that appears at St Bees (Chaplow, 1996; Allen et al., 1997; Benton et al., 2002).

The St Bees Sandstone Formation sandstones have plane bedding, planar tabular and trough cross-bedding, and are well-cemented. Ripples, planar- and cross-lamination are common, and some conglomerates occur as lag deposits resting on erosion surfaces, scour and erosion

surfaces showing multi-storey channel systems. The deposits at the field site are interpreted as deposits of a braided river system flowing north-north-west (Chaplow, 1996; Allen et al., 1997; Benton et al., 2002). Rare aeolian units with a fine- to medium-grained sandstone of about 5m thick with well rounded and frosted grains has been recognized in the St Bees Sandstone Formation in NIREX borehole 12A and 14A (Jones and Ambrose, 1994).

The sediment dips towards south-south-west direction, for example dipping 12 degrees at St Bees Head and rarely in a southeast direction as seen at Fleswick Bay (Benton et al., 2002). Allen et al. (1997) indicated that the mudstone units interbedded with the sandstone units were deposted by periodic flood events. The sandstones is cemented by calcite, silica and iron oxide (Benton et al., 2002).

The sandstone at the St Bees Head is interpreted as a deposit of north- north-westerly flowing, sandy, low-sinuosity, braided systems (Jones and Ambrose, 1994; Allen et al., 1997; Akhurst et al., 1997; Benton et al., 2002). At the study site, the St Bees Sandstone Formation is divided into two parts with following features:

The lower part comprises red, brownish-red, very fine- to fine-grained sandstone with bluish-grey bands of mudstone (Fig.3-5, and Fig.3-8). Depositional structures consist of sheet-like sandstone beds with abundant laminations and ripple marks (Fig.3-10b), desiccation cracks, horizontal and sub-horizontal layers. The lower part of the St Bees Sandstone Formation is interpreted as the North Head Member (Benton et al., 2002). John & Ambrose (1994) showed that this part represents sheetflood sandstones.

The upper part of the Formation consists of fine- to medium-grained, micaceous sandstone, laminated flaggy sandstones, and occasional pale green beds. The sedimentary structures of this part include large-scale erosion surfaces, multi-storey channel systems (Fig.3-5, Fig.3-7 and

Fig.3-8), planar tabular and trough cross-bedding, ripple cross-lamination, and water-escape/slump structures (Fig.3-11a,b), discrete bleached layers, and bleached bands (Figs.3-6, 3-7, and 3-8). The sandstone is well-cemented by silica (Strong et al., 1994; Barnes et al., 1994) and carbonate (Fig.3-12a,b). The characteristics of the upper part support Jones and Ambrose's (1994) suggestion of a change from sheetflood sandstone in the lower part to stacked channel sandstone in the upper part.

Fig.3-13 generates vertical cross-section the sandstone cliffs at St Bees Head. It shows transition from the lower part (horizontal stratified sandstones) to the upper parts with cross-stratified sandstone with multiple stacking channels. Widths of channels are in range from tens to hundreds of metres, though it is not easy to see the orientation relative to the thalweg of main channels. Bed thickness are variable, ranging from few cm to about 2 m.

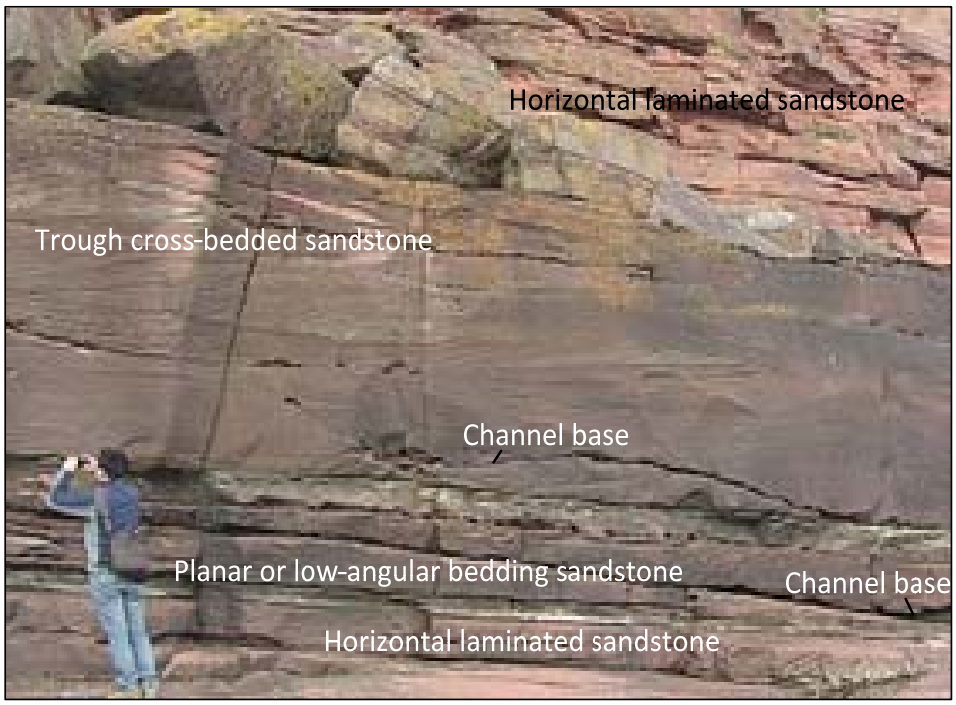

Fig.3-5. Flatform at lower part of the St Bees Sandstone showing horizontally-laminated sandstone at the lower part and channel bases, scour, cross-bedding at the upper part.

Fig.3-6. Planar bedded sandstone interbedded with thin layers of fine, laminated sandstone.

Fig.3-7. Channel base with bleached channel-fill bands above (at the upper part of the picture). This outcrop section is about 3m high by 4m wide.

Fig.3-8. Cross-bedding above bleached lenses of channel-fill (solid arrow) and channel base (open arrow) sandstone.

a) b)

Fig.3-9. a) Cross-bedding overlian by bleached band and plane laminated sandstone, b) multi-set of planar tabular and trough cross-bedded sandstone interbedded with plane laminated sandstone.

a) b)

Fig.3-10. a) Trough cross-bedded sandstone at the hammer; b) Ripple marks.

a) b)

Fig.3-11. a) Deformation structures at the upper part of St Bees Formation: water-escape structures above horizontal laminated sandstone; b) Water-escape deformation structures above horizontal laminated sandstone and below a discontinuous bleached layers.

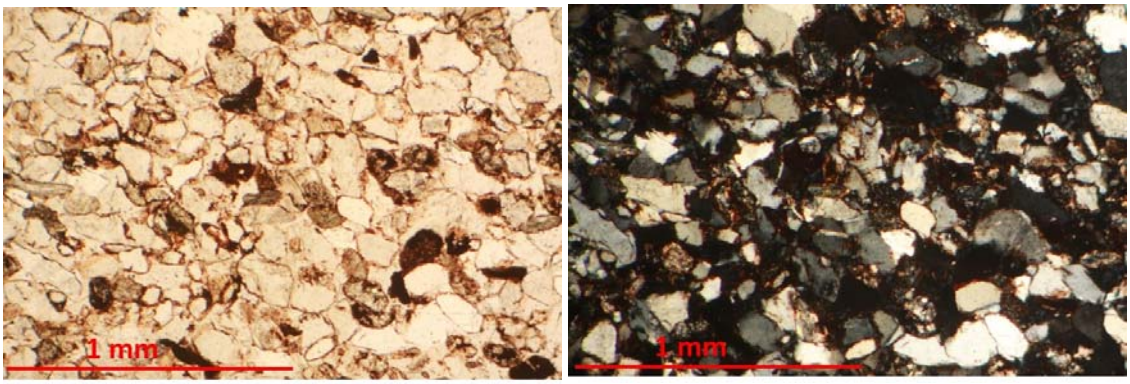

a) b)

Fig.3-12. Photomicrographs of St Bees sandstone at St Bees Head, West Cumbria, showing sandstone of sub-rounded, moderately well-sorted grains, and well cemented: a) with plane light, b) with cross polars.

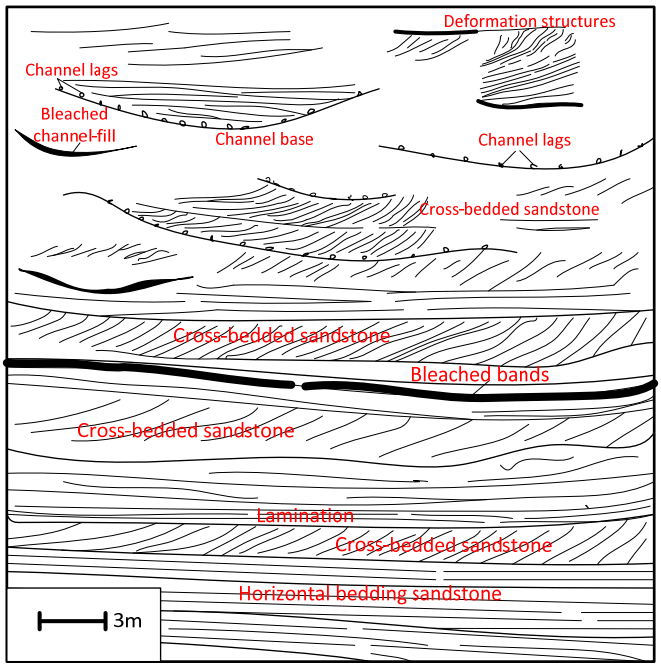

Fig.3-13. Sketch cross-section generating of sea cliff at St Bees Head, West Cumbria, northwest England.

3.4.3 Hydraulic properties

There has been a number of studies on the hydraulic properties of the St Bees Sandstone Formation (e.g. Nirex, 1993; Chaplow, 1996; Black and Brightman, 1996; Heathcote et al., 1996; Littleboy, 1996; Allen et al., 1997). In this study 8 core plug samples were taken from three different beds (C1, C2, C3) of channel fill facies at the St Bees Sandstone Formation at the Bees Head cliffs to determine their hydraulic properties (Table 3-1 and Fig.3-14).

Table 3-1 Sedimentary description for samples collected at St Bees Head, west Cumbria.

Bed/lithofacies	Sample ID	Brief discription
Bed C1	C1-1, C1-2*, C1-3	Very fine- to fined grained, micaceous, low-angle laminated sandstone. Channel fill facies. Samples are separated by 1m to 30m within the bed C1
Bed C2	C2-1, C2-3, C-4*	Very fine- to fined grained, tabular cross-lamianted sandstone interbeded with thin layers of mudstone. Channel fill facies. Samples are separated by 2m to 15m within the bed C2
Bed C3	C3-1, C3-4*	Very fine- to fined grained, tabular cross-laminated sandstones. Channel fill facies. Samples are within a block in bed C3

* vertically oriented sample

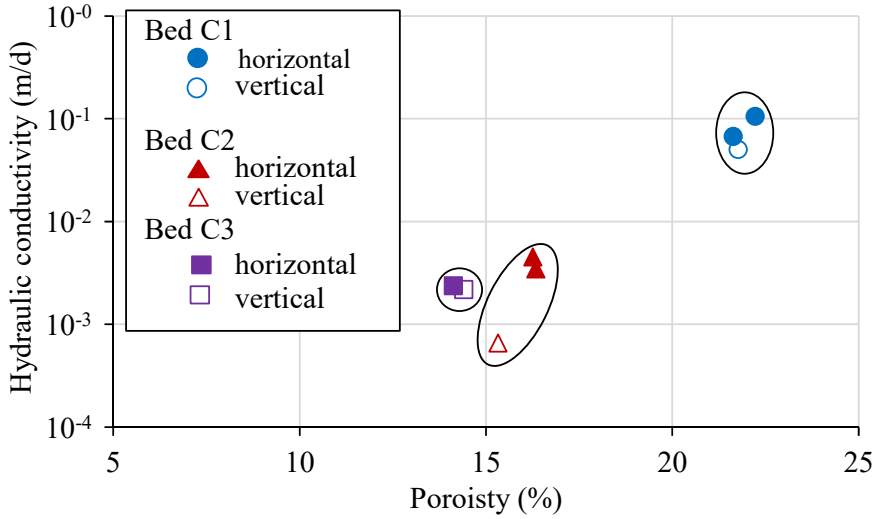

Fig.3-14. Hydraulic conductivity versus porosity for the samples taken at St Bees Head, Cumbria.

Fig.3-14 shows porosity and hydraulic conductivity variations within and between beds (circled) for the St Bees Head Sandstone at St Bees Head, west Cumbria. The low hydraulic conductivity of Bed 2 and Bed 3 reflects the presence of thin mudstone layers and cement. Within bed variation at Bed 1 and 2 probably is caused by thin laminations which may restrict vertical flow.

For the whole region, porosity and hydraulic conductivity (permeability) and their relationship, anisotropy and comparison between fluvial and aeolian systems are described in the following subsections.

3.4.3.1 Porosity

Table 3-2 summarises porosity values for the St Bees Sandstone as collated by Allen et al. (1997). The porosity values range from 13 to 35 %. The samples collected in the current work have porosities from 14 to 22 % with a mean of 18 % and these values are generally in agreement with those reported by Allen et al. (1997).

Table 3-2. Summary porosity dataset for the St Bees Sandstone.

Area	Range (%)	Interquartile range (%)	Median (%)	Mean (%)	Author
Carlisle Basin and Vale of Eden	19.3-34.9	25.3-30.1	26.9	27.4	Allen et al. (1997)
West Cumbria	14.1-22.2	15.1-21.7	16.3	17.8	This study
Cumbria	3.7-27.2	12.9-20.2	15.2	16	Allen et al. (1997)

3.4.3.2 Hydraulic conductivity

Core hydraulic conductivities of the St Bees Sandstone presented by Allen et al. (1997) are given in Table 3-3. The hydraulic conductivities vary over seven orders of magnitude from 1.9 x 10^{-6} to 46 m/d. The wide range in hydraulic conductivity reflects varying grain size and grain sorting, but particularly type and degree of cementation. As with porosity values, higher values of hydraulic conductivity come from the north in Carlisle Basin and Vale of Eden, whereas lower values are from the south in Cumbria.

For the St Bees Sandstone Formation, pumping test hydraulic conductivity (around 2 m/d; Table 3-4) are much greater than core hydraulic conductivity (0.0017 m/d), suggesting the significant effect of fracture flow in the pumping test. Regional hydraulic conductivity obtained from calibrated flow models, however, suggest that the contribution of the matrix hydraulic conductivity dominates.

Table 3-3. Summary hydraulic conductivity for the St Bees Sandstone Formation.

Area	Range (m/d)	Interquartile range (m/d)	Median (m/d)	Geometric mean (m/d)	Author
West Cumbria	0.0007-0.11	0.0023-0.054	0.004	0.0081	This study
Cumbria	$1.9x10^{-6}$ – 0.94	$1.9x10^{-4}$–0.014	0.0013	0.0013	Allen et al. (1997)
Carlisle Basin and Vale of Eden	$5.5x10^{-3}$ -46	0.14 – 0.39	0.23	0.24	Allen et al. (1997)

Table 3-4. Hydraulic conductivity values at different scales of measurement for the St Bees Sandstone Formation in West Cumbria (After Allen et al. 1997).

Measurement method	Hydraulic conductivity (m/d)	
	K	K_h/K_v
Core permeametry	0.0017	4
EPM	0.0026	50
Pumping test bulk K	0.07 - 3.7 (about 2)	-
Model	0.3 - 8.6 x 10^{-4}	4

EMP: Environmental Pressure Measurements
K_h: horizontal hydraulic conductivity; K_v: vertical hydraulic conductivity.

3.4.3.3 Anisotropy

Hydraulic conductivity anisotropy is quantified by calculating the ratio of the geometric means of the horizontal and vertical hydraulic conductivities. Horizontal and vertical hydraulic conductivities and anisotropies for the Permo-Triassic Sandstone in the northwest England are given in Tables 3-4 and 3-5. Normally, horizontal hydraulic conductivity is greater than vertical hydraulic conductivity. The anisotropy ratio for the region ranges from slightly greater than 1 to 4. In West Cumbria, the anisotropy ratio is 4:1 being more permeable in bedding direction (BGS, Nirex, 1993). The anisotropy ratio found in this work at West Cumbria is 1.8:1. Further north this ratio reduces to 1.2:1. EPM (Environmental Pressure Measurement) shows the

anisotropy ratio is up to 50:1. This ratio is greater than core and model anisotropies (4:1) for the St Bees Sandstones.

Table 3-5. Horizontal and vertical hydraulic conductivities for the St Bees Sandstone.

Formation	Area	Direction	Range (m/d)	Interquartile range (m/d)	Median (m/d)	Geometric mean (m/d)	Anisotropy ratio (Kh/Kv)	Author
St Bees Sandstone	West Cumbria	K_h	0.002-0.11	0.004-0.07	0.005	0.04	1.8	This study
		K_v	0.001-0.051	0.002-0.027	0.002	0.022		
	Cumbria	K_h	$1.9x10^{-6}$-0.94	$3x10^{-4}$ - 0.025	$2.9x10^{-3}$	$2.3x10^{-3}$	4.1	Allen et al. (1997)
		K_v	$1.9x10^{-6}$-0.21	$1.4x10^{-4}$-$5.5x10^{-}$	$7x10^{-4}$	$7.2x10^{-4}$		
	Carlisle Basin and Vale of Eden	K_h	$5x10^{-3}$-4.4	0.16-0.41	0.26	0.26	1.2	Allen et al. (1997)
		K_v	0.01-4.5	0.12-0.37	0.21	0.21		

K_h: horizontal hydraulic conductivity, K_v: vertical hydraulic conductivity.

3.4.3.4 Correlation between hydraulic conductivity and porosity

Fig.3-15a,b shows the correlation between core porosity and log hydraulic conductivity for the St Bees Sandstone Formation and the Sherwood Sandstone Group as a whole.

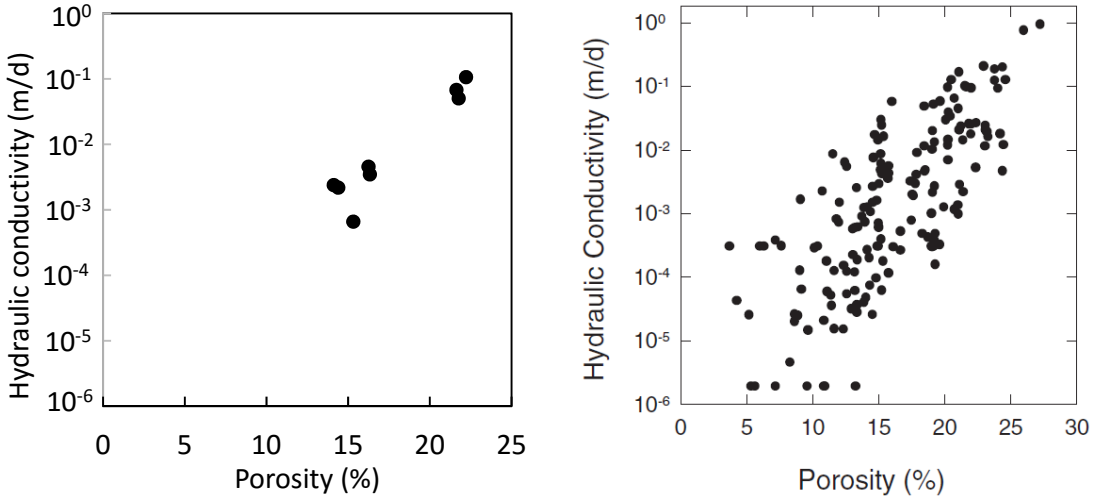

a) b)

Fig.3-15. Hydraulic conductivity versus porosity in West Cumbria:
a) St Bees Sandstone Formation at St Bees Head (This study); b) the Sherwood Sandstone Group (from Allen et al., 1997).

3.4.3.5 Fluvial versus aeolian

The Permo-Triassic sandstones in the northwest originate from both fluvial and aeolian systems. The Permian Penrith Sandstone Formation consists of aeolian well-sorted, well-rounded, medium- to coarse-grained sandstone and fluvial poorly sorted, fine- to coarse-grained sandstones with interbedded siltstones. In West Cumbria, the St Bees Sandstone represents a fluvial environment with multiple channel structures, and the Calder Sandstone Formation are deposits of an aeolian system. Generally, the aeolian Calder Sandstone Formation has higher hydraulic conductivity (permeability) than the fluvial St Bees Sandstone Formation (Table 3-6). In West Cumbria, aeolian sandstones that occur towards the top of the Sherwood Sandstone Group have higher porosity than fluvial sandstones (Allen et al., 1997).

Table 3-6. Hydraulic properties for fluvial and aeolian dominated sandstones in West Cumbria (after Allen et al., 1997).

System	Formation	Hydraulic conductivity (m/d)				Arithmetic mean porosity (%)
		Range	Interquartile range	Median	Geometric mean	
Fluvial	St Bees Sandstone Formation	$1.9x10^{-6}$ - 0.94	$1.9x10^{-4}$- 0.014	0.0013	0.0013	17.8
Aeolian	Calder Sandstone	$1.7x10^{-4}$- 0.545	-	0.0433	0.0414	19.5*

** Median value.*

Median, arithmetic mean, geometric mean were median, arithmetic and geometric averages of median, arithmetic and geometric means of all the relevant formations respectively.

3.5 Cheshire

3.5.1 Geological setting

The extent of the Permo-Triassic sandstones in Cheshire are shown in Fig.3-16 and their stratigraphy is detailed in Table 3-7 (Warrington et al., 1980; Allen et al., 1997; Benton et al., 2002; Ruffell et al., 2006).

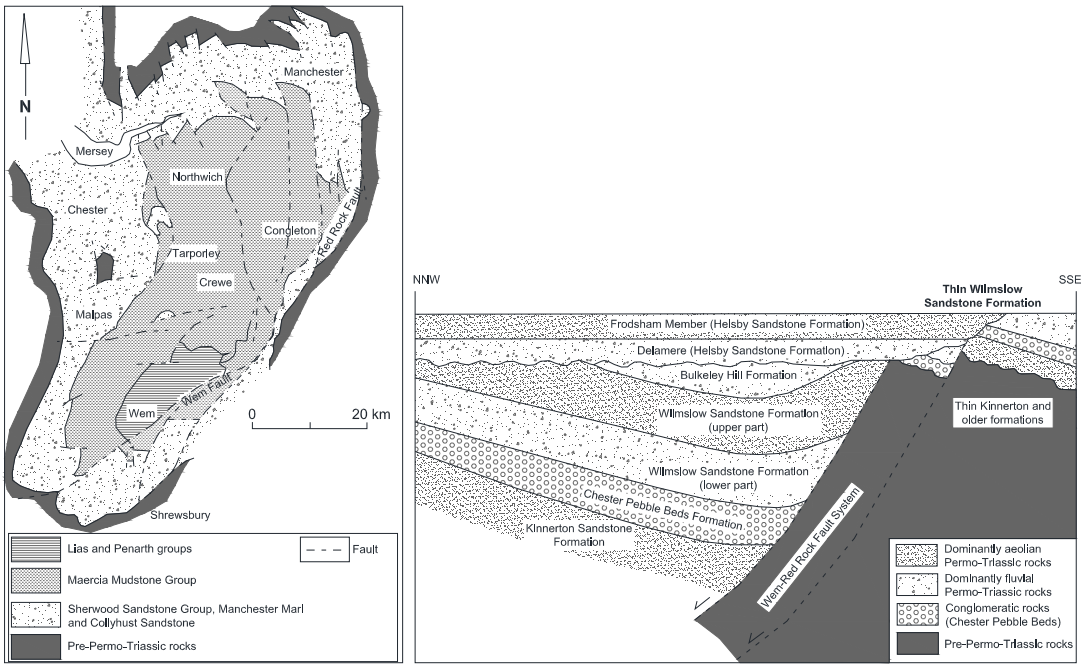

a) b)

Fig.3-16. a) Geological map; (b) and cross-section of the Permo-Triassic of Cheshire basin (after Benton et al., 2002).

Table 3-7. Summary stratigraphy of the Permo-Triassic sandstones in Cheshire.

Age	Group	Formation	Area	Lithology	Dominated system	Author/observer
Triassic	Mercia Mudstone	Various Tarporley Siltstone	Cheshire and south Lancashire	Mudstones, siltstones	Marine and arid periods	Warrington et al. (1980), Allen et al. (1997) and others
	Sherwood Sandstone	Helsby/Ormskirk Sandstone	In the Abbey Arms Wood borehole	Sandstones	Fluvial	Bloomfield et al. (2006)
			Cheshire and south Lancashire	Sandstones		Warrington et al. (1980), Allen et al. (1997), Hounslow and Ruffell (2006)
		Wilmslow Sandstone	At Rawhead outcrop	Sandstones	Fluvial	This study
			In the Abbey Arms Wood borehole	Sandstones	Aeolian	Bloomfield et al. (2006)
			Cheshire and south Lancashire	Sandstones	Fluvial	Warrington et al. (1980), Allen et al. (1997), Hounslow and Ruffell (2006)
		Chester Pebble Beds	Cheshire and south Lancashire	Conglomerates, pebbly sandstone	Fluvial	Allen et al. (1997)
		Kinnerton Sandstone	Cheshire and south Lancashire	Sandstone	Aeolian	Warrington et al. (1980), Allen et al. (1997),
Permian		Manchester Marl/ Bold	Cheshire and south Lancashire	Mudstones		Allen et al. (1997), Ruffell et al. (2006)
		Collyhurst Sandstone	Cheshire and south Lancashire	Sandstones	Aeolian	Allen et al. (1997), Ruffell et al. (2006)

3.5.2 Studied site: Raw Head outcrop, south Cheshire (SJ 510540)

The Raw Head outcrop is located in the Bickerton Hill area, south Cheshire (Fig.3-17). Deposits here include, in upward succession, the Wilmslow Sandstone Formation, the Bulkeley Hill Sandstone Formation, the Delamere Member of the Helsby Sandstone Formation and at top the Tarporley Siltstone Formation (Benton et al. 2002) (Fig.3-17). The Wilmslow Sandstone Formation crops out at Raw Head, and it consists of thick, red sandstones, varying in grain size from very fine, through fine to medium. Sand grains are comprised mainly of quartz and

feldspar (together accounting for about 65% of total volume), sub-rounded to rounded and moderately sorted (Fig.3-20a). Overgrowths and grain coatings on sand grains are common along with calcite cementation (Fig.3-20b).

Sedimentary structures include small scale cross-bedded sandstone (Fig.3-19b, Fig.3-21), low-angle cross-stratification (Fig.3-18a,b), and plane and pseudo-pin-striped cross bedding, a poorly developed channel base filled with channel lags (Fig.3-19a, Fig.3-21). The sandstones are poorly cemented with honeycomb weathering (Fig.3-19b, Fig.3-21). The Wilmslow Sandstone is interpreted as being deposited from a sandy braided river flowing towards the northwest and north-north-west (Benton et al., 2002).

At Raw Head only one channel structure was observed in all sections examined. It appeared to be a metre or so in depth and in the exposed section orientation about 30m wide, though this distance is not necessarily perpendicular to the channel axis. This indicates that it is rare for channel structures to be preserved at this site (and this was a common observation elsewhere).

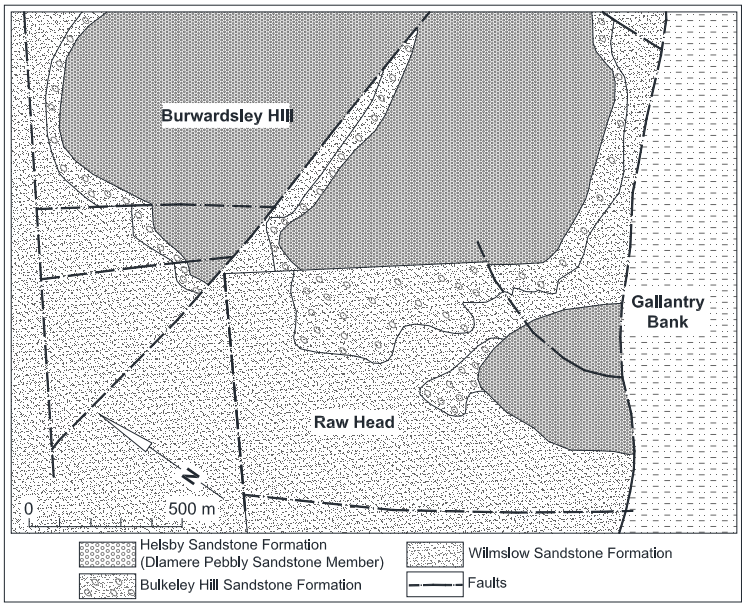

Fig.3-17. Geology map of Bickerton Hill (after Benton et al. 2002).

a) b)

Fig.3-18. The Wilmslow Sandstone at RawHead, a) Plane bedded sandstones; b) Plane bedded sandstones with extensive honeycomb development.

a) b)

Fig.3-19. a) A vague channel base structure (just right below the pencil); b) Cross-bedded sandstone above the channel filled unit and below planar beds.

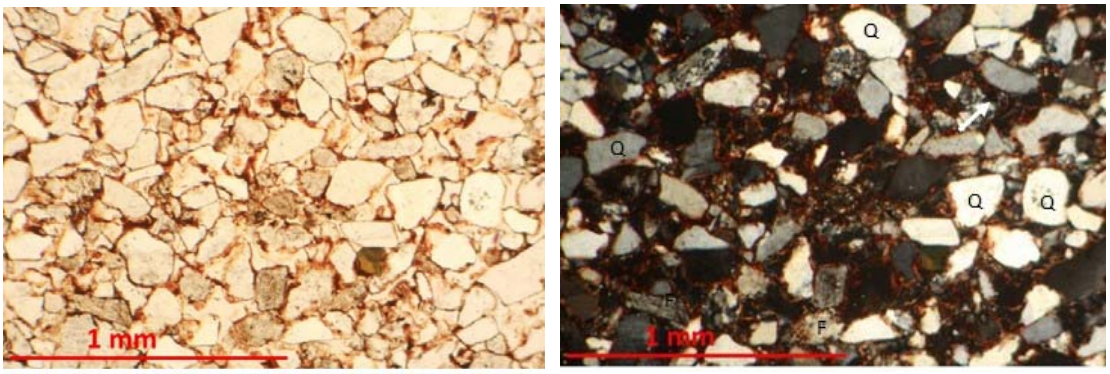

a) b)

Fig.3-20. Photomicrographs of the Wilmslow Sandstone at Rawhead, a) plane polarised light: sub-rounded to rounded, moderately well-sorted sand grains; b) cross polarised light showing quartz (Q) and felspar (F) grains with grain coatings and overgrowths.

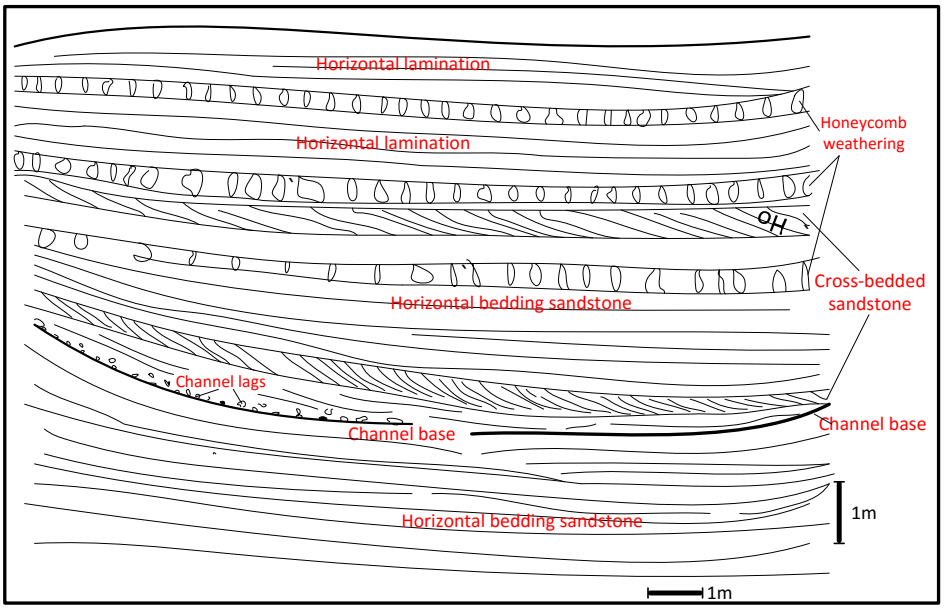

Fig.3-21. Interpretation of sedimentary structures of the Raw Head sandstone outcrop.

3.5.3 Hydraulic properties

Table 3-8 and Fig. 3-22 gives a description for samples taken at Raw Head during this study and analysed by Hallett (2014).

Table 3-8. Sedimentary description for samples collected at Raw Head (after Hallett, 2014).

Bed/lithofacies	Sample ID	Brief discription
Channel lags (Bed 1)	R2-1, R2-2, R4-1	Fine- to very coarse- grained, matrix supported sandstone with dominated calcite cement. Samples are separated by 20m.
Tabular sandstones (Bed 2 and Bed 3)	R6-1, R7-1, R7-2, R8-1, R8-2	Medium silt to fine sand, moderate well-sorted, plannar, wavy and irregular lamination. Samples R7 and R8 are separated by 21m within Bed 2. Samples R6 in Bed 3 which is overlain by Bed 2.
Tabular sandstones (Bed 0)	R0-1, R0-2	Medium-grained, moderate well-sorted, sandstone with some mudstones. R0-1 and R0-2 are within a block of sample.

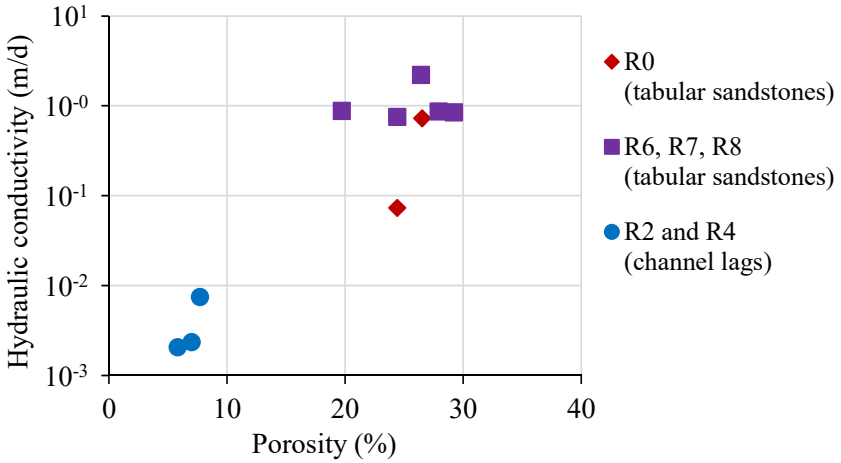

Fig.3-22. Hydraulic conductivity versus porosity for the samples at Raw Head (after Hallett, 2014).

Fig.3-22 shows porosity and hydraulic conductivity variations between beds/lithofacies at the Raw Head outcrop. The low porosities and hydraulic conductivities of samples R0 and R4 (channel lag in Fig.3-21) is due to the dominance of calcite cement in these samples (Hallett, 2014). Increasing in porosity and permeability (hydraulic conductivity) for the tabular cross-stratified channel field is probably caused by poorly cemented and weathered (it showed honeycomb weathering) features.

Generally, it appears that hydraulic conductivity (permeability) can vary laterally and vertically, but with these outcrop samples the main controls seem to have been the presence of cement (Fig.3-18a,b and Fig.3-22).

Porosity and hydraulic conductivity and their relationship, anisotropy and comparison between fluvial and aeolian systems for the region are described in the following subsections.

3.5.3.1 Porosity

Porosity of the Permo-Triassic sandstones in the Cheshire varies widely from 6 % to 35 % (Table 3-9). However, ranges, median values and mean values vary little with formation despite the differences in palaeoenvironment.

Table 3-9. Core porosity for Permo-Triassic sandstones in Cheshire Basin (and south Lancashire).

Formation	Area	Range (%)	Interquartile range (%)	Median (%)	Arithmetic mean (%)	Author
Helsby Sandstone	The Abbey Wood borehole, Cheshire	15.4-26.6	18.1-20.7	19.8	19.7	Bloomfield et al. (2006)
	Cheshire south Lancashire	20.2-32.9	23.2-28.6	25.1	25.8	Allen et al. (1997)
Wilmslow Sandstone	Rawhead, Cheshire	5.8-29.2	10.7-26.5	24.4	19.9	Hallett (2014)
	The Abbey Wood borehole, Cheshire	5.9-26.1	19.96-22.8	21.2	20.6	Bloomfield et al. (2006)
	Cheshire and south Lancashire	6.2-34.7	22.0-26.9	24.9	24.3	Allen et al. (1997)
Chester Pebble Beds	Cheshire south Lancashire	11.6-29.2	20.4-25.8	23.1	22.6	
Collyhurst/ Kinnerton Sandstone	Cheshire south Lancashire	13.3-32.1	23.1-27.2	25.8	25.0	

3.5.3.2 Hydraulic conductivity

Table 3-10 shows intergranular hydraulic conductivity data for the Permo-Triassic sandstones in Cheshire. Hydraulic conductivities range over about six orders of magnitude, from 4 x 10^{-5} m/d to 15 m/d. Hydraulic conductivity variation shows no apparent trend with depth in the upper 150 m depth where the samples have been collected.

The Permian Kinnerton (Collyhurst) Sandstone Formation has hydraulic conductivity range from 4x10^{-5} m/d to 10 m/d with a geometric mean of 0.4 m/d. Low permeability is caused by occurrences of fine-grained layers and mudstone lenses rather than cementation which is poor according to Allen et al. (1997). The Kinnerton Sandstone Formation is aeolian in origin and the medium- to coarse-grains lack cementation. This explains the higher proportion of hydraulic

conductivities of over 1 m/d in the Kinnerton Sandstone Formation than both the overlying Chester Pebble Beds and Wilmslow Sandstone Formation (Allen et al., 1997).

The Triassic Sherwood Sandstone Group has similar hydraulic conductivity range from about 3 x 10^{-4} m/d to 15 m/d (Table 3-10).

The Chester Pebble Beds has interquartile range of core hydraulic conductivity from 0.05 to 0.98 m/d and a geometric mean of 0.17 m/d. The wide range (2.5 x 10^{-4}- 15 m/d) is attributed to a combination of lithology and cementation (Allen et al., 1997). Outcrop samples are likely to give higher hydraulic conductivities due to subaerial weathering (Lovelock, 1977).

The Wilmslow Sandstone Formation shows core hydraulic conductivity with an interquartile range from 0.06 to 1.13 m/d and a geometric mean of 0.22 m/d. Clean, fine- to medium-grained sandstones have high permeability, whilst mud-rich beds show lower permeability (Allen et al., 1997). Weakly cemented, silicified vein bearing sandstones have low permeability (Lovelock, 1977). The values obtained by Hallett (2014) from Raw Head may be high because of the weathered nature of the outcrop sampled.

Core hydraulic conductivity of the Helsby/Ormskirk Sandstone Formation has a high interquartile range from 0.56 to 4.1 m/d and a geometric mean of 1.2 m/d, higher than even the aeolian Collyhurst Sandstone Formation. Cementation is high in the formation, but occurs only at contact points between grains. The sandstones are clean, coarse-grained, well-sorted, leading to their highly permeable nature. Less permeable sediments are fine- to medium-grained sandstone layers with subordinate mudstone laminae (Allen et al., 1997).

Table 3-10. Core hydraulic conductivity for sandstones at Cheshire Basin (and south Lancashire).

Formation	Area	Range (m/d)	Interquartile range (m/d)	Median (m/d)	Geometric mean (m/d)	Author
Helsby Sandstone	The Abbey Arms Wood borehole, Cheshire	0.01-6.6 0.01-4.31* 0.003-4.97**	0.25-2.43 0.19-0.98* 0.08-1.09**	0.61 0.69* 0.38**	0.38 0.42* 0.27**	Bloomfield et al. (2006)
	Cheshire and south Lancashire	$3.1x10^{-4}$-15	0.56-4.1	1.8	1.2	Allen et al. (1997)
Wilmslow Sandstone	Rawhead Outcrop, Cheshire	0.002-2.2	0.02-0.9	0.7	0.14	Hallett (2014)
	The Abbey Arms Wood borehole, Cheshire	0.001-2.32 0.001-1.72* 0.005-5.37**	0.11-0.93 0.09-0.71* 0.16-1.13**	0.3 0.24* 0.47**	0.23 0.19* 0.39**	Bloomfield et al. (2006)
	Cheshire Cheshire and south Lancashire	$2.6x10^{-4}$-13	0.056-1.13	0.25	0.22	Allen et al. (1997)
Chester Pebble Beds	Cheshire and south Lancashire	$2.5x10^{-4}$-15	0.05-0.98	0.33	0.17	Allen et al. (1997)
Collyhurst/ Kinnerton Sandstone	Cheshire and south Lancashire	$3.7x10^{-5}$-10	0.13-1.8	0.8	0.4	

** Permeability measured on core plugs using a probe/mini permeameter.*
*** Permeability measured on whole borehole core using a probe/mini permeameter.*

Permeability for the Permo-Triassic sandstones in Cheshire and Lancashire has been measured at different scales (Table 3-11). The core scale permeability (hydraulic conductivity), as above, give information on intergranular or matrix permeability and it has a range from 10^{-5} to 15 m/d with geometric means from 0.2 to 1.2 m/d. Packer tests can be strongly influenced by fracture flow and shows geometric means from 2.1 to 6.8 m/d. University of Birmingham (1981 ; 1984) confirmed the significant impact of fracture flow a borehole scale by summarising pumping

tests that show bulk permeability range from 0.2 to 50 m/d with a geometric mean of 2.5 m/d. However, fracture flow loses its importance at regional scale for which numerical model permeabilities show geometric mean of 1.7 m/d that is fairly close to the geometric mean of intergranular permeability (Table 3-11).

Table 3-11. Permeability of the Permo-Triassic sandstone for Cheshire and south Lancashire at different scales (after Allen et al., 1997).

Measurement method	Permeability type	Permeability (m/d)	
		Range	Geometric mean
Core permeametry	Intergranular	10^{-5} - 15	0.2 – 1.2
Packer- predominantly	Fracture	-	2.1 – 6.8
Pumping test	Bulk	0.2 - 50	2.5
Model	Regional	-	1.7

3.5.3.3 Anisotropy

The ratio of the horizontal to vertical geometric mean permeabilities (hydraulic conductivities) gives the permeability anisotropy ratio. In Cheshire and South Lancashire area, Allen et al. (1997) recorded the same anisotropy of 2.4 for both the Sherwood Sandstone Group and the Permian Collyhurst-Kinnerton Sandstone (Table 3-12). Bloomfield et al. (2006) found an anisotropy of 2.8 in the Abbey Arms Wood borehole near Delamere, Cheshire, but anisotropy of 0.8 for core permeability measured with a mini-permeameter (Table 3-12).

The Chester Pebble Beds at Kenyon Junction, near Warrington, show permeability increasing with increase in grain size: in contrast, anisotropy decreases with increase in grain size (Table 3-13). Permeability anisotropies for individual core samples vary from less than 1 to over 50. There were only 8 % of the samples with vertical permeability greater than horizontal permeability (Birmingham, 1981).

Table 3-12. Horizontal and vertical core hydraulic conductivity for Permo-Triassic sandstones in Cheshire and south Lancashire.

Formation/ Group	Orientation	Range (m/d)	Interquartile range (m/d)	Median (m/d)	Geometric mean (m/d)	Kh/Kv (Geometric mean)	Author
Sherwood Sandstone Group	Horizontal (Kh)	$6.7x10^{-4}$-6.6 1.2x10-3-4.3*	0.1-1.1 0.1-0.8*	0.4 0.4*	0.3 0.2*	2.8 0.8*	Bloomfield et al. (2006)
	Vertical (Kv)	$1.2x10^{-4}$-6.3 0.11-3.7*	0.19-0.4 0.1-1.0*	0.2 0.3	0.1 0.3*		
	Horizontal	$2.5x10^{-4}$-15	0.14-2.37	0.72	0.4	2.4	Allen et al. (1997)
	Vertical	$2.6x10^{-4}$-13	0.04-1.21	0.29	0.17		
Collyhurst/ Kinnerton Sandstone	Horizontal	$1.6x10^{-3}$-10	0.15-3.2	1.2	0.78	2.4	
	Vertical	$3.8x10^{-5}$-4.9	0.1-2.9	1.0	0.32		

** Permeability measured on core plugs using a probe/mini permeameter.*

Table 3-13 Correlation of grain size and permeability measured with gas permeametry on Chester Pebble Beds Formation samples at Kenyon Junction, near Warrington (from Allen et al., 1997).

Grain size	Average intrinsic permeability (millidarcies)#		Ratio kh/kv
	Horizontal (k_h)	Vertical (k_v)	
Medium to coarse	2049	13480	1.5
Medium	629	281	2.2
Medium to fine	56	14	4
Fine	14	2	7
Very fine	< 0.01	< 0.01	-
Weighted mean	928	494	1.9

 # 1 millidarcy is equal to about 0.64 m/d for water at 10^0 C.

3.5.3.4 Porosity versus hydraulic conductivity

Fig.3-23a-f shows core hydraulic conductivity plotted against porosity for Cheshire and south Lancashire. Generally, permeability increases with porosity in the sandstones, but the degree of this correlation varies within and between formations (Fig.3-23a-f). For a particular porosity, permeability can vary by four or five orders of magnitude. Bloomfield et al. (2006) found unclear correlation between permeability and porosity as a whole in a borehole near Delamere

(Fig.3-23a, d). Overall a good correlation between hydraulic conductivity and porosity occurs at samples with hydraulic conductivity greater than 0.1 m/d (Fig.3-23a-f).

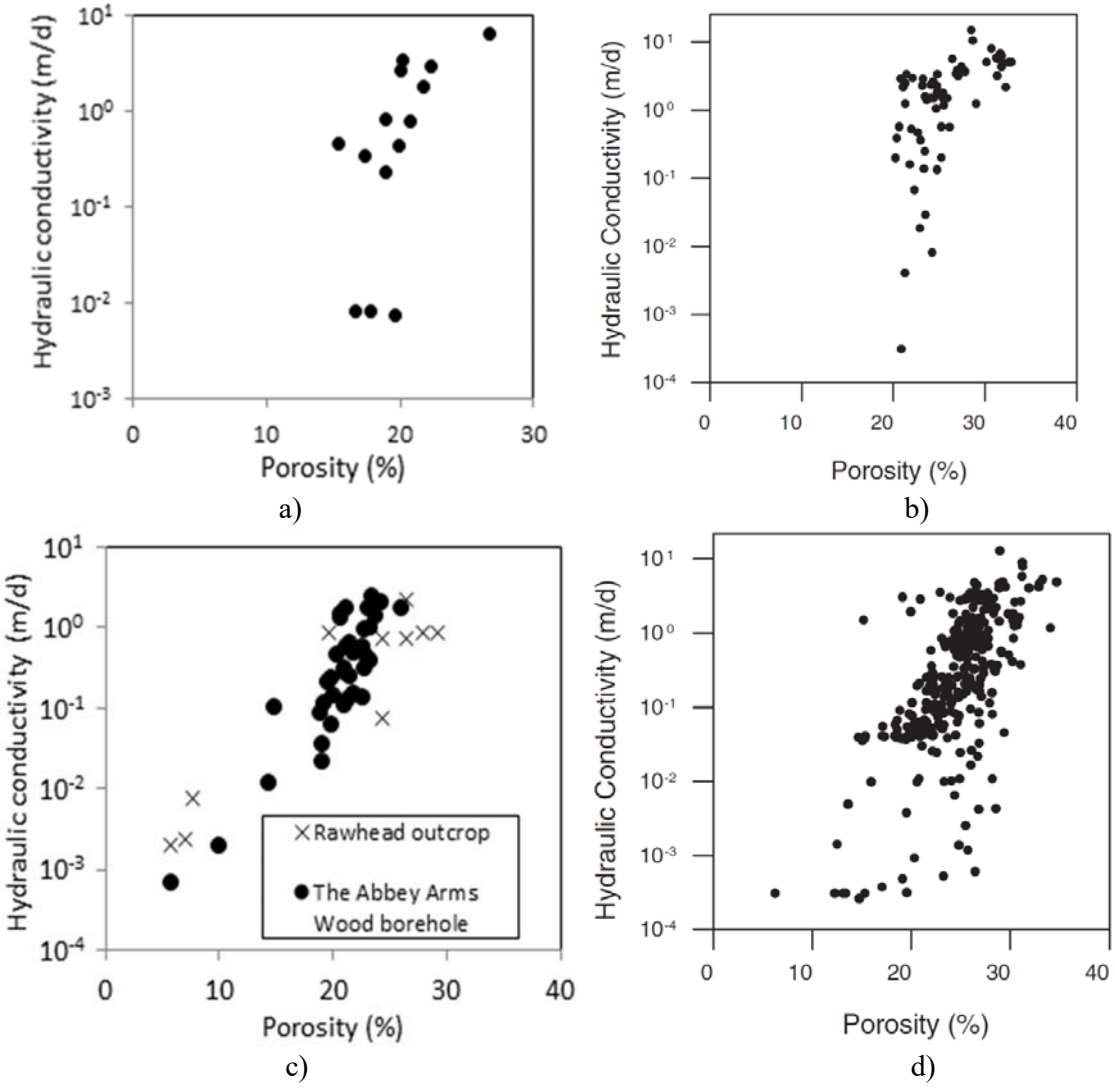

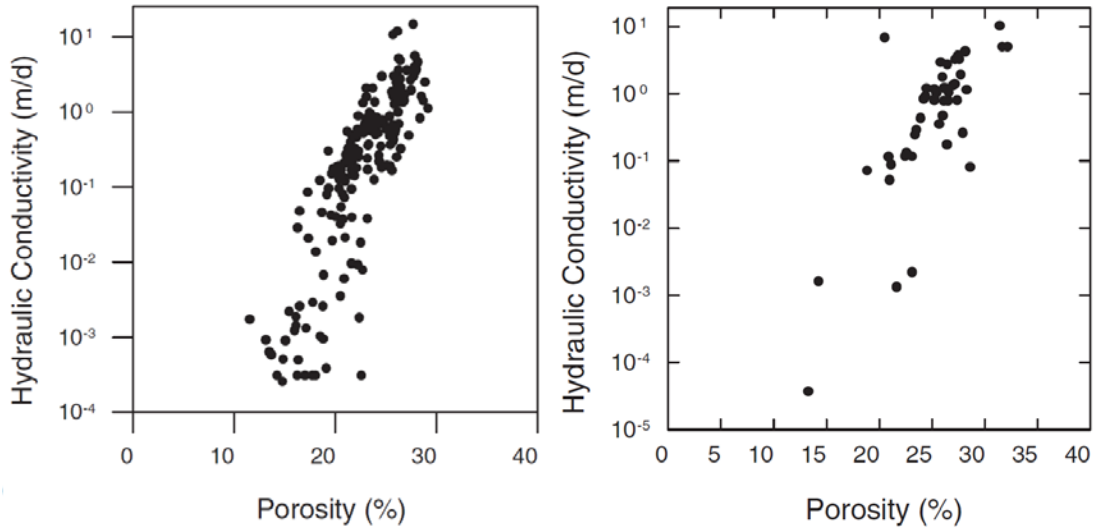

e) f)

Fig.3-23. Correlation of core sample hydraulic conductivity and porosity for Permo-Triassic sandstones in Cheshire and south Lancashire as function of the formations, a) Helsby Sandstone Formation at the Abbey Wood borehole; b) Helsby Sandstone Formation in Cheshire ; c) Wilmslow Sandstone Formation at Rawhead outcrop and in the Abbey Wood borehole; d) Wilmslow Sandstone Formation in Cheshire and south Landcashire; e) Chester Pebble Beds Formation in Cheshire and south Lancashire; f) Collyhurst-Kinnerton Sandstone Formation in Cheshire and south Lancashire.

Data sources: The data in Cheshire and south Lancashire are from Allen et al. (1997)
The Abbey Arms Wood borehole data are from Bloomfield et al. (2006)
The Raw Head outcrop data are from Hallett (2014).

3.5.3.5 Aeolian versus fluvial sandstones

Hydraulic conductivities and porosities of the Permo-Triassic sandstones in Cheshire and south Lancashire are retabulated to allow comparison of fluvial and aeolian environments (Table 3-14). Generally aeolian sandstones that have well-sorted, well-rounded grains have greater hydraulic property values than fluvial sandstones. The hydraulic conductivities of aeolian dominated sandstones have interquartile ranges from 0.08 to 2.43 m/d with median from 0.61 to 0.8 m/d and geometric means from 0.27 to 0.42 m/d, whereas the hydraulic conductivities of fluvial dominated sandstones show interquartile ranges from 0.09 to 1.13 m/d with medians from 0.24 to 0.47 and geometric means from 0.19 to 0.39 m/d.

Bloomfield et al. (2006) studied sandstones from the Abbey Arms Wood borehole and classified six major facies, including two fluvial facies: fine-grained fluvial channel fill and coarse-grained fluvial channel fill, three aeolian facies: aeolian sandsheets; aeolian sandy sabkha; and aeolian dune, and massive sandstones facies that is mixed of fluvial and aeolian systems. The permeability distribution for each facies is statistically distinct. The three aeolian facies have systematically greater permeabilities than the two fluvial facies and the massive sandstone facies. Within the aeolian sandstones, the sandy sabkha facies has lower permeability than the other facies (Fig.3-24).

Table 3-14. Hydraulic properties for fluvial and aeolian dominated sandstones in Cheshire.

System	Formation	Hydraulic conductivity (m/d)			Arithmetic mean porosity (%)	Author
		Interquartile range	Median	Geometric mean		
Fluvial	Wilmslow Sandstone in the Abbey Arms Wood	0.11-0.93 0.09-0.71* 0.16-1.13**	0.3 0.24* 0.47**	0.23 0.19* 0.39**	20.6	Bloomfield et al. (2006)
	Chester Pebble Beds Formation	0.05-0.98	0.33	0.17	22.6	Allen et al. (1997)
Aeolian	Helsby Sandstone in the Abbey Arms Wood	0.25-2.43 0.19-0.98* 0.08-1.09**	0.61 0.69* 0.38**	0.38 0.42* 0.27**	19.7	Bloomfield et al. (2006)
	Collyhurst/ Kinnerton Sandstone	0.13-1.80	0.8	0.4	25	Allen et al. (1997)

** Permeability measured on core plugs using a probe/mini permeameter*
*** Permeability measured on borehole core using a probe/mini permeameter.*

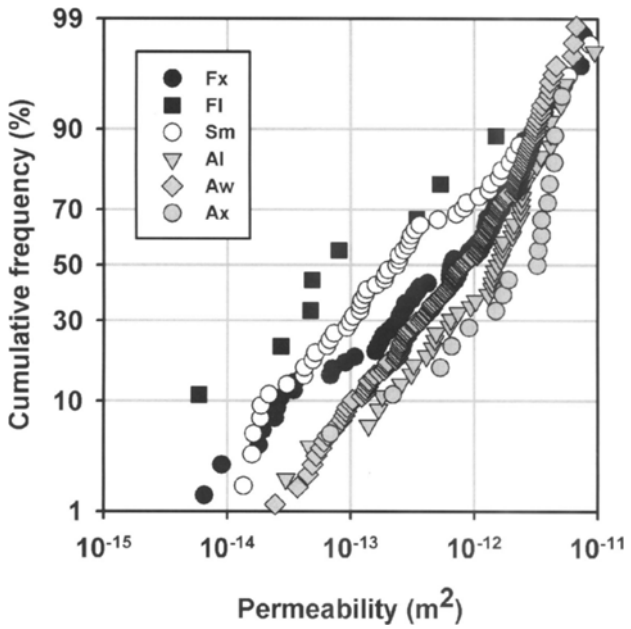

Fig.3-24. Cumulative probability plots of corrected permeability measured with a minipermeameter on the whole borehole core for different facies. Fx is the fluvial coarse-grained channel fill; Fl is the fluvial fine-grained channel fill; Sm is the massive sandstone; Al is the aeolian sandsheets; Aw is the aeolian sandy sabkha; and Ax is the aeolian dune sandstone (from Bloomfield et al., 2006).

3.6 Shropshire

3.6.1 Geological setting

Table 3-15 summaries stratigraphy of the Permo-Triassic sandstones in Shropshire, and Fig.3-25 shows a geological map of the region. Details are provided in Appendix 6.

In this study, five outcrops are have been studied, including outcrops at Bridgnorth (the Bridgnorth Sandstone Formation), Grinshill Old Quarries (the Wildmoor Sandstone Formation), Grinshill working quarries (the Helsby Sandstone Formation), Nesscliffe, and Leaton (the Wildmoor Sandstone and Helsby Sandstone Formations).

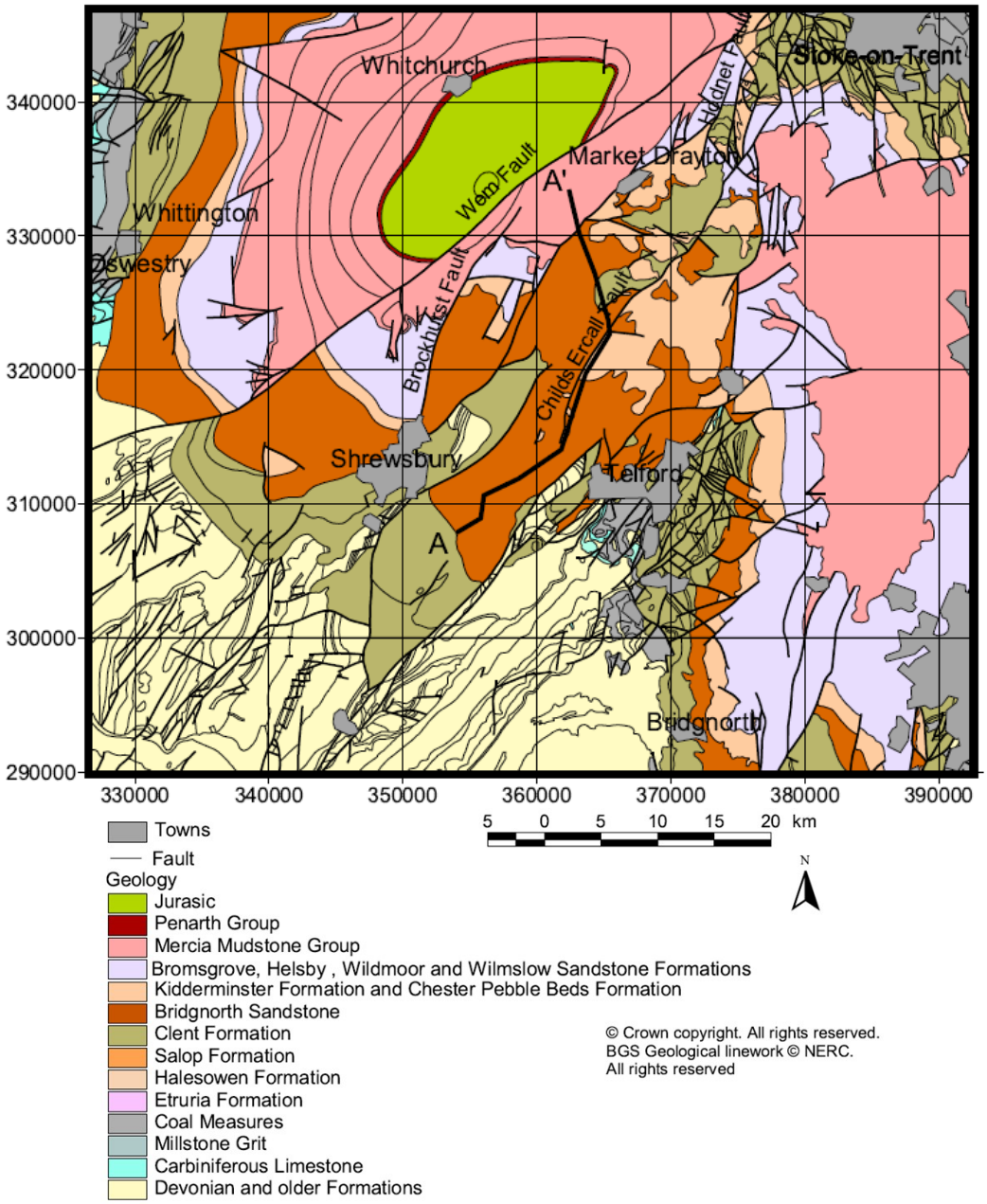

Fig.3-25. Geology of Permo-Triassic sandstones of Shropshire (from Smedley et al., 2005).

Table 3-15. Summary stratigraphy of the Permo-Triassic sandstones in Shropshire.

Age	Group	Formation	Area	Lithology	Predominant environment	Author/observer
Triassic	Mercia Mudstone	Mercia Mudstone Group	Shopshire	Mudstone	Marine, and arid periods	Warrington et al. (1980), Toghill (1990), and others
	Sherwood Sandstone	Helsby or Bromsgrow Sandstone	Grinshill Working Quarry	Sandstone, conglomerates	Mainly fluvial and minor aeolian	Warrington et al. (1980), Toghill (1990), and others
		Wildmoor or Wilmslow Sandstone	Grinshill Old Quarries, Nesscliffe	Sandstone	Mainly aeolian and minor fluvial	Warrington et al. (1980)Toghill (1990), and others
		Kidderminster Sandstone or Chester Pebble Beds	Shropshire	Conglomerates, pebbly sandstones	Fluvial	Warrington et al. (1980)Toghill (1990), and others
Permian		Bridgnorth or Kinnerton Sandstone	Leaton	Sandstone	Aeolian	This study

3.6.2 Studied sites: Bridgnorth

A series of spectacular sandstone outcrops occur at Bridgnorth Town (SO 717928) and at Hermitage (SO 727934) which is about 1.3 km north of Bridgnorth Town. The sandstones are of the Permian Bridgnorth Sandstone Formation (Toghill, 1990; Benton et al., 2002; Smedley et al., 2005; Holloway, 1985). The Bridgnorth Sandstone Formation is unconformably overlain by the Triassic Kidderminister Formation (Fig.3-28a).

The Bridgnorth Sandstone Formation at the sites are dominantly aeolian sediments of reddish brown, reddish orange, fine- to medium-grained sandstone. Sedimentary structures include large-scale planar and trough cross-stratified (Fig.3-26a,b, Fig.3-27a,b, and Fig.3-30), dunes climbing back of other dunes, planar bedding, lamination, graded bedding (Fig.3-30, Fig.3-32a,b), bounding and reactivation surfaces (Fig.3-30). Shotton (1956) recorded the Bridgnorth Sandstone as deposit of large-scale, crescentic barchan dunes with prevailing wind from the east. Mader and Yardley (1985) found the bounding surfaces with complex hierarchy, probably four levels, and suggested that the Formation is formed by major draa bedforms bearing

superimposed small-scale transverse dunes. Karpeta (1990) identified three major aeolian facies associations, including (1) isolated transverse draa with superimposed oblique crescentic and linear dunes (Fig.3-30 and Fig.3-32a); (2) grouped barchanoid draa with superimposed oblique crescentic and linear dunes (Fig.3-32b); and (3) sand sheets with isolated dome dunes (Fig.3-32c). The long term wind direction has come from the east and controlled draa orientation. Medium-term wind direction from the north has created the orientation of the superimposed dunes and short-term wind may create internal scour surfaces within dune and dara foresets (Fig.3-32a-c) (Karpeta, 1990).

The Kidderminster Formation lies unconformably on the Bridgnorth Sandstone Formation (Fig.3-28a). It consists of red pebbly sandstone, conglomerates and mudstone beds (Smedley et al., 2005).

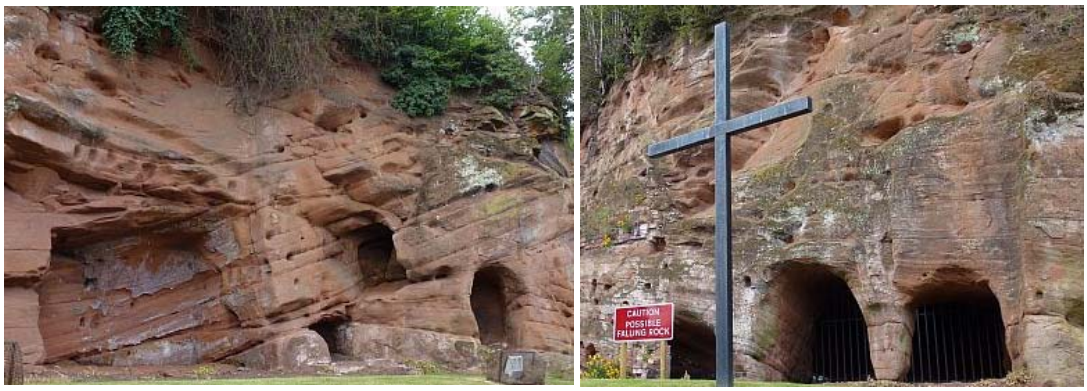

a) b)

Fig.3-26. The Bridgnorth Sandstone Formation in Bridgnorth: a) Large-scale barchanoid dune-bedding; b) Rock-house showing 3D structure of the formation.

a) b)

Fig.3-27. a) Cross-bedded sandstone (two group sets of barchanoid draa); b) Medium-grained sandstone in inclined bedding.

a) b)

Fig.3-28. Hermitage, Bridgnorth a) The overlying fluvial Kidderminister Sandstone resting unconformably on the underlying aeolian Bridgnorth Sandstone; b) the aeolian Bridgnorth sandstone.

a) b)

Fig.3-29. a) Cross-bedded sandstone below overlain by lines of extensive hollows as bounding and reactivation surfaces of a set of cross-bedded layers, b) Close view of the reddish-brown, medium low angular bedding, poorly cemented sandstone with hollows incised on the surface.

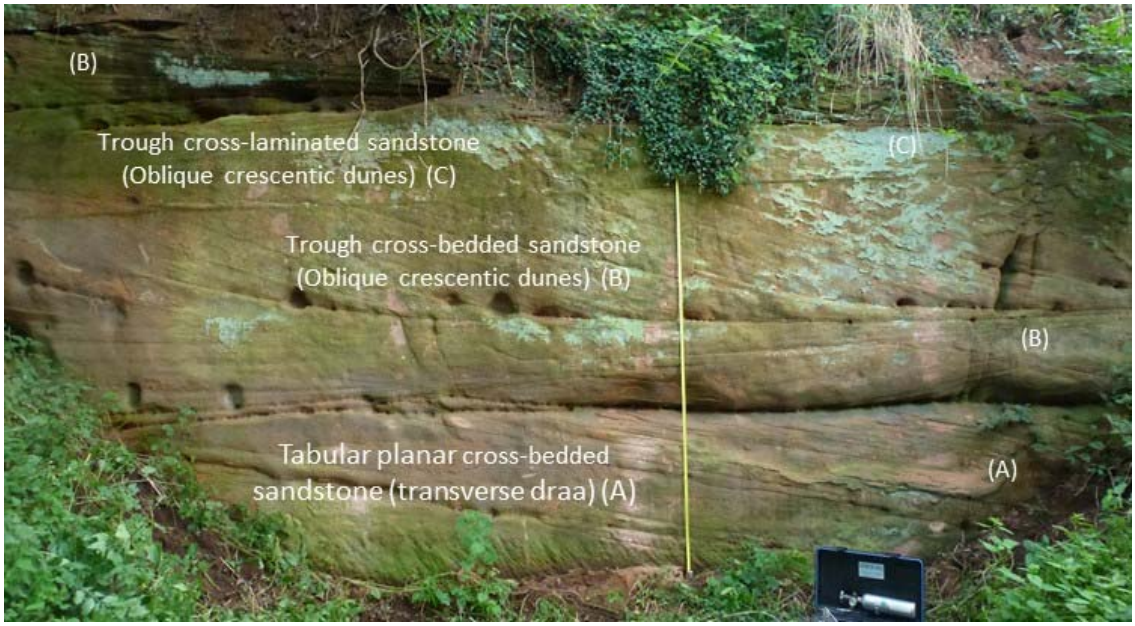

Fig.3-30. Cross-stratification of the Bridgnorth sandstone (the rule tape is 2.6 m high).

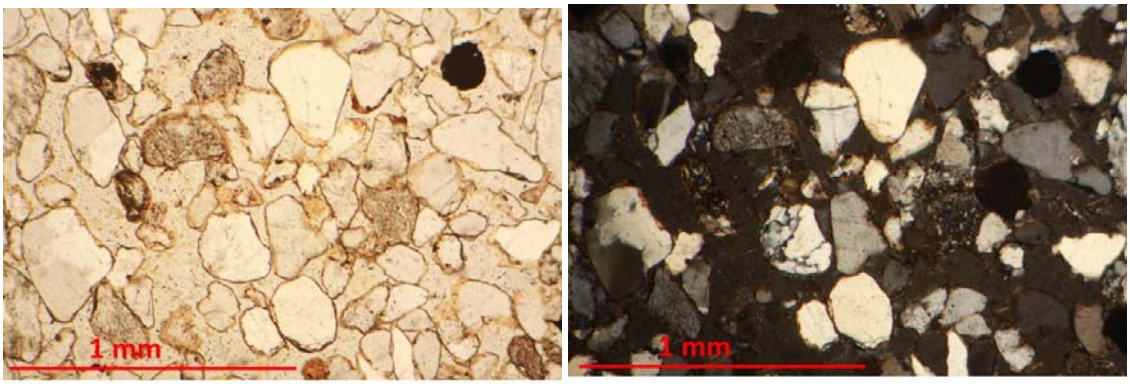

a) b)

Fig.3-31. Photomicrographs of the Brignorth Sandstone showing well-rounded and well-sorted, coating grains, a) with plane light; b) with cross polars.

3.6.3 Studied sites: Grinshill Quarries

Grinshill working quarry (SJ 525238)

In the Grinshill area (Fig.3-33), there are many sandstone quarries for building and decoration stones, but currently almost all quarries are disused except one (Fig.3-33).

The current working quarry is located at the far eastern side of the Grinshill old quarries in Shropshire (Fig.3-33). The sandstones at the site are exposed over hundreds of metres and up to 20 m high, and consist of hard, white, pale, greyish yellow, fine- to medium-grained sandstone of the Helsby Sandstone Formation and the Tarporley Silstone Formation (Fig.3-34 and Fig.3-35) (Toghill, 1990; Benton et al., 2002). The Helsby Sandstone in the working quarry is paler and harder than the Helsby Sandstone Formation in other areas (e.g. at Nesscliffe and Leaton sites below). These differences could be caused by Tertiary igneous activity about 50 million years ago when dolerite intrusions and mineralisation altered the colour of the sandstone from red to buff and strengthened the rock (Toghill, 1990). The Helsby Sandstone Formation at the quarry is interpreted as deposits of aeolian systems, probably of large, transverse barchan

dunes having main wind direction towards the west (Macchi and Meadows, 1987; Benton et al., 2002).

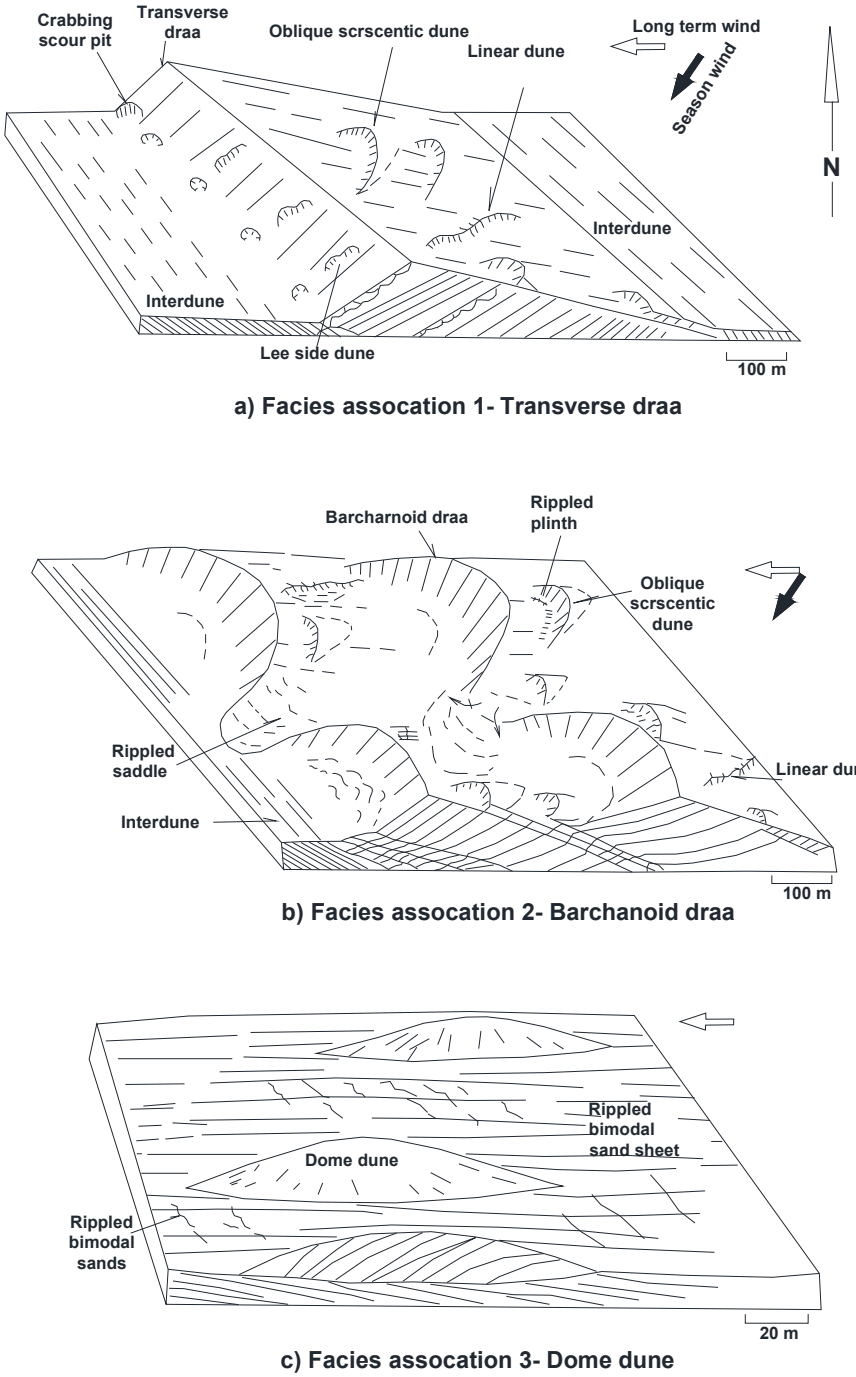

Fig.3-32. Facies association model for the aeolian Bridgnorth sandstones (from Karpeta, 1990).

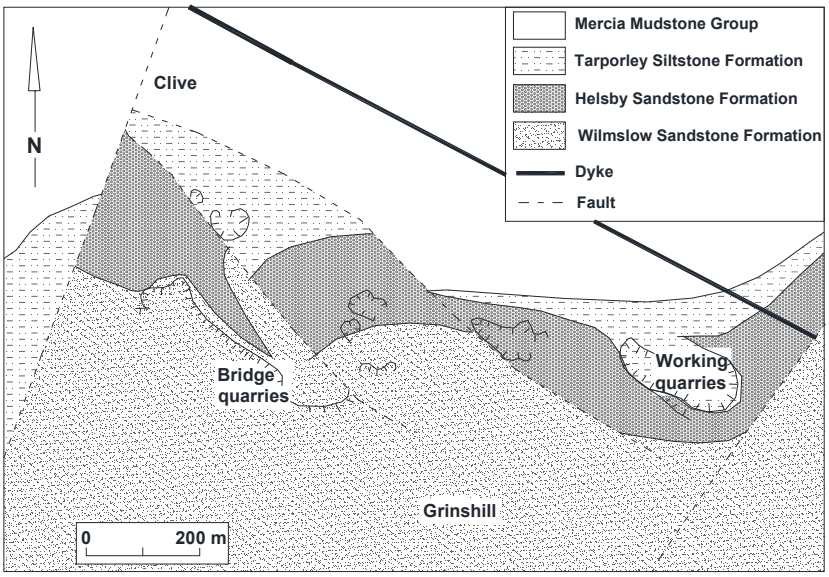

Fig.3-33. Schematic map of geology of Grinshill quarries area (after Benton et al., 2002).

The following is a detailed section studied by Geological Survey in 1920 and by Pocock and Wray (1925) for the working quarry:

Merica Mudstone Group	Thickness (m)
Bolin Mudstone Formation: Free red marl	0.6
Tarporley Siltstone Formation:	
Flag rock: light yellow, grey sandstone, evenly bedded, ripple marks	6.1
Esk bed: yellowish grey unconsolidated sand, sandstone, with specks of manganese dioxide	0.22
Sherwood Sandstone Group	
Helsby Sandstone Formation	
Hard burr: grey, hard, coarse-grained sandstone	0.76
Building stone: hard yellowish freestone	0.76
Building stone: pale, white, yellow freestone	10.06
Building stone: white freestone with speckled and iron-stained patches.	1.68

Fig.3-34. Lower part: massive pale Helsby Sandstone (about 2.5 m thick) with cross-bedding overlain by thin (about 0.3 cm) bed of grey sand, sandstone (the Esk bed) which in turn overlain by flaggy Tarporley Siltstone (about 4 m thick), and at top is 1.5 m thick of the Mercia Mudstone Group.

Fig.3-35. Quarry working wall of white sandstone of the Helsby Sandstone at about 1.5m lower part and overlying 6 m-thick of the flaggy Tarporley Siltstone, and about 2m-thick of red mudstone-rich unit of the Mercia Mudstone Group at top.

a) b)

Fig.3-36. a) Sub horizontal bedding planes of the Helsby Sandstone Formation; b) Ripple mark strustures of the Tarporley Silstone.

Grinshill Old Quarry (SJ 522238)

This quarry is located at centre of the Grinshill local map (Fig.3-33) and, as with many other quarries, is abandoned. The rock at the quarry is the Wildmoor Sandstone Formation (equivalent to the Wilmslow Sandstone Formation in Cheshire). The Wildmoor Sandstone Formation crops out largely at the quarry sites with quarry faces up to 30 m high, consisting of pink, reddish brown, well sorted, fine- to medium-grained sandstones. The sedimentary structure includes large-scale planar tabular trough cross-stratified sandstones (Fig.3-37a,b, Fig.3-38a,b), laminations and deformation structure such as slumped beds (Fig.3-37a,b), well-spaced joints (Fig.3-38a), and bounding and reactivation surfaces (Fig.3-37a,b). The sandstone formation represents deposits of a large-scale cross-stratified, aeolian systems of transverse barchans dunes having the main wind direction from the east (Macchi and Meadows, 1987; Benton et al., 2002).

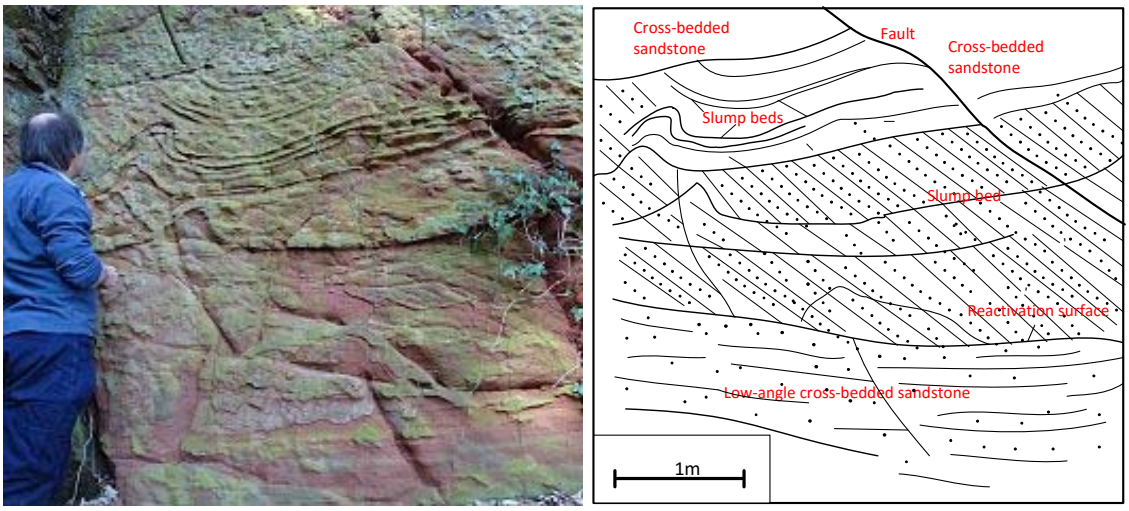

a) b)

Fig.3-37. Deformation structures of the Wildmoor Sandstone Formation: slumped beds of mudstone resting on cross-bedding sandstones with boundary surfaces.

a) b)

Fig.3-38. Sandstone of the Wildmoor Sandstone Formation at the Grinshill Old Quarry. a) an 3D scale cross-bedding sandstone showing cross-stratification and bounding and reactivation surfaces, b) a big 3D scale aeolian sandstone showing thick cross-strtified beds with bounding suface and fractures.

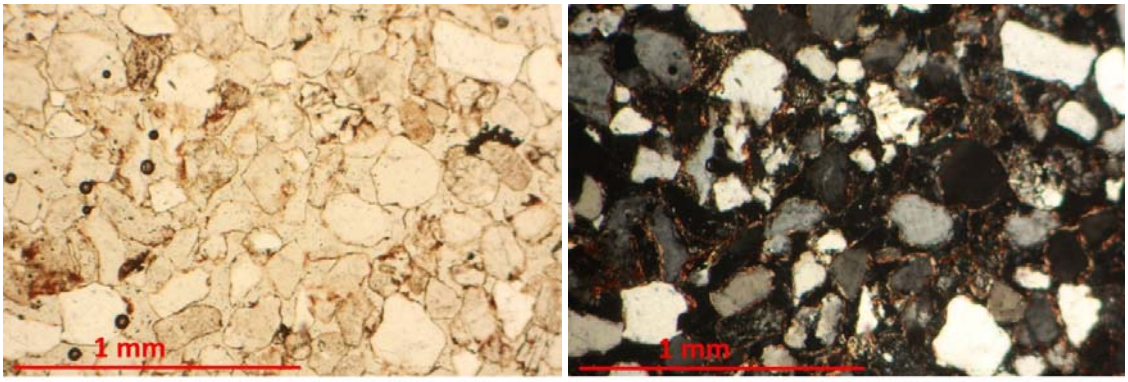

a) b)

Fig.3-39. Photomicrographs of the Wildmoor Sandstone at Grinshill Old Quarry showing sand grains of sub-angular to sub-rounded, moderately well-sorted, a) with plane light; b) with cross polars.

3.6.4 Studied Sites: Nesscliffe (SJ 385194) and Leaton (SJ 472181) outcrops

The sandstones of the underlying Wildmoor Sandstone Formation and the overlying Helsby Sandstone Formation cropout at Nesscliffe exposing 70 m of strata (Fig.3-40a,b) and at Leaton (Fig.3-42a,b, Fig.3-43a). It is difficult to distinguish these two formations in west Shropshire as outcrops at Nesscliffe and Leaton are similar in colour. No abrupt change from underlying redder, hard sandstone of the Wildmoor Sandstone up to less red, slightly harder sandstone of the Helsby Sandstone Formation is seen. However, the distinction is obvious in a quarry at about 1 km southeast of Myddle, where the underlying redder Wildmoor Sandstone is overlain by paler, harder Helsby Sandstone (Toghill, 1990).

In both locations sandstones are reddish brown, pinkish brown, hard with well-spaced joints (Fig.3-40a,b, Fig.3-41a, and Fig.3-43a,b) and irregular granulation seams (Fig.3-41b). Aeolian structures include large-scale cross-bedding (Fig.3-40a, Fig.3-42a), planar bedding, massive sandstone (Fig.3-41a), and lamination (Fig.3-43b).

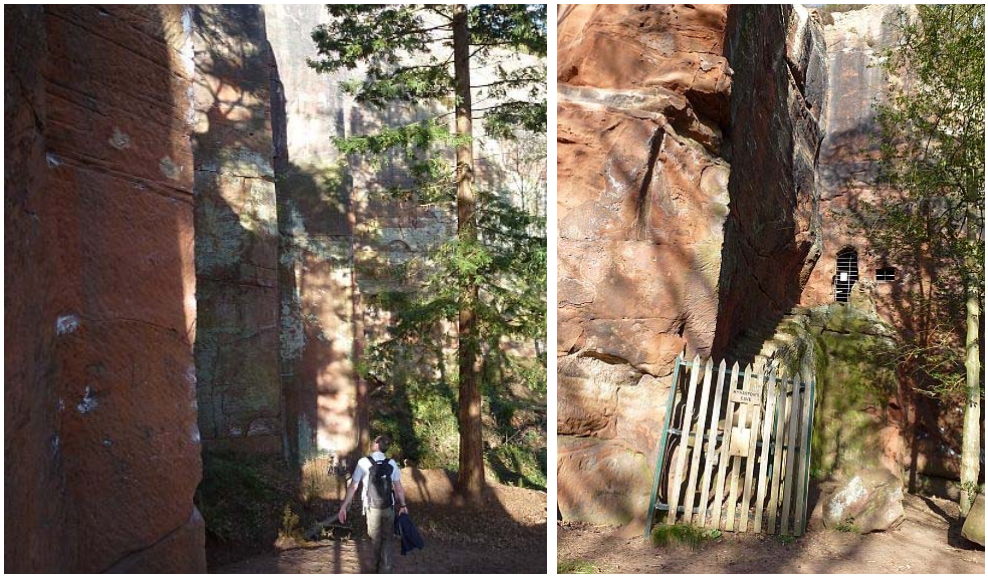

a) b)

Fig.3-40. Sandstone outcrop at Nesscliffe including Wildmoor Sandstone, bottom, and Helsby Sandstone at top; b) a rock house showing 3D massive sandstone structures at Nesscliffe.

a) b)

Fig.3-41. The sandstones at Nesscliffe site: planar laminated, massive-shape sandtones interbedded with lamiantion, deformation structure (slumped beds) at top (arrow); b) Medium-grained sandstone with granulation seams (arrow).

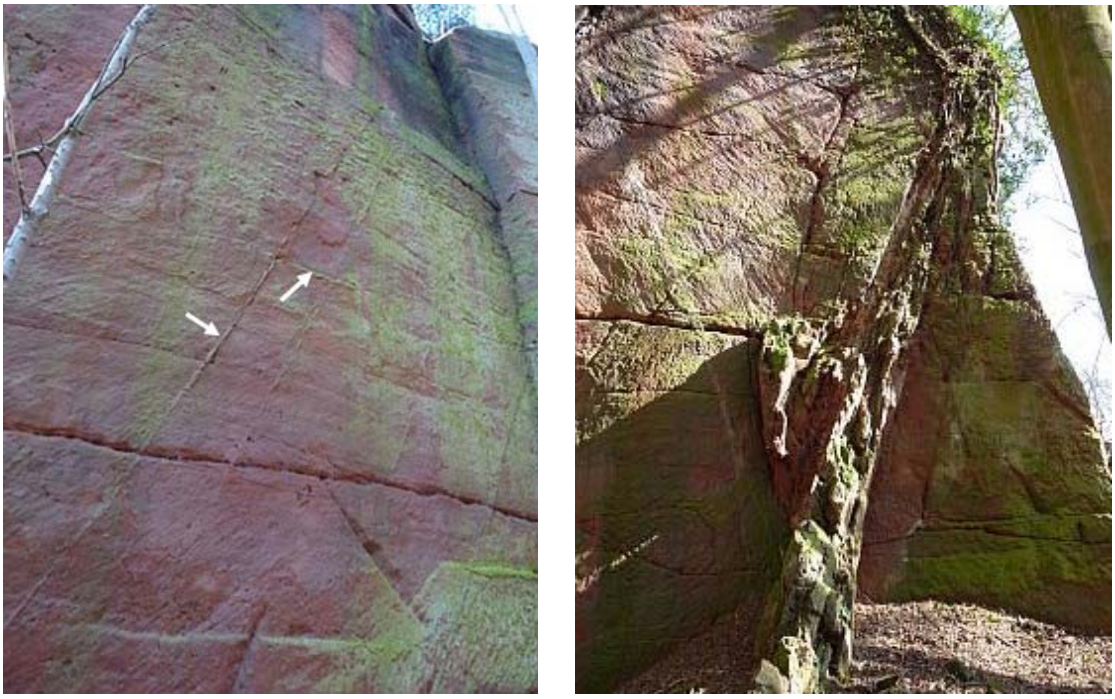

a) b)

Fig.3-42. The sandstones at Leaton site: reddish pink cross-bedded sandstone with granulation seams (arrows) and lamination at the top; b) Cross-bedded sandstone with bounding surfaces (left) and fractured-beds (middle).

a) b)

Fig.3-43. a) Large-scale aeolian cross-bedded sandstone with joints (Leaton site); b) Reddish brown, fine-to medium-grained sandstone with occasional harder laminae and granulation seams (arrows) (Leaton site).

3.6.5 Hydraulic properties

In this study, 16 samples from five beds are collected at Bridgnorth Hermitage outcrop (Table 3-16) and their hydraulic properties are plotted in Fig.3-44. A detailed set of permeability measurements using a mini-permeameter at the site is described in detail in Chapter 5. Fig.3-44 shows porosity and hydraulic conductivity variation between and within beds. Beds 1, 2, and 3 show similar porosity and hydraulic conductivity variations owing to similar lithology characteristics, while B5 shows lower porosity and hydraulic conductivity (possibly caused by large variation in grain size and thin laminae). Laminations (in beds B2 and B5) probably cause drop in permeability for vertical flow (Fig.3-44). Generally, aeolian sandstones as at Bridgnorth show relatively high permeability. This is because of the well rounded, and well sorted sand grains, and the absence of pore-filling cement.

Table 3-16. Sedimentary description for samples collected at Bridgnorth site.

Bed/lithofacies	Sample ID	Brief discription
Bed B1	B1-1, B1-2*	Fine- to medium, medium-grained size, well sorted, planar or low-angle cross-laminated sandstones, some magnetite. Aeolian dune. Samples are separated by 30 cm within the bed B1
Bed B2	B2-1, B2-2	Medium-grained size, well sorted, cross-laminated sandstones, some magnetite, bleaching (yellow). Samples are within a block in bed B2
Bed B3	B3-1, B3-2	Fine- to medium-, medium-grained, medium sorted, low-angle cross-lamminated sandstones. Aeolian dune. Samples are separated by 30 cm within the bed B3
Bed B5	B5-1*, B5-2, B5-3, B5-4, B5-5*, B5-6, B5-7, B5-8, B5-9*, B5-10	Very fine- to medium-grained size, thin planner crossed-laminated sandstones. Aeolian dune. Samples are separated by 30 cm to 1.5 m within the bed B5

* vertically oriented samples

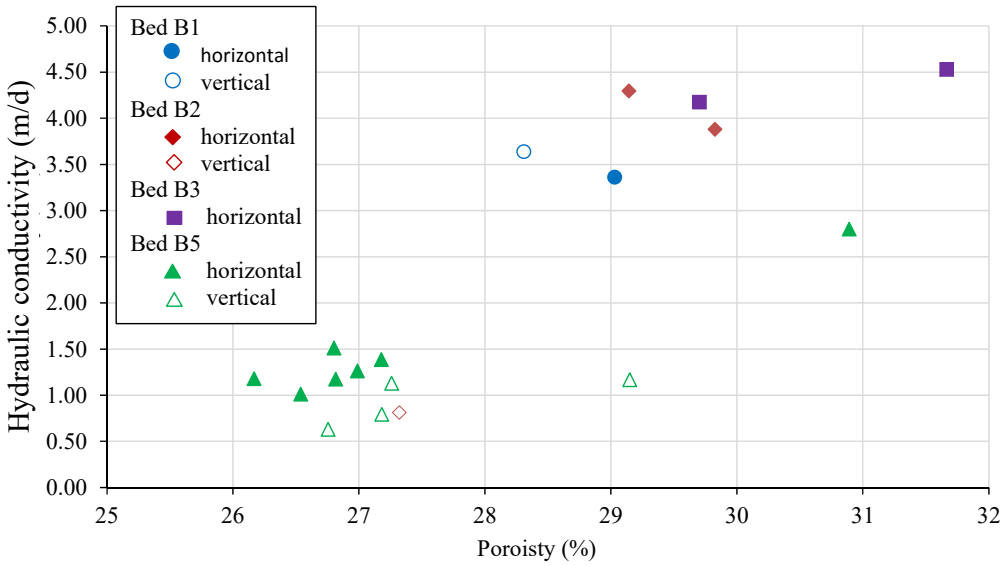

Fig.3-44. Hydraulic conductivity versus porosity for Bridgnorth samples.

Table 3-17 and Fig.3-45a,b summarise sedimentary characteristics and hydraulic properties of samples collected at Grinshill Old Quarries and Nesscliffe and analysed by Hallett (2014).

For Grinshill Old Quarry sites, three locations (Location 1, 2, and 3) were studied. Porosity and permeability values show slight variations between and within locations (Fig.3-45a). Location 1 with greater grain size variation and poorly sorted possesses lower permeability compared with Locations 2 and 3 which have narrower variation in grain sizes and better sorted grains, but there is only one sample at Location 3.

For the Nesscliffe site, 11 core samples were drilled from blocks of samples and measured for hydraulic properties (Table 3-17 and Fig.3-45b). Fig.3-45b shows porosity and hydraulic conductivity variations as function of grain sizes for the samples. There is a hydraulic conductivity/grain size correlation with greater hydraulic conductivities for coarser-grained samples, but porosities show little variation with grain size.

Table 3-17. Sedimentary description for samples at Grinshill Old Quarries and Nesscliffe (data from Hallett, 2014).

Site	Location	Sample ID	Brief discription
Grinshill	1	G1-1.1/2, G1-2, G1-3.1/2, G1-4.1/2, G1-5, G1-6	Aeolian dune: fine- to coarse-grained, poorly sorted, well consoliated sandstones. Samples are separated by 1m to 10m within the site
	2	G2-1.1, G2-2.1/2, G2-3.1/4, G2-5.1/2, G2-6.1/2, G2-7, G2-8, G2-9.1/2, G2-10U.1/2, G2-11U.1/2	Aeolian dune: fine- to medium, moderate-well sorted, plane or cross-lamination. Samples are separated by 1m to 15 m within the site. Site 1, 2, 3 are 30 to 100m apart.
	3	G3-f2	
Nesscliffe		M1-11	Aeolian dune: fine- to medium-grained, well sorted, massive sandstones with mud lamination and occastionally bleaching. Samples are separated by 2m to 50m.

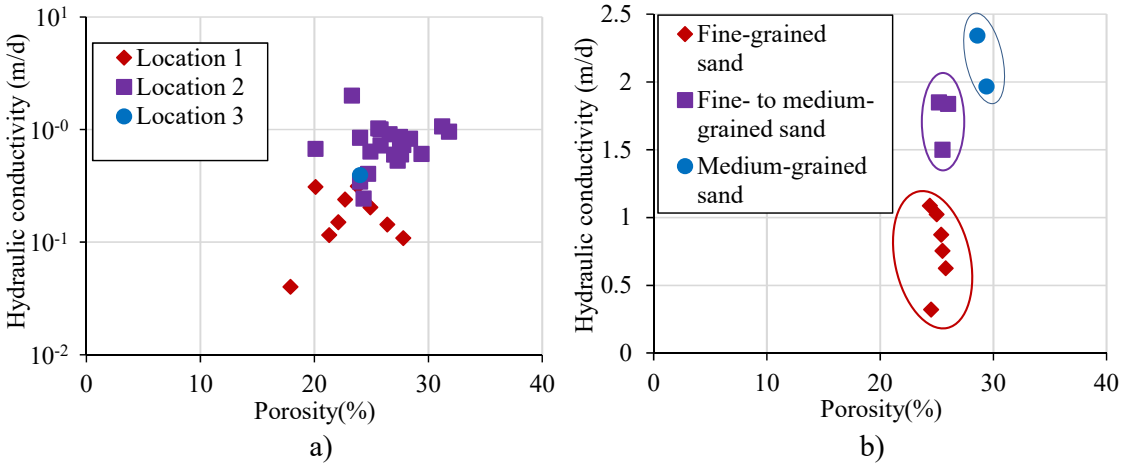

Fig.3-45. Hydraulic conductivity versus porosity at: a) Grinshill Old Quarry; b) Nesscliffe (data from Hallett, 2014).

The Permian Bridgnorth Sandstone Formation and Triassic Sherwood Sandstone Group each act as aquifers with the Chester Pebble Beds of the latter being less porous due to a higher degree of cementation (Allen et al., 1997). In the following subsections, field samples along with the existing data set reported by Allen et al. (1997) are used to quantify the hydraulic properties of the Permo-Triassic sandstones and to compare hydraulic characteristics between fluvial and aeolian systems in the region.

3.6.5.1 Porosity

Recorded porosities of the Permo-Triassic sandstone in Shropshire vary from 6 % to 34% (Table 3-18). This wide range is due to variation in grain size, grain sorting and shape (roundness), type and degree of cementation, and extent of weathering (Allen et al., 1997). The Bridgnorth Sandstone Formation has the greatest range in porosity (6% to 34%). The lower limit is associated with cemented siltstone towards the top of the Formation, whilst the upper limit value corresponds to the less or free-cemented, 'millet-sand' grain at the lower part of the Formation (Allen et al., 1997). The samples collected in this study have porosity values in the upper limit of the range recorded by Allen et al. (1997). The Chester Pebble Beds has porosity ranging from about 12% to 33%. Low porosity values correspond to well-cemented materials, and high values are attributed to less cemented, coarser cleaner sands (Allen et al., 1997). The Wilmslow Sandstone Formation has a porosity range from 17 % to 32%. The Helsby Sandstone Formation has a similar porosity range (from 15 % to 31 %) to the Wilmslow Sandstone Formation. Samples collected at Grinshill Old Quarry and Nesscliffe as part of the present study and analysed by (Hallett, 2014) are similar to those given by Allen et al (1997) (Table 3-18).

Table 3-18. Core porosity for Permo-Triassic sandstones in Shropshire.

Formation	Area	Range (%)	Interquartile range (%)	Median (%)	Arithmetic mean (%)	Author
Hesby Sandstone	Grinshill Old Quarries	17.9-31.8	23.9-27.5	25.6	25.3	Hallett (2014)
	Nesscliffe	24.4-29.4	25.1-25.9	25.5	25.9	
	Shropshire	14.7-31.2	19.4-28.7	25.6	24.2	Allen et al. (1997)
Wilmslow Sandstone	Shropshire	17.0-31.8	24.5-29.3	27.4	26.5	Allen et al. (1997)
Chester Pebble Beds		12.4-33.2	19.4-27.1	23.5	23.2	
Bridgnorth or Kinnerton Sandstone		5.5-34.0	20.0-27.6	23.9	23.2	
	Bridgnorth	26.2-31.7	26.9-29.2	27.3	28.2	This study

3.6.5.2 Hydraulic conductivity

Hydraulic conductivities of the Permo-Triassic sandstones in Shropshire are derived from core sample tests, *in situ* mini-permeameter measurements and borehole pumping tests (Tables 3-19, and Table 3-20). At core scale, hydraulic conductivity ranges over six orders of magnitude from 2 x 10^{-5} m/d to 15 m/d. As with the porosity, there is no apparent trend of hydraulic conductivity variation in the top 140 m (Allen et al., 1997; Cheney et al., 2004).

The Permian Bridgnorth Sandstone Formation shows the widest range of core permeability (hydraulic conductivity), from 2 x 10^{-5} m/d to 15 m/d, with a median of 0.4 m/d (Table 3-19). This variation is due to variability of lithology. The low values of permeability are associated with siltstone and fine-grained sandstone towards the top of the Formation, whilst high values come from coarser, 'millet-seed' sandstone at the base of the formation, and intermediate values are from muddier sandstones (Allen et al., 1997). Mini-permeameter derived permeabilities at outcrop and from core samples produced as part of the current study show similar values (from 0.6 to 4.5 m/d, with a geometric mean of 1.7 m/d).

The Chester Pebble Beds Formation has core hydraulic conductivities ranging from 3 x 10^{-4} to 15 m/d. The degree of cementation rather than grain size contributes to this variation (Allen et al., 1997). Limited core samples from the Wilmslow Sandstone Formation show hydraulic conductivity ranges from 9 x 10^{-3} to 6 m/d, with a median of 1.3 m/d. The fine-grained sandstone appears in both cemented and uncemented versions (Allen et al., 1997). The Helsby Sandstone Formation has core hydraulic conductivity ranging from 1.5 x 10^{-3} to 3 m/d, with a median of 0.86 m/d. Hallett (2014) reported hydraulic conductivities of the samples taken from the Helsby Sandstone Formation at Grinshill Quarry and Nesscliffe (see above) with a range from 0.3 to 2.3 m/d, and a median of 0.6 m/d for the Nesscliffe and 0.04 to 2.0 m/d, and a median of 1.1 m/d for the Grinshill Old Quarry. Coarse-grained, cemented sandstones at the base of the Formation and very fine-grained sandstone towards the top of the Formation show low hydraulic conductivity, whereas the cross-bedded sandstones in the middle of the Formation have the highest hydraulic conductivity (Allen et al., 1997).

To access the significance of fracture flow to the formations, Allen et al. (1997) converted transmissivity data obtained from pumping tests to bulk hydraulic conductivity. These bulk hydraulic conductivities are tabulated (Table 3-20) and can be directly compared to the intergranular (core) hydraulic conductivities above.

As a whole, bulk hydraulic conductivity ranges from 0.09 to 46 m/d, with a median of 3.8 m/d and a geometric mean of 3.9 m/d (Table 3-20). The lower limit of the bulk hydraulic conductivity range is about four orders of magnitude greater than the lower limit of the core permeability range. This difference is matter of scaling aspects; the core sample is centimetre-scale that can contain entirely less permeable units which is not the case at the borehole scale. The upper limit for the bulk hydraulic conductivity range (46 m/d) is also greater than that of

the core hydraulic conductivity range (15 m/d). This difference is caused by effects of fracture flow at borehole scale (Allen et al., 1997).

The bulk hydraulic conductivities were classified into particular formations: The Permian Bridgnorth Sandstone and the Chester Pebble Beds (Kidderminster Formation) (Table 3-20). The Chester Pebble Beds have similar hydraulic conductivity values for the upper limit of the range for both core and borehole scale (15 m/d), whereas, the lower limit of the bulk hydraulic conductivity (0.3 m/d) is significantly greater than that of the core hydraulic conductivity (3 x 10^{-4}m/d), as expected from the scale effect mentioned above. The Bridgnorth Sandstone Formation, in contrast, shows not much difference at the lower limit for both measurement scales, whilst the upper limit of the bulk hydraulic conductivity (25 m/d) is greater than that of the core hydraulic conductivity (15 m/d), suggesting the significant contribution of fracture flow in boreholes.

Table 3-19. Core hydraulic conductivity for sandstones at Shropshire England.

Formation	Area	Range (m/d)	Interquartile range (m/d)	Median (m/d)	Geometric mean (m/d)	Author
Helsby Sandstone	Grinshill Old Quarries	0.04-2.0	0.3-0.8	0.6	0.6	Hallett (2014)
	Nesscliffe	0.3-2.3	0.8-1.8	1.1	1.3	
	Shropshire	$1.5x10^{-3}$ – 2.9	0.56-4.1	0.86	0.33	Allen et al. (1997)
Wilmslow Sandstone	Shropshire	$9.3x10^{-3}$ – 6.0	0.056-1.13	1.28	0.7	
Chester Pebble Beds or Kidderminster	Shropshire	$3.1x10^{-4}$ – 15	0.1-3.4	1.5	0.57	
Bridgnorth or Kinnerton Sandstone	Shropshire	$2x10^{-5}$ – 15	0.02-2.6	0.44	0.16	
	Bridgnorth	0.63-4.53 0.62-4.73*	1.1-3.6 1.25-2.34*	1.33 1.8*	1.74 1.76*	This study

** Permeability measured on outcrop face using a probe/mini permeameter*
Permeability unit conversion from mD to m/d were made here and elsewhere in this Chapter and the thesis with reference temperature of 20^0 C.

Table 3-20. Bulk hydraulic conductivity for Permo-Triassic sandstones of Shropshire (after Allen et al., 1997).

Formation/Group	Range (m/d)	Interquartile range (m/d)	Median (m/d)	Geometric mean (m/d)
All	0.093-46	1.8-8.4	3.84	3.94
Chester Pebble Beds or Kidderminster	0.33-16	1.3-8.4	3.86	3.28
Bridgnorth Sandstone	0.094-25	5.9-15	10.6	6.94

3.6.5.3 Anisotropy

The ratio of geometric mean of horizontal to vertical core hydraulic conductivity gives the anisotropy ratio. The anisotropy ratios of the Permian Bridgnorth Sandstone Formation and the Triassic Sherwood Sandstone Group in the Shropshire are shown in Table 3-21. The anisotropy ratio ranges from 2.2 to 3. The samples collected at the Bridgnorth outcrop in this study show an anisotropy of 2.6. Generally, horizontal permeability is greater than vertical permeability.

Table 3-21. Horizontal and vertical hydraulic conductivity for Permo-Triassic sandstones of Shropshire.

Formation/ Group	Orientation	Range (m/d)	Interquartile range	Median (m/d)	Geometric mean (m/d)	Anisotropy (Kh/Kv)	Author
Sherwood Sandstone	Horizontal (Kh) Vertical (Kv)	$2.0x10^{-5}$ - 15 6.2x10-5 - 12	0.06-2.62 0.02-1.89	0.82 0.28	0.31 0.14	2.2	Allen et al. (1997)
Kinnerton or Bridgnorth Sandstone	Horizontal Vertical	$2.0x10^{-5}$ - 15 6.2x10-5 - 12	0.039-2.8 2.9x10-3 -1.9	0.51 0.12	0.22 0.07	3.0	
	Horizontal Vertical	-	1.3-3.9 0.8-1.1	2.8 0.81	2.26 0.88	2.6	This study

3.6.5.4 Hydraulic conductivity versus porosity

Core hydraulic conductivities versus porosities for different formations of the Permo-Triassic sandstone in Shropshire are summarized in Fig.3-46a-f. Overall, the correlation between permeability and porosity is very broadly similar across the region, but there are local differences, even within a region (cf. the two relationships in Fig.3-46b). The Wilmslow Sandstone Formation has the strongest correlation between permeability and porosity (Fig.3-

46c), and the Chester Pebble Beds and the Kinnerton Sandstone the broadest scatter (assuming the Helsby Sandstone has two distinct trends).

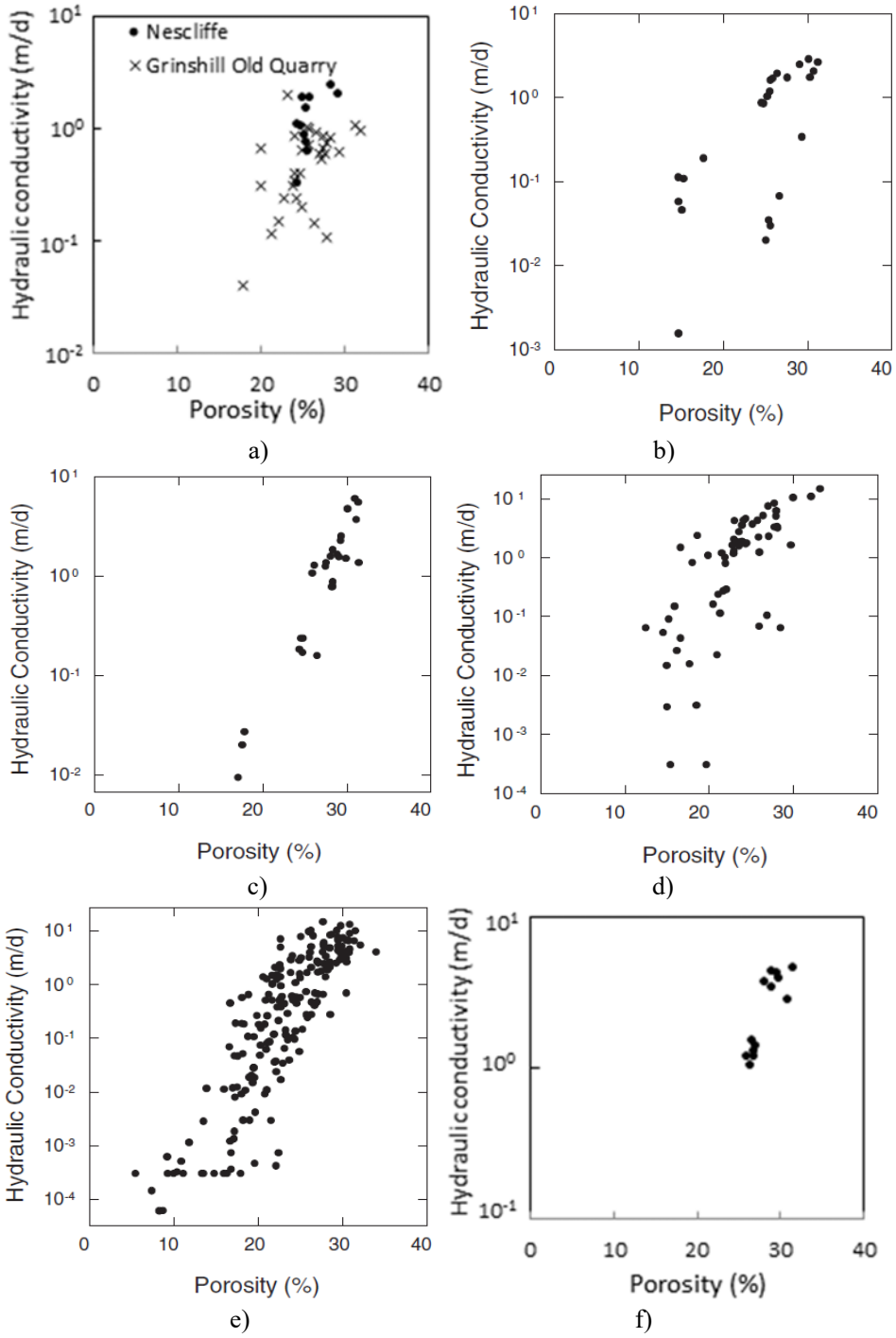

Fig.3-46. Core porosity versus hydraulic conductivity for Permo-Triassic sandstones in Shropshire for different formations, a) Helsby Sandstone at Grinshill Old Quarry and Nescliffe (data from Hallett, 2014); b) Helsby Sandstone (from Allen et al. 1997); c) Wilmslow Sandstone (from Allen et al. 1997); d) Chester Pebble Beds (from Allen et al. 1997); e) Kinnerton Sandstone (from Allen et al. 1997); f) Bridgnorth Sandstone (this study).

3.6.5.5 Fluvial system versus aeolian system

Aeolian and fluvial systems are both represented in the Permo-Triassic sandstone of Shropshire with the former dominating in the Permian Bridgnorth (Kinnerton) Sandstone Formation, whereas the latter significant in the Triassic sequences. The core sample hydraulic properties of the formations of the Permo-Triassic sandstone are retabulated to compare between fluvial and aeolian systems in the region (Table 3-22).

The tendency for the permeability (hydraulic conductivity) of aeolian sandstones to be greater than that of fluvial sandstones seen in other areas is less clear here. There is not much difference of permeability of the aeolian Bridgnorth Sandstone and the fluvial dominated Triassic sandstones, and this is also seen with porosity. Within the Bridgnorth Sandstone Formation, the lower part has high values of hydraulic properties as the sediments are general coarser, indicating that local issues can dominate.

Table 3-22. Hydraulic properties for fluvial and aeolian sandstones of Shropshire.

Dominated system	Formation	Area	Hydraulic conductivity (m/d)			Arithmetic mean porosity (%)	Author
			Interquartile range	Median	Geometric mean		
Fluvial	Helsby Sandstone	Grinshill Quarries	0.3-0.8	0.6	0.6	25.3	Hallett (2014)
		Nesscliffe	0.8-1.8	1.1	1.3	25.9	
		Shropshire	0.56-4.1	0.86	0.33	24.2	Allen et al. (1997)
	Chester Pebble Beds	Shropshire	0.1-3.4	1.5	0.57	23.2	
Aeolian	Wilmslow or Wildmoor Sandstone	Shropshire	0.056-1.13	1.28	0.7	26.5	
	Bridgnorth or Kinnerton Sandstone	Shropshire	0.02-2.6	0.44	0.16	23.2	
		Bridgnorth	1.1-3.6 1.25-2.34*	1.33 1.8*	1.74 1.76*	28.2	This study

** Permeability measured on outcrop face using a probe/mini permeameter.*

3.7 West Midlands

3.7.1 Geological setting

The Permo-Triassic sandstone sequences in the West Midlands occur in several interconnected basins, including the Stafford, Needwood, Hinckley, Knowle, and Worcester basins (Fig.3-47). The stratigraphy of the Permo-Triassic sandstones in the West Midlands is given in Table 3-23.

A total of five outcrops of the Permo-Triassic sandstones have been examined in this study. The aeolian Permian Bridgnorth Sandstone Formation is seen at outcrops at Kinver Edge and Kingsford, and the fluvial Triassic Kidderminster Formation is seen at the Hulme Quarries, Croxden Quarry, and Wolverley outcrops.

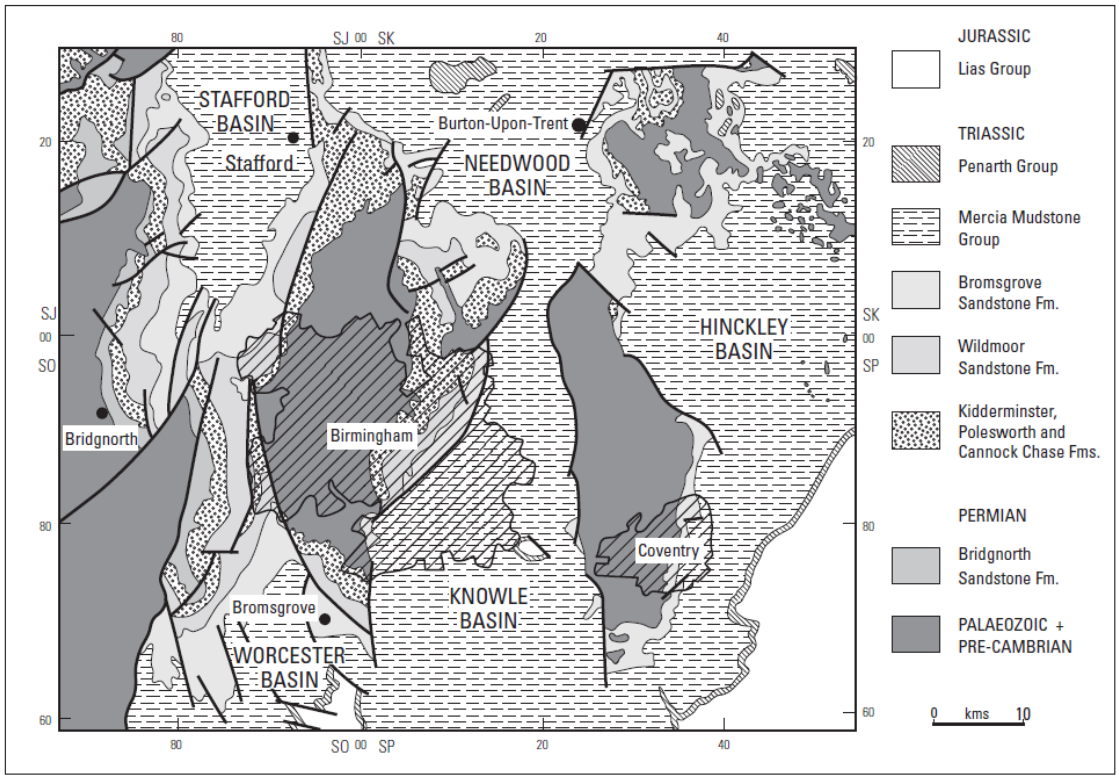

Fig.3-47. Geology and Permo-Triassic basins in West Midlands (from Allen et al., 1997).

Table 3-23. Summary stratigraphy of Permo-Triassic sandstones in West Midlands.

Age	Group	Formation	Area	Lithology	Predominant environment	Author/observer
Triassic	Mercia Mudstone	West Midlands	West Midlands	Mudstones	Marine, and arid periods	Warrington et al. (1980), Benton et al. (2002)
	Sherwood Sandstone	Bromsgrove Sandstone	West Midlands	Breccias and conglomerates at lower part and sandstones at upper part	Fluvial	Warrington et al. (1980), Benton et al. (2002), Cheney et al. (2004)
		Hawksmoor Formation,	Croxden Quarry	Conglomerate, sandstone	Fluvial	This study
		Wildmoor Sandstone	Boreholes at Birmingham University Campus	Sandstone	Fluvial, aeolian	Bouch et al. (2006)
		Cannock Chase or Kidderminster	Hulme Quarries	Conglomerates, sandstone	Fluvial	This study
Permian			Woverley outcrop, Kidderminster	Sandstone	Aeolian	
	Bridgnorth Sandstone		Kinver, Kingsford, Bridgnorth	Sandstone	Aeolian	

3.7.2 Studied sites: outcrops at Kinver Edge, south Staffordshire and Kingsford, Worcestershire (SO 836835)

A series of 'Rock houses' exposing 3D large-scale aeolian sandstones exists at the Holy Austin Rock at Kinver Edge, South Staffordshire (Fig.3-48) and at Vale's Rock at Kingsford, Worcestershire (Fig.3-52a,b).

The sandstones at the sites are of the Bridgnorth Sandstone Formation (Tyler-Whittle et al., 2002, Benton et al., 2002) characterized by red, reddish-brown, pale, occasionally green, fine- to medium-grained, well-rounded sandstones (Fig.3-54a,b). Sedimentary structures include plane bedding or low-angular cross-bedding (Fig.3-49a,b), tabular and trough cross-bedding

(Fig.3-49a,b, Fig.3-53a), lamination (Fig.3-50b), some bleaching along horizontal bands, and reactivation surfaces (Fig.3-49a, Fig.3-50a).

The Bridgnorth Sandstone Formation at these sites is interpreted as deposits of large-scale, crescentric barchan dunes with prevailing wind from the east (Shotton, 1937; 1956). Mader and Yardley (1985) identified bounding surfaces with a complex hierarchy, probably of four levels, and suggested that the Formation formed by major draa bedforms being superimposed small-scale transverse dunes. Karpeta (1990) studied the Brignorth Sandstone Formation in the Bridgnorth area and reported three major aeolian facies associations: transverse draas, barchanoid draas, and dome dunes (see at Bridgnorth in Shropshire above) with long term winds from the east which controlled the shapes of the transverse draas and dome dunes, and seasonal winds from northeast which controlled the barchanoid draas and oblique cresentic dunes on the lee face of the transverse draas (Fig.3-32).

Fig.3-48. ‘Rock’ houses at Kinver Edge showing large-scale cross-bedding sandstone.

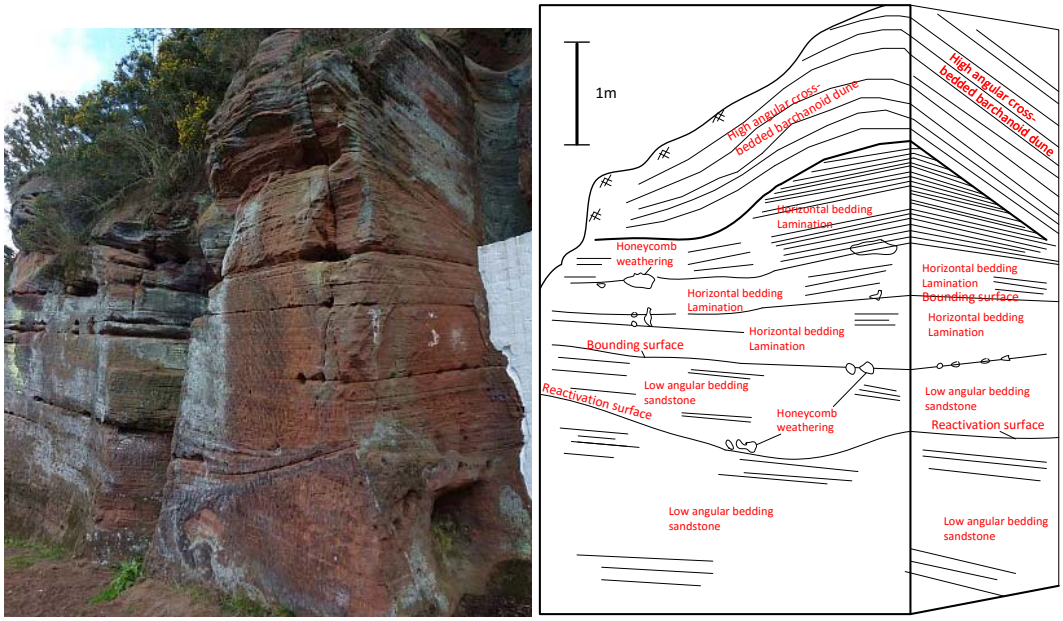

a) b)

Fig.3-49. A photograph (a) and diagram (b) of the Bridgnorth sandstone showing a spectacular bachanoid dune set (Brian and Christopher, 2000).

a) b)

Fig.3-50. a) Sanstone with reaction suface (close view from Fig.4.3a); b) Flat-bedding sandstone and lamination.

. a) b)

Fig.3-51. Large-scale planar cross-bedding.

The Vale's Rock at Kingsford, Worcestershire (SO 829818)

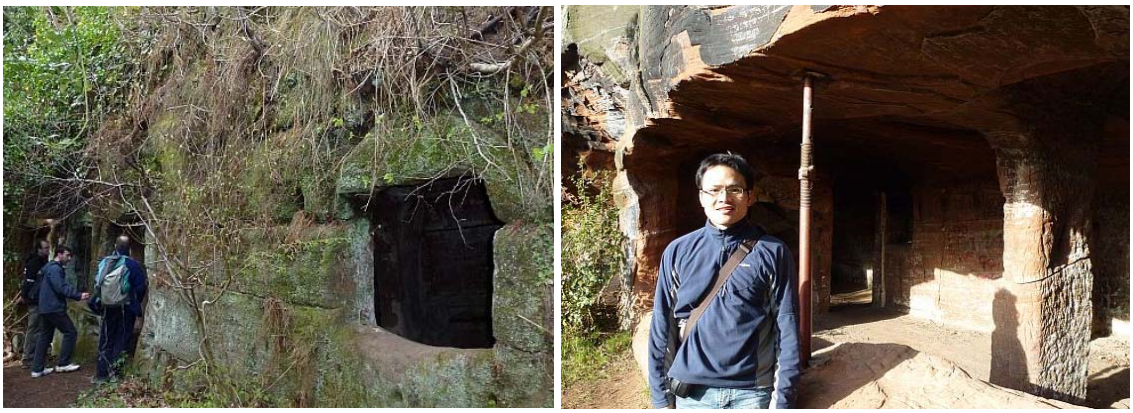

a) b)

Fig.3-52. a-b Multi-room rock house showing 3D structure of Bridgnorth sandstone at the Vale's Rock.

a) b)

Fig.3-53. a) Inside of a rock house; b) Wetted medium-grained sandstone above coarse sandstone with presumably higher water entry pressure.

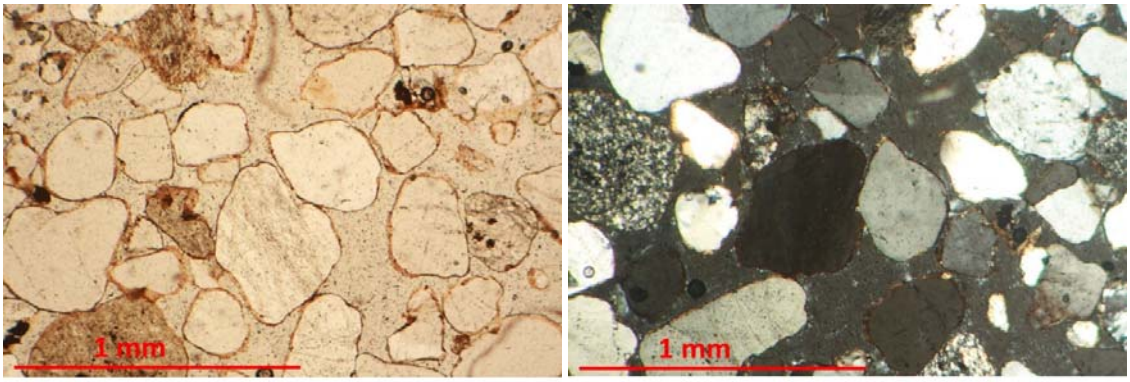

a) b)

Fig.3-54. Photomicrographs of Bridgnorth Sandstone at the Kingsford site, showing well-rounded, well-sorted, coated sand grains with highly connected pores leading to high porosity and permeability, a) plane-polarized light; b) cross-polarized light.

3.7.3 Studied sites: Hulme Quarry, Staffordshire (SJ 926445)

The Hulme Quarry at Stoke-On-Trent, Staffordshire demonstrates excellent outcrops of pebble beds of the Cannock Chase Formation (Fig.3-55, and Fig.3-56) (Benton et al., 2002), equivalent to the Kidderminster Formation of the Worcester Basin, Polesworth Formation of the Hinckley Basin, and the Chester Pebble Beds of the Cheshire Basin (Warrington et al., 1980). There were five facies identified by Steel and Thompson (1983) (Table 3-24) including: A-Flat-stratified poorly sorted conglomerate with thickness from 1-5 m, commonly 1-3 m, generally showing upward-coarsening (from Fig.3-57 to Fig.3-60); B- Cross-stratified conglomerates, interbeddeing with sandstone, thickness normally varying from 2-5 m, sometimes much thicker (from Fig.3-57 to Fig.3-60); C- Cross-bedded, medium-grained sandstone, co-operating with pebbles, varying in thickness from 2-5 m (Fig.3-57, Fig.3-59a,b, and Fig.3-60); D- Argillaceous and thick fine-grained, cross-bedded sandstone, some with slump, soft sediment deformation structures (from Fig.3-57 to Fig.3-60); and E- Dominated by fine-grained, parallel bedded sandstone, with interbedded red micaceous shales and argillaceous silty-sandstone, impersistent in thickness and being up to 1 m thick, normally interbedded with facies C and D.

The sedimentary structures vary with both planar and trough cross-bedding, re-activation surfaces, erosion surfaces, texturally mature conglomerates of poorly sorted in horizontal units or better sorted in cross-bedded units and soft sediment deformation. Interbedded sandstones are associated with thick layers of conglomerates, in coarsening-upwards units and rapid lateral changes from conglomerate to sandstone (Benton et al., 2002) (Fig.3-61).

The Cannock Chase Formation is interpreted as being deposited by high-energy braided river system flowing north or northwest, or by a low-sinuosity channel with ephemeral pools (Steel and Thompson, 1983). Facies A, featuring coarse grains, poorly sorted, flat-stratified was probably deposited under high-energy flow reign in flow with high sediment supply. Facies B, coarse-grained, cross-bedded conglomerates formed in foresets on the lee face of river bars, showing ability of waning river when carrying large material (Fig.3-62). The facies C and D were formed in broad channels and present migration of sandwaves in channels. Facies E present a deposition in ephemeral pools or in abandoned channels (Steel and Thompson, 1983).

Table 3-24. Five facies classified by Steel and Thompson (1983) at Hulme Quarry.

Facies	Lithology / structures	Sedimentary Interpretation
A	Horizontally-stratified, poorly sorted conglomerate	Deposited in high-energy flow regime with high sediment supply.
B	Cross-stratified conglomerate	Avalanched down the lee slop of bars
C	Cross-stratified pebbly sandstone	Deposited in broad channels
D	Argillaceous, fine-grained, cross-bedded sandstones	Deposited in broad channels
E	Fine-grained sandstone, micaceous shales, and argillaceous silty sandstones	Deposited in ephemeral pools

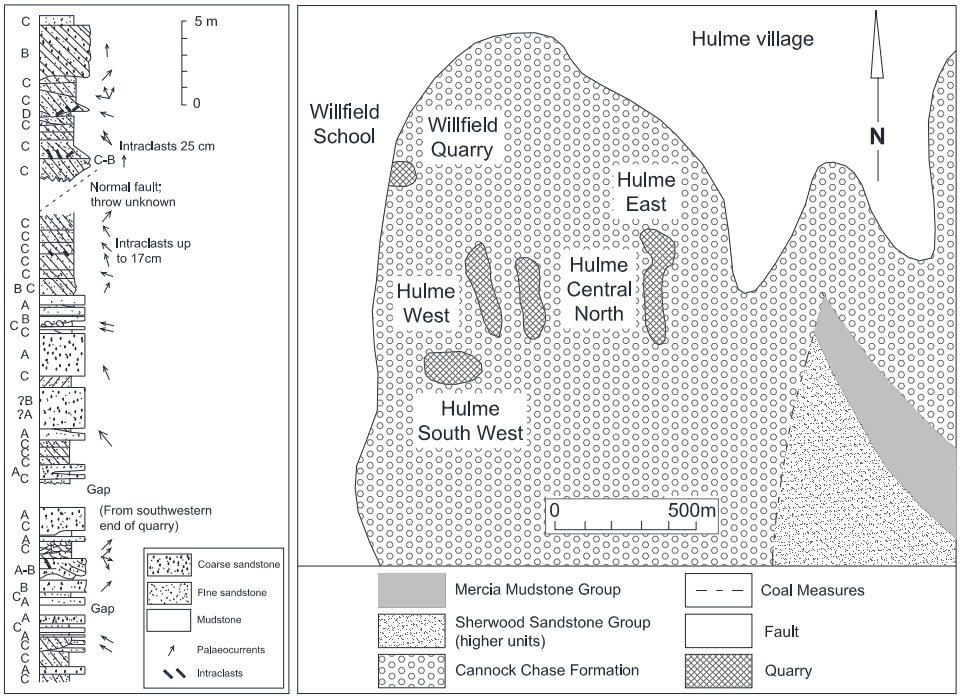

Fig.3-55. Schematic map of Hulme Quarries and their lithological logging (after Steel and Thompson, 1983; Benton et al., 2002).

Fig.3-56. Outcrop at the Hulme Quarry showing thick conglomerate bes interbedded with sandstone (The quarry is about 12m high and 100m long).

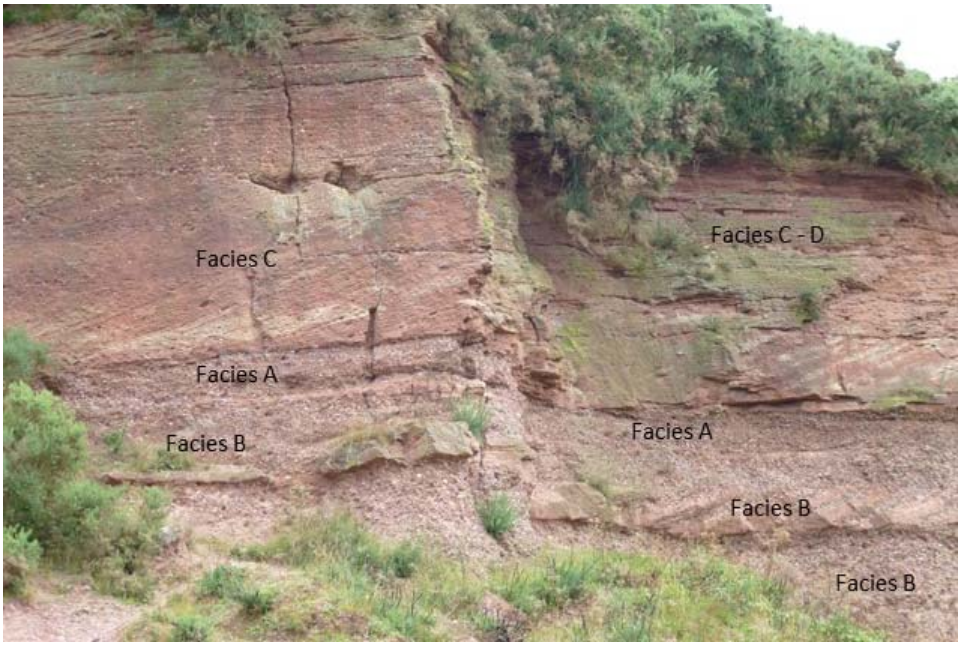

Fig.3-57. Closed view of the outcrop at Hulme Quarry (outcrop height is about 12 m): location of Facies A to Facies D.

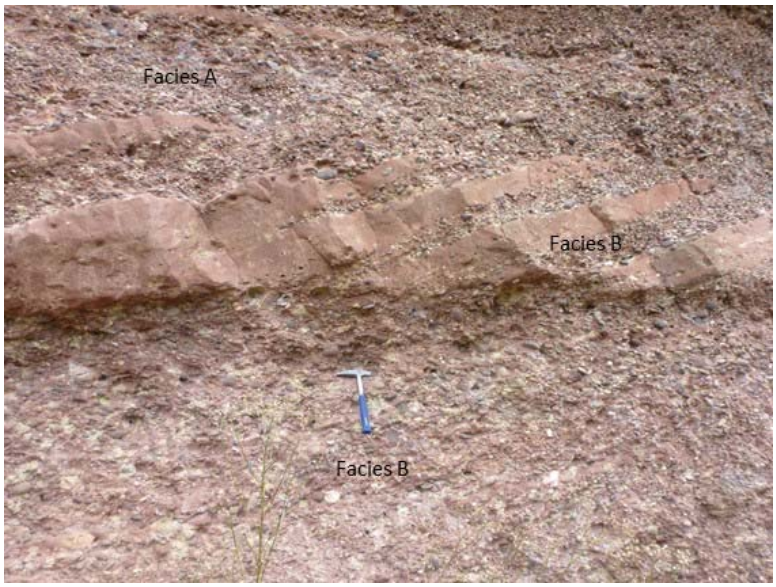

Fig.3-58. Foreset of the cross-bedded sandstone interbedded with foresets of conglomerate (Facies B), which are in turn sandwiched by planar cross-bedded conglomerates (Facies B) below and flat-stratified conglomerates (Facies A) above.

a) b)

Fig.3-59. a) Thick tabular planar and trough cross-bedded sandstone Facies C with some yellow bleached cross-beds overlying the flat-stratified conglomerates Facies A with interbedded cross-stratified sandstone; b) Cross-bedded, discontinuous sandstone layer in thick poorly sorted pebble beds of Facies A.

Fig.3-60. Quarry wall showing cross-bedding Facies C and probably Facies D at the upper part and Facies A, B in the lower part (outcrop 12 m high).

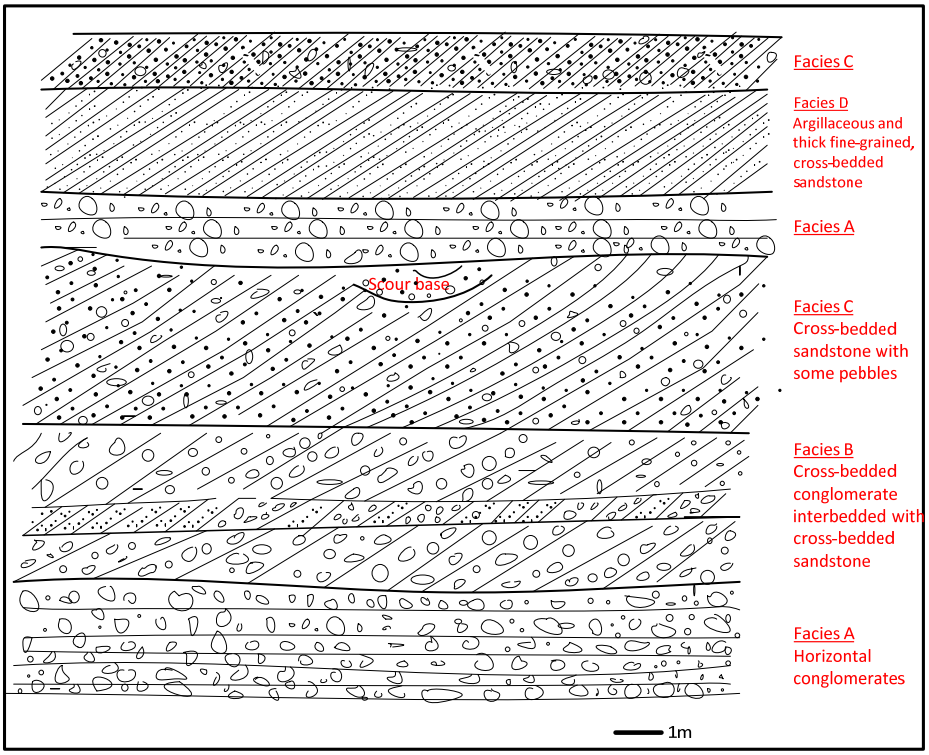

Fig.3-61. Sketch cross-section at Hulme Quarry showing grain-size varying from pebbles, conglomerate sandstone to fine sandstones and mudstone forming different facies.

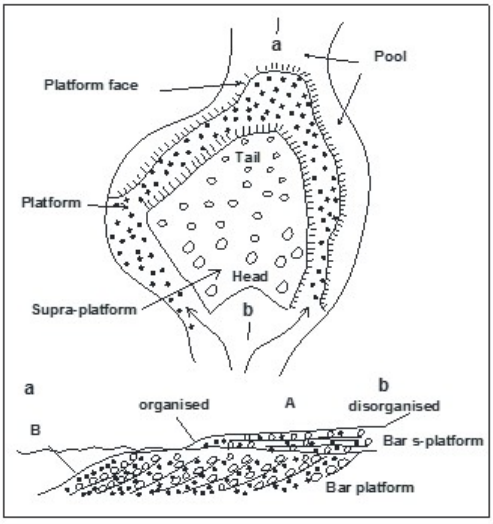

Fig.3-62. Interpretation of facies A and B and their relationship (from Steel and Thompson, 1983).

3.7.4 Studied sites: Croxden Quarry, Staffordshire (SK 016413)

Croxden Quarry is located south Cheadle in Staffordshire and currently operated by Tarmac Quarry Products Ltd. In the Cheadle district, the Sherwood Sandstone Group overlies Carboniferous rocks, though it is possible that part of the Sherwood Sandstone Group may be Permian in age (Rogers et al., 1981). The Sherwood Sandstone Group in the district includes, in upwards succession, the Huntley (Ambrose et al., 2014), Hawksmoor, and Hollington formations (Rogers et al., 1981) and are probably equivalents of the Kidderminster Formation in the Worcester Basin, Cannock Chase Formation in the Stafford Basin and Kinnerton Formation in the Cheshire Basin. The Hawksmoor Formation is only and well exposed at the Croxden Quarry and is further divided into two members: the underlying Freehay Member, most common at the quarry, and the overlying Lodgedale Member (Rogers et al., 1981). The Freehay Member consists of conglomerates and interceded discontinuous sandstones bands and lenses. The Lodgedale Member comprises of pebbly sandstone with generally impersistent conglomerates (Rogers et al., 1981).

The conglomerates at the quarry are reddish brown, horizontally stratified, poorly cemented interbedded with pink, pale-brown, flat-bedded or low-angle bedded (Fig.3-63a) or planar and trough cross-bedded sandstone of about 0.1 to 1.5 m thick (Fig.3-63b). The conglomerate layers are friable (Fig.3-63a,b) consisting of pebbles/cobble and gravels of mainly quartzite, vein-quartz and some rock fragments and are up to 56 m thick in the east and up to 28 m thick in south-eastern Cheadle (Rogers et al., 1981). The conglomerates with clasts of up to 10 cm in diameter are matrix- supported by red, fine sand (Moore, 1996).

The sandstones form bands and lenses of 0.1 m to 1.0 m thick, and are discontinuous in length from 0.5 to 20 m long, consisting of reddish brown, fine- to medium-grained sandstone (Fig.3-

63a,b). Sedimentary structures include flat or low-angle cross-bedding, tabular planar and trough cross-bedding. The sandstones increase in proportion and divide up the conglomerates into thinner layers in the southeast of Cheadle.

The Lodgedale Member at the south of the Croxden Quarry includes light brown, pale, hard, medium-grained, pebbly sandstones, flat-bedded, cross-bedded sandstones, and pebbly sandstone lenses of about 0.2 to 0.7 m thick (Fig.3-64a,b).

Deposits of the Harksmoor Formation are interpreted to present deposition of the high-energy braided river systems (Rogers et al., 1981).

a) b)

Fig.3-63. The Freehay Member deposit (Hawksmoor Formation) at the Croxden Quarry: a) Horizontally bedded conglomerates interbedded with planar stratified sandstone; b) Cross-bedded sandstone interbedded with planar bedded sandstone resting on thick layer of conglomerate.

a) b)

Fig.3-64. Pebbly sandstones of the Lodgedale Member (Hawksmoor Formation), a) Flat-bedded sandstone overlain by cross-bedded pebbly sandstone which in turn is overlain by cross-bedded sandstone; b) Grey, low-angle cross-bedded, pebbly sandstone at base with overlying reddish brown, cross-bedded sandstone, lense of pebbly sandstone and again cross-bedded sandstone at top.

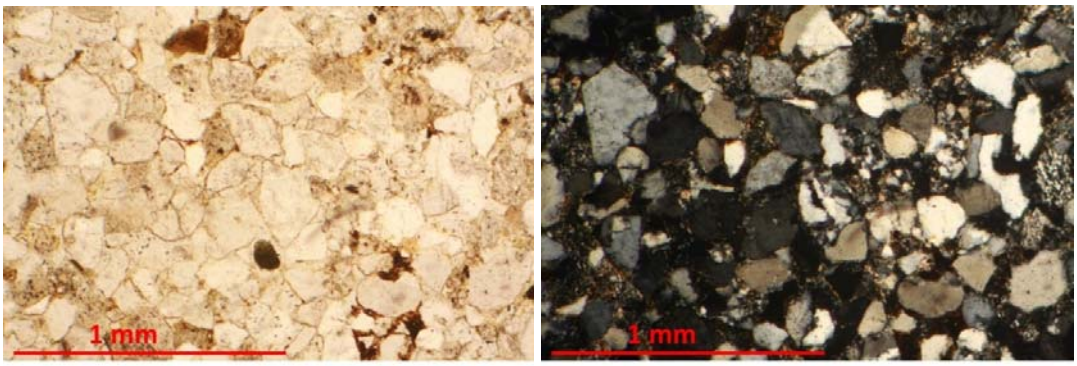

a) b)

Fig.3-65. Photomicrographs of the sandstone at Croxden Quarry, showing sub-angular, moderately well-sorted grains with some calcite cement, a) with plane light; b) with cross polars.

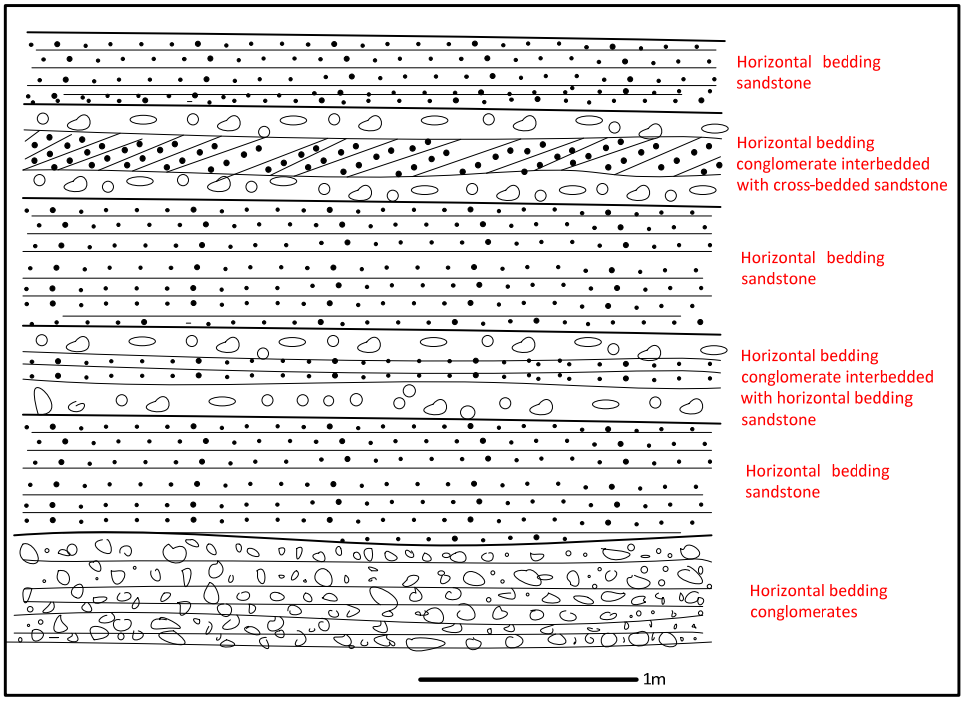

Fig.3-66. Sketch cross-section generating sediment at Croxden Quarry.

3.7.5 Studied sites: Wolverley sandstone outcrop (SO 827794)

The Wolverley sandstone outcrop is located at the Queen's Head Pub carpark, Wolverley, Worcestershire (Fig.3-67, Fig.3-68a,b). The outcrop is of pebbly sandstone of the Kidderminster Formation. The Formation comprises reddish brown, greyish brown, fine- to coarse-grained sandstone with pebbles up to 10 cm long representing channel lags (Fig.3-68a,b Fig.3-69a,b). Sedimentary structures include: horizontally stratified sandstones (Fig.3-67, Fig.3-68a,b), planar and cross-bedded pebbly sandstone (Fig.3-67, Fig.3-68a,b, and Fig.3-69a,b); cross-lamination; reactivation surfaces (Fig.3-69a,b); multi-channel structures (Fig.3-67, Fig.3-68a,b); pebbles lying in foresets and interbedded with sandstone; thin bedded sandstone; some beds wedged or truncated by bounding surfaces. The Kidderminster Formation, which unconformably overlies the aeolian Bridgnorth Sandstone Formation, is

interpreted as being deposited under fluvial conditions (Tyler-Whittle et al., 2002), and probably in high-energy braided river systems.

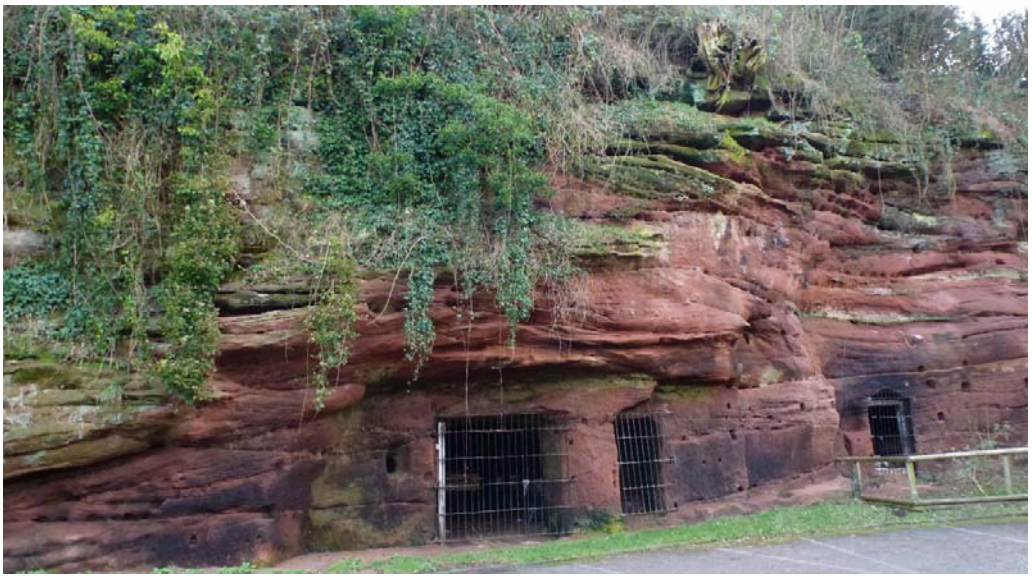

Fig.3-67. 'Rock' houses carved in the Kidderminster Sandstone Formation (rock house gates are about 2.5m high).

a)

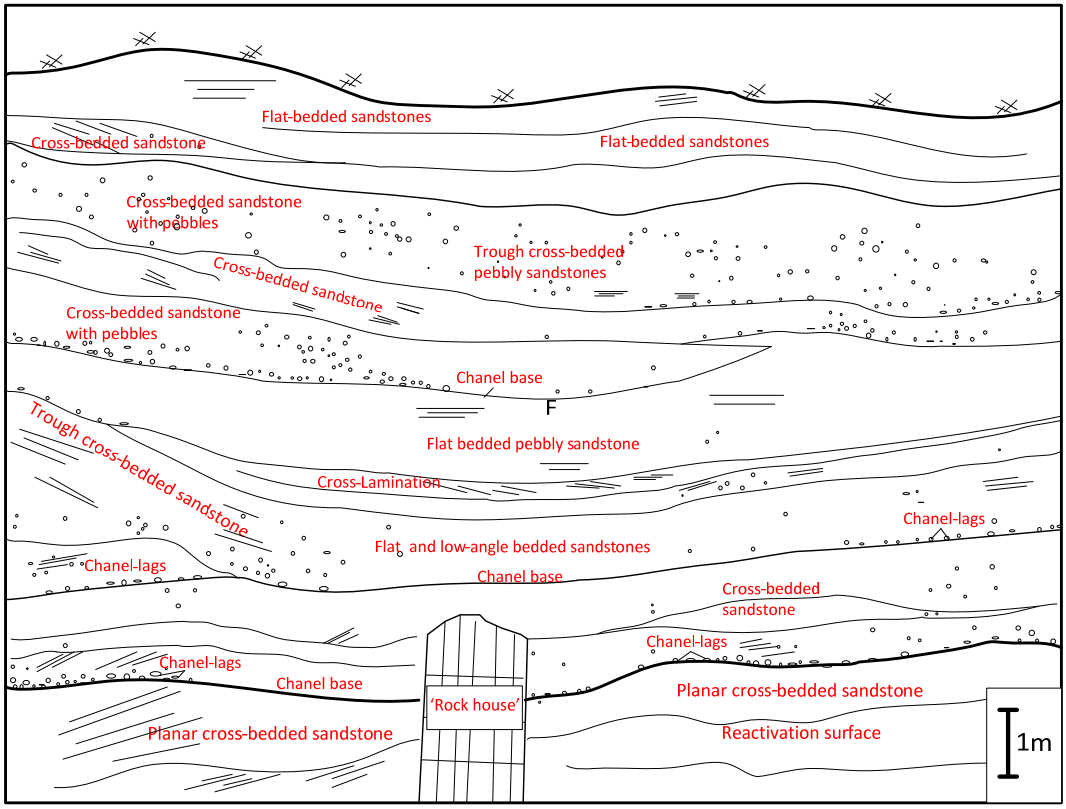

b)

Fig.3-68. a) Outcrop face showing fluvial sandstones of the Kidderminster Sandstone (the house gate is about 2.5 m high); b) Sketch of the interpretation for the sandstones at the outcrop.

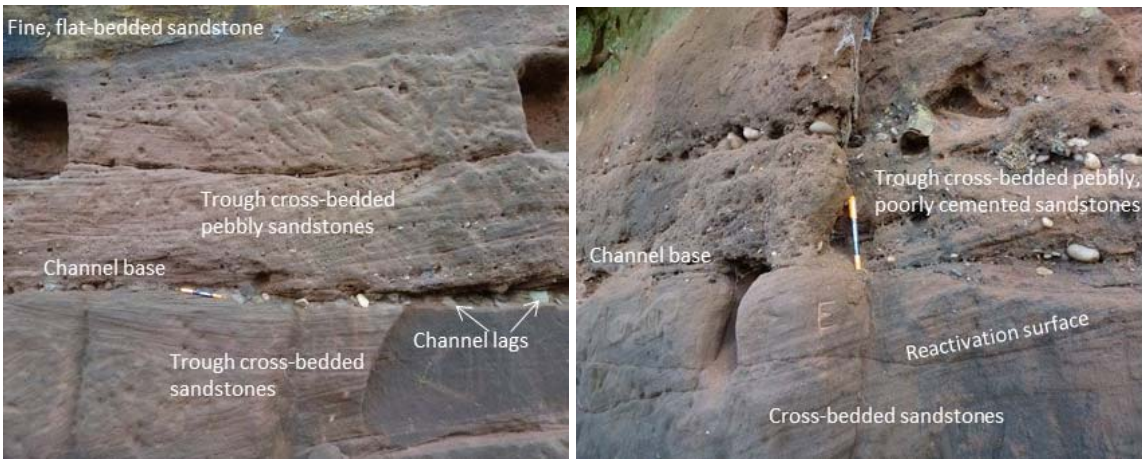

a) b)

Fig.3-69. a-b. Close view of the outcrop face: Relatively hard planar (left) and trough cross-bedded sandstone overlain by channel base which in turn is overlain by channel lags of pebble of size up 10 cm in diameter and trough cross-bedded, poorly cemented, pebbly sandstone as channel fills.

3.7.6 Hydraulic properties

Hydraulic properties of the Permo-Triassic sandstones in the West Midlands come from Allen et al. (1997), Bouch et al. (2006), Hallett (2014), and this study and are summarised in Table 3-26 to Table 3-29. Much of the data come from core-scale measurement (e.g in Allen et al., 1997; Hallett, 2014). Permeability assessments from a borehole (BH3) at Univeristy of Birmingham and at Wolverley outcrop have been performed with mini-permeametry measurements. These core-scale permeabilities (hydraulic conductivities) provide information at matrix-scale of the Permo-Triassic sandstone. However, some pumping test data are also available.

Table 3-25 and Fig.3-70 show sedimentary descriptions and hydraulic properties of samples collected at Kingsford and analysed by Hallett (2014). The porosities have similar range seen at the Bridgnorth site (Fig.3-44). According to Hallett (2014), lack of pore-filling cement seen in thin sections from these samples is the cause of their relatively large porosity, and the presence of thin laminations leads to a decrease in hydraulic conductivity of sample K1 (Fig.3-70). The effect of thin lamination in decreasing hydraulic conductivity and porosity is also seen in the Bridgnorth samples (Bed 5 in Fig.3-44). Generally, then, better rounding of grains, moderately-good sorting, and absence of cement cause high hydraulic conductivity values for the Kingsford samples.

There are only two core samples for the Croxden Quarry in this study (Table 3-25). The samples have porosities of 23.1 and 23.4%, and hydraulic conductivities of 0.12 and 0.78 m/d. Thin sections show secondary calcite cement in these samples (Fig.3-65), suggesting effects of cements on hydraulic conductivity variations at Croxden Quarry. As there are vertical variations in lithology (conglomerates, gravels, pebbly sandstones, to fine sandstones) (Figs.3-63, 3-66),

vertical variation in permeability seems very likely. Lateral and vertical variations in permeability will be likely to occur at Hulme Quarry as it has similar lithology/sedimentary structure variation as seen at Croxden Quarry.

Table 3-25. Sedimentary description for samples at Croxden Quarry and Kingsford.

Site	Bed/lithofacies	Sample ID	Brief discription
Croxden Quarry	Channel fill	L1, L2	Very fine- to fine-grained, tabular cross-laminated sandstones
Kingsford	Aeolian dune	K1-1/6	Fine- to coarse-grained sandstones, thin lamination, moderrate-well sorted, friable
	Aeolian dune	K3-1, K4-1/2, K5-3/4, K6-1/2, K7-1	Fine- to coarse-grained, moderate-well sorted, cross-bedding and lamination sandstones, friable

The Kingsford data are from Hallett (2014).

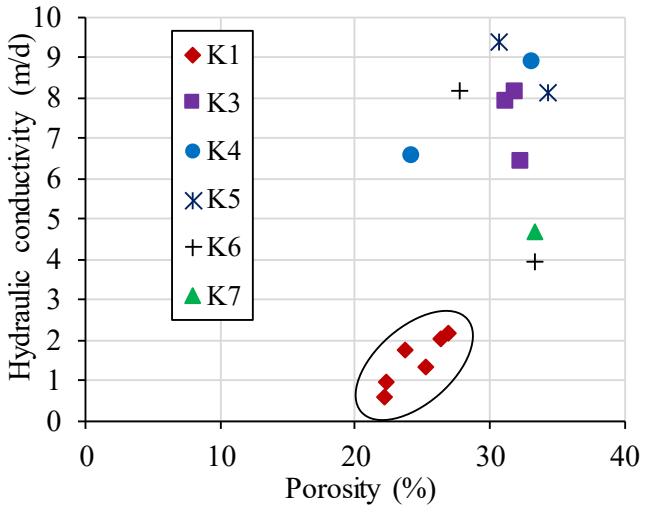

Fig.3-70. Hydraulic conductivity versus porosity for the samples at Kingsford (data from Hallett 2014).

3.7.6.1 Porosity

Core porosity varies significantly from about 4% (in the Kidderminister Formation) to about 36% (in the Bromsgrove Sandstone Formation) (Table 3-26). This variation is attributed to variation in grain size, grain sorting and shape (roundness), type and quantity of cementation, extent of diagenesis and weathering. As with the Permo-Triassic sandstone in Shropshire, no

apparent large-scale variation in porosity with depth is observed in the upper 140 m of the aquifer where samples were selected (Cheney et al., 2004).

The Permian Bridgnorth Sandstone Formation has porosity values in the upper part of the range (about 17 % to 34%), and with the highest median value (about 29%) and highest mean value (about 28%). This high porosity value is due the well-sorted, well-rounded, weakly cemented nature of these sandstones. The lower limit of the porosity range is significantly higher for the Bridgnorth Sandstone in West Midlands than in Shropshire (6%). The lowest porosity value in Shropshire reflects the presence of cemented siltstones towards the top of the Formation.

In the Triassic sequences, the Kidderminster/Cannock Chase Formation shows the widest range in porosity (from about 4% to 34%). This Formation is often well-cemented, and/or poorly sorted, leading to significant reduction in porosity. Higher porosity values relate to the coarser grained, more friable, weakly cemented materials (Lovelock, 1977). The porosity range for the Wildmoor Sandstone Formation is about 18% to 35% with lower values corresponding to the presence of silt and clay contents and cementation, while higher values come from medium-grained, clean sandstone and less cemented, friable zones (Cheney et al., 2004).The porosity of the Wildmoor Sandstone Formation is broadly similar to its equivalent Wilmslow Sandstone Formation in Shropshire (17% - 32 %). The Bromsgrove Sandstone Formation has a porosity range of 8% to about 36%, and this range is wider than that of the Helsby Sandstone Formation in Shropshire (from 15 % to 31 %). The lowest porosity corresponds to fine-grained, well-cement sandstone, while high values relate to clean, medium-grained, clean sandstone (Cheney et al., 2004).

Table 3-26. Porosity data for the Permo-Triassic sandstones of the West Midlands.

Formation	Area	Range (%)	Interquartile range (%)	Median (%)	Arithmetic mean (%)	Author
Bromsgrove Sandstone	West Midlands	8.0-36.2	25.7-29.7	27.4	26.8	Allen et al. (1997)
	Staffordshire	22.7-25.7	24.3-24.5	24.4	24.3	Hallett (2014)
Wildmoor Sandstone	West Midlands	17.6-35.3	24.2-28.2	26.9	26.4	Allen et al. (1997)
Kidderminster or Cannock Chase Formations	West Midlands	3.6-33.8	19.6-28.4	25.7	23.8	Allen et al. (1997)
Bridgnorth Sandstone	Kingsford	22.2-34.3	25.1-32.5	29.2	28.7	Hallett (2014)
	West Midlands	16.6-33.6	27.5-31.8	29.5	28.4	Allen et al. (1997)

3.7.6.2 Hydraulic conductivity

Core (matrix) and bulk hydraulic conductivities of the Permo-Triassic sandstone of the west Midland are summarised in Table 3-27 and Table 3-28 respectively. As with the porosity, there is no apparent variation in hydraulic conductivity within upper 140 m depth where the samples have been collected (Cheney et al., 2004). Hydraulic conductivity in the region ranges over 6 orders of magnitude, from 4 x 10^{-6} m/d to about 18 m/d. This wide range, as with porosity, is due to variation in grain size, degree of sorting and roundness, type and degree of cementation, extent of diagenesis and weathering.

The Bromsgrove Sandstone Formation shows a wide range from 2.6 x 10^{-4} to about 17 m/d. Higher hydraulic conductivity corresponds to coarser grained sediment. Lovelock (1977) recorded variation in horizontal permeability with changes in grain sizes from 206 samples from south Staffordshire, Birmingham, and Warwickshire:

Coarser sands: 6 m/d

Medium sands: 1.3 to 6 m/d

Silty sands: 0.26 to 0.39 m/d

The Wildmoor Sandstone Formation has hydraulic conductivity range from 3.1 x 10^{-4}-12.0 m/d. Higher permeability corresponds to cleaner sands, whereas lower values are related to muddy horizons (Allen et al., 1997). Bouch et al. (2006) studied sandstone from boreholes at the University of Birmingham and found permeability is consistent with that published by Allen et al. (1997), and palaeosols and mudstone at abandoned channels can act as baffles to vertical flow at decimetre-scale, granulation seams can have the same effect on permeability at the small scale.

The Kidderminister Formation reveals widest range in hydraulic conductivity in the region (4.6 x 10^{-6} - 17.8 m/d). The lowest values occur in strongly cemented horizons where fluid flow is most likely to come from fractures. Intermediate values come from medium-grained units, whereas higher values are related to interbedded coarser sands; the most permeable units of the Permo-Triassic sandstones of the West Midlands (Allen et al., 1997). Permeability measured with a mini-permeameter at the Wolverley outcrop shows a range from 3 x 10^{-3} to 5.5 m/d, which is consistent with that published by Allen et al. (1997).

The Permian Bridgnorth Sandstone Formation has hydraulic conductivity range from 2.5 x 10^{-4} - 9.4 m/d (about four orders of magnitude). Permeability variation is attributed to grain size variation rather than cementation (Allen et al., 1997). The low values are associated with the siltstones and very fine-grained sandstones of the upper part of the Formation; the intermediate values come from muddier sandstones; and the highest values correspond to coarser 'millet-seed' sandstone at lower part of the Formation; laminated sandstone causes strong permeability

anisotropy (Cheney et al., 2004). Hallett (2014)'s samples with well-sorted, well-rounded, weakly cemented sandstone (Fig.3-54a,b) from the Kingsford outcrop give hydraulic conductivity values at the higher part of the range recorded by Allen et al. (1997).

Table 3-27. Core hydraulic conductivity results for sandstones at West Midlands.

Formation	Area	Range (m/d)	Interquartile range (m/d)	Median (m/d)	Geometric mean (m/d)	Author
Bromsgrove Sandstone	West Midlands	$2.6x10^{-4}$-16.4	0.28-2.16	1.28	0.5	Allen et al. (1997)
	Staffordshire	0.3-0.9	0.5-0.7	0.6	0.55	Hallett (2014)
Wildmoor Sandstone	West Midlands	$3.1x10^{-4}$-12.0	0.12-1.58	0.73	0.37	Allen et al. (1997)
	Borehole BH3 at University of Birmingham	$4x10^{-4}$- 4.74	0.05-0.68	0.28	0.16	Bouch et al. (2006)
Kidderminster	Woverley outcrop	$3x10^{-3}$-5.52*	0.16-1.41*	0.49*	0.41*	This study
Kidderminster Cannock Chase	West Midlands	$4.6x10^{-6}$ - 17.8	0.18-3.5	1.48	0.49	Allen et al. (1997)
Bridgnorth Sandstone	Kingsford outcrop	0.6-9.4	2.0-8.1	5.5	3.75	Hallett (2014)
	West Midlands (Bridgnorth)	$2.5x10^{-4}$ - 9.4	1.1-4.01	1.95	0.95	Allen et al. (1997)

* *Permeability measured at the outcrop using a probe/mini permeameter.*

Allen et al. (1997) attempted to convert the pumping test transmissivity to bulk hydraulic conductivity for the Permo-Triassic sandstones of the West Midlands (Table 3-28). This allows a comparison with the matrix (core) hydraulic conductivity and indicates the effects of fractures on contribution to bulk hydraulic conductivity, though differences in values are also affected by the models used to interpret T, assumptions made to convert T to K and scale effects. The West Midlands bulk hydraulic conductivity estimated from the pumping test data ranges from 0.01 to 486 m/d, with a median of 2.9 m/d. The lower limit (0.01 m/d) of the bulk hydraulic

conductivity range is about four orders of magnitude greater than the lower limit (4 x 10^{-6} m/d) of the matrix hydraulic conductivity. This is because scale of measurement: core samples at the centimetre-scale comprise entirely low permeable materials; while these low hydraulic conductivitis are not dominant at the pumping borehole scale which can capture more permeable zones. Significant contribution of fracture flow to bulk hydraulic conductivity can be seen at the upper limit (486 m/d) which is greater than the upper limit (18 m/d) of the matrix permeability. Within bulk hydraulic conductivity of the West Midlands, the Bromsgrove Sandstone Formation shows the widest range (0.014 - 486 m/d), but narrowest interquartile range (0.53 - 2.71 m/d), the lowest median (1.58 m/d) and lowest geometric mean (1.58 m/d).

Comparing the bulk hydraulic conductivities in the West Midlands with those in Shropshire (Table 3-20) indicates that the upper limit values in the West Midlands are much greater than the upper limits values in Shropshire as a whole and for particular formations, suggesting that the sediments are more fractured in the West Midlands than in Shropshire, especially towards the top of the Sherwood Sandstone Group, the Helsby Sandstone in Shropshire and the Bromsgrove Sandstone in West Midlands (Allen et al, 1997).

Table 3-28. Bulk hydraulic conductivity for sandstones in the West Midlands (Allen et al., 1997).

Formation/Group	Range (m/d)	Interquartile range (m/d)	Median (m/d)	Geometric mean (m/d)
All	0.014 - 486	1.02 - 9.90	2.93	3.00
Bromsgrove Sandstone	0.014 - 486	0.53 - 2.71	1.58	1.58
Wildmoor Sandstone	0.77 - 62.6	3.06 - 19.1	12.1	8.06
Kidderminster	0.14 - 69.2	1.14 - 33.3	4.79	4.93

3.7.6.3 Anisotropy

The hydraulic conductivity anisotropy ratios of the West Midlands Permo-Triassic sandstones are given in Table 3-29. The anisotropy ratios range from 1.1 to 4. Horizontal permeability is generally greater than vertical permeability. In the West Midlands, however, the Bromsgrove

Sandstone shows some ratios to be <1. Ramingwong (1974) reported the anisotropy ratio from 5.2 to 0.24 for 104 core samples from the Bromsgrove Sandstone Formation. The core-scale anisotropy enhances aquifer-scale anisotropy, because of layering of less permeable finer-grained and more permeable coarser-grained sediments, but larger scale features, e.g. the presence of mudstone units, is likely to have a rather more profound effect on flows around boreholes, for example (Allen et al., 1997; Cheney et al., 2004).

Table 3-29. Anisotropy ratio of hydraulic conductivity of the west Midlands (After Allen et al., 1997).

Formation	Direction	Interquartile range (m/d)	Median (m/d)	Geometric mean (m/d)	Anisotropy ratio (K_h/K_v)
Bromsgrove Sandstone	Horizontal (K_h) Vertical (K_v)	0.29-2.59 0.31-1.90	1.2 1.31	0.51 0.48	1.1
Wildmoor Sandstone	Horizontal (K_h) Vertical (K_v)	0.19-2.75 0.05-1.46	0.83 0.39	0.56 0.2	2.8
Kidderminster Sandstone	Horizontal (K_h) Vertical (K_v)	0.55-4.10 0.06-2.27	2.29 1.03	0.86 0.23	3.7
Bridgnorth Sandstone	Horizontal (K_h) Vertical (K_v)	1.4-5.07 0.81-2.22	2.6 1.4	1.43 0.36	4.0

3.7.6.4 Hydraulic conductivity versus porosity

Fig.3-71a-e shows plots of core sample porosity against the logarithm (base 10) of hydraulic conductivity for the Permo-Triassic sandstones of the West Midlands. The correlation between hydraulic conductivity and porosity shows some degree of variation, but generally the higher the porosity the higher the hydraulic conductivity. Rocks of the same porosity may have different hydraulic conductivities as pore throat size is a more dominant control on hydraulic conductivity (permeability).

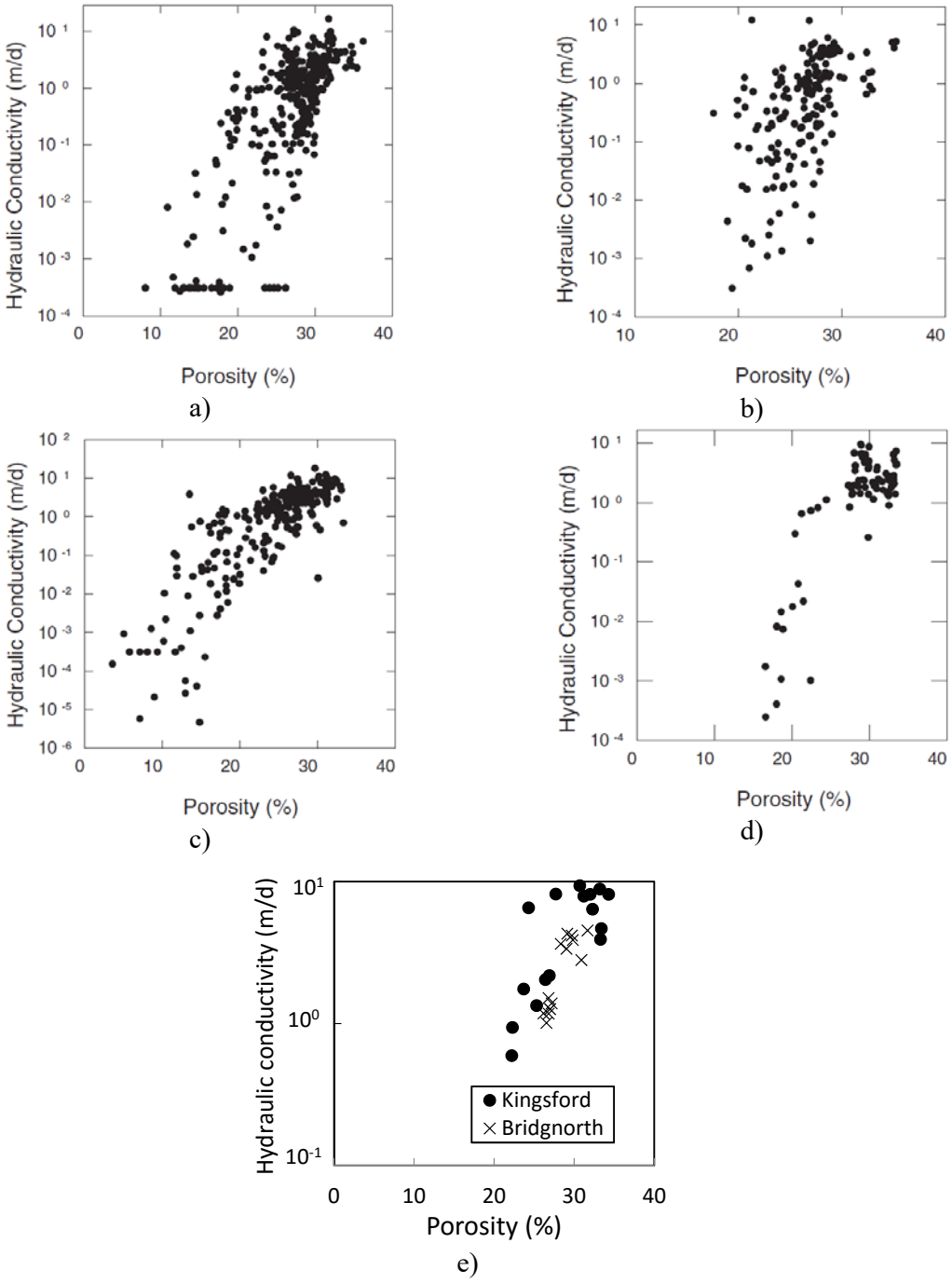

Fig.3-71. Core porosity versus hydraulic conductivity for Permo-Triassic sandstones in the West Midlands for different formations, a) Bromsgrove Sandstone (from Allen et al. 1997); b) Wildmoor Sandstone (from Allen et al. 1997); c) Kidderminster Formation (from Allen et al. 1997); d) Bridgnorth Sandstone (from Allen et al. 1997); e) Bridgnorth Sandstone at Kingsford (Hallett, 2014) and Bridgnorth (this study).

3.7.6.5 Fluvial versus aeolian sandstones

The Permo-Triassic sandstones of the West Midlands as a whole appear as a mixture of fluvial and aeolian environments. The Triassic sandstone sequence in the region is predominantly fluvial in origin, whereas the Permian Bridgnorth Sandstone Formation is aeolian (Table 3-30). The permeability (hydraulic conductivity) and porosity of the Permo-Triassic sandstones in the region are given in Table 3-30 in order to compare fluvial and aeolian systems. Generally, the aeolian sediments have both porosity and permeability greater than those of the fluvial deposits. The greater hydraulic property values of the aeolian sediments are attributed to cleaner, better-sorted, better-rounded, less cemented nature of the aeolian sediments.

Table 3-30. Hydraulic properties for fluvial- and aeolian- dominated sandstones in the West Midlands.

Dominated system	Formation	Area	Hydraulic conductivity (m/d)			Arithmetic mean porosity (%)	Author
			Interquartile range	Median	Geometric mean		
Fluvial	Bromsgrove Sandstone	West Midlands	0.28-2.16	1.28	0.5	26.8	Allen et al. (1997)
	Wildmoor Sandstone	West Midlands	0.12-1.58	0.73	0.37	26.4	
		BH3 at University of Birmingham	0.05-0.68	0.28	0.16	-	Bouch et al. (2006)
	Kidderminster Formation	Wolverley	0.16-1.41*	0.49*	0.41*	-	This study
		West Midlands	0.18-3.5	1.48	0.49	23.8	Allen et al. (1997)
Aeolian	Bridgnorth Sandstone	Kingsford	2.0-8.1	5.5	3.75	28.7	Hallett (2014)
		West Midlands	1.1-4.01	1.95	0.95	28.4	Allen et al. (1997)

** Permeability measured using a probe/mini permeameter.*

3.8 Southwest England

3.8.1 Geological setting

The Permo-Triassic succession in southwest England crops out in a north-south line extending from Exmouth in the south to Minehead in the north (Fig.3-72). These strata have total thickness of about 2.7 km (Laming 1965, Benton et al. 2002), dip gently east at about 10-12^0 (Allen et al., 1997; Benton et al., 2002), and rest uncomfortably on pre-Permian rocks (Warrington and Scrivener, 1990; Allen et al., 1997; Benton et al., 2002; Hounslow and Ruffell, 2006). The Permo-Triassic stratigraphic successions of the southwest are shown in Fig.3-72 and Table 3-31. Details of the succession are given in Appendix 6.

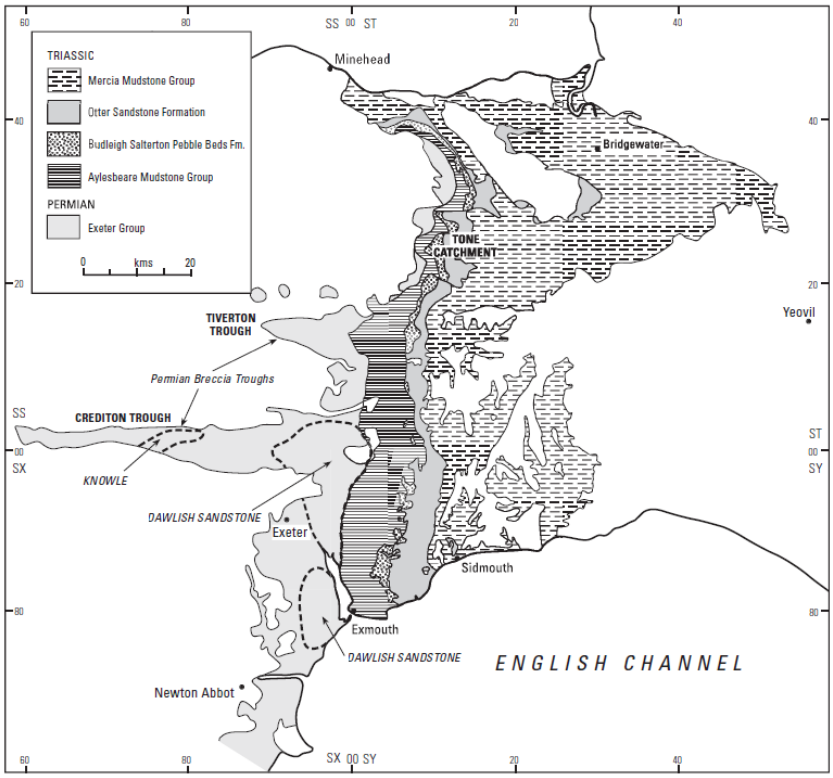

Fig.3-72. Schematic geological map of southwest of England (from Allen et al., 1997).

Table 3-31. Summary stratigraphy of Permo-Triassic sandstones in southwest England.

Age	Group	Formation	Area	Lithology	Predominant environment	Author/observer
Triassic	Mercia Mudstone		Sidmouth	Mudstone, siltstone	Marine and arid periods	Warrington et al. (1980), Allen et al. (1997), Benton et al. (2002)) and others
	Sherwood Sandstone	Otter Sandstone	Ladram, Sidmouth	Sandstones	Fluvial and aeolian	This study, Newell (2006)
		Budleigh Salterton Pebble Beds	Southwest	Conglomerate, sandstone	Fluvial	Warrington et al. (1980), Allen et al. (1997), Benton et al. (2002)) and others
	Aylesbeare Mudstone	Littleham Mudstone,	Southwest	Mudstone	sabkha-playa	Warrington et al. (1980), Allen et al. (1997), Benton et al. (2002)) and others
		Exmouth Mudstone and Sandstone	Southwest	Mudstone, sandstone		Warrington et al. (1980), Allen et al. (1997), Benton et al. (2002)) and others
Permian	Exeter	Dawlish Sandstone	Dawlish	Sandstones, breccias	Fluvial and aeolian	This study, Ian West (2008), Newell (2001)
		Knowle Sandstone	Southwest	Sandstones		Allen et al. (1997), Benton et al. (2002)) and others
		Cadbury, Bow and Crediton Breccias	Southwest	Breccias	Alluvial fan	Allen et al. (1997), Benton et al. (2002) and others

3.8.2 Studied sites: Dawlish coastal cliffs (SX 971774)

The outcrop is of the upper part of the Permian Dawlish Sandstone Formation (Smith et al., 1974; Selwood et al., 1984; Benton et al., 2002). The Dawlish Sandstone Formation comprises aeolian and fluvial sandstones and some interstratified breccias and breccio-conglomerates (Newell, 2001; Benton et al., 2002).

The Dawlish Sandstone Formation is probably divided into two parts (Benton et al., 2002) as follows:

The lower part is dominantly aeolian with red, reddish brown, well-sorted, well-rounded sandstone, mainly with large-scale planar-wedged dune sets, minor planar-tabular and trough cross-bedded sand dune or flood-reworked aeolian sandstone, cross-lamination, and occasionally fluvial sandstone units (Benton et al., 2002), and extensive honeycomb weathering development.

The upper part is fluvially dominated having channels with breccia-conglomerate-fills cut into the aeolian sandstone below (Fig.3-73). Some sand is reworked from the underlying aeolian units (Fig.3-73, Fig.3-75a) (Laming, 1966; 1982; Benton et al., 2002). Flash-flood breccia with their erosional bases cutting into the aeolian unit below are interbedded with low angular ripple-laminated sandstone units (Fig.3-74, Fig.3-75b). The uppermost part of the upper sandstone shows an unconformable boundary between the underlying Dawlish Sandstone Formation and the overlying Exe Breccia sediments above (Benton et al. 2002) (Fig.3-75b).

Newell (2001) recorded two types of bounding surface between fluvial flash-flood conglomerates and aeolian sandstones. The first boundary is a planar bounding surface which occurs mainly in the lower part of the Dawlish Sandstone Formation where there is equivalent amounts of fluvial and aeolian units. This boundary separates the tabular conglomerate with the aeolian or flood-reworked aeolian sandstones and it is formed by combination of windblown and fluvial actions. The second boundary is an incised bounding surfaced formed by fluvial down-cutting and occurring mainly in the upper part of the Formation that is fluvially-dominated (Newell 2001).

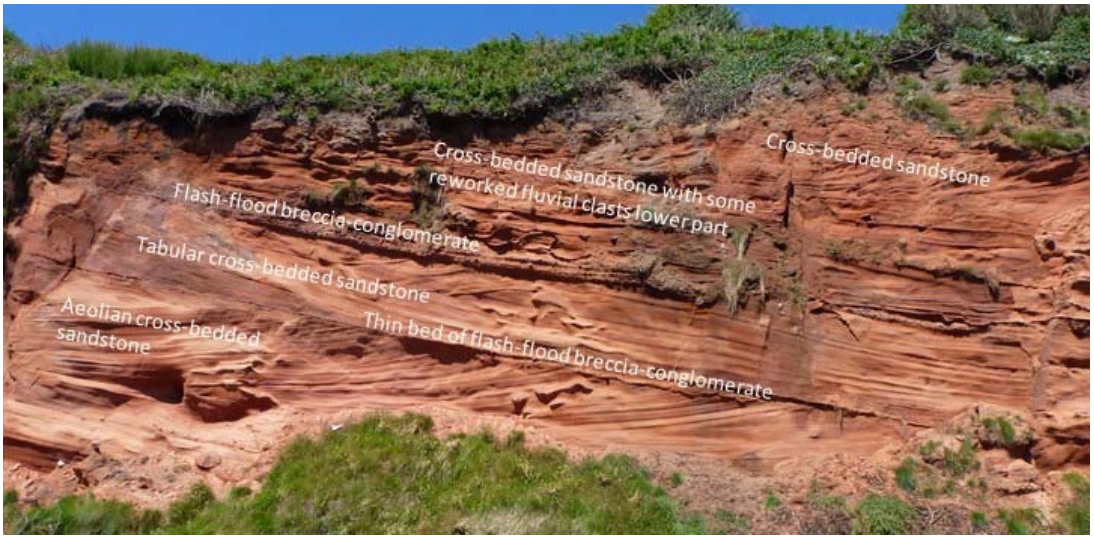

Fig.3-73. Upper part of the Dawlish Sandstone Formation showing mixing of aeolian cross-bedded sandstone and flood-reworked aeolian sandstone with fluvial flash-flood breccia-conglomerates (interpretations were made based on data from Ian West, 2008).

Fig.3-74. Mixing between aeolian cross-bedded or flood-reworked aeolian sandstones with fluvial flash-flood breccia-conglomerates. Note: the base of the flash-flood breccia-conglomerate shows an incised boundary into the underlying aeolian sandstone; rail lines for idea of scale (interpretations were made based on data from Ian West, 2008).

a) b)

Fig.3-75. a) Extensive development of honeycombs at lower part aeolian; b) immature breccia-conglomerate consisting of poorly cemented pebbly breccio-conglomerate resting on fluvial flash-flood breccia-conglomerate and aeolian cross-bedded sandstone (interpretations were made based on data from Ian West, 2008).

3.8.3 Studied sites: Ladram Bay coastal outcrops (SY 095849)

Coastal cliffs and stacks at Ladram Bay area reveal the exposure of the upper part of the Otter Sandstone Formation, Sherwood Sandstone Group (Fig.3-76). The Formation predominantly reflects fluvial conditions with multi-storey channel systems (Fig.3-77, Fig.3-78) and has been considered as major aquifer in East Devon (Allen et al., 1997), and an oil reservoir at Wytch Farm in East Dorset (McKie et al., 1998). The Formation is underlain by the conglomeratic Budleigh Salterton Pebble Beds and overlain by the Mercia Mudstone Group with the boundary seen at the High Peak Hill, on the eastern side of Ladram Bay.

The Formations are of fine-to medium-grained, moderately well-sorted sandstone, intraformational conglomerates, with erosive surfaces (scours and channels). Sedimentary structures include planar tabular and trough cross-bedding, trough cross-stratified conglomerates, ripple lamination, mudclast-lined erosion surfaces, and carbonate concretions (calcrete) (Newell, 1992; Newell, 2006; Benton et al., 2002). A series of fining-upwards cycles up to about 2 m thick are present (Newell, 2006). These cycles rest on erosion surfaces which

were commonly overlain by thin beds of conglomerate; finer-grained siltstone or mudstone units occur at the tops of some cycles (Newell, 1992; Benton et al., 2002). The depositional environment is interpreted as fluvial. The presence of rhizocretions in the lower part indicates the sequence was deposited under monsoonal regime, and the upper part was formed on an extensive alluvial plain (Benton et al., 2002; Newell, 2006).

Newell (2006) reported three types of early diagenetic calcite cementation at Ladram Bay and adjacent areas, including rhizocretions (mostly vertical orientation, elongate cylindrical calcretes), calcrete sheets and reworked calcrete conglomerates. At the macroscopic scale, calcrete conglomerate can exist as 100 m wide low permeability sheets acting as baffles to vertical flows in the aquifer (Newell, (2006). At the macro-mesocopic scale, calcretes which form horizontal or sub-horizontal or inclined layers of up to several tens of metres wide can act as baffles to flow and increase the tortuosity of flow in the aquifer. The calcrete cementation in cross-bedding, lamination, bedding layers can significantly increase anisotropy of the sandstone according to Newell (2006). Rhizocretions appearing as vertical cylindrical forms have least effect as flow barriers, but cause some flow heterogeneity. Calcrete in whatever form can reduce porosity of the Otter Sandstone Formation up to 20-30 % and permeability to less than 10^{-15} m^2 (8.4×10^{-4} m/d) (Newell, 2006), see below.

The lower part of the outcrop at Ladram Bay includes in its western part red, reddish-brown, occasionally pale, fine- to medium-grained sandstones, moderately well-sorted, with multi-storey channel associations including erosion bases, ripples, lamination and abundant calcretes (rhizocretions, calcrete sheets and reworked calcrete conglomerates).

The rhizocretions occur mostly as vertically cylindrical forms with occasional horizontal off-shoots (Fig.3-79a,b). The rhizocretions consist of non-ferroan calcite and corroded silicate

materials (Purvis and Wright, 1991). The length and shape of rhizocretions suggest that they are formed around tap roots of phreatophytic plants (Purvis and Wright, 1991). The second type of calcretion is calcrete sheets which appear widely at the outcrop faces (Fig.3-77, Fig.3-79a, and Fig.3-80a) and often associated with rhizocretions (Fig.3-78, Fig.3-79a). The calcrete sheets are laterally continuous and discontinuous, consisting of fine- to medium-grained crystalline sparry calcite cement with silicate (Purvis and Wright, 1991). The calcrete sheets also compose the cement in cross-bedded units (Fig.3-81a,b). The third type of calcrete is calcrete conglomerates which appear with vertical separations every 1 to 10 m up the cliff face (Fig.3-77). The calcrete conglomerates occur as laterally continuous, horizontal or sub-horizontal layers normally with a sharp top and erosional base (Fig.3-77, Fig.3-80b, and Fig.3-83), and consist predominantly of reworked calcrete fragments and subordinate clasts of sandstone, mudstone, quartz and vertebrate bone with a clast-supported and sandy matrix (Newell, 2006). The shapes of the calcrete conglomerate units vary vertically in the sandstone outcrop. In lower calcrete-rich multi-channel storey system, reworked calcrete conglomerate appears as lenses several tens of metres wide and up to 1 m thick, with irregular erosional bases forming deep scouring (Fig.3-80b). In contrast, the calcrete conglomerates in the upper calcrete-poor channel system have sheet-like forms with a thickness of less than 0.5 m and width of up to 150 m (Newell, 2006). Within the multi-storey sandstone system, the calcrete conglomerates form channel fills and channel belt bases and represent channel lags (Newell, 2006). The calrete-rich multi-channel system is interpreted by Newell (2006) as being deposited rapidly in channels with limited time for lateral extensive migration in ephemeral flow systems.

The upper part of the cliff at Ladram Bay and its western side is comprised of calcrete-poor multi-storey channel systems with red, reddish-brown, fine- to medium-grained, micaceous sandstone and mudstones. The sandstone is massive or cross-bedded with structures varying

from horizontal sheet-like deposits to channelled sands with erosive bases interbedded with mudstone. As it is a transition from the underling Otter Sandstone Formation (Sherwood Sandstone Group) to the overlying Mercia Mudstone Group, the grain size and sandstone thickness decrease upwards from medium-grained sandstone to siltstone, while presence of mudstone increases upwards (Newell, 2006).

Fig.3-76. Sea stack (in front) of cliff outcrops of the Otter Sandstone Formaton, showing multi-storey channel systems at Ladram Bay.

Fig.3-77. Coastal cliff wall of interval calcrete conglomerates, calcretion sheets and cross-bedded sandstones.

Fig.3-78. Calcretes of different forms in the lower part overlain by channels base, channel filled cross-bedded and ripple marked sandstone with calcrete conglomerate and discontinuous sheets of calcretes at top.

a) b)

Fig.3-79. a) sub-vertical (rhizocretions) and horizontal calcretes; b) Closer view of sub-vertical rhizocretions.

a) b)

Fig.3-80. a) Discontinuous calcrete sheets; b) Reworked calcrete conglomerates (just above the hammer).

a) b)

Fig.3-81. a) Calcrete forming cross-bedding cementation in trough cross-bedded sandstone; b) calcrete forming foresets in the trough cross-bedded sandstone (top right and right below the hammer).

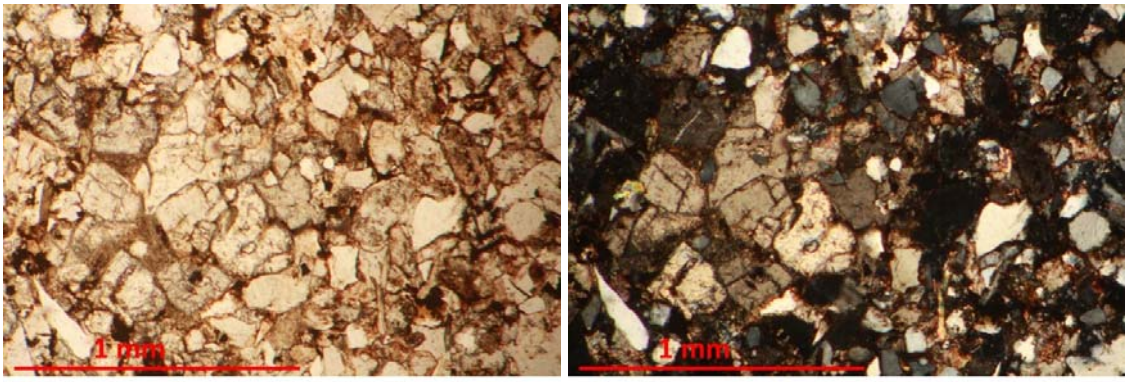

a) b)

Fig.3-82. Optical micrographs showing sub-angular, poorly to moderately sorted sand grains with calcite cements in the Otter Sandstone at Ladram Bay a) with plane light; and b) with cross polars.

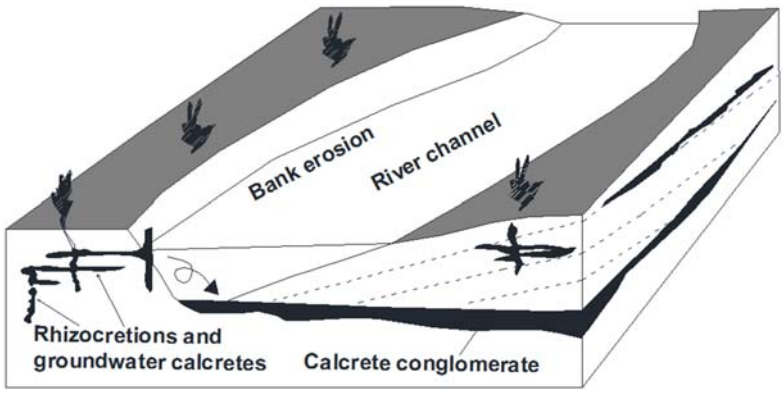

Fig.3-83. Diagram of a fluvial channel system characterized by calcretes (from Newell 2006).

3.8.4 Studied sites: Sidmouth coastal cliffs

The formations cropping out along the beaches at Sidmouth and the adjacent areas show a transition from underlying Otter Sandstone Formation Group to the overlying Mercia Mudstone Group (Fig.3-84, Fig.3-85a,b).

The underlying Otter Sandstone Formation comprises reddish-brown fine- to medium-grained sandstone interbedded with siltstone, with planar bedding, planar tabular cross-bedding and cross-lamination (Fig.3-85b). In the western part of Sidmouth (SY 105861), the upper Otter Sandstone has calcrete cementing the foresets of the cross-bedded sandstone (Fig.3-85b), while

in the eastern side it shows plane and planar tabular cross-bedding and is free of calcretes (Fig.3-86a,b).

In western Sidmouth, the upper Mudstone Group is weathered, brown, reddish-brown siltstone, claystone, structureless or planar bedded, with laminated interbedding with lenses of sandstone (Fig.3-84, Fig.3-85a,b). In the eastern Sidmouth (SY 129873), the Mercia Mudstone overlies interbedded discrete green-coloured sandstone layers (Fig.3-86a).

Fig.3-84. Boundary (white dashed line) between the underlying Otter Sandstone Formation and the overlying Mercia Mudstone Group (the cliff is about 20 m high).

a) b)

Fig.3-85. a) Mercia Mudstone Group resting on the upper part of the underlying Otter Sandstone Formation in western Sidmouth; b) Cross-bedded sandstone with calcrete in form of cross-stratification cement of foreset laminae.

a) b)

Fig.3-86. Otter Sandstone Formation and overlying Mercia Mudstone Group in eastern Sidmouth. a) Green (organic) sandstone forming disconective units interbedded with cross-bedded sandstone and siltstone; b) Uppermost part of the Otter Sandstone Formation showing plane, planar tabular, and cross-bedded sandstone.

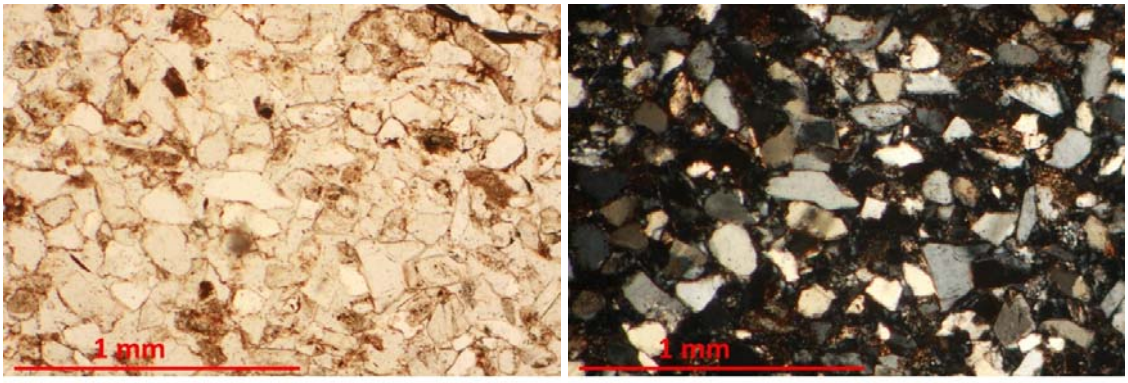

a) b)

Fig.3-87. Photomicrographs of the Otter Sandstone at Sidmouth, showing sub-rounded to angular, moderately-well sorted sand grains with some calcite cement a) with plane light; b) with cross polars.

3.8.5 Hydraulic properties

Hydraulic property values of the Permo- Triassic Sandstone of southwest England are available mainly from literature (Allen et al., 1997) (Table 3-33 and Table 3-34), from Newell (2006) and from measurements undertaken during this study (Table 3-32). There is no sample from the Dawlish Sandstone Formation as it was inaccessible at the outcrops visited during the present study. However, Allen et al. (1997) reported high bulk values of permeability for the Dawlish Sandstone Formation (pumping test hydraulic conductivity of the Exeter Group from 1.7 to 5.7 m/d), and depending on their grain size, with fine sandstones with silt to coarse to very coarse sandstones having intergranular hydraulic conductivities ranging from 8×10^{-4} to about 4×10^{-1} m/d respectively.

Table 3-32. Sedimentary descriptions for the samples collected at Ladram Bay and Sidmouth.

Location	Sample ID	Brief discription
Ladram Bay	L1, L2, L3, L4, L5	Very fine- to fine-grained size, micaceous low angle cross-laminated sandstone, some interbedded with thin layers of mudstones. Channel fill lithofacies. Samples are separated by 1m to 20m
Sidmouth	S1, S2, S3, S4	Very fine- to fine-grained tabular cross-laminated sandstones. Channel fill lithofacies. Samples S1, and S2 are within a block, S3 and S4 are separated by 15m

3.8.5.1 Porosity

In this study, nine core plug samples were taken from the Otter Sandstone Formation, including five samples from Ladram Bay and four from Sidmouth (Table 3-32 and Fig.3-88a). These values along with porosity values reported by Allen et al. (1997) for the Permo-Triassic sandstones in southwest England are given in Table 3-33. The porosity of the Permo-Triassic sandstones in the region varies widely from 2 to 35% with a wider range for the Sherwood

Sandstone Group than the Permian sandstones. The Permian sandstones have a higher mean porosity (23%) than that of the Sherwood Sandstone Group (16%).

The samples from this study show a porosity range from 15 to 21 % with a mean of 18% at Ladram Bay and from 28 to 32% with a mean of 30% at Sidmouth. These differences may be due to the relatively more rounded and better sorted, less cemented nature of the sandstone at Sidmouth (Fig.3-87a,b) than the samples at Ladram Bay (Fig.3-82a,b).

Table 3-33. Core porosity results for the Permian-Triassic sandstones in the southwest England.

Formation	Area	Range (%)	Interquartile range (%)	Median (%)	Arithmetic mean (%)	Author
Otter Sandstone	Ladram Bay coastal cliff	14.9-20.7	15.7-20.1	16.1	17.5	This study
	Sidmouth coastal cliff	28.3-31.8	29.8-31.4	30.7	30.4	
	Ladram Bay coastal cliff and a borehole	7.0 - 34.0	-	-	-	Newell (2006)
	Southwest	8.3-33.8	15.5-32.7	24.6	23.4	Allen et al. (1997)
Budleigh Pebble Beds	Southwest	6.9-34.1	8.1-10.3	9.4	13.0	
Sherwood Sandstone Group	Southwest	2.2-34.6	9.9-19.5	14.8	15.5	
Permian Sandstones	Southwest	6.5-32.5	19.7-25.8	22.4	22.8	

3.8.5.2 Hydraulic conductivity

The core hydraulic conductivity of the Permo-Triassic sandstone in southwest England varies over seven orders of magnitude, from 1.9 x 10^{-6} to 5.3 m/d, with a geometric mean of 0.017 m/d. Generally, the Sherwood Sandstone Group has wider range than the Permian sandstones. The Permian sandstones have higher hydraulic conductivity (a median of 0.35 m/d and geometric mean of 0.14 m/d) than the Sherwood Sandstone Group does (a median of 0.024 m/d

and geometric mean of 0.011 m/d). This is due to the more-rounded, better-sorted, less cemented nature of the aeolian sandstones of the Permian.

As with porosity, the samples collected at Ladram Bay have lower hydraulic conductivity than the samples at Sidmouth (Table 3-34, Fig.3-88a). This is due to the relatively poorly sorted, less rounded, and more cemented nature of the samples. This supports the work of Newell (2006) who studied the effects of calcretes on the Otter Sandstone Formation with 36 samples collected from the Formation and concluded that these calcretes can reduce effective porosity of the Formation by up to 30 % (to less than 12 %) and permeability to less than 10^{-15} m^2 (8.44 x 10^{-4} m/d at 20°C) (Fig.3-88c), and especially, reworked calcrete conglomerate can form very low permeability sheets of lateral extent of up to 1 km which can act as barriers to vertical flow (Fig.3-83). The uppermost part of the Otter Sandstone Formation crops out in Sidmouth (Fig.3-85a). Here there is very little or no calcrete, resulting in more permeable sandstones.

Table 3-34. Core hydraulic conductivity for Permo-Triassic sandstones of southwest England.

Group/ Formation	Area	Range (m/d)	Interquartile range (m/d)	Median (m/d)	Geometric mean (m/d)	Author
Otter Sandstone	Sidmouth coastal cliff	1.0-2.8	1.1-2.2	1.50	1.60	This study
	Ladram Bay coastal cliff	$8x10^{-4}$- 0.057	$9x10^{-4}$- 0.0078	0.0012	0.003	
	Ladram Bay coastal cliff and a borehole	3.4x 10^{-5}- 0.84	-	-	-	Newell (2006)
	Southwest	1.0x 10^{-5}- 5.4	0.04-1.95	0.69	0.17	Allen et al. (1997)
Budleigh Pebble Beds	Southwest	4.0x 10^{-5}-1.8	0.0001 - 0.006	0.003	0.002	
Sherwood Sandstone Group	Southwest	$2.1x10^{-6}$ - 5.8	$3.9x10^{-4}$- 0.31	0.024	0.011	
Permian Sandstones	Southwest	$4.77x10^{-5}$ - 4.3	0.028 -2.10	0.35	0.14	
Permo-Triassic (all data)	Southwest	$1.9x10^{-6}$ - 5.8	$5.9x10^{-4}$- 0.66	0.034	0.017	

The permeability (hydraulic conductivity) so far discussed is that measured on core samples. However, Allen et al. (1997) also reported 'bulk' hydraulic conductivity for the Permo-Triassic sandstones in the region from pumping tests. The Permo-Triassic sandstones as a whole have bulk hydraulic conductivity range from 0.023 to 38 m/d, interquartile range from 0.92 to 4.3 m/d, a median of 1.9 m/d and a geometric mean of 1.7 m/d. Comparing these bulk hydraulic conductivities with core hydraulic conductivities for the Permo-Triassic sandstone sequences (Table 3-34), the bulk hydraulic conductivity is significantly greater than the core hydraulic conductivity. This reflects important contribution of fracture flows to boreholes.

3.8.5.3 Anisotropy

Table 3-35 and Fig.3-88c show the anisotropy data available for core permeability for the Otter Sandstone Formation and the Permo-Triassic Sandstone in general in southwest England. Generally, the horizontal hydraulic conductivity is greater than vertical hydraulic conductivity. Allen et al. (1997) found the horizontal hydraulic conductivity is about 2.5 - 3 times higher than the vertical hydraulic conductivity for the Sherwood Sandstone Group and the Permian Sandstone (the Exeter Group) respectively. Newell (2006) found little difference between horizontal and vertical permeabilities for calcrete-free sandstones, calcrete-extensive sandstones and reworked calcrete conglomerates (Fig.3-88c), but calcretes in all forms can cause heterogeneity at larger scales in the Otter Sandstone, as discussed above.

Table 3-35. Core horizontal and vertical hydraulic conductivities for the Permo-Triassic sandstones of southwest England (from Allen et al. 1997).

Formation/ Group	Orientation	Range (m/d)	Interquartile range (m/d)	Median (m/d)	Geometric mean (m/d)	Anisotropy (Kh/Kv)
Sherwood Sandstone Group	Horizontal (K_h) Vertical (K_v)	$1.9x10^{-6}$ -1.19 1.9x10-6 - 4.3	$1.3x10^{-4}$- 0.27 7.5x10-5- 0.69	$8.9x10^{-3}$ $2.4x10^{-3}$	$5.6x10^{-3}$ $2.2x10^{-3}$	2.5
Permian sandstones	Horizontal (K_h) Vertical (K_v)	$5.9x10^{-5}$ - 4.3 4.8x10-5 - 4.3	0.12 -1.9 0.01 - 2.2	0.71 0.10	0.24 0.08	3.0

3.8.5.4 Hydraulic conductivity versus porosity

Generally, there is a correlation between porosity and hydraulic conductivity of the Permo-Triassic sandstone sequences in southwest England (Fig.3-88a,b), but the scatter is as usual significant.

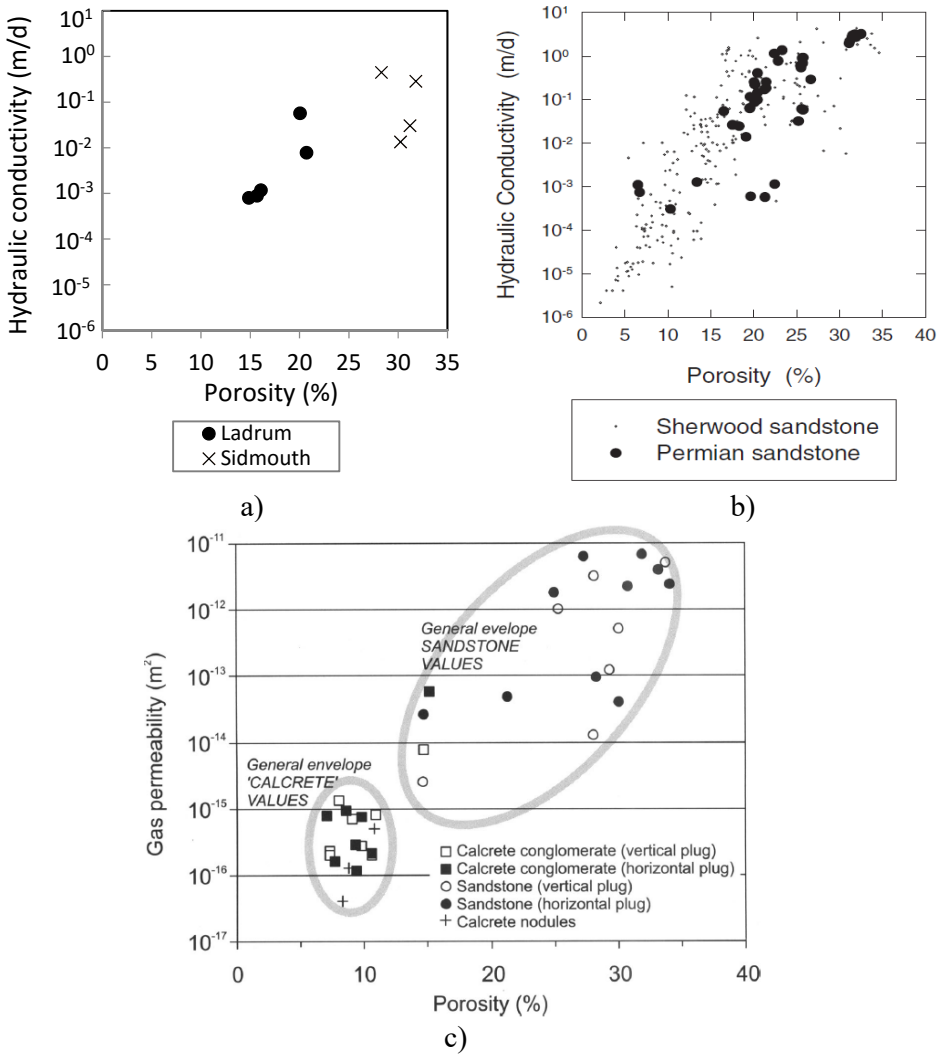

Fig.3-88. Core porosity versus hydraulic conductivity (permeability) for Permo-Triassic sandstones in southwest England for different formations, a) Otter Sandstone at Ladram Bay and Sidmouth (This study), b) Sherwood Sandstone Group and Permian sandstones (Allen et al., 1997), c) effect of calcrete on hydraulic properties of the Otter Sandstone Formation (Sherwood Sandstone Group) (from Newell, 2006).

3.8.5.5 Fluvial system versus aeolian systems

The Permo-Triassic sandstones in southwest England represent both aeolian and fluvial environments, but the latter is dominant. The Permian breccias are overlain by the Dawlish Sandstone Formation that is aeolian in its lower part and fluvial in its upper part. The Triassic Sherwood Sandstone Group commences with the Budleigh Salterton Pebble Beds formed under fluvial braided systems, followed upwards by the Otter Sandstone Formation which is mainly of aeolian origin in its lower part and fluvial in its upper part.

The samples collected in this study are from the upper part of the Otter Sandstone Formation, i.e. mainly fluvial, but it is unclear what the palaeoenvironment was for the samples from other studies (Allen et al., 1997) though it is more likely Otter Sandstone samples will be fluvial. Thus hydraulic properties of the Permo-Triassic sandstones in the region (Table 3-36) generally represent fluvial dominant units and can probably be used to compare with the other fluvial (or aeolian) sandstones in other regions.

Table 3-36. Hydraulic properties for fluvial and aeolian dominated sandstones of southwest England.

Dominated system	Group	Formation	Hydraulic conductivity (m/d)			Arithmetic mean porosity (%)	Author
			Interquartile range	Median	Geometric mean		
Fluvial	Sherwood Sandstone	Otter Sandstone	0.001-1.1	0.06	0.05	23.2	This study
		Otter Sandstone	0.04-1.95	0.69	0.17	23.4	Allen et al. (1997)
		Budleigh Salterton Pebble Beds	0.0001-0.006	0.003	0.002	13.0	
		All data	0.0004 - 0.31	0.024	0.011	15.5	
	Permian sandstones		0.03-2.1	0.35	0.14	22.8	

3.9 Conclusions

3.9.1 Geological and hydraulic property characteristics

Overall, of the total sixteen visited sites (outcrops and quarries) seven sites are sediments dominated by fluvial sandstones (St Bees in west Cumbria, Raw Head, Hulme Quarry, Croxden Quarry, Wolverley, Ladram Bay and Sidmouth), seven sites are in aeolian sandstones (Grinshill Old quarries, Grinshill working quarry, Nesscliffe, Leaton, Bridgnorth, Kinver and Kingsford), and the Dawlish sea cliff represents mixed fluvial and aeolian conditions.

The sandstones at different outcrops show different characteristics. The St Bees sandstone at Bees Head, west Cumbria is dominated by multi-channel systems that are well-cemented which causes significantly reduced porosity and permeability. Farther southeast, the sandstones at Raw Head, south Cheshire show developed fluvial structures, with Hulme Quarry and Croxden Quarry at Stoke-on-Trent, Staffordshire containing conglomerates, with thick, plane or cross-bedding, interbedded with sandstone with dispersed pebbles and their permeability are possible to vary significantly between and within beds. To the south, the sandstones are predominantly aeolian in origin. At the Grinshill Old Quarries, Nesscliffe and Leaton in Shropshire and Kinvern Edge, South Staffordshire and Kingsford in Worcestershire the sandstones contain/are characterised by large-scale aeolian bedforms, and have high porosity and permeability. The sediments at Bridgnorth and adjacent area (Hermitage), Shropshire, are aeolian (Bridgnorth Sandstone Formation) overlain by fluvial deposits (Kidderminster Formation). The fluvial Kidderminster Sandstone Formation crops out again at Wolverley, Worcestershire, where there is excellent 3D exposure of the fluvial structures. At Dawlish, west Devon, the sandstone sequence demonstrates a mixture of aeolian units with dune structures and overlying fluvial deposits with occasional flash-flood breccias and laminated, fine sandstone layers along with

some reworked aeolian clasts. Eastwardly, especially at Ladram Bay and its western side there are spectacular exposures of the upper part of the Otter Sandstone Formation (Sherwood Sandstone Group) which crops out as fluvially dominated sediments and contains distinctive calcretes in parts (rhizocretions, calcrete sheets and reworked calcrete conglomerates). The distinct calcretes at Ladram Bay and adjacent areas play an important role in reducing porosity and permeability of the sandstone (e.g. Newell, 2006). Further east at Sidmouth an increase in the proportion of fine-grained material and mudstone occurs, representing the transition between the Sherwood Sandstone Group and the Mercia Mudstone Group.

The core plug data from the studied sites show porosities and hydraulic conductivities to vary within and between outcrops, with some significant differences (e.g. St Beed Head, Raw Head, Grinshill Old Quarries, Kingsford, Bridgnorth, and Ladram Bay) as seen in Fig.3-89 (for porosities) and Fig.3-90 (for permeabilities). Permeabilities (and porosity) vary within and between beds (St Bees Head, Raw Head, Bridgnorth, Kingsford, and possibly at Croxden and Hulme quarries). Sedimentary characteristics pose important controls on permeability (and porosity) as with pore-filling cements (as the samples at St Bees Head, Ladram Bay, Croxden Quarry), varying grain sizes (Nesscliffe), and lamination and bedding structures (Kingsford, and Bridgnorth). Permeability (and porosity) vary within and between locations in a field site as seen at Grinshill Old Quarry areas. Though the data presented in this reconnaissance study are limited, there is usually a larger difference in hydraulic properties between beds than within beds, suggesting potentially a significant difference between permeability (and porosity) for different lithofacies (‘sub-lithofacies’). However, differences between basins cannot be ignored (cf. St Bees and Sidmouth), but there may not even be consistency within a basin (cf. Ladram Bay and Sidmouth).

A wide range in palaeo-environments were seen for fluvial and aeolian sandstones across the studied sites. For fluvial systems, wide range in sedimentary structures within and between sites and regions occurs, with plane bedding, lamination, and planar, cross-bedding or cross-lamination, ripples, wavy lamination, and soft-sediment deformation. Complete channel structures are rarely preserved at outcrops, but can see width of channels ranging from centimetres to metres (scours), to tens of metres, with some cyclic sequences observed. However, the predominant structure is layered, presumably the result of laterally moving channels. In some cases the grain size variation from bed to bed is large, with sand bodies alternating with conglomerates (e.g. Hulme and Croxden quarries). For aeolian systems, distinct large-scale cross-stratification, grainfall, grainflow, and pinstripe lamination structures are often seen.

The fracture characteristics and behaviours marked as a feature of the Permo-Triassic sandstone are complex throughout the sequences, and, unfortunately, its examination is beyond scope of this chapter though it is possible that there is a correlation between fracture characteristics and lithofacies, but this is currently unknown (Tellam and Barker, 2006).

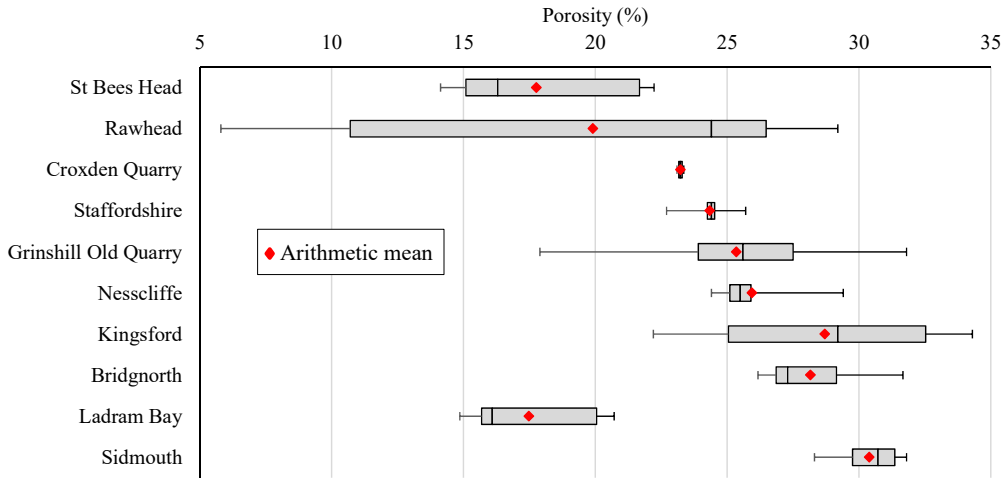

Fig.3-89. Box and wisker plots of the studied sites versus core porosity. Uprights, left to right, are: minimum; lower quartile, median, upper quartile, and maximum. The data for the Raw Head, Staffordshire, Grinshill Old Quarries, Nesscliffe, Kingsford are from Hallett (2014).

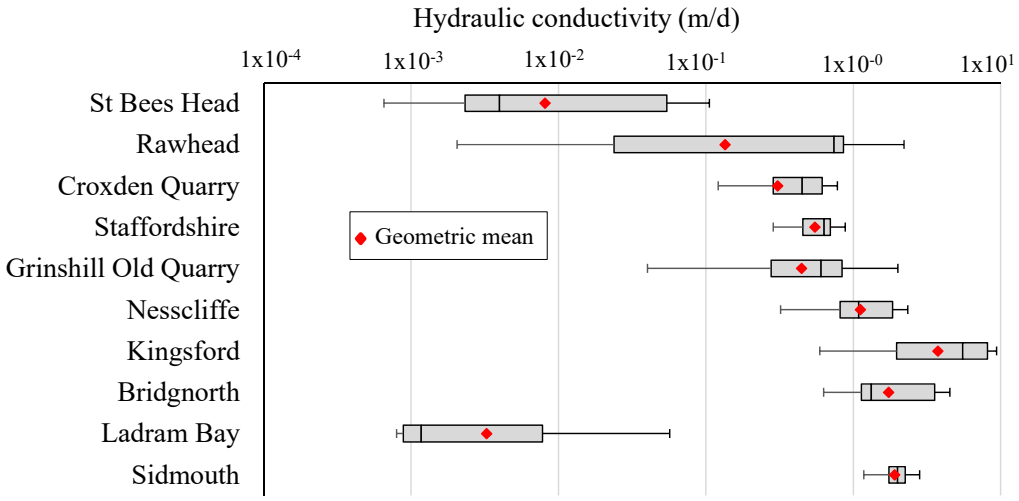

Fig.3-90. Box and whisker plots of the studied sites versus core hydraulic conductivity. Uprights, left to right, are: minimum; lower quartile, median, upper quartile, and maximum. The data for the Raw Head, Staffordshire, Grinshill Old Quarries, Nesscliffe, and Kingsford are from Hallett (2014).

3.9.2 Fluvial system versus aeolian system

The porosities and core permeabilities (hydraulic conductivities) of fluvial and aeolian sandstones of the Permo-Triassic red bed sequences are plotted in Fig.3-91 and Fig.3-92 respectively. Clearly, the aeolian sediments with characteristics of greater well-rounded, well-sorted, and a lesser degree of cementation have greater porosities and permeability than the poorly sorted, more cemented fluvial sediments.

For porosity values of the Permo-Triassic sandstones, the West Cumbria fine-grained, well cemented sediments have the smallest mean porosities for both fluvial (17.8 %) and aeolian (19.5 %) sediments, whereas the West Midlands has highest mean porosities for both fluvial (25.7 %) and aeolian (28.6 %) systems (Fig.3-91).

For core hydraulic conductivities, values of the Permo-Triassic sandstones, as with porosity, the West Cumbria has the smallest median and geometric hydraulic conductivity values for both fluvial and aeolian systems. The Shropshire localities have the highest median and

geometric hydraulic conductivities for fluvial systems, but the West Midlands has the greatest mean and geometric hydraulic conductivities for the aeolian systems (Fig.3-92).

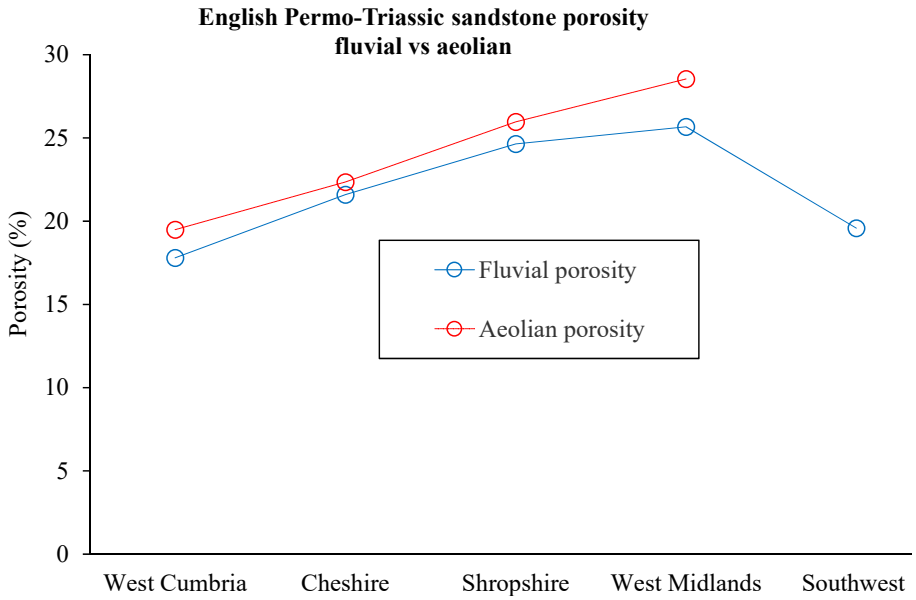

Fig.3-91. Summary porosity values of the fluvial and aeolian Permo-Triassic sandstones for different areas. The data from Allen et al. (1997), Bloomfield et al. (2006), Boutch et al. (2006), Hallett (2014) and this study as mentioned in the previous relevant sections.

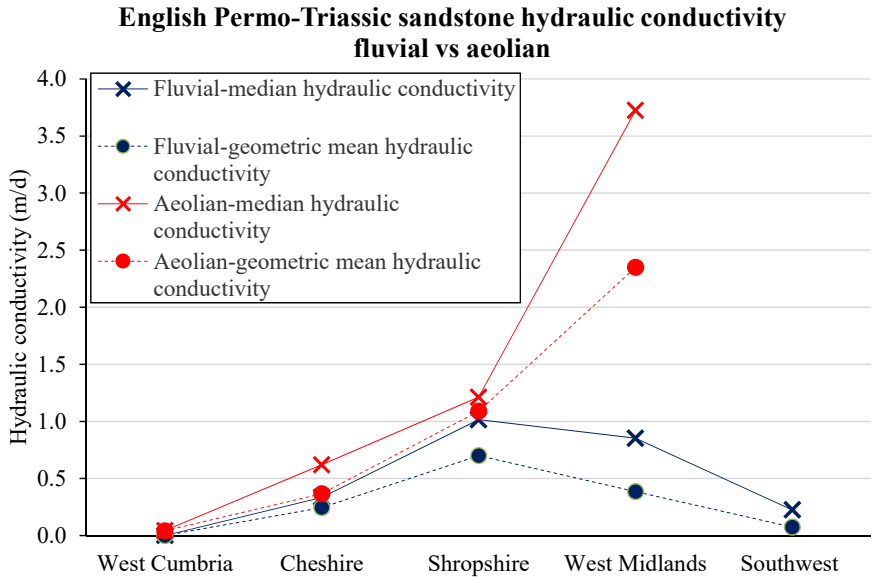

Fig.3-92. Summary hydraulic conductivity values of the fluvial and aeolian Permo-Triassic sandstones for different areas. The data from Allen et al. (1997), Bloomfield et al. (2006), Boutch et al. (2006), Hallett (2014) and this study as mentioned in the previous relevant sections.

3.9.3 Concluding remarks

Generally, the Permo-Triassic sandstone sequences across England show wide range of sedimentary structures and represent a range of palaeo-environments, as well as variability in hydraulic properties, particularly permeability. The lithological characteristics, and the sedimentary structures, and palaeo-environments vary within and between outcrops, and within and between regions with distinct sandstone formations appearing at different sites. As with lithological sedimentary and palaeo-environmental features, hydraulic properties of the sandstones, particularly permeability varies within and between beds, widely within and between outcrops and locations. Variation in grain size, grain sorting, and grain shape (roundness), and type and degree of cementation have a great influence on porosity and permeability of the sandstones (from this study and Hallett, 2014). Generally, the aeolian sandstones with well-sorted, well-rounded sand grains have higher permeability than the fluvial sandstones.

CHAPTER 4

CORRELATION BETWEEN CONTINENTAL REDBED SANDSTONE LITHOFACIES AND PERMEABILITY

4.1 Introduction

Correlation between sandstone lithofacies and permeability, as mentioned earlier in the introduction of the thesis, plays important role in early stage of approaches to improve prediction for solute transport in sandstone hydrogeology. The correlation has been found previously in the English Permo-Triassic sandstones (e.g. Moran, 2008; Bloomfield et al., 2006; McKinley et al., 2011). However, the strength of the correlations, especially for sublithofacies still remain little known. This chapter, therefore, aims to determine whether there is a correlation between sandstone lithofacies and matrix permeability within an example continental fluvial Triassic sandstone sequence from northern England, and to determine the strengths of any correlations found. A 60-m borehole core was examined to determine lithofacies; in excess of several 1000 permeability measurements, and also 172 porosity measurements, were undertaken in technique development and determination of core properties; initial hydraulic properties measurements from 63 core plugs and 170 mini-permeameter measurements from the pilot phase of the study undertaken by Moran (2008) were added; the data were examined statistically using a range of techniques; and the spatial distribution of properties was investigated. Finally, effect of pellet (mudstone clasts) on permeability in the borehole core were investigated, then used to adjust the correlation between lithofacies and permeability.

4.2 Location of the borehole from which the core used in the study was taken

The core used for this work is from the Preston Laundry borehole located in the city of Preston in northern England (SD53915 30208). The borehole is drilled into the Triassic Sherwood Sandstone Group, a major UK aquifer (Allen et al., 1997; Tellam and Barker, 2006), and is located in the West Lancashire Basin, an offshore extension of the Irish Sea Basin. The borehole was drilled with the rotary method (water flush) to depth of 110.2 m below ground level (m bgl) and cased down to 45.0 m bgl. The borehole was cored from 45.3 m to depth of 110.2 m with 97% core recovery. The aquifer at this location is unconfined (Allen et al., 1997) (see Chapter 3).

4.3 Methods

4.3.1 Sample preparation

In the initial study performed by Moran (2008), a total of 63 core plug samples at different depths from different lithofacies were made. Detail for sample preparations for and water saturation methods to measured hydraulic properties were detailed in Chapter 2. No core plugs are available for mudstone or friable sandstones, classified as lithofacies 1 and lithofacies 5 as below, as they are not stable enough to be cored.

726 measured points of permeability were undertaken using a mini-pemeameter at depth intervals of roughly 5 cm and 10 cm for the whole borehole core in the current study, adding to the 170 permeability measurements undertaken using the same minipermeameter during a pilot study performed by Moran (2008). The core plugs were also tested with the mini-permeameter to compare with the hydraulic conductivity from falling head measurement.

In the current study, a total of 172 samples of size of 1-2 cm wide by 1 cm thick by 2 cm long were extracted from the borehole core in order to determine porosity and moisture content. These samples were selected at core locations where permeability had been measured using the mini-permeameter and at the same depth but at about 5-10 cm distant. These samples are termed 'core samples' below, distinguishing them from the core plug samples.

4.3.2 Water chemistry

Artificial groundwater was used for falling head permeameter tests, reflecting typical fresh groundwater sandstone cation compositions and ionic strength (about 0.01 M), as there exist a few studies suggesting that similar onshore UK sandstone permeability is sensitive to change in water chemistry (Braney et al 2001 and Michener 2003 in Tellam and Barker, 2006).

4.3.3 Lithofacies identification

Cyclicity in Permo-Triassic sandstones has been recorded in some studies (e.g. Allen, 1964; Duff et al., 1967; Thompson, 1970; Wills, 1970; Selley, 1988; Bloomfield et al., 2006). Bloomfield et al. (2006) reported metre-scale fining-up and drying-up cycles in the Sherwood Sandstone Group. Lithofacies of the Preston borehole cores were initially identified by Moran (2008) on basis of colour, grain size, grain packing, and sedimentary structures.

4.3.4 Water saturation measurement

4.3.4.1 Porosity

All the core plugs and core samples were measured for porosity. Detail for determination of porosity were mentioned in Chapter 2.

4.3.4.2 Hydraulic conductivity using falling head permeametry

During the initial phase of the study, Moran (2008) performed falling head permeameter testing for 63 core plugs. Each measurement was repeated immediately using the same flow direction and for the opposite flow direction. The tests had an averaged coefficient of variation of about 3%.

4.3.5 Mini-permeameter measurements

4.3.5.1 Introduction, the device used and its basic operation

Gas permeametry was undertaken using a mini-permeameter. An introduction to the use of the minipermeameter is described in Chapter 2. A Temco Mini-perm/probe permeameter MP-402, with the software "SmartPerm for MP-402", was employed to perform the measurements (Chapter 2).

For the borehole core measurements, every measurement point was performed at a depth interval of 5 cm to 10 cm along the core, and at each point 3 to 5 measurements were averaged to obtain a representative permeability value: the measurements at a given depth had an averaged coefficient of variation of 2.5%.

The mini-permeametry was undertaken with great care to avoid errors caused by gas leakage, inadequate probe force, and tip leakage on curved surfaces: the slippage effect (Klinkenberg, 1941) has a significant effect mostly only with samples of permeability lower than those determined here. The gas leakage through the seal of the probe tip was minimized by using a good rubber tip and by repeating measurements where there was any doubt. Injecting pressures were increased only to the point where they were sufficient to achieve a stable recorded pressure gradient. Where measurements took a very long time to achieve a stable flow rate, or where

there was some nearby fracture causing exceptionally high permeability values, these values were excluded from the permeability data sets reported.

The permeameter tip used in the measurements had a manufacturer's reported effective penetration depth of 0.7 to 1.2 cm (Chapter 2). The core plugs used here have diameters of 3.15 cm, which are sufficiently large to allow adequate measurements on both ends of the core plugs. This was confirmed by measurements on the exposed ends of half-size-heat-shrinkable tubing wrapped cores: the results were effectively identical to measurements on the same cores with the wrapping removed (slope = 0.98, $R^2 = 0.98$).

No systematic differences were found between measurements made on the curved and slabbed, flat, surfaces of the same sections of core.

4.3.5.2 Permeability calibration

Permeability measured using liquid and gas permeameter values are known to differ, even after slippage corrections (e.g. Monicard, 1980), and this is true of UK Permo-Triassic sandstone sequences (Campbell, 1982). As is often the case, it will here be assumed that the hydraulic conductivity determined by falling head liquid permeametry is a better estimate than that produced by the mini-permeameter. Accordingly, all core plugs were measured using both techniques, the data plotted, and the correlation determined by linear regression. Core plug permeability derived from mini-permeametry was averaged from 3 to 5 permeability measurements on both ends of the core plugs.

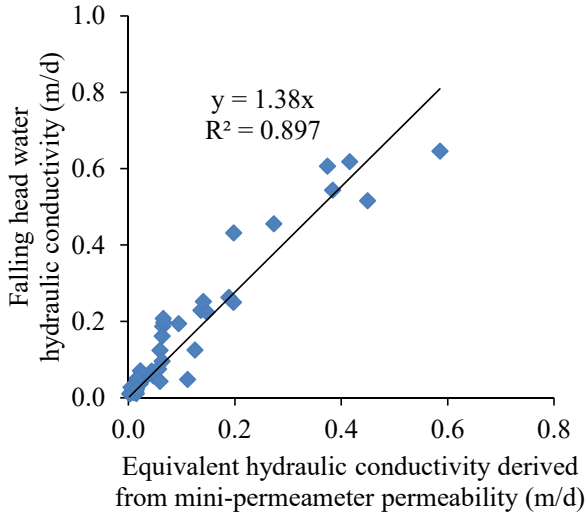

Fig.4-1. The hydraulic conductivity determined from mini-permeameter intrinsic permeability plotted against hydraulic conductivity determined by falling head permeameter on all core plugs.

Fig.4-1 shows the relationship between the permeability estimates. Because of the likely sampling bias with mainly core plug samples from LF3 and LF4, only one sample from LF2 and no sample from LF1 and LF5 and the difference between liquid and gas as permeants generally observed (Monicard, 1980), no calibration of the mini permeameter values using the falling head permeameter values was made. All the permeabilities measured by the mini permeameter were kept as their own values instead. This relationship, however, results in a difference of permeabilities measured by falling head permeameter and the mini permeameter. Bloomfield et al. (2006) also worked on the Sherwood Sandstone Group and used the same mini-permeameter as in the current study. They calibrated their mini-permeameter results using results from a conventional constant head gas permeameter, finding that the ratio of gas constant head to mini-permeameter values was 1.475 (R^2=0.85). It is suggested that this factor may represent a correction to the geometry factor (G) in Equation 2-5 (Chapter 2), and that the difference between this factor and the factor in Fig. 4-1 is due to any changes in operational procedures between the two studies and also the difference, as mentioned above, usually found between liquid and gas measurements.

4.3.5.3 The effect of moisture content

As moisture content may affect permeability measurement, the borehole cores and plugs were measured for permeability using the mini-permeameter under different saturation levels. Detail for measurement of moisture content was described in Chapter 2.

Fig.4-2 shows plots of saturation against permeability and normalized differences in permeability. A significant reduction in permeability with increasing saturation level is seen with almost all samples. For permeable core samples, about 10 % of saturation can cause permeability differences of up to 45 %, while for core plugs, a saturation of as low as 2% can cause measurement difference of up to 30% (Fig.4-2d), though in most samples this is much less.

Generally, moisture has significant effect on permeability performance using a minipermeameter with reducing permeability as saturation levels increase. Halvorsen and Hurst (1990) also investigated the effect of moisture on mini-permeameter measurements and found a significant impact only on samples of permeability between 2 x 10^{-15} and 2 x 10^{-14} m^2 (2-20 mD), and effectively unmeasurable for samples of greater than 9.9 x 10^{-14} m^2 (100 mD). This trend, however, is not really seen in the results obtained here: this is an important area for further study, especially for field mini-permeametry as fully drying rock surfaces is rarely possible.

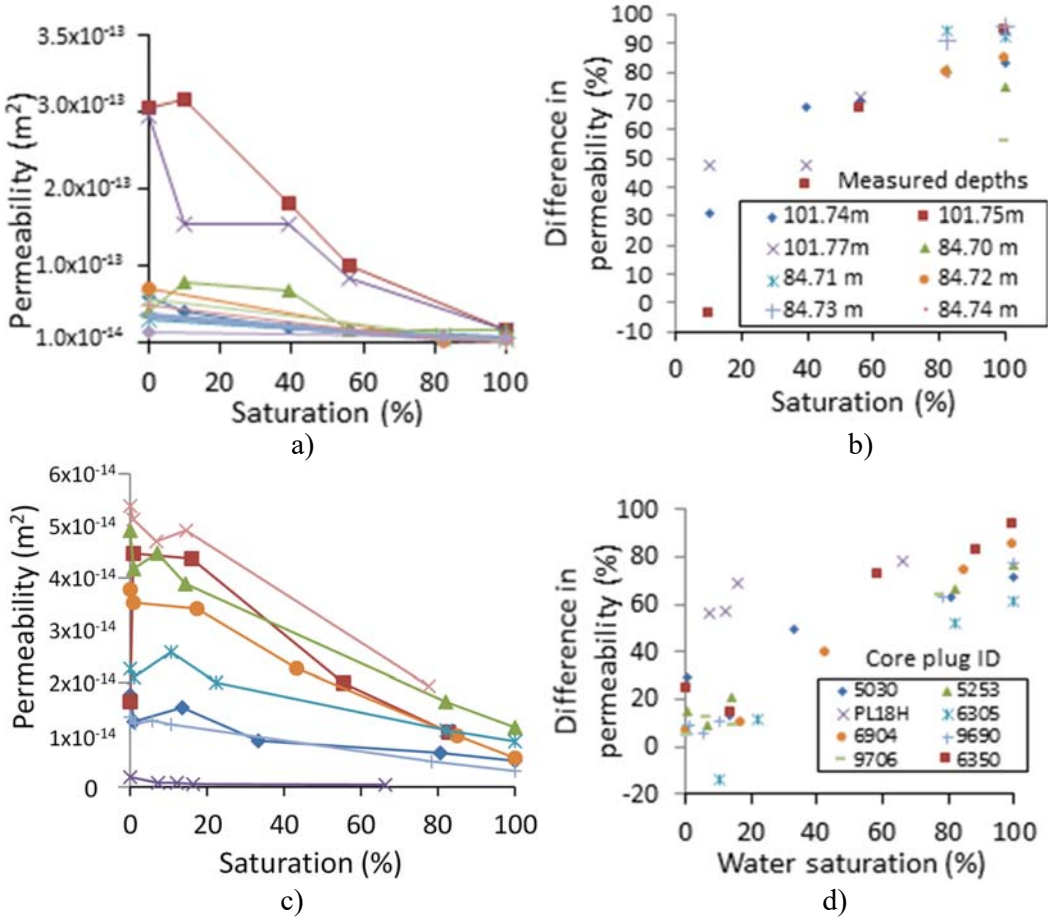

Fig.4-2. Effects on permeability of saturation levels and permeability difference $(k_{dry} - k_{wet})/k_{dry}$ as a function of saturation level. a) and b): core samples; c) and d) core plugs.

As permeability measurement can be affected by the moisture content of the samples, the borehole core was measured for moisture content. A total of 172 samples at 125 depths capturing all the lithofacies types except mudstone were subjected to moisture content determination. As the moisture content experiment was performed after permeability measurement, there is a possibility that the core had further dried after the permeability measurement. Another possibility is that the cores may have been further dried by the mini-permeability measurement itself. To address with this, at each depth, 2 to 3 samples were measured, one where there was a measured permeability and the other(s) at location(s) 5 cm or 10 cm laterally away from the first point. There were 38 double-samples at a distance of 5cm

and 8 double-samples also at 10 cm distance. This was done to try and avoid the possible drying zone of the original measurements.

Table 4-1 summarises the moisture content results for all samples and grouping depths. The moisture contents for all the samples have a range from 0 % (completely dried) to 2.17 %, with a mean of 0.44 %, a median of 0.42 %, a standard deviation of 0.24 %, and an interquartile range (IQR) from 0.29 to 0.55 %.

Table 4-1. Summary statistics for Preston core moisture content.

	All 172 samples	125 depths
Numbers of sample	172	125 depths
Mean (%)	0.44	0.42
Std. dev (%)	0.24	0.23
Max (%)	2.17	1.58
Upper quartile (%)	0.55	0.53
Median (%)	0.42	0.41
Lower quartile (%)	0.29	0.28
Min (%)	0.00	0.00

It is concluded that the moisture contents during the measurements were very low (~0.5%), and that any error associated with this is small in comparison with heterogeneity of the core (about 48%, see below), the uncertainty in the difference between liquid- and mini- permeameter measurements (about 30%), and the inherent precision of the measurements (about 2%, see above).

4.3.5.4 Permeability heterogeneity and anisotropy investigations

Heterogeneity of the borehole core was examined by measuring permeability using the mini-permeameter at different points at the sample depth: on an imagined perimeter running around the cores at a certain depth, the first measurement is labelled k1, the second at 5 cm from the first k2, and the third at 10 cm from the first k3. In addition, a separate set of measurements

was carried out on the curved outer core surface and also on the slabbed surfaces at the sample depth to see the effect of sedimentary structure on permeability measurement.

Anisotropy of the core samples was also studied by measuring permeability in horizontally and vertically oriented directions. The core plugs were generally drilled horizontally so that they could supply information on sub-horizontal permeability when mini-permeameter measurements were carried out on the ends of the core plugs and information on sub-vertical permeability when the core plugs were measured on their sides.

4.3.6 Effects of pellets on permeability

4.3.6.1 Introduction

Effects of mudstone on sandstone permeability depend on nature and spatial extent of mudstone (see in Chapter 1). It is not always easy to discriminate pellet-bearing layers from mudstone with the use of natural gamma ray and resistivity log only (Tellam and Barker, 2006). Given adverse effects of pellets on permeability, however, there has been limited quantitative studies distributions and permeability of mudstone, especially mudstone as in the form of pellets in sandstone sequences. This subsection, thus, hopes to introduce an approach to examine the effects of pellets in sandstone, particularly fluvial sandstones in the Preston Laundry Borehole core.

4.3.6.2 Pellet identification in the Preston Borehole core

In quantifying the presence of pellets in the Preston Laundry Borehole cores, Jaweesh (In preparation) found that pellets predominantly appear in the two coarsest lithofacies (i.e. LF4 and LF5 in Section 4.4.2 below) (Table 4-2). Numbers and sizes of pellet were quantified manually on horizontal and vertical surfaces of each sample. Density of pellets is estimated by

undertaking a picture to horizontal and vertical core surface for each sample and then calculated the area of the sandstone and the area of the pellets using a software Sigmaplot (www.sigmaplot.co.uk/products/sigmaplot/sigmaplot-details.php). Horizontal density of pellets was then estimated as a ratio of area occupied by the pellets to total area of horizontal core surface. Similar calculation, but in vertical direction was made to estimate vertical density of pellets.

Pellet sizes vary from 0.1 cm long by 0.1 cm wide by 0.1 cm thick to 2 cm long by 2 cm wide by 0.2 cm thick with the most common sizes being 0.2 cm by 0.2 cm by 0.1 cm thick (531 pellets, accounting for 46.2% of the total pellets) and 0.5 long cm by 0.5 cm wide by 0.1 cm thick (228 pellets, accounting for 19.8% of the total pellets) (Table 4-2). Density of pellets in horizontal and vertical plane respectively for the three coarsest lithofacies are shown in Table 4-3 and Table 4-4 respectively.

Table 4-2. Pellet sizes and their corresponding numbers in Preston Laundry Borehole core.

LF	Pellet sizes in cm (length x width x thickness)										
	0.1x0.1x0.1	0.2x0.2x0.1	0.3x0.3x0.1	0.5x0.5x0.1	0.5x0.5x0.2	0.7x0.7x0.1	1x1x0.1	1x1x0.2	1x1x0.5	2x1x0.2	2x2x0.2
3	24	27	4	6	1	2	0	0	0	0	1
4	30	232	9	96	2	19	27	8	0	3	5
5	122	272	11	126	44	6	30	19	8	8	7
Combination of LF3, LF4, and LF5	176	531	24	228	47	27	57	27	8	11	13
	15.3%	46.2%	2.1%	19.8%	4.1%	2.3%	5.0%	2.3%	0.7%	1.0%	1.1%

Data from Jaweesh (In preparation).

Table 4-3. Horizontal occurrence of pellets in Preston Laundry Borehole core.

LF	Numbers of sample	Pellet density (%)					
		Min	Max	Arithmetric mean	Median	Q1	Q3
3	1	0.3	0.3	0.3	0.3	0.3	0.3
4	15	0.2	11.5	2.8	1.2	0.7	2.9
5	11	0.7	20.4	3.9	1.7	0.9	2.7

Data from Jaweesh (In preparation).

Table 4-4. Vertical occurrence of pellets in Preston Laundry Borehole core.

LF	Numbers of sample	Pellet density (%)					
		Min	Max	Arithmetric mean	Median	Q1	Q3
3	10	0.1	37.9	7.1	2.2	0.7	5.7
4	38	0.2	57.0	13.5	8.2	1.5	20.1
5	32	0.9	50.4	20.4	21.4	7.8	29.0

Data from Jaweesh (In preparation).

4.3.6.3 Modelling the influence of pellets on permeability using a numerical model

Effects of pellets on permeability in sandstone were estimated by using numerical simulation. Pellet size and density were taken into account in a matrix of size of 1 m long by 1 m wide by 1 m thick using Visual Basic Application in Microsoft Excel (VBA). The output from VBA model was inputted into MODFLOW models embedded in Groundwater Vistas (ESI) (detail below) to simulate flow. The flows outputted from Groundwater Vistas were then used to calculate bulk permeability of the pellet-containing rock.

a) Creation matrix input

A VBA code was developed to create permeability structure of the pellet-containing sandstone. The two most common pellet sizes in the Preston Laundry Borehole core (0.2 by 0.2 by 0.1 cm and 0.5 by 0.5 by 0.1 cm) (Table 4-2) were used in the flow simulation. Pellet density was set to vary from 0.5 to 50% for both LF4 and LF5. Detail of the VBA code can be found in Appendix 4.

b) Numerical models used to estimate bulk permeability

The outputs from VBA model was used as input to the MODFLOW package (McDonald and Harbaugh, 1984) embedded in the Groundwater Vistas (www.esinternational.com/groundwater-vistas-2/).

Ground Water Vistas which was used to simulate the flow model in this chapter and the solute transport in Chapter 6 is a sophisticated Windows graphics user interface for modelling 3D groundwater flow and transport. The software is developed and marketed by Environmental Simulations International (ESI) Ltd., UK (http://esinternational.com/groundwater-vistas-2/). Ground Water Vistas supports MODFLOW 2000, MODFLOW 2005, MODPATH, MT3D/MT3DMS, etc. The version used was Ground Water Vistas version 5.18.

MODFLOW (Modular Finite-Difference Groundwater Flow Model) (McDonald and Harbaugh, 1984) is a computer software code for modelling groundwater flow systems. It simulates three-dimensional groundwater flow using a block-centred finite difference method. The model code was first published by the U.S Geological Survey in 1984 (McDonald and Harbaugh, 1984). It has been developed through several versions: MODFLOW-88, MODFLOW-96, MODFLOW-2000 (Harbaugh et al., 2000; Hill et al., 2000), and the current version MODFLOW-2005 (Harbaugh 2005). The MOFLOW package has the advantage of being a public-domain, open-source code, and easy to understand and to operate.

A model grid of 1000 rows by 1000 columns one layer thick was used to represent a vertical cross section of the sandstone once cell thick in the direction perpendicular to the flow. Row heights and column widths were both set at 0.001 m. The layer thickness was set at 1 m. The model domain was hence 1 m long by 1 m wide by 1 m thick with considerable discretization in the vertical direction.

The upstream and downstream boundaries were assigned to be constant head boundaries of 10 m and 9 m respectively, creating a hydraulic gradient of 1 ((10-9)/1) The side boundaries are set as sloping linear-head boundaries from 10 m (upstream end) to 9 m (downstream end).

The pellets were assigned to have hydraulic properties of mudstone (LF1 identified in Section 4.4.2 below) with hydraulic properties of 3.6 x 10^{-6} m/d (after Curião unpublished data 2002). A sandstone matrix permeability was set to be those of LF4 (equivalent geometric mean hydraulic conductivity of 0.042 m/d) and another matrix permeability was set to be those of LF5 (equivalent geometric mean hydraulic conductivity of 0.081 m/d). These permeabilities are from Table 4-10 (Section 4.4.3.2) below (Table 4-5).

Table 4-5. Permeability (equivalent hydraulic conductivity) used in model to simulate the effects of pellets on permeability.

	Equivalent hydraulic conductivity (m/d)
Pellet	3.6 x 10^{-6}
LF4- matrix	0.042
LF5- matrix	0.081

The bulk permeabilities were then calculated by analysing the mass balance from the MODFLOW steady state models and Darcy's Law as follows

$$Q = AKi \tag{4-1}$$

where:

Q is flow rate [L^3T^{-3}], and can be taken from the Modflow model mass balance

A is cross section area [L^2]

K is bulk permeability [LT^{-1}]

i is hydraulic gradient [-], and equal to 1 in the model systems

From Equation 4-1, bulk permeability was calculated as

$$K = \frac{Q}{Ai} \tag{4-2}$$

The ratio of bulk permeability (bulk_K) to matrix permeability (matrix_K) was then calculated and plotted.

4.4. Results and discussions

4.4.1 Introduction

In the following subsections, the lithofacies definitions are first established (Section 4.4.2). Porosity (Section 4.4.3.1) and then permeability (Section 4.4.3.2) variation with depth and lithofacies is then presented, followed by an analysis of the variations in the permeability/porosity ratio (Section 4.4.3.4). The cyclicity of lithofacies and thence hydraulic properties are analysed (Section 4.4.4). Finally, effect of pellet on permeability is simulated and their effects on the correlation of lithofacies and permeability are updated (Section 4.4.5).

4.4.2 Lithofacies classification and distribution

Lithofacies from the Preston Laundry Borehole were initially identified by Moran (2008). Lithofacies have been defined using a simple approach of logging the following properties of the core: colour, grain size, lamination style (massive, plane, low angle, and high angle), presence of visible mica, presence of mudclasts, and presence of pebbles. These properties, supported by thin section analysis, were then combined into 5 classes ('lithofacies'), the properties of which were then used to assign tentative palaeoenvironmental interpretations. Detailed interpretations, e.g. following (Miall, 1985), were not attempted as this was not thought viable for the majority of cores or geophysical well logs available in practice.

Table 4-6 and Figs.4-3a-k show the classification of lithofacies from the Preston borehole core.

Lithofacies 1 (LF1) is dark reddish-brown mudstone, mainly containing clay, silt and very fined-grained sand (Figs.4-3a,b). LF1 is thought to be deposited by overbank flood plain events or possibly in abandoned channels.

Lithofacies 2 (LF2) is reddish-brown, very fine-grained, mudclast- and pebble- free sandstone with much mica and flat to low-angle lamination (Figs.4-3c,d). LF2 is interpreted as overbank material deposited by waning flow.

Lithofacies 3 (LF3) is light to dark reddish-brown, fine- to medium-grained sandstone with occasional mudclasts (Figs.4-3e,f). LF3 contains common mica and planar or gently inclined lamination. LF3 is interpreted as a channel fill deposit.

Lithofacies 4 (LF4) is light to medium reddish-brown, medium- to coarse-grained friable sandstone, containing many mudclasts and also mica (Figs.4-3g,h). LF4 has gentle to high-angle cross lamination, and is interpreted to be a channel fill deposit formed by faster flow than LF3. It has occasional pebbles.

Lithofacies 5 (LF5) is red or reddish-brown, medium- to coarse-grained, massive sandstone with occasional pebbles and many mudclasts (Figs.4-3i,k). LF5 is interpreted as a channel lag deposit.

a) LF1 at depth of 53 m bgl

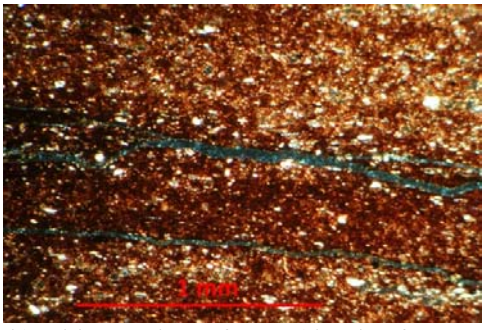

b) Thin-section of LF1 (depth of 56.45 m bgl) with crossed polars

b) LF2 (depth of 60.22 m bgl)

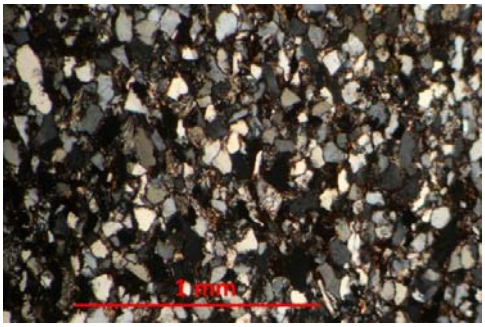

d) Thin-section of LF2 (depth of 67.2 m bgl) with crossed polars

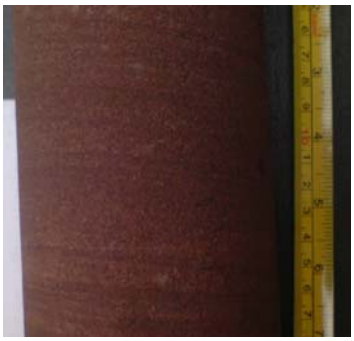

e) LF3 (depth of 48.0 m bgl)

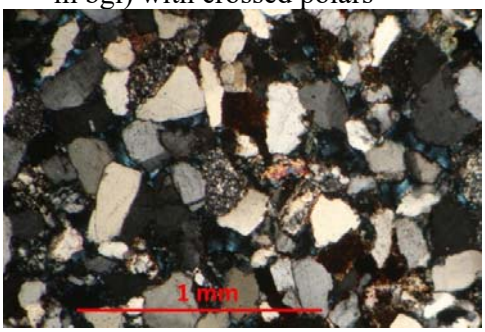

f) Thin-section of LF3 (depth of 50.15 m bgl) with crossed polars

g) LF4 (depth of 59.40m bgl)

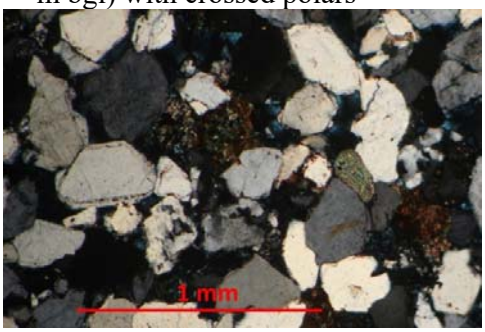

h) Thin-section of LF4 (depth of 59.18 m bgl) with crossed polars

i) LF5 (depth of 70.05 mbgl)

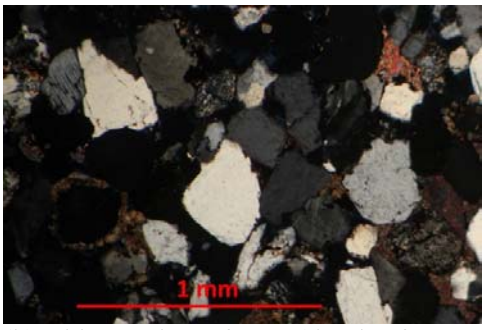

(k) Thin-section of LF5 (depth of 73.14 m bgl) with crossed polars

Fig.4-3. Lithofacies identified from Preston Laundry Borehole core.
The core pictures are from Moran (2008).

Table 4-7. Summarizes the relative abundance of the lithofacies in the borehole. LF3 and LF4 occur most frequently and have the thickest beds with 47 and 39 single beds and total thicknesses of 31.38 and 27.57 m respectively, together accounting for 91.3% of the total core thickness. LF1 is the least common lithofacies with only 3 beds compared with 15 beds and 26 beds found for LF2 and LF5 respectively, and together occupying only 8.7 % of the core thickness. All lithofacies except possibly LF1 occur distributed throughout the whole borehole. There is no clear trend of lithofacies frequency varying with depth. Cyclicity is examined in Section 4.4.4.

Table 4-6. Summary lithofacies classification of the Preston Laundry borehole core (adjusted from Moran 2008).

LF	Sedimentary characteristics				Interpreted palaeoenvironment
	Gain size	Mudclasts/ pebbles	Mica	Lamination	
1	Mudstone	no	yes	Wavy	Abandoned channel or flood deposits
2	Very fine sand	no	much	Flat to low-angle	Overbank deposit
3	Fine to medium sand	occasional	yes	Flat or gently inclined	Channel fill
4	Medium to coarse sand	often	yes	Gently inclined or steep	Channel fill
5	Medium to coarse sand	many	yes	None (massive)	Channel lag

Table 4-7. Preston borehole core lithofacies units.

LF	Numbers of bed	Depth (m bgl)		Thickness (m)								
		From	To	Min	Max	Mean	Median	SD	Q1	Q3	Total	% of core
1	3	53.50	67.15	0.04	0.5	0.23	0.15	0.2	0.1	0.32	0.7	1.00%
2	15	46.62	107.50	0.01	0.46	0.15	0.1	0.2	0.04	0.18	2.32	3.60%
3	47	45.30	107.95	0.05	2.41	0.67	0.45	0.6	0.27	0.96	31.4	48.40%
4	39	45.90	110.20	0.07	2.4	0.71	0.4	0.6	0.28	0.95	27.6	42.50%
5	26	46.50	102.25	0.01	0.52	0.11	0.05	0.1	0.02	0.17	2.95	4.50%

SD: standard deviation;
Q1 and Q3: first and third quartiles.

4.4.3 Hydraulic properties

4.4.3.1 Porosity

Fig.4-4 shows porosities as a function of lithofacies varying with depth, and Table 4-8 summarises statistics for porosities from the 63 core plugs and 125 core samples. The results

for these two sets of samples are consistent, with means of 18.27 and 18.14 % and medians of 18.40 and 18.22 % respectively. The porosities for both the core plugs and samples are normally distributed, and there is no systematic variation of porosity with depth, though there is possibly slightly less variation at deeper levels (Fig.4-4).

The Preston core porosities are generally consistent with data reported by Allen et al. (1997) for the region. Allen et al. (1997) reported porosities ranging from 5.4 to 31 % with no systematic variation with depth, but suggest a rather higher mean (23 %) and larger inter-quartile range (20-26 %).

Kolmogorov-Smirnov (K-S) tests (Kirkman, 1996) were used to determine whether each lithofacies had a distinctive porosity distribution. Table 4-9 summarises the results for the core samples: it proved impossible to determine the porosity of LF1 using saturation methods. At the 99% or higher confidence level, there is a statistical distinction in porosity between LF2 and both LF4 and LF5, and between LF3 and both LF4 and LF5. LF2 and LF3 have similar porosity distributions, as do LFs 4 and 5.

Table 4-8. Summary statistics for Preston core porosity.

	Core plugs	Core fragment samples
Numbers of sample	63	125
Mean (%)	18.27	18.14
Std. dev (%)	2.15	3.22
Max (%)	22.30	25.08
Upper quartile (%)	19.80	20.28
Median (%)	18.40	18.22
Lower quartile (%)	16.90	16.26
Min (%)	11.90	9.43

Core plug data from Moran (2008).

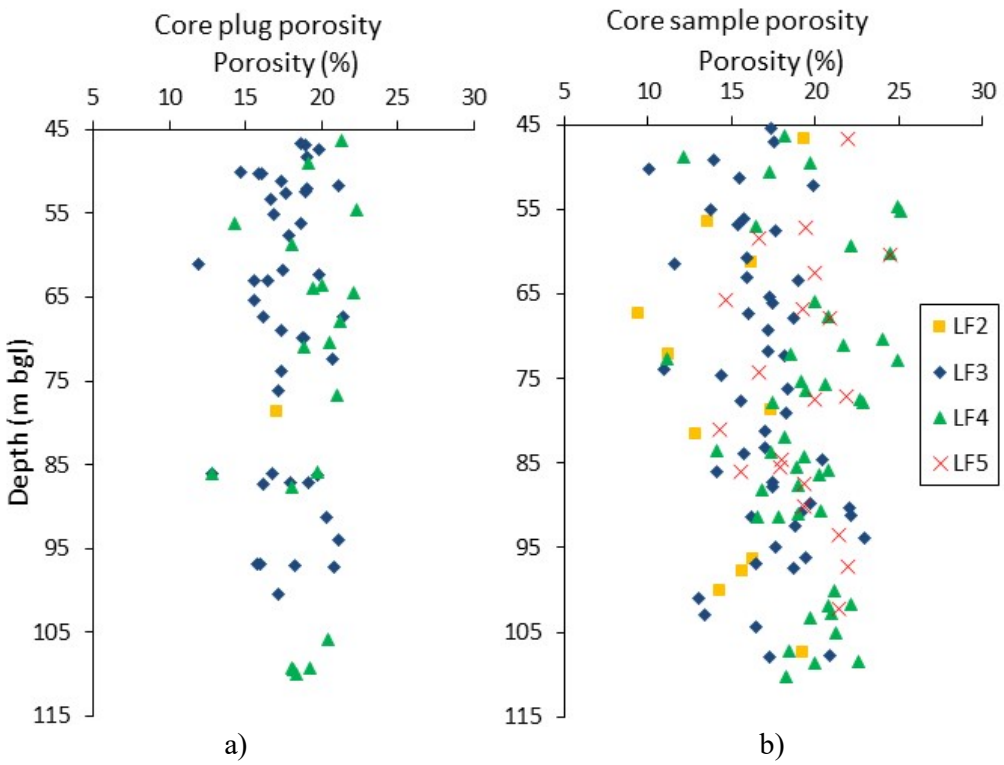

Fig.4-4. Porosity as a function of lithofacies and depth: a) core plugs; b) core samples.

Table 4-9. Kolmogorov-Smirnov test for porosity of the borehole core samples.

p values					Summary statistics								
LF	2	3	4	5	Num. of measured point	Min	Max	Mean	Median	SD	Q1	Q3	Distribution
2	-	0.2	0.00	0.01	11	9.43	19	15.0	15.7	3.13	13	17.3	normal
3		-	0.00	0.00	49	10.1	23	17.0	17.2	2.71	16	18.7	normal
4			-	0.77	45	11.1	25	19.7	19.7	3.02	18	21.5	normal
5				-	20	14.3	25	19.2	19.4	2.7	17.0	21.4	normal

Variograms have been successfully used to characterize spatial heterogeneity of hydraulic properties (Ritzi et al., 2004; Huysmans et al., 2008; e.g.,McKinley et al., 2011). Experimental variograms are obtained by plotting γ against lag distance h, γ being defined as follows:

$$\gamma(h) = 0.5/N \sum_{i=1}^{N}(X_i - X_{i+h})^2 \qquad (4\text{-}3)$$

where:

N is the number of sample pairs and

X_i, X_{i+h} are the values of the measured variable, in this case porosity, in two samples separated by distance h.

Fig.4-5 shows experimental and fitted modelled variograms for the porosities of the core samples with a unit lag distance of 0.3 m (i.e. lag distances are an integer multiple of 0.3 m, and 0.3 m is the minimum lag distance). The variograms suggest a range of 0.7 m and "holes" at distances of 2.5, 7.5, 13, 19.6, and 24.6. It is not easy to relate these holes to the plot of porosity with depth shown in Fig. 4-4b, but there are trends of quite regular increase and decrease in porosity as seen in Fig.4-4b. These trends are centred at around depths of 62.56, 70.37, 72.76, and 97.22 m and distances between these depths match the above holes.

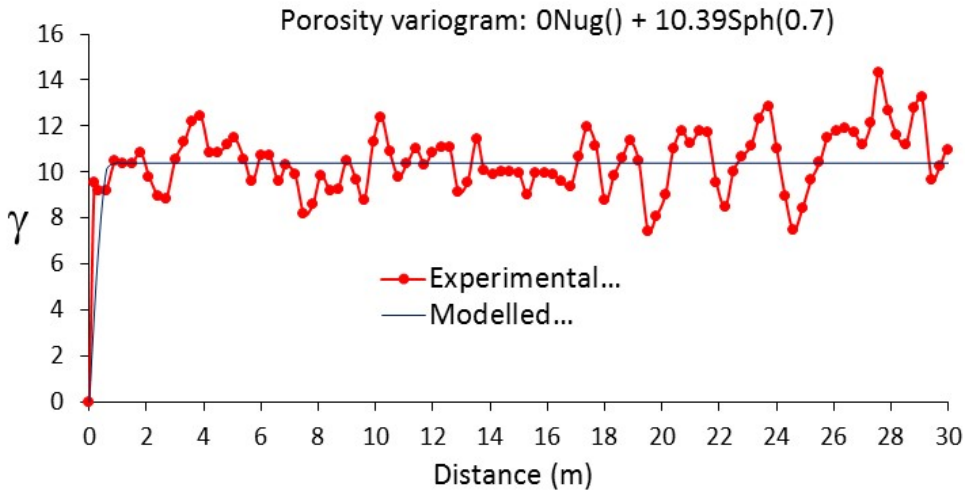

Fig.4-5. Porosity variograms for the core samples.

Note that the range of 0.7 m is about the same as the mean thicknesses of LF3 (0.67 m) and LF4 (0.71 m). These LFs appear most commonly in the core, together accounting for about 91% of the core (Table. 4-7).

4.4.3.2 Permeability

a) Falling head permeameter measurements of hydraulic conductivity

The 63 core plugs were subject to hydraulic conductivity measurements using the falling head technique. Moran (2008) reported that results show hydraulic conductivity varying by about 4 orders of magnitude from 8.24 x 10^{-4} to 1.11 m/d with a geometric mean of 0.10 m/d, a median of 0.12 m/d, a standard deviation of 0.24 m/d, and an interquartile range of 0.26 m/d (from 4.31 x 10^{-2} to 0.26 m/d). The core plug hydraulic conductivity distribution is approximately log-normal.

There is no apparent trend of hydraulic conductivity variation with depth (Fig.4-6), though the dataset is affected by many fewer core plugs from LF2, LF1 and LF5. It became clear that many more samples were required and that it was necessary to find a technique that avoided the problems of coring friable samples, and hence recourse was made to mini-permeametry.

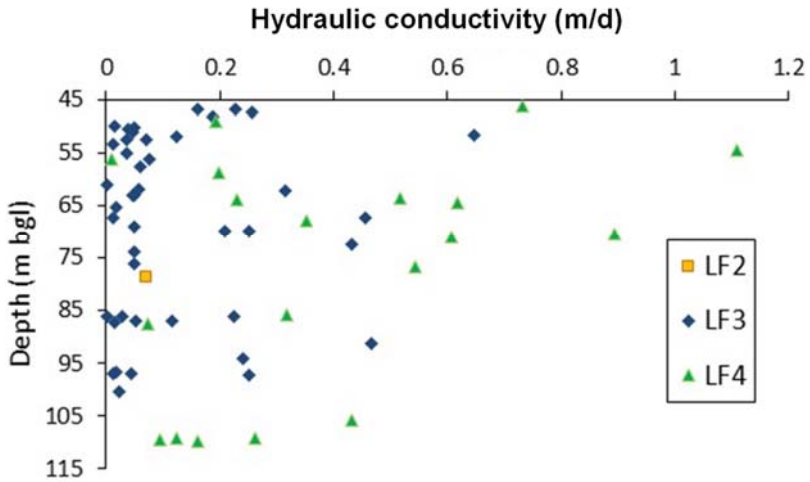

Fig.4-6. Falling head permeameter-measured hydraulic conductivity as a function of lithofacies and depth.

b) Mini-permeameter measurements of intrinsic permeability

A total of 726 points on the borehole core were measured for permeability using the minipermeameter. Even so, no permeability measurement was possible for LF1, the mudstone, because of its extremely low permeability (probably around 10^{-18} m^2 from previous water permeametry measurements on similar mudstone beds from the Cheshire Basin (e.g. Tellam and Lloyd, 1981; Tellam and Barker, 2006; Curião unpublished data 2002), well below the operating range of the minipermeameter used). All permeability values for LF1 used for studying below are taken from Curião (unpublished data 2002).

Table 4-10 shows a summary of the permeability values obtained. LF2, LF3, LF4 and LF5 have, respectively, the following numbers of measured points: 17, 346, 333, and 29. Permeability ranges over about 3 orders of magnitude from 1.1 x 10^{-15} to 5.7 x 10^{-13} (equivalent to a hydraulic conductivity range of about 0.001 – 0.5 m/d at 20^o C), with a geometric mean of 3.3 x 10^{-14} m^2 (0.028 m/d), a median of 3.4 x 10^{-14} m^2 (0.028 m/d), and an interquartile range of 6.2 x 10^{-14} m^2 (from 1.5 x 10^{-14} to 7.7 x 10^{-14} m^2 (0.013- 0.065 m/d)).

Table 4-10 indicates the permeability geometric means increasing from 4.2 x 10^{-18} m^2 (3.6 x 10^{-6} m/d) for LF1 (Curião unpublished data 2002) to 3 x 10^{-15} m^2 (0.0025 m/d) for LF2 to 9.5 x 10^{-14} m^2 (0.081 m/d) for LF5, this increasing trend also being seen with median values. LF4 shows the widest range of permeability values (2.2 x 10^{-15}- 5.1 x 10^{-13} m^2), while LF1 shows the narrowest range, but with many fewer measured points.

The permeability is approximately log-normally distributed and there is no apparent trend of permeability variation with depth (Fig.4-7). The permeability variation is consistent with the range given by Allen et al. (1997) for the area (Fylde region including Preston area) (1 x 10^{-4} to 4 m/d (1.2 x 10^{-16} – 4.7 x 10^{-12} m^2)).

Box and whisker plots and cumulative frequency of permeability determined for each lithofacies are given in Fig.4-8 and Fig.4-9. Though there is an overlap of permeability ranges seen for LF3, LF4 and LF5, in general the data show a regular increase in values from LF1 to LF5 (Fig.4-8): statistical values for LF1 are much less than for any other lithofacies; the first quartile (Q1) for LF2 is about the same as the minimum permeability value of LF3; Q1 of LF3 is roughly equal to the maximum permeability of LF2; the median of LF3 is approximately equal to Q1 for LF4; and Q3 of LF3 is roughly equal to the median of LF4. A similar trend is also seen for LF4 and LF5. Generally, therefore, there is a systematically increasing permeability from LF1 to LF2 (finest grained measured LF in the core) to LF5 (coarsest grain measured LF) with a "quartile step" seen for each successive lithofacies. This suggests that the permeability distribution for each lithofacies is distinct, and this will now be tested statistically.

Table 4-10. Mini-permeameter intrinsic permeability results, with equivalent hydraulic conductivities at 20° C.

LF	No. of point	Min m^2 (m/d)	Max m^2 (m/d)	Arithmetic mean m^2 (m/d)	Geometric mean m^2 (m/d)	Median m^2 (m/d)	Std. dev m^2 (m/d)	IQR m2 (m/d)		Distribution
								Q1	Q3	
LF1*	42	$1.1x10^{-18}$ ($9.0x10^{-7}$)	$5.8x10^{-17}$ ($4.9x10^{-5}$)	$7.1x10^{-18}$ ($6.0x10^{-6}$)	$4.2x10^{-18}$ ($3.6x10^{-6}$)	$3.6x10^{-18}$ ($3.0x10^{-6}$)	$1.0x10^{-17}$ ($8.4x10^{-6}$)	$2.1x10^{-18}$ ($1.8x10^{-6}$)	$7.5x10^{-18}$ ($6.4x10^{-6}$)	lognormal
LF2	17	$1.1x10^{-15}$ ($9.6x10^{-4}$)	$1.1x10^{-14}$ ($9.3x10^{-3}$)	$4.0x10^{-15}$ ($3.3x10^{-3}$)	$3.0x10^{-15}$ ($2.5x10^{-3}$)	$2.9x10^{-15}$ ($2.5x10^{-3}$)	$3.0x10^{-15}$ ($2.5x10^{-3}$)	$1.4x10^{-15}$ ($1.2x10^{-3}$)	$6.0x10^{-15}$ ($5.0x10^{-3}$)	lognormal
LF3	349	$1.6x10^{-15}$ (0.001)	$3.7x10^{-13}$ (0.311)	$3.8x10^{-14}$ (0.032)	$2.3x10^{-14}$ (0.019)	$2.3x10^{-14}$ (0.019)	$4.2x10^{-14}$ (0.035)	$1.2x10^{-14}$ (0.010)	$4.8x10^{-14}$ (0.041)	lognormal
LF4	328	$2.2x10^{-15}$ (0.002)	$5.1x10^{-13}$ (0.434)	$8.6x10^{-14}$ (0.073)	$4.9x10^{-14}$ (0.042)	$5.1x10^{-14}$ (0.043)	$9.7x10^{-14}$ (0.082)	$2.4x10^{-14}$ (0.020)	$1.0x10^{-13}$ (0.086)	Neither normal nor lognormal
LF5	32	$8.2x10^{-15}$ (0.007)	$5.7x10^{-13}$ (0.479)	$1.4x10^{-13}$ (0.110)	$9.5x10^{-14}$ (0.081)	$1.1x10^{-13}$ (0.091)	$1.2x10^{-13}$ (0.104)	$4.5x10^{-14}$ (0.038)	$2.3x10^{-13}$ (0.192)	lognormal
Combined (LF2 to LF5)	726	$1.1x10^{-15}$ (0.001)	$5.7x10^{-13}$ (0.479)	$6.3x10^{-14}$ (0.053)	$3.3x10^{-14}$ (0.028)	$3.4x10^{-14}$ (0.028)	$8.2x10^{-14}$ (0.069)	$1.5x10^{-14}$ (0.013)	$7.7x10^{-14}$ (0.065)	Approximately lognormal

** data from Curião (unpublished data 2002)*
Q1, Q3: first and third quartile respectively
IQR: interquartile range (i.e. Q3 – Q1).

Table 4-11. K-S test results on the intrinsic permeability variation with lithofacies.

p values						Numbers of measured point
LF	1	2	3	4	5	
1*	-	0.000	0.000	0.000	0.000	31
2		-	0.000	0.000	0.000	17
3			-	0.000	0.000	349
4				-	0.009	328
5					-	32

** data from Curião (unpublished data 2002).*

Table 4-11 summarises the results of applying K-S tests to determine whether the permeability results for each lithofacies are likely to come from different populations. The results confirm that the permeability distribution for each lithofacies is distinct (at 99% confidence level). It is noted, however, that the test results may show some bias as the number of samples for LF1 (31), LF2 (17) and LF5 (32) are relatively small compared with those of LF3 (349) and LF4 (328).

An alternative set of LF definitions has been proposed by Mould (2007) for the core; using these, the correlation with permeability was investigated and found to be non-significant, providing some encouragement that the present LF definitions are reasonable, and also indicating that choice of LF definitions is crucial.

Variograms have been used to search for structure in the variation of log(k) values with a unit lag distance of 0.05 m (Fig.4-10). The model variogram shows no nugget effect, a correlation length of 0.4 m, and some relatively big ‘holes’ at around 2 m, 5.5 m, 14.5 m and 24.5 m. For comparison, Fig.4-11 shows the data and model variograms for the lithofacies codes with 0.05 m unit lag distance: the plots for log(k) and lithofacies numbers are very similar indeed, supporting the results of the K-S tests. As for the porosity data, the ‘holes’ are not obvious in the profiles of permeability and lithofacies code with depth, but some regular fluctuations in

permeability centre at depths of about 55.5, 61.0, 75.5, 77.5, and 102.0 m bgl and the distances between these depths are 5.5, 14.5, 2, and 24.5 m, corresponding to the holes.

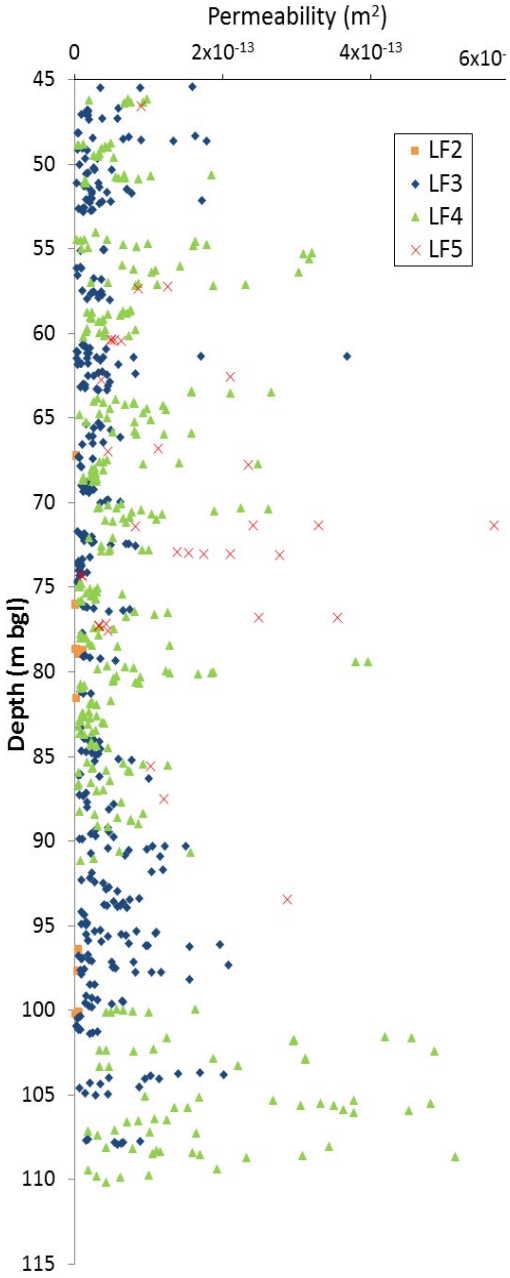

Fig.4-7. Permeability and lithofacies varying with depth.

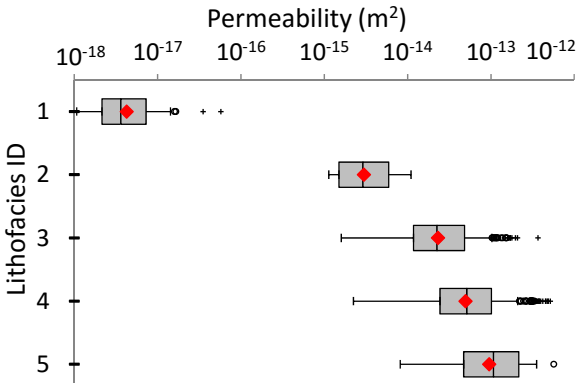

Fig.4-8. Box and whisker plots of Preston lithofacies versus k. Uprights, left to right, are: minimum; lower quartile, geometric mean, median, upper quartile, and maximum.

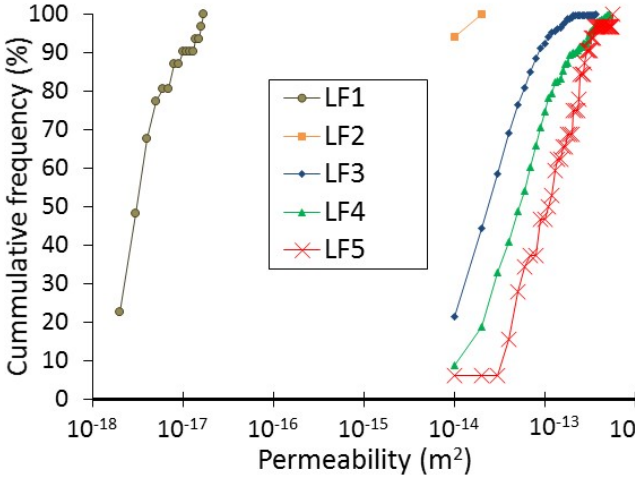

Fig.4-9. Cumulative frequency distribution of permeability of lithofacies.

For comparison to porosity, a variogram of log(k) at the same unit lag distance of 0.3 m as for porosity variogram model (Fig.4-5) was conducted (Fig.4-12). Fig.4-12 shows the two

variogram profiles have similar ranges and 'holes'. Note that the variogram for log(k) with a unit lag distance of 0.05 m has a range of 0.4 m (Fig.4-10). The difference can be caused by a change in unit lag distance: longer unit lag distance can miss out some important features.

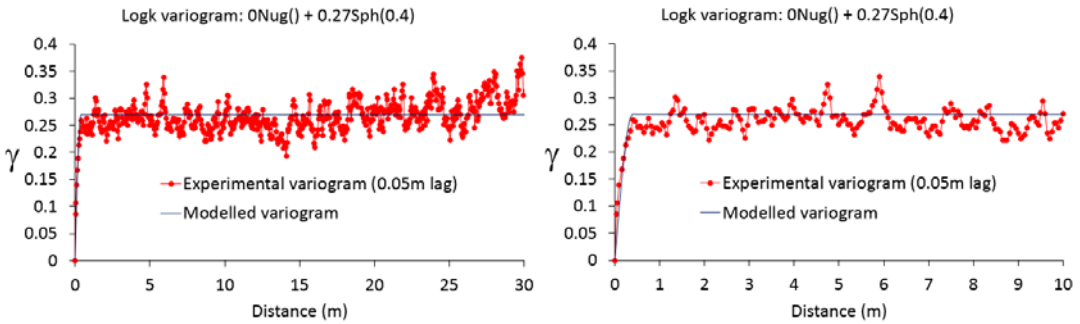

Fig.4-10. Experimental and best fitted model variograms of log(k[k in mD]) values (unit lag distance of 0.05 m); zooming in distance from left to right.

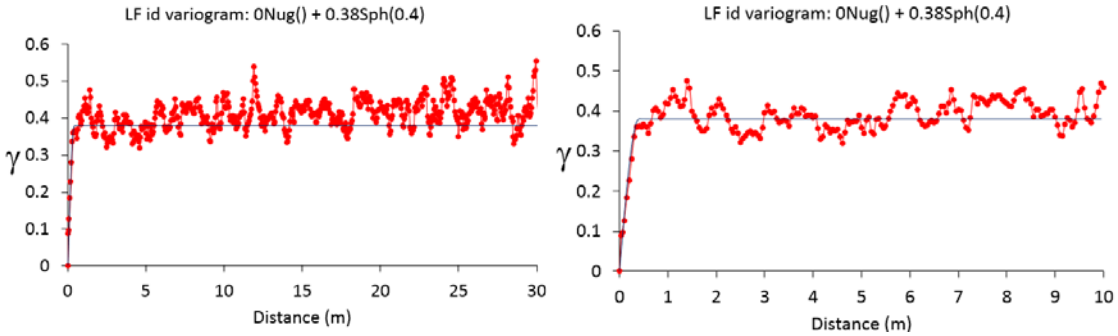

Fig.4-11. Experimental and best fitted model variograms of lithofacies code; zooming in distance from left to right.

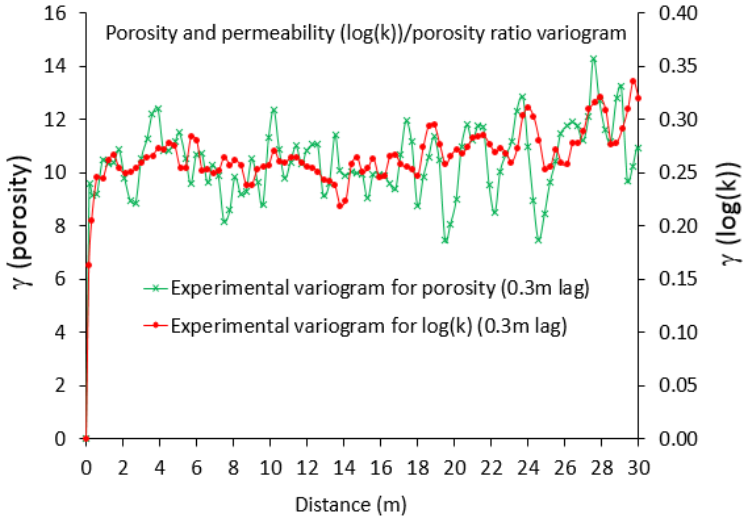

Fig.4-12. Experimental variograms of logarithm base 10 of permeability (permeability in mD) and porosity (unit lag distance of 0.3 m).

Overall we conclude from the basic statistics (cumulative probability plots, box-and-whisker plots), the K-S tests, and the variogram analyses, that permeability is correlated with lithofacies as defined in Section 4.4.2. The structure of LF and hydraulic properties is complex with depth, as indicated by the plots of properties with depth and the distribution of variogram 'holes'.

c) Within LF and within bed permeability heterogeneity

A measure of the permeability heterogeneity within each LF can be obtained using the ratio of interquartile range to median for the permeability data of Table 4-10. The ratios range from 0.92 to 1.61 (respectively, LF1 to 5, 0.92, 1.52, 1.61, 1.5, and 1.57), suggesting that apart from LF1 each LF has a similar degree of heterogeneity, as indeed seems to be indicated by Fig.4-8.

To investigate the within-bed heterogeneity, mini-permeameter measurements were taken at two locations at every depth, separated by 5 cm around the circumference of the borehole core. The measurements are referred to here as k1 and k2. Fig.4-13 indicates that local heterogeneity is considerable. Taking as a measure of within-bed heterogeneity the ratio $H = |k1-k2|/k_m$, where k_m is the mean k value at the depth concerned, heterogeneity as indicated by the mean H for each LF is as follows: 0.39 (LF2); 0.47 (LF3); 0.5 (LF4); 0.48 (LF5). It is again concluded that each LF has a similar degree of heterogeneity within bed as seen within LF.

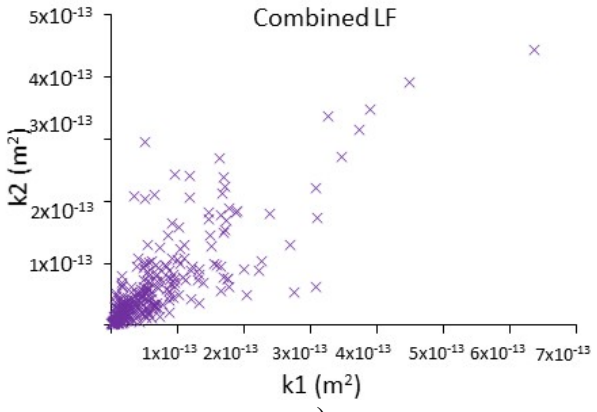

a)

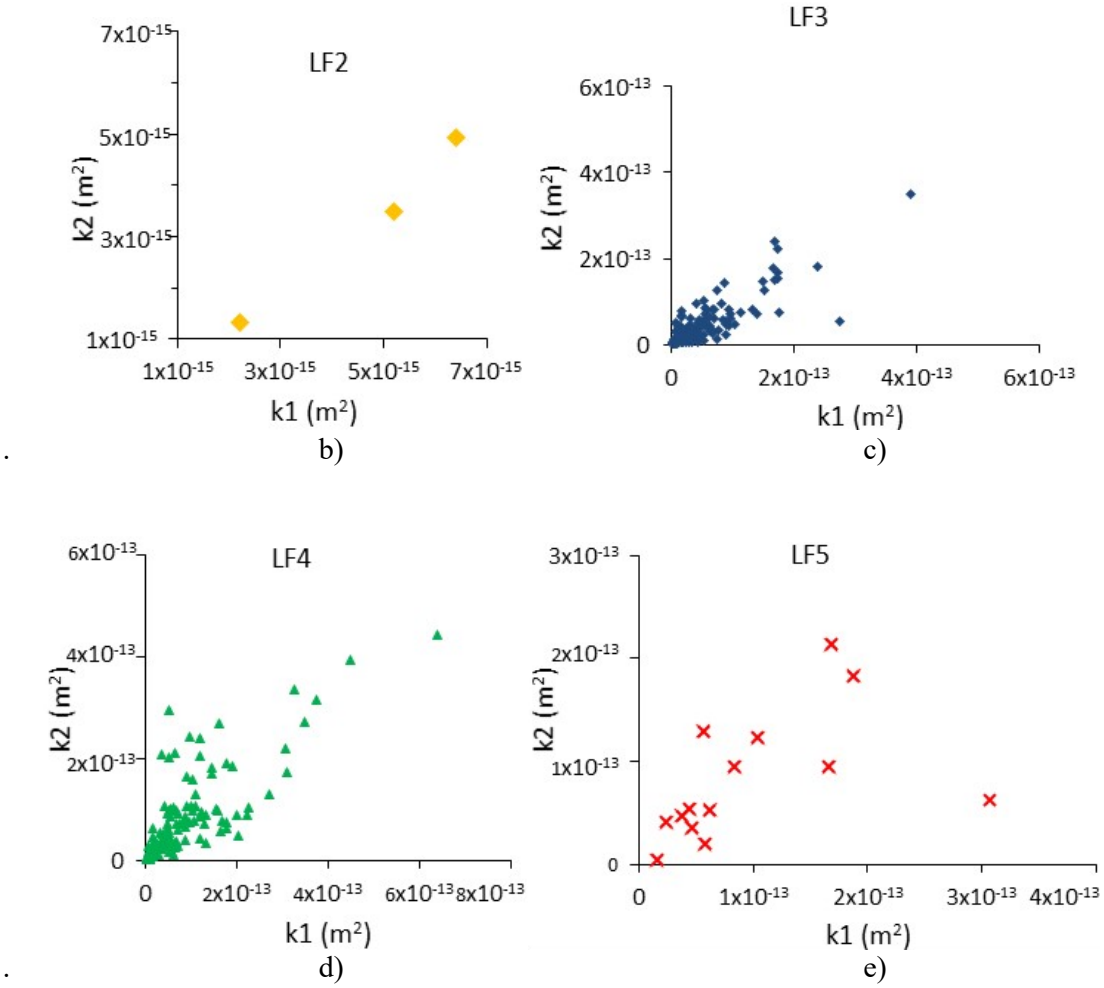

Fig.4-13. Heterogeneity as determined by mini-permeameter permeability measurements on the borehole core: a): all measurements; b) to e): LF2 to LF5. K1 is permeability measured at the first point; k2: permeability measured at a point 5 cm distance from k1 at the same depth.

d) Anisotropy as determined using mini-permeametry

Both borehole cores and plugs were examined for anisotropy and results are shown in Figs.4-14a,b. Ratios of horizontal permeability to vertical permeability (k_H/k_V) vary from 0.3 to 4.7 for core plugs, with 57% of the 42 samples having a ratio of less than 1. For the borehole cores the ratios vary from 0.2 to 5.3, with 63% having a ratio of less than 1. There is no systematic variation of anisotropy with depth or lithofacies (Figs.4-14a,b), though very few data are available for LF2 and LF5.

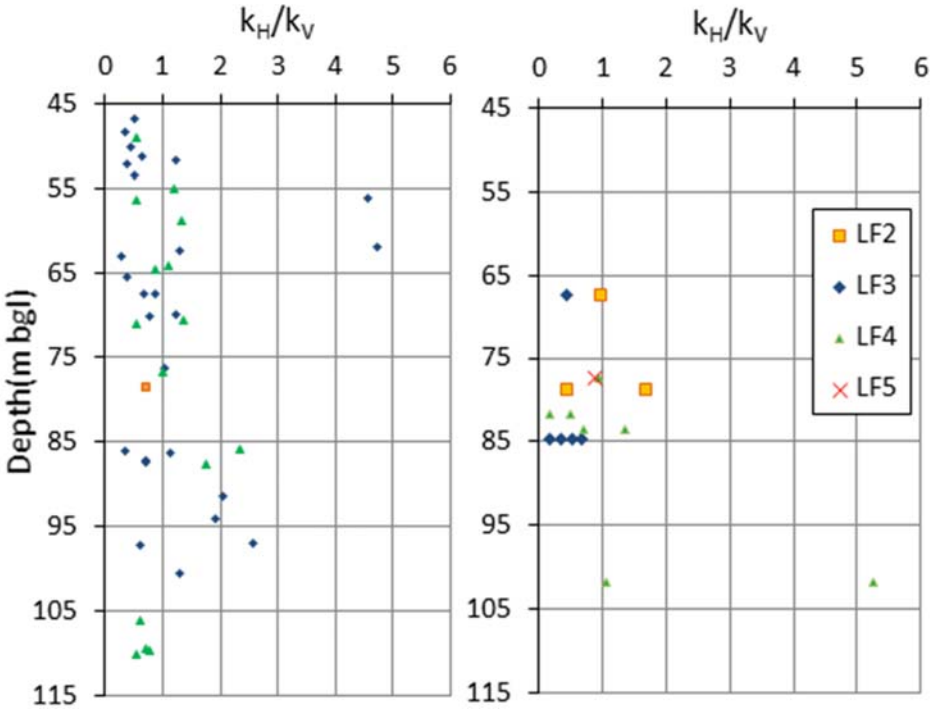

Fig.4-14. Sandstone anisotropy: ratio horizontal permeability ($k_{H.}$) to vertical permeability (k_V) versus depth and lithofacies. a) core plug; b) core samples.

It is reported for the Sherwood Sandstone Group that lamination, where present, can cause horizontal to vertical anisotropy ratios of usually about 1-3, but can be up to 50. For example, Bloomfield et al. (2006) found a value of 3, whilst Campbell (1982) showed values ranging from less than 1 to greater 100. Though the results presented here are broadly consistent in upper values of the anisotropy ratio, it is clear that there is an unusually high proportion of ratios less than 1 – roughly the same as those greater than 1. This is probably due to the small scale of measurement of the mini-permeameter and the significant local heterogeneity of the rock.

4.4.3.3 Permeability – porosity relationship

In general for rocks of a similar fabric, it is expected that there would be a positive correlation between porosity and permeability (e.g. Allen et al., 1998).

Figs.4-15a,b shows plots of log(k) against porosity as a function of lithofacies for the 63 core plugs and for 97 core samples. The core plug samples were measured using the falling head technique, but in Fig.4-15 the hydraulic conductivities have been converted to intrinsic permeabilities. The core plugs show a good correlation with an R^2 of 0.87 (Fig.4-15a), while the borehole cores display a significantly weaker correlation with an R^2 of 0.38 (Fig.4-15b). The latter include much higher proportions of LF2 and LF5 samples, whose fabrics are probably less similar than those of LFs 3 and 4, but the main difference is probably again connected with the scale of measurement: the core plug permeability and porosities have both been measured at the scale of the whole plug, i.e. over a volume of between approximately 40 and 50 cm^3, whereas the core samples were measured at penetration of about 1.2 cm: in addition, the core sample porosities were of necessity measured at a much larger scale than the mini-permeameter permeabilities. Again the local heterogeneity (Fig.4-13) appears to be of importance.

The relationship between porosity and permeability appears, as far as the data in Fig.4-15 can discern, to be similar for all four lithofacies.

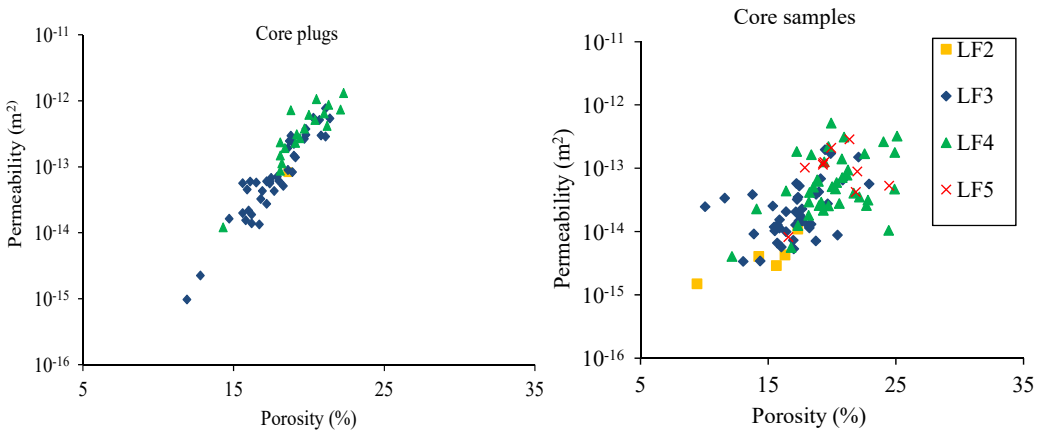

Fig.4-15. Plots of the relationship between porosity and the logarithm of intrinsic permeability. a) Core plugs (falling head permeameter results); b) Core samples (mini-permeameter results).

4.4.3.4 Permeability / porosity ratio

Average linear velocity is dependent on the ratio of permeability to porosity, and hence it is important also to examine how this ratio varies with lithofacies.

Table 4-12 shows the K-S test results for the permeability/porosity ratios for the core plugs and the core samples. For the core plug / falling head permeameter data, only sufficient samples were available to compare LF3 and 4. The results (Table 4-12) show that the difference between these lithofacies is significant (at 95% confidence level). More core sample / mini-permeameter data were available, but again insufficient to examine LF2 relationships. For this dataset, distinctive porosity/permeability ratios were found between LF3 and LF4, and LF3 and LF5. LF4 and LF5 appear to have more similar permeability: porosity ratio distribution: these lithofacies also have very similar porosity distributions (Table 4-9). The permeability / porosity ratios are consistent with lognormal distributions in almost all cases.

Table 4-12. K-S test (p values) of the ratio of permeability to porosity.

Core plugs							Core sample						
p values					Num. of sample	Distribution	p values					Num. of sample	Distribution
LF	2	3	4	5			LF	2	3	4	5		
2	-	-	-	-	1	-	2	-	-	-	-	5	-
3		-	0.000	-	43	Lognormal	3		-	0.001	0.002	43	Lognormal
4			-	-	19	Normal and lognormal	4			-	0.130	39	lognormal
5				-	0	-	5				-	10	Lognormal

Fig.4-16 shows experimental variogram and best fit variogram model for the ratio of intrinsic permeability to porosity of the core samples. As with porosity (Fig.4-5) and log(k) (Fig.4-10), at the same lag distance, the variogram for permeability/porosity ratio also has a range of 0.6 m, and almost the same 'hole' locations.

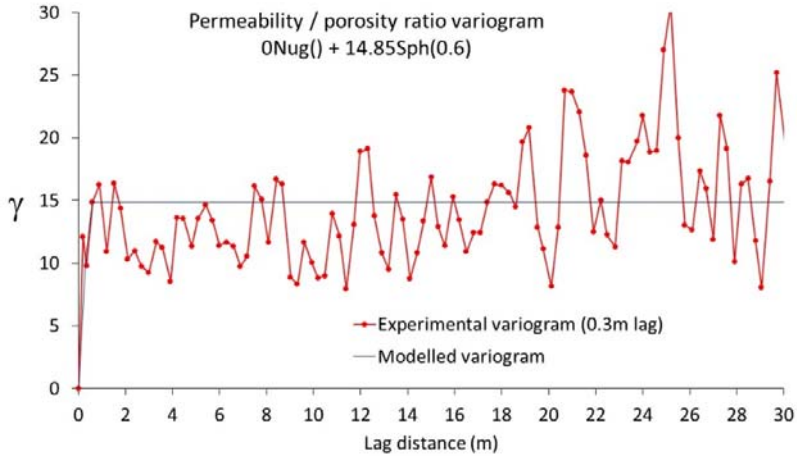

Fig.4-16. Experimental and best fitted model variograms of permeability / porosity ratio (unit lag distance of 0.3 m).

4.4.4 Lithofacies sequences

4.4.4.1 Introduction

Having established that there is a correlation between LF and hydraulic properties, and that there is no obvious variation of hydraulic properties with depth, it is appropriate to try and determine any structure within the LF sequence, as this would result in hydraulic property structure. Accordingly, cyclicity within the LF sequence will first be examined, and then the implications of this for hydraulic property structures will be considered.

4.4.4.2 Lithofacies cyclicity analysis using the Markov chain approach

The vertical cyclicity of the Preston borehole core was analysed with Markov chains (Miall, 1973; Ahmad et al., 2012). Firstly a transition count matrix (Table 4-13) was built by counting the number of times that all the row lithofacies (i) pass immediately upwards into the column lithofacies (j). The transition count matrix is then converted to a transition probability matrix (Table 4-14). This was done by dividing the number in each cell by the row total in the transition matrix. Next was to build a random probability matrix (Table 4-15), representing the transitions

expected form purely random transitions. The value in each cell in Table 4-15 was calculated using the following equation

$$R_{ij} = S_j/(T - S_i) \qquad (4\text{-}4)$$

where the following definitions apply:

R_{ij}: random probability of transition from lithofacies i to j

S_j: random number of occurrences of lithofacies j (i.e. column total for lithofacies j)

S_i: random number of occurrences of lithofacies i (i.e. row total for lithofacies i)

T: total number of transitions for all lithofacies.

A transition difference matrix (Table 4-16) was built by subtracting the transition probability matrix (Table 4-14) by the random probability matrix (Table 4-15). Positive values in the difference matrix (Table 4-16) indicate transitions which have occurred at greater than random frequency.

Note that in all the matrices, all the diagonal cells have a value of zero, i.e. assuming no multi-storey lithofacies are present (Selley, 1969). This is not necessarily the case, but including a range of possible multi-storey occurrences (they cannot be identified unambiguously in the core) produces a similar overall result. This is characteristic feature of an embedded Markov chain (Krumbeiwn and Daceym, 1969; Miall, 1973).

Fig.4-17 shows the difference matrix (Table 4-16) in diagrammatic form, connecting lithofacies with the high positive values in the difference matrix. The cyclicity of lithofacies was also examined using standard chi-square tests, and results suggest markovity and cyclicity of lithofacies transitions within the Preston sequence.

Table 4-13. Transition count matrix.

	LF1	LF2	LF3	LF4	LF5	Row total
LF1	0	0	1	1	1	3
LF2	2	0	5	5	3	15
LF3	0	13	0	17	16	46
LF4	1	1	31	0	6	39
LF5	0	1	10	15	0	26
Column total	3	15	47	38	26	**129**

Table 4-14. Transition probability matrix.

	LF1	LF2	LF3	LF4	LF5
LF1	0	0.00	0.33	0.33	0.33
LF2	0.13	0	0.33	0.33	0.20
LF3	0.00	0.28	0	0.37	0.35
LF4	0.03	0.03	0.79	0	0.15
LF5	0.00	0.04	0.38	0.58	0

Table 4-15. Random probability matrix.

	LF1	LF2	LF3	LF4	LF5
LF1	0	0.12	0.37	0.3	0.21
LF2	0.03	0	0.41	0.33	0.23
LF3	0.04	0.18	0	0.46	0.31
LF4	0.03	0.17	0.52	0	0.29
LF5	0.03	0.15	0.46	0.37	0

Table 4-16. Difference matrix.

	LF1	LF2	LF3	LF4	LF5
LF1	0	-0.12	-0.04	0.03	0.13
LF2	0.11	0	-0.08	0.00	-0.03
LF3	-0.04	0.10	0	-0.09	0.03
LF4	-0.01	-0.14	0.27	0	-0.14
LF5	-0.03	-0.11	-0.07	0.21	0

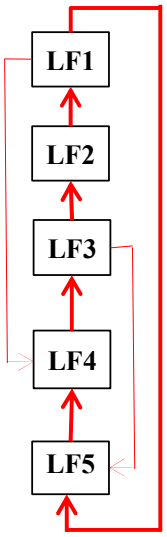

Fig.4-17. Lithofacies transition relationships in the Preston borehole core.

From Table 4-16, there are three most likely types of sequence in the borehole cores (Fig.4-17) (upwards direction):

(1) LF5- LF4- LF3- LF2-LF1

(2) LF4-LF3-LF2-LF1

(3) LF5-LF4-LF3-LF5-LF4-LF3

However, all transitions do occur, even if some rather infrequently. The three most common sequences are fining up in nature.

(1) is the full representation of the cycle, but this occurs only twice in the core: from 67.0 to 67.8 m bgl (0.8 m thick); and from 56.41 to 57.35 m (0.94 m thick). However, there are some depths where this sequence appears except for LF1 (e.g. at depths of around 72.1, 76, and 78.5 m bgl). LF1, the mudstone, in these sequences could be eroded away or washed out during coring, especially if it was represented only by thin units. That this happens often is indicated by the frequency of pellets.

The second type of fining-up sequence (2), again lacking LF1, appears quite frequently (six times at depths from 46.62 to 110.2 m) in the borehole. The last type of fining-up sequence, (3), appears more frequently (nine times at depths from 45.3 to 85.58 m) with both LF1 and LF2 being eroded away at top of the cycles.

4.4.4.3 Cyclicity and hydraulic properties

Two complete (LF5 to LF1) sequences at depths from 67.25 to 67.79 m bgl (0.54 m thick) and from 76.02 to 77.29 m bgl (1.27 m thick), and eight partial sequences (LF4-LF3-LF2 and LF5-LF4-LF3) at depths between 45.4 and 103.3 m bgl (Table 4-17) were measured for permeability using the mini-permeameter.

Overall, there are trends of increasing permeability with depth seen within the two complete sequences (Fig.4-18) as expected. Similar trends are also seen in sub-completed sequences (Fig.4-19).

Table 4-17. Completed and partial cyclic sequences within the Preston borehole cores.

Sequences	#	From (m bgl)	To (m bgl)	Length (m)	LF	Trend of sequence
Complete	1	67.00	67.80	0.80	1,2,3,4,5	Fining up
	2	56.41	57.35	0.94	1,2,3,4,5	Fining up
	3	75.95	77.3	1.35	2,3,4,5	Fining up
Partial	1	45.40	46.58	1.18	3,4,5	Fining up
	2	68.82	71.43	1.18	3,4,5	Fining up
	3	72.23	73.11	0.88	3,4,5	Fining up
	4	78.68	80.95	2.27	3,4,5	Fining up
	5	84.57	85.56	0.99	3,4,5	Fining up
	6	87.53	88.09	1.61	5,4,3	Coarsening up
	7 & 8	97.70	103.30	5.60	2,3,4,2,3,4	Cyclic, fining up

A general implication of the fining up nature of this sequence is that it is more likely that a bed is followed upwards by a bed of lower permeability, but when it is followed upward by a bed of higher permeability the difference in permeabilities is likely to be greater.

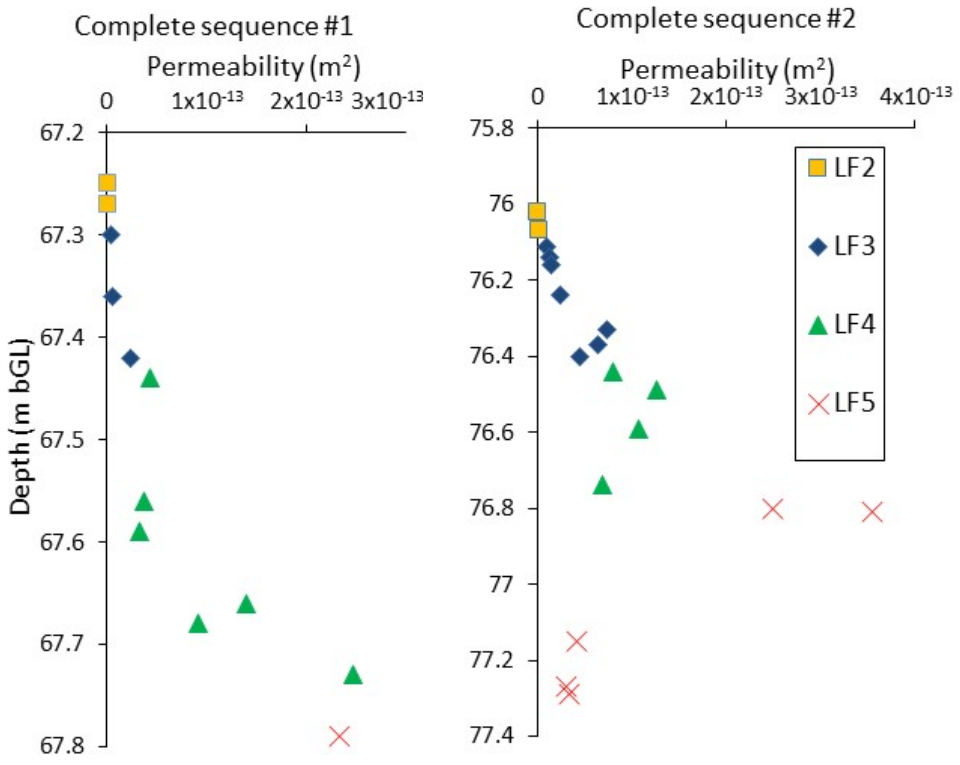

Fig.4-18. Permeability variation with depths of two completed sequences.

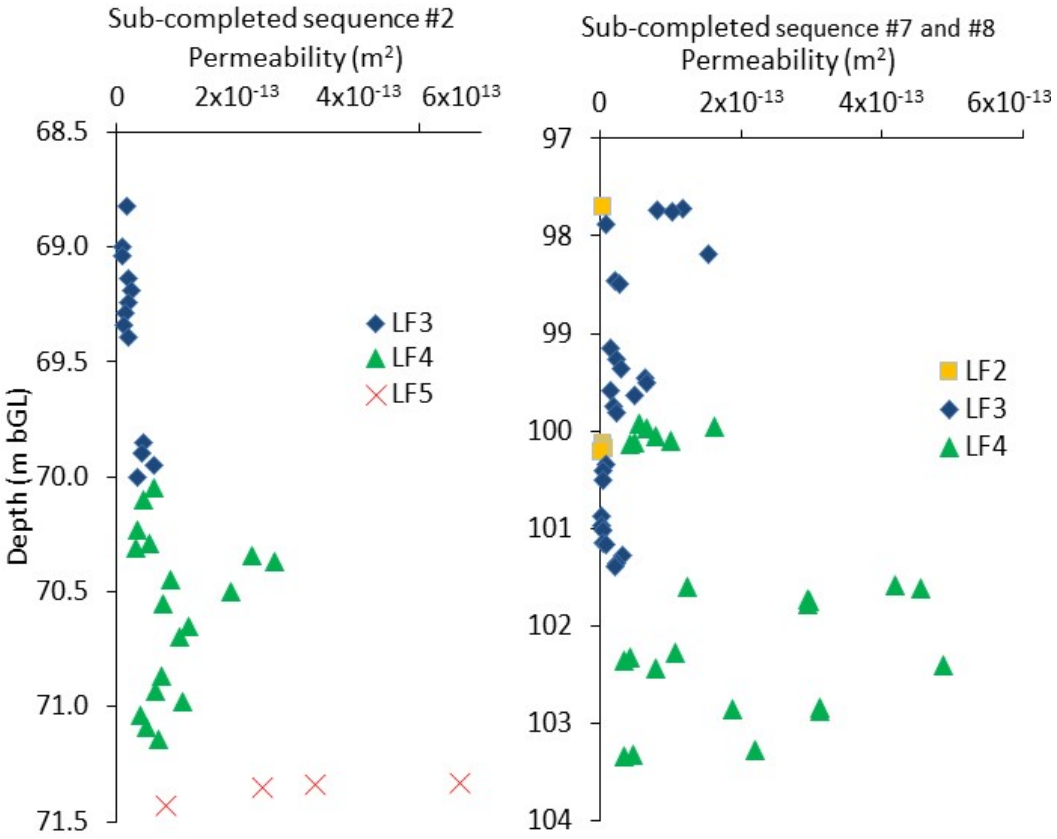

Fig.4-19. Permeability variation with depths of two sub-completed sequences.

4.4.5 Effects of pellet on macroscopic permeability

4.4.5.1 Effects of pellet density on permeability

It should be noted that the permeability of LF4 and LF5 as recorded in the figures and tables above is the permeability of the matrix, i.e. excluding the effect of the mudstone pellets. Following subsections show results from modelling the effect of the pellets on macroscopic permeability of the LF4 and LF5, and their effects on the lithofacies and permeability correlations.

Fig.4-20 shows effects of pellets on permeability as function of pellet size for horizontal and vertical flow directions. Generally, increasing density of pellets results in significantly reducing bulk permeability, and greater sized pellets cause more reduction in permeability for vertical

flow, but less for horizontal flows. With as little as 0.5% pellets, there is little change in permeability, but increasing pellet density to 10% can reduce permeability to 85%. A 20% pellets, the average values for LF5, decreases permeability by roughly 50%. Increasing pellets to 50% leads to reduction in permeability to about 1% (Fig.4-20).

For vertical flow, longer pellets cause greater reduction in permeability as expected. For horizontal flow, as the model domain is fixed (1 m long by 1 m wide by 1 m thick), increasing size of pellets causes reducing numbers of pellets in the model as the pellet density is fixed. This leads to a smaller reduction in permeability than seen with greater numbers of small pellets (Fig.4-20).

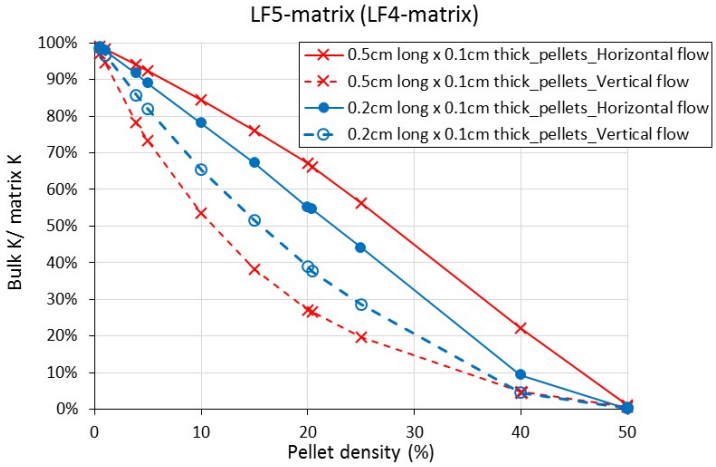

Fig.4-20. Effects of the proportion of pellets present on matrix permeability in the Preston Laundry Borehole core as function of pellet sizes for LF4 and LF5.

To illustrate the effect of the pellets on permeability in the Preston Laundry Borehole core, the results for the average density of pellets along with the most common pellet sizes (0.2 long cm by 0.2 wide cm by 0.1 thick cm) have been considered (Table 4-18).

For LF4 permeability, pellet densities of 2.8% and 13.5% for horizontal and vertical flow respectively leads to permeability reduction to about 94% (4.0 x 10^{-2} m/d) and 55% (2.3 x 10^{-2} m/d) for horizontal and vertical flow respectively (Table 4-18).

For LF5 permeability, pellet densities of 3.9% and 20.4% for horizontal and vertical flow respectively leads to reductions in permeability to about 92% (7.4 x 10^{-2} m/d) and 38% (3.1 x 10^{-2} m/d) (Table 4-18).

Table 4-18. Averaged pellet occupations and their effect on permeabilities.

LF	Mean pellet occupation (%)		Most frequent pellet size (cm)	Bulk K/matrix K		Geomeantric mean Permeability (m/d)			Arithmetic mean Permeability (m/d)		
	Horizontal flow	Vertical flow		Horizontal flow	Vertical flow	Original value	With pellet effect		Original value	With pellet effect	
							Horizontal flow	Vertical flow		Horizontal flow	Vertical flow
4	**2.8**	13.5	0.2x0.2x0.1	**94.1%**	55.3%	0.042	0.040	0.023	0.07	0.07	0.040
5	**3.9**	20.4	0.2x0.2x0.1	**91.7%**	37.7%	0.081	0.074	0.031	0.12	0.11	0.045

4.4.5.2 Effect of pellet sizes on permeabilities

Effects of pellet sizes on permeabilities are examined here in more detail. Models of matrix permeability for LF5 (permeability of 0.081 m/d) having a pellet density of 3.9% (Table 4-3) were created with VBA for a range of pellet sizes, and the hydraulic conductivities of these media were determined using MODFLOW.

Figs.4-21a, b show the effects of pellet size on matrix permeabilities for the models with horizontal and vertical flow respectively. For horizontal flow, pellet length has little effect on matrix permeability, though thicker pellets cause slightly greater reduction in matrix permeabilities, especially for short pellets (Fig.4-21a). For vertical flow, longer pellets lead to greater reduction in matrix permeabilities, and more reduction in permreability is seen with systems with thinner pellets.

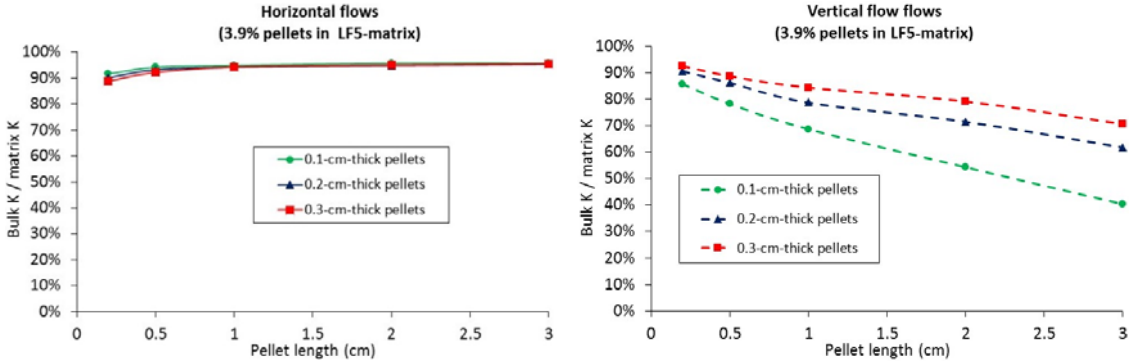

.a) b)

Fig.4-21. Effects of pellet sizes on matrix permeabilities with pellet density of 3.9%: a) horizontal flows; b) vertical flows.

4.4.5.3 Effects of the pellets on the correlation of lithofacies and permeability

Permeability corrected for the effects of pellet (pellet size of 0.2 by 0.2 by 0.1 cm with pellet density of 2.8% for LF4 and 3.9% for LF5) were used to update the correlation between sandstone lithofacies and permeability. Table 4-19 summaries the permeability with correction for the pellet effect. Fig.4-22, Fig.4-23, and Fig.4-24 show variation with depth, whisker plot box and cumulative plots for permeability corrected with the effect of pellet respectively. A comparison for K-S test for permeability data before and after accounting pellet effect is also shown in Table 4-20.

There is very little change from these plots (Fig.4-22, Fig.4-23, and Fig.4-24) and Table 4-19 compared with the initial plots (Fig.4-7, Fig.4-8, and Fig.4-9) and Table 4-10. The K-S tests for pellet-effect corrected permeability show the same p values for all pairs of lithofacies except for LF4 and LF5 that suggests statistically slightly more similar between LF4 and LF5 ($p = 0.014$) than the initial LF4 and LF5 ($p = 0.009$). Both permeabilities of LF4 and LF5 after correction for pellet effect are still distinctive to those of LF3 and LF2 (Fig.4-23, Fig.4-24, and Table 4-20). Thus it could have very little effect on discriminating LF5 from LF4 (with about

2 % more similar). Overall with the effects of pellet, each lithofacies still has a distinct permeability distribution.

The permeability corrected with the effect of pellet (Table 4-19) along with corresponding porosity values (Table 4-9) will be employed as hydraulic properties for synthetic fluvial channel systems in which solute transport will be modelled (Chapter 6).

Table 4-19. Mini-permeameter intrinsic permeability with the effects of pellets (pellet size of 0.2 by 0.2 by 0.1 cm; pellet densities: 2.8% for LF4 and 3.9% for LF5), with equivalent hydraulic conductivities at 20° C.

LF	No. of point	Min m^2 (m/d)	Max m^2 (m/d)	Arithmetic mean m^2 (m/d)	Geometric mean m^2 (m/d)	Median m^2 (m/d)	Std. dev m^2 (m/d)	IQR m2 (m/d)		Distribution
								Q1	Q3	
LF1*	42	$1.1x10^{-18}$ ($9.0x10^{-7}$)	$5.8x10^{-17}$ ($4.9x10^{-5}$)	$7.1x10^{-18}$ ($6.0x10^{-6}$)	$4.2x10^{-18}$ ($3.6x10^{-6}$)	$3.6x10^{-18}$ ($3.0x10^{-6}$)	$1.0x10^{-17}$ ($8.4x10^{-6}$)	$2.1x10^{-18}$ ($1.8x10^{-6}$)	$7.5x10^{-18}$ ($6.4x10^{-6}$)	lognormal
LF2	17	$1.1x10^{-15}$ ($9.6x10^{-4}$)	$1.1x10^{-14}$ ($9.3x10^{-3}$)	$4.0x10^{-15}$ ($3.3x10^{-3}$)	$3.0x10^{-15}$ ($2.5x10^{-3}$)	$2.9x10^{-15}$ ($2.5x10^{-3}$)	$3.0x10^{-15}$ ($2.5x10^{-3}$)	$1.4x10^{-15}$ ($1.2x10^{-3}$)	$6.0x10^{-15}$ ($5.0x10^{-3}$)	lognormal
LF3	349	$1.6x10^{-15}$ (0.001)	$3.7x10^{-13}$ (0.311)	$3.8x10^{-14}$ (0.032)	$2.3x10^{-14}$ (0.019)	$2.3x10^{-14}$ (0.019)	$4.2x10^{-14}$ (0.035)	$1.2x10^{-14}$ (0.010)	$4.8x10^{-14}$ (0.041)	lognormal
LF4	328	$2.1x10^{-15}$ (0.002)	$4.8x10^{-13}$ (0.409)	**$8.1x10^{-14}$ (0.068)**	**$4.7x10^{-14}$ (0.040)**	$4.8x10^{-14}$ (0.041)	$9.2x10^{-14}$ (0.077)	$2.3x10^{-14}$ (0.019)	$9.6x10^{-14}$ (0.081)	Neither normal nor lognormal
LF5	32	$7.5x10^{-15}$ (0.006)	$5.2x10^{-13}$ (0.439)	**$1.2x10^{-13}$ (0.100)**	**$8.8x10^{-14}$ (0.074)**	$9.8x10^{-14}$ (0.083)	$1.1x10^{-13}$ (0.095)	$4.2x10^{-14}$ (0.035)	$2.1x10^{-13}$ (0.176)	lognormal

** data from Curião (unpublished data 2002)*
Q1, Q3: first and third quartile respectively
IQR: interquartile range (i.e. Q3 – Q1).

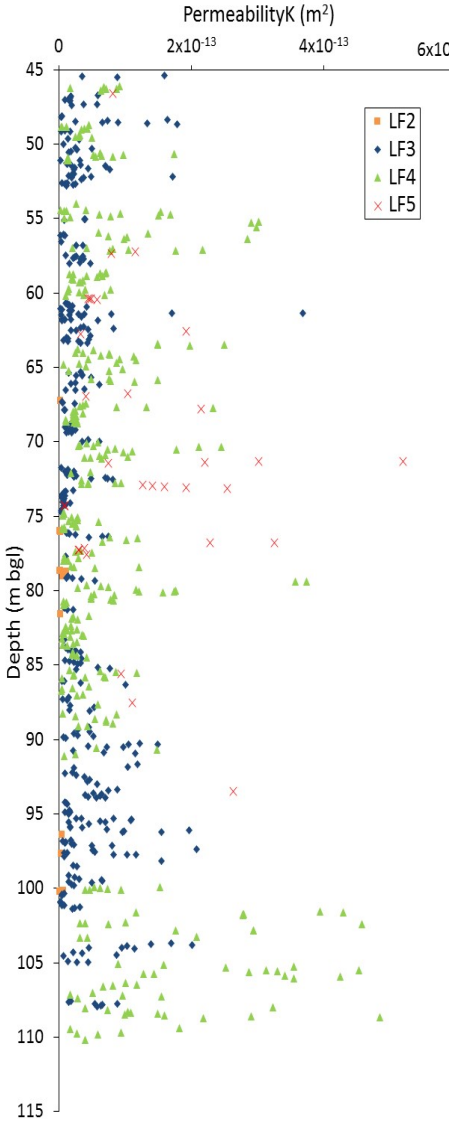

Fig.4-22. Permeability with the pellet effects and lithofacies varying with depth.

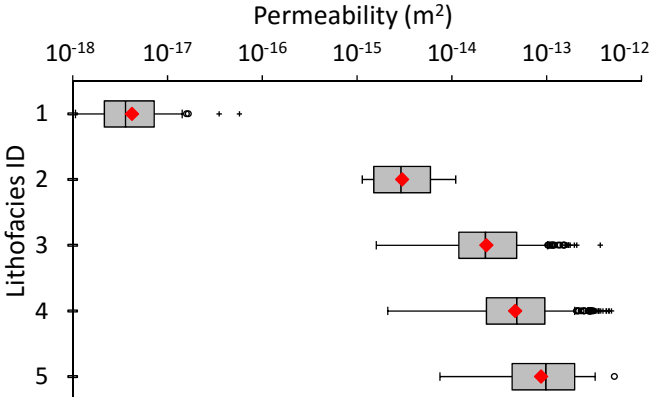

Fig.4-23. Box and whisker plots of Preston lithofacies versus permeability with pellet effects. Uprights, left to right, are: minimum; lower quartile, geometric mean, median, upper quartile, and maximum.

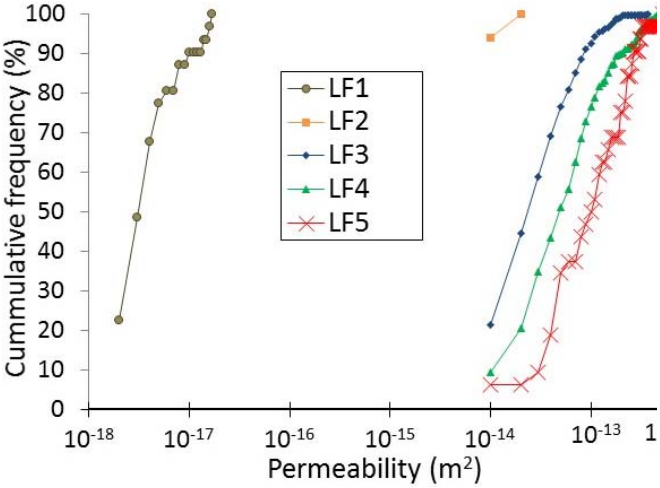

Fig.4-24. Cumulative frequency distribution of pellet-effect accounted permeability of lithofacies.

Table 4-20. Kolmogorov-Smirnov test results on the intrinsic permeability variation with lithofacies before and after accounting for the effects of pellet.

p values									Numbers of point	Distribution
	Without effects of pellet				With effects of pellet					
LF	2	3	4	5	2	3	4	5	31	Lognormal
2	-	0.000	0.000	0.000	-	0.000	0.000	0.000	17	Lognormal
3		-	0.000	0.000		-	0.000	0.000	349	Lognormal
4			-	0.009			-	0.014	328	Neither normal nor lognormal
5				-					32	Lognormal

4.5 Conclusions

The aim of this chapter has been to determine the strengths of correlation between hydraulic properties of a fluvial sandstone sequence as the first step in attempting to develop better approaches for predicting solute transport in such sequences.

A 60 m sandstone aquifer sequence has been investigated and shown to consist of a sequence of fluvial lithofacies (LF) with fining-upwards structure typical of many braided river systems (LF5 channel lag; LF4 and 3 channel fill higher energy; LF2 channel fill lower energy; LF1 low energy (mudstone)). Examination of its hydraulic properties has found that:

- There is a correlation between LF and porosity, LF and permeability, and LF and the ratio of permeability to porosity at 95 % confident level (99% if the effect of mudpellets on permeability are ignored).
- Only LF4 and LF5 were affected by pellets with resulting reductions in permeabilities by 6 % and 8 % respectively, leading to statistically slightly more similar between LF4 and LF5.
- The porosity of the two coarsest LF cannot be distinguished, and neither can LF3 from LF2

- Though each LF has a distinctive distribution of permeability, the permeability ranges overlap significantly in the three coarser LFs, a feature thought to be exaggerated by the small scale of measurement of the main technique employed (mini-permeametry); the finer two LF are associated with significantly lower permeability values. The permeability overlap could also be caused by the broad classification employed to describe lithofacies (e.g. some overlap in grain sizes of the three coarser lithofacies).
- The permeability/porosity ratio distributions for LF3 can be distinguished from those of LFs 4 and 5, but LFs 4 and 5 are less distinct, and too few data exist to determine differences involved with LFs 1 and 2, though the differences in permeability suggest that they would have been distinctive.

The LF units do not show an obvious trend in occurrence with depth, but do have a cyclicity that therefore is reproduced in the hydraulic property variation with depth. Some care was taken to define the LF appropriately, and this seems to be important: another set of definitions based on a much less detailed examination of the sequence resulted in little if any correspondence between LF and hydraulic properties.

These findings support those of Moran (2008) who reported on the initial phase of this study, and of Bloomfield et al. (2006) for a similar aged English but aeolian-fluvial dominated sequence. This suggests that such correlations are likely to be commonly found. If so, they could form the basis for improving prediction of solute transport in groundwaters provided LF can be determined, using the property structures deduced to bias stochastic modelling for example. The main properties used in the LF definitions (matrix grain size, sedimentary structure types, and presence of mudclasts and pebbles) are amenable to geophysical logging approaches, especially if optical televiewer equipment is available.

CHAPTER 5

PERMEABILITY CONFIGURATION AT OUTCROP SCALES

5.1 Introduction

An effective approach to understanding heterogeneity of the subsurface porous media is to study an outcrop 'analogue'. Outcrop studies provide insights to conceptualize aquifer heterogeneity (Davis, 1994). Outcrop studies for heterogeneity using geostatistics have been carried out by many workers (e.g. Goggin et al., 1988; Kittridge et al., 1990; Dreyer et al., 1990; Davis, 1994; Kupfersberger and Deutsch, 1999; Brian and Christopher, 2000; McKinley et al., 2004; McKinley et al., 2011).

In this chapter, outcrop scale studies of heterogeneity were undertaken at two sites where the two most frequent depositional environments of the English Permo-Triassic sandstone sequences, fluvial and aeolian, were present. Fluvial sandstone sequences were studied at the Wolverley sandstone outcrop at Wolverley village, Worcestershire, and aeolian sandstones were examined at the Bridgnorth sandstone outcrop at Bridgnorth, Shropshire, England. At each site, the relationship between observed sedimentary features and permeability was assessed. The following section describes the methods used.

5.2 Methods

5.2.1 Introduction

Outcrop-scale studies of the heterogeneous nature of sandstone involves firstly understanding the depositional system at the site, then mapping the sedimentary features and permeability, and finally correlating the sedimentary features or depositional processes with the permeability values collected (Davis, 1994). The following sub-sections describe in detail the methods used in the three stages.

5.2.2 Mapping sedimentary structures at outcrop

The Wolverley and Bridgnorth sandstone outcrops are already briefly mentioned in Chapter 3. From these descriptions, the detailed sedimentary characteristics of the two outcrop were mapped using photographs.

The Wolverley outcrop is about 3 m high by about 3.5 m wide (Fig.5-1a,b). At the Bridgnorth site, two nearby outcrops were investigated and marked as Site 1 and Site 2. Site 1 is about 2.8 m high by 6 m wide (Fig.5-7). Site 2, which is about 3 m distant from Site 1, is 3 m high by 4 m wide (Fig.5-9).

At each outcrop face, lithofacies (or sublithofacies) were defined on basic sedimentological features such as grain size, sorting, and sedimentary structures (stratification characteristics and bounding surfaces).

5.2.3 In situ measurement of permeability using an air mini-permeameter

In situ permeability was obtained from the sites using the air mini-permeameter described in Chapter 2. The work was undertaken on a sunny day in order to minimize the moisture effects on permeability measurements (Chapter 2 and Chapter 4). Prior to the in situ measurements of permeability, the outcrops were gently cleaned of surface coatings using a wire brush.

At the Wolverley outcrop, two lines, Line 1 and Line 2, were subjected to air permeability measurements (Fig.5-1b). There were nine points of permeability measurements on Line 1 and 46 points on Line 2 (Fig.5-1b, and Fig.5-2a,b). The points for permeability measurement were located to capture vertically all lithofacies present.

At the Bridgnorth outcrop, a total of 51 permeability measurements were made at Site 1 (Fig.5-7), and 19 at Site 2 (Fig.5-9).

For each measured point, three to five permeability readings were made, and the geometric mean was taken as the representative permeability value. Values of measured permeabilities using the air mini-permeameter for each site were compared with permeability values derived from conventional methods used for available core plug samples and with permeability for the same formations from literature (Chapter 3).

Using the mini-permeameter in the field is more difficult than in the laboratory as the seal between tip and rock is determined by the operator using a rifle-like should attachment rather than a fixed stress determined by a loading jig (Chapter 2). The operator has to make sure that enough force is applied and that the direction of the force is appropriate. With practice and by careful observation of the apparent permeabilities, repeatable values were obtained (typically ±5%).

5.2.4 Statistical analysis

It is hypothesized that each population (lithofacies) has a different permeability distribution. To test this hypothesis, Kolomogrov-Sminov (K-S) tests (Kirkman, 1996) were applied. The K-S test is based on comparisons of expected and observed relative frequencies to determine differences between two populations. The K-S test is non-parametric, thus no assumption about population was required prior to the comparisons.

For each outcrop, K-S tests were performed by estimating the probability distribution from the measured permeability datasets, then comparing the difference between two populations (lithofacies) for each value of permeability datasets. The maximum difference is then compared to a critical value based on the significant level and number of samples in each population. A p value was used to assess the difference between two populations; smaller value of p indicates a lower chance for two populations to come from the same distribution.

Spatial variations of permeability were characterized using a variogram estimator (Davis, 1994). The experimental variogram, γ, is already defined by Equation 4-3 (Chapter 4).

The experimental variogram can be fitted by a mathematical model which is referred to as the variogram model, the parameters of which are: range (or correlation length); sill; nugget; and 'hole'. The range is the distance at which the variogram no longer increases. The sill is the maximum value of the variogram and, for stationary processes, it is equal to the variance of the population. A nugget expresses the spatial variation at a scale which is finer than the minimum sample spacing (Deutsch and Journel, 1998) or within the error of measurement (McKinley et al., 2011). A 'hole' is produced by a repetitive structure within the dataset.

For the Wolverley site, the variogram was estimated and fitted with a model in the vertical direction for logarithm base 10 of permeability measured along Line 2. For the Bridgnorth site, directional variograms were estimated and modelled for Site 1, and a vertical variogram estimated at Site 2. All experimental and modelled variograms were simulated using the geostatistics computer software WinGlib (http://www.statios.com/wingslib/; Deutsch and Journel, 1998).

All original data for the in situ measurements of permeabilities and Kolomogrov-Sminov tests can be found in Appendix 2 and Appendix 3 respectively.

5.3. Wolverley sandstone outcrop

5.3.1 Introduction to the site

The Wolverley sandstone outcrop is located in the carpark of the Queen Head Pub, in Wolverley village, Worcestershire (National Grid Reference SO 82726 79405). The outcrop is 12-15 m high by 50 m long with a 'house' dug into it (Fig.5-1a). The geological features of are described in Chapter 3. The sequence consists of reddish brown, greyish brown, fine- to coarse-grained sandstones with pebbles of various sizes up to 10 cm long. Sedimentary structures include horizontal bedding, plane and cross-lamination, cross-stratification, and multichannel structures. The sandstones are of the Kidderminister Formation that is interpreted as being deposited under fluvial systems (e.g. Tyler-Whittle et al., 2002), probably by high-energy braided river systems.

5.3.2 Sedimentary mapping

Fig.5-2a,b show the sedimentary feature interpretation, and Table 5-1 summarizes the lithofacies descriptions and interpretations.

A total of six lithofacies were defined in the study outcrop: FA, FB, FC, FD, FE, and FF (Fig.5-2b, and Table 5-1). Sandstone sequences occurs throughout this outcrop and is described in detail as the six lithofacies (Table 5-1).

The outcrop probably has representatives of four sandstone cycles, but only one (the upper) is close to complete, including a channel lag, channel fill, and standing water body deposit.

Table 5-1. Summary lithofacies description at the Wolverley sandstone outcrop.

Lithofacies code	Lithofacies description	Thickness (m)	Interpretation	Location and number of measurements
FA	Coarse- to very coarse-grained, pebbly sandstone, no lamination, lots of pebbles	0.1-0.15	Uppermost channel lag	Line 2: 43, 44
FB	Very fine- to fine-grained, laminated sandstone, probably deposited from suspension from standing water body	0.2	Standing water body	Line 2: 33,34,42
FC	Medium- to very coarse-grained, planar or low angle-cross-bedded sandstone, some pebbles	0.6-0.8	Upper channel fill	Line 2: 35-40
FD	Coarse- to very coarse-grained, pebbly sandstone, no lamination, some pebbles	0.15	Upper channel lag	Line 1: 9 Line 2: 29, 41, 45, 56
FE	Medium- to coarse-grained, planar and cross-bedded sandstone, occasional pebbles	0.5	Middle channel fill	Line 1: 4, 5, 6, 7, 8 Line 2: 24-32
FF	Fine- to medium-grained, faint structure or low angle cross bedding sandstone, occasionally pebbles	> 1.2	Lower channel fill	Line 1: 1-3 Line 2: 1-23

5.3.3 In situ measurements of mini-permeability and geostatistical analysis of the measured permeabilities

Permeabilities derived from the mini-permeameter along Lines 1 and 2 (Fig. 5-2b) vary by about 4 orders of magnitude, ranging from about 4 mD (about 0.003 m/d at 20^{o}C) to about 8200 mD (6.8 m/d), with a geometric mean of 483 mD (0.4 m/d), interquartile range (IQR) from 191 mD (0.16 m/d) to 1696 mD (1.41 m/d) (Table 5-2). The measured permeability values are in agreement with the range reported by Allen et al. (1997) for the Kidderminster Sandstone Formation (Chapter 3).

There is an upward increase in permeability in the outcrop except for FB (Fig.5-3a,b) which has the lowest permeability with a geometric mean of about 12 mD (0.009 m/d). This is due to the very fine-grained, laminated sandstone of lithofacies FB. FA, as expected for the uppermost channel lag, has the highest geometric mean (5002 mD (4.17 m/d)), but the maximum individual values (8193 mD, about 6.83 m/d) was measured for FD, the upper channel lag. Permeability increases upwards from FF, the lower channel fill, to FE, the middle channel fill, and to FC, the upper channel fill, with geometric means of 279 mD (0.23 m/d), 969 mD (0.81 m/d), and 2676 mD (2.23 m/d) respectively (Table 5-2 and Fig.5-3a,b). The permeabilities follow neither normal nor log-normal distribution.

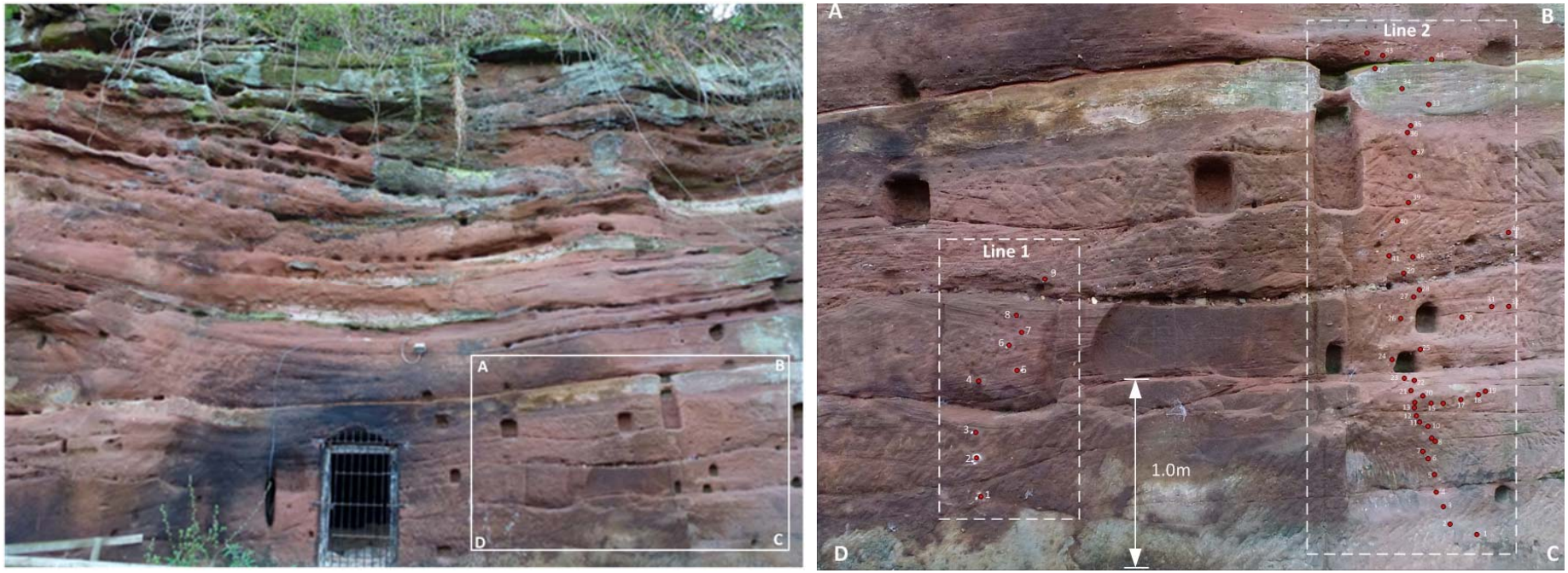

a) b)

Fig.5-1. Outcrop faces showing fluvial sandstones of the Kidderminster Sandstone Formation: a) The overall outcrop face with the 'rock house' dug in side; the house gate is about 2.5 m high, and the location of detailed study (the rectangle ABCD); b) Detailed study area (ABCD in a)) and location of points for the air permeability measurements.

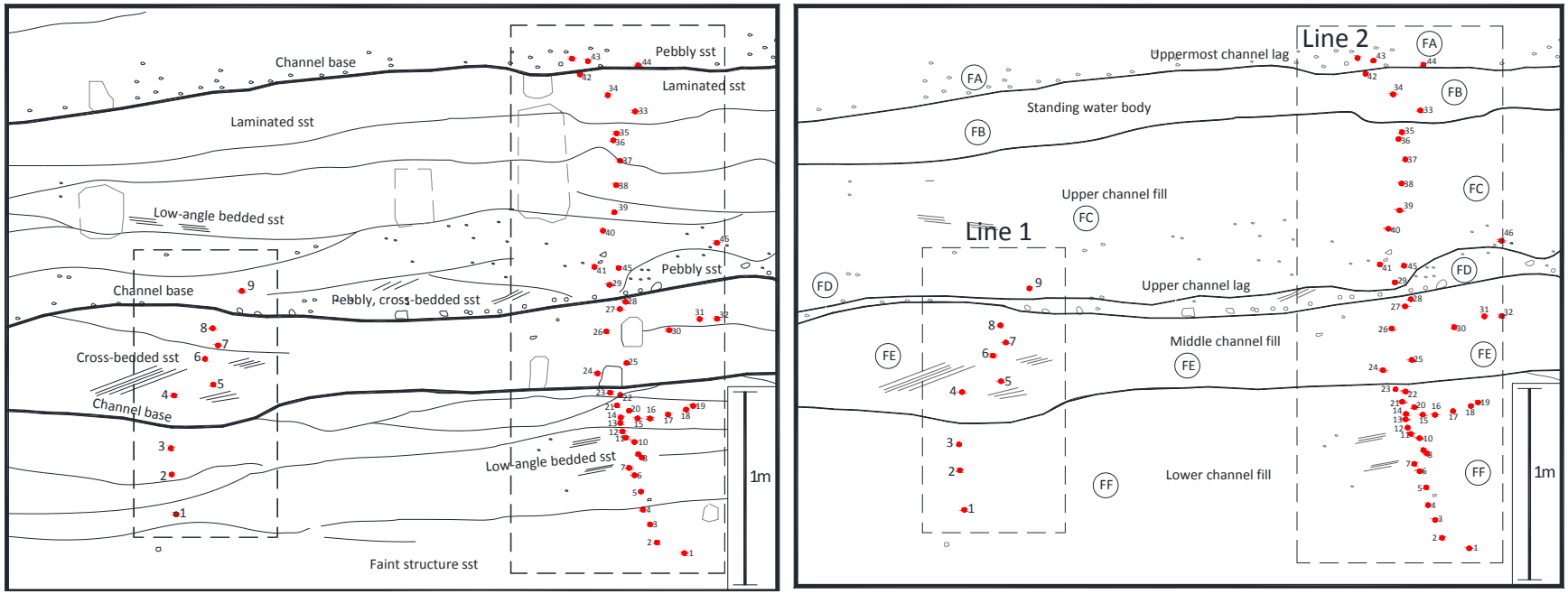

a) b)

Fig.5-2. Sketches of the detailed study outcrop (ABCD rectangle in Fig.5-1): a) Lithological features and the two subvertical lines for measurements of air permeability; b) Interpretation sedimentary features with lithofacies codes FA: coarse- to very coarse-grained, pebbly sandstones; FB: very fine- to fine-grained, laminated sandstones; FC: medium- to very coarse-grained, planar or low-angle cross-bedded sandstones; FD: coarse- to very coarse-grained, pebbly sandstone with some pebbles; FE: medium- to coarse-grained, planar or cross-bedded sandstones; FF: fine-to medium-grained, faint structure sandstones.

Table 5-2. Statistics of permeability measured by mini-permeameter at the Wolverley outcrop.

LF code	Num.	Min mD (m/d)	Max mD (m/d)	Mean* mD (m/d)	Median mD (m/d)	Std. dev mD (m/d)	IQR mD (m/d)		Distribution
							Q1	Q3	
FA	4	3777 (3.15)	6629 (5.52)	5002 (4.17)	5199 (4.33)	1645 (1.370	3777 (3.15)	6624 (5.52)	NA
FB	10	4.1 (0.003)	41.3 (0.034)	12.4 (0.01)	11.2 (0.009)	12.9 (0.011)	6.9 (0.006)	25.4 (0.021)	Log normal
FC	10	1193 (0.99)	4826 (4.02)	2676 (2.23)	2526 (2.10)	1200 (1.00)	2108 (1.76)	4043 (3.37)	Normal and log normal
FD	17	1107 (0.92)	8193 (6.83)	2095 (1.75)	1815 (1.51)	2093 (1.74)	1483 (1.24)	2154 (1.79)	Neither normal nor log normal
FE	44	234 (0.19)	2925 (2.44)	969 (0.81)	972 (0.81)	647 (0.54)	607 (0.51)	1759 (1.47)	Log normal
FF	83	37 (0.03)	7639 (6.37)	279 (0.23)	218 (0.18)	1090 (0.91)	124 (0.10)	581 (0.48)	Neither normal nor log normal
All LFs	168	4.1 (0.003)	8193 (6.83)	483 (0.40)	592 (0.49)	1503 (1.25)	191 (0.16)	1696 (1.41)	Neither normal nor log normal

Mean: geometric mean*
Std. dev: standard deviation
Q1, Q3: first and third quartile respectively
IQR: interquartile range (i.e. IQR = Q3 – Q1)
All LFs: combination of all the lithofacies
m/d: equivalent conductivities at 20°C.

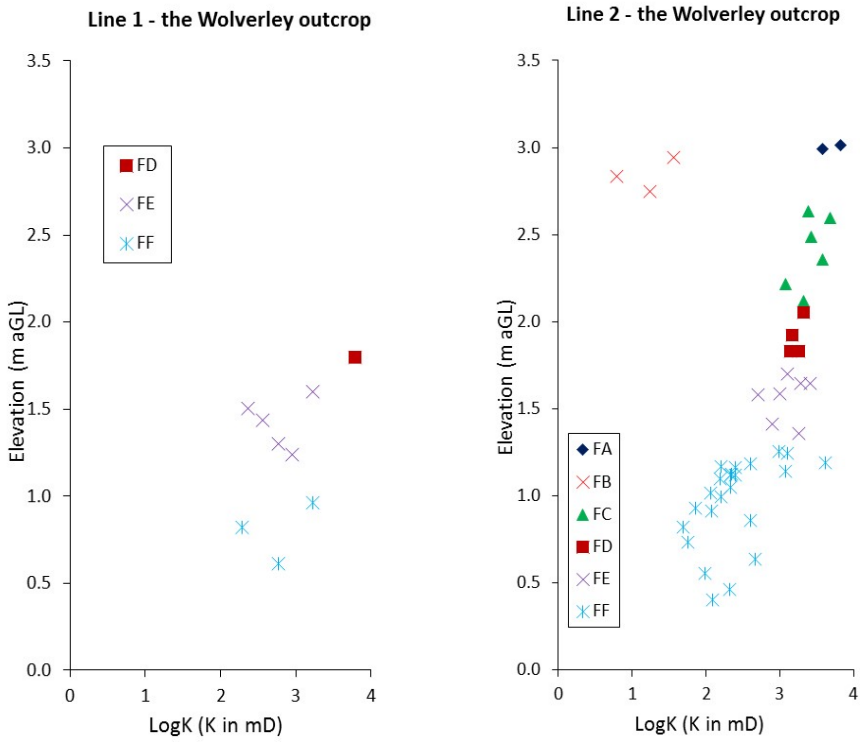

a) b)

Fig.5-3. Plots of log-transformed permeability (permeability in mD) versus elevation (depth) as function of lithofacies at the Wolverley sandstone outcrop: a) at Line 1; b) at Line 2.

Table 5-3. Summary of grain size, pebble present and permeability as function of lithofacies.

Lithofacies code	Grain size	Pebble present	Geomeytric mean permeability mD (m/d)
FA	Coarse to very coarse	lots	5002 (4.17)
FB	Very fine to fine	no	12.4 (0.010)
FC	Medium to very coarse	some	2676 (2.23)
FD	Coarse to very coarse	some	2095 (1.75)
FE	Medium to coarse	occasionally	969 (0.81)
FF	Fine to medium	occasionally	279 (0.23)

Box and whisker and cumulative frequency plots of the log-transformed permeabilities for the lithofacies are shown in Fig.5-4 and Fig.5-5. Except for FB whose permeability values are far below those of the other lithofacies, permeability values gradually increase upward from FF to FA. FF shows the widest range in permeability, whereas FA appears with the narrowest range. Q3 (seventy-fifth percentile) permeability value of FF is equal to Q1 (twenty-fifth percentile) of FE whose Q3 is similar to medium values of FD. Q3 of FD is similar to Q1 of FC whose Q3

is equal to Q1 of FA. Though there is some overlap between FE and FD, there is systematically increasing permeability from FF (the lowest channel bottom with finer grain) to FA (uppermost channel lag with coarsest grain) (as seen with Fig.5-3 a,b) with a "quartile step" seen for each successive lithofacies. A similar trend was also seen at the Preston Laundry borehole core (Chapter 4). This, thus, along with distinct permeability distribution for FB suggests that each lithofacies has a distinct permeability distribution.

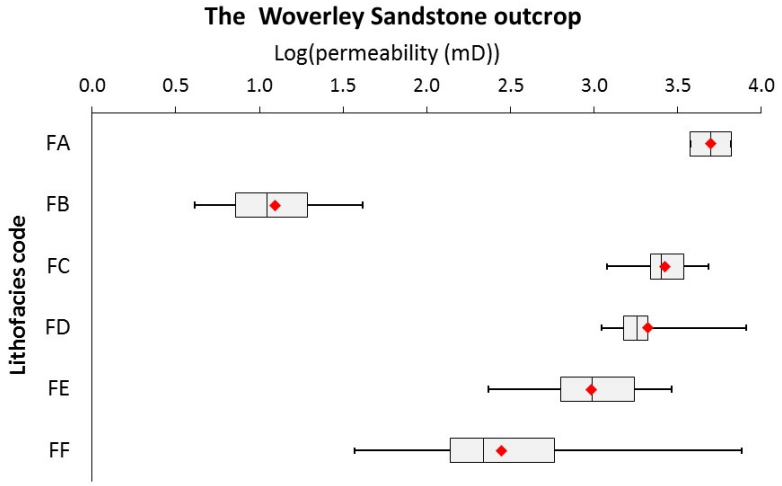

Fig.5-4. Box and whisker plots of Wolverley lithofacies versus log-transfered permeability (permeability in mD).

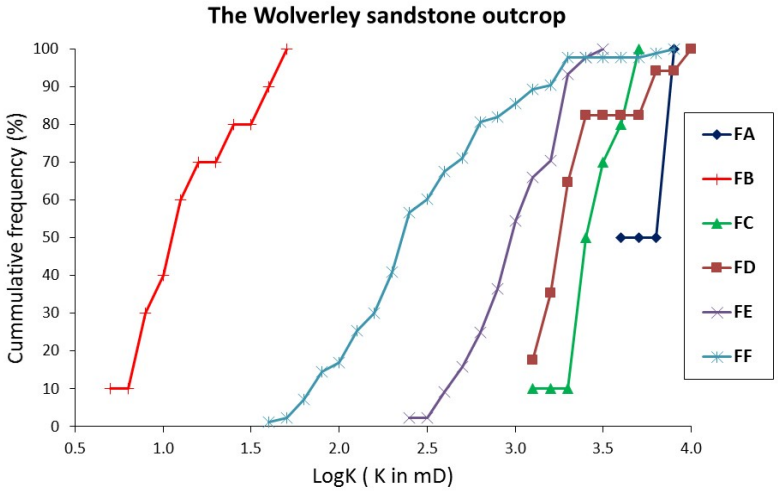

Fig.5-5. Cumulative frequency distribution of log-transferred permeabilities of the lithofacies.

Results for the Kolmogorov-Smirnov (K-S) tests which statistically determine whether permeabilities for two lithofacies come from the same population are summarized in Table 5-

4. No K-S test relating to FA was made because of insufficient numbers of measurements. Since almost all p values are zero to 3 decimal places (Table 5-3), permeability for each lithofacies is consistent with coming from different populations at 95% confidence level. This confirms that permeability distribution for each lithofacies is distinct. However, it is noted that number of samples for FB (10), FC (10), FD (17) are relatively small compared with those for FE (44) and FF (83). The distinct permeability distribution for each lithofacies suggests the importance of sedimentary features, particularly grain size, and occurrence of pebbles in controlling permeability of the sandstone sequences (Table 5-3).

Table 5-4. Kolmogorov-Smirnov test results on the permeability variation with lithofacies.

Lithofacies code	p values						Number of measurement
	FA	FB	FC	FD	FE	FF	
FA	-	NA	NA	NA	NA	NA	4
FB		-	0.000	0.000	0.000	0.000	10
FC			-	0.011	0.000	0.000	10
FD				-	0.000	0.000	17
FE					-	0.000	44
FF						-	83

The vertical variogram estimation for Line 2 is presented in Fig.5-6. The experimental variogram was fitted by a spherical-type model that has a sill (variance) of 0.48 and a range (correlation length) of 0.2 m. Some ‘holes’ at lag distances of 0.13, 0.5, 0.85, and 0.95 m are seen. The range (0.2 m) reflects permeability correlation estimation within beds. Note that the range is similar to the thickness of the most permeable lithofacies: FC and FA (about 0.15 m) and least permeable lithofacies FB (0.2 m). From 0.2 to 0.8 m lag there will be some comparison from bed to bed, but still mainly within one bed as FE and FF which dominate in term of numbers are 0.5-1.2 m thick. At lag distance of 0.8 m and beyond, there is general increase in gamma, suggesting that almost all pairs of measurements will be across beds. No variogram

was estimated for the Line 1 because of insufficient numbers of measured points on the line.

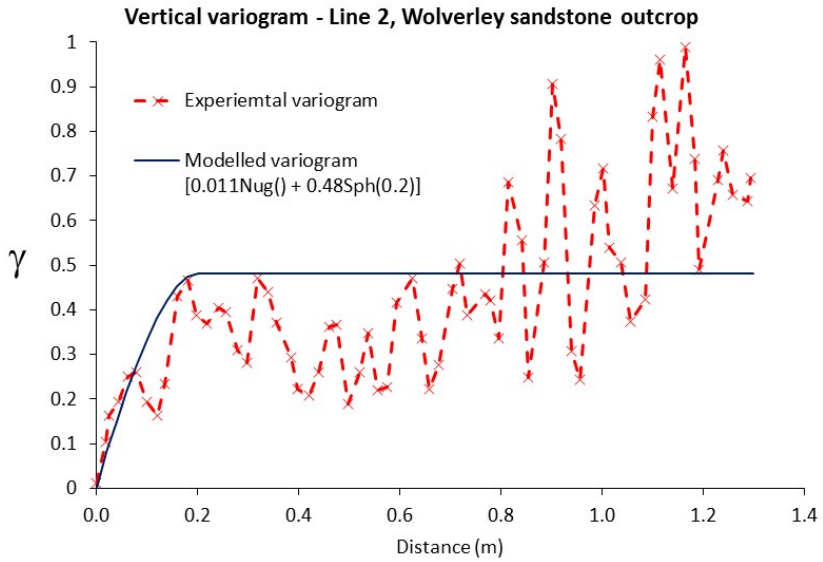

Fig.5- 6. Vertical experimental and best fitted variogram model of log-transformed permeabilities (permeability in mD) measured at Line 2, Wolverley outcrop.

5.3.4 Limitations

There are limitations to the in situ air permeability measurements at the Wolverley sandstone outcrops.

A shortage of permeability data prevent estimation of a horizontal variogram and may cause some bias to the K-S tests. Although there had been sunny days before taking the measurements, the moisture contents of the sandstone were unknown and could have caused significant effects on the permeability measurements (Chapter 2 and Chapter 4). In situ measurement using an air mini-permeameter requires care from the operator as it is easy to cause gas leaking through inadequate sealing against outcrop face. Since the outcrop could not be sampled to do conventional tests, no checking of in situ measurements could be undertaken.

5.3.5 Conclusions and future work

An outcrop-scale study of sandstone heterogeneity was taken at the village of Wolverley where the sandstones are belong to the Triassic Kidderminster Sandstone Formation, and following conclusions were made.

At the study outcrop, fluvial sandstone units were mapped out, and the following six lithofacies were defined on the basis of sedimentary features: lower channel fill (FF); middle channel fill (FE); upper channel lag (FD); upper channel fill (FC); standing water body (FB); and uppermost channel lag (FA) deposits. These lithofacies probably represent three channel sequences, of which only one is complete.

Permeabilities derived from the mini-permeameter are overall neither normally nor lognormally distributed. Permeability, as a whole, varies over about 4 orders of magnitude, ranging from 4 mD (equivalent to about 0.003 m/d at 20^{o} C) to about 8200 mD (6.8 m/d).

Statistical and geostatistical analyses show that permeability distribution for each lithofacies is distinct. Variogram analysis suggests that the correlation length reflects the within beds permeability estimation, and the correlation length is similar to the thickness of the most permeable lithofacies (FC and FA), and the least permeable lithofacies (FB). The variogram indicates the existence of some comparisons from bed, but still within bed to be at lag distance of 0.2 – 0.8 m, and across beds for lag distance of greater than 0.8 m.

Since a small number of permeability measurements were obtained for some lithofacies, geostatistical tests (K-S test and variogram estimations) may be not fully describe the sedimentary structures and environment at the study outcrop. Therefore, it is worth gaining

more in situ measurements, particularly along Line 1, and between Line 1 and Line 2. It would also be useful to collect enough data along the units to determine horizontal variograms. Collection of samples for conventional liquid permeametry, though potentially very useful, is not possible for aesthetic reasons.

5.4 Bridgnorth sandstone outcrop

5.4.1 Site introduction

The study outcrop is located in Hermitage area (National Grid Reference SO 727934) (Chapter 3). Two sub-sites, Site 1 (Fig.5-7) and Site 2 (Fig.5-9), were selected. The sandstones are of the Permian Bridgnorth Sandstone Formation. (Toghill, 1990; Benton et al., 2002; Smedley et al., 2005; Holloway, 1985). This Formation is unconformably overlain by the Kidderminister Formation (Chapter 3) which crops out at the Wolverley site described above.

The Bridgnorth Sandstone Formation is of aeolian dominated sediments, consisting of reddish brown, reddish orange, fine- to medium-grained sandstones. Sedimentary structures consist of large-scale planar and trough cross-stratification, horizontal stratification, lamination, and graded bedding (Toghill, 1990; Karpeta, 1990; Benton et al., 2002), with a hierarchy level of bounding surfaces (Benton et al., 2002). The Bridgnorth Sandstones are interpreted as being deposited by large-scale, crescentic barchan dunes with a prevailing wind from the east (Shotton, 1956). Karpeta (1990) identified 3 major aeolian facies associations for the Bridgnorth Sandstone Formation at and around the site, including: 1) “isolated transverse draa with superimposed oblique crescentic and linear dunes”; 2) “grouped barchanoid draa with superimposed oblique crescentic and linear dunes”; and 3) “sand sheets with isolated dome

dunes". The long term wind direction was from east and controlled the orientation of the draa. According to Karpeta (1990), winds from the north built up the orientation of the superimpose dunes and short-term winds may have created internal scour surfaces within the dune and draa foresets (Chapter 3). In this study, sandstones at the two sites of the Bridgnorth outcrop were lithologically described, and interpreted guided by the detailed work of Karpeta (1990).

5.4.2 Sedimentary mapping

Site 1 is about 2.8 m high by 6 m wide (Fig.5-7), and at 3 m distance is Site 2 which is 3 m high and 4 m wide (Fig.5-9). There are three lithofacies identified at the sites as sequence from base upward: F1 ("Facies A" in Karpeta, 1990), F2, and F3 ("Facies C" in Karpeta, 1990). Table 5-5 summaries the lithofacies description and interpretation.

Table 5-5. Summary lithofacies description at the Bridgnorth sandstone outcrop.

Lithofacies code	Lithofacies description	Thickness (m)	Interpretation	Location and number of measurements
F1	Fine- to medium- grained, tabular planar cross-stratified sandstones	0.5 - 1.7	Foresets of a large, solitary tranverse draa migrated westwards ("Facies A" in Karpeta, 1990)	Site 1: 19 points Site 2: 18 points
F2	Fine- to medium grained, trough cross-stratified sandstones	0.2- 0.9	Foresets of oblique crescentic dunes superimposed on the back of the tranverse draa and migrated the same direction (westwards) ("Facies C" in Karpeta, 1990)	Site 1: 13 points Site 2: 1 point
F3	Fine-grained, fine- to medium-grained, low angle cross-stratified, trough cross-stratified sandstones	0.3-0.9	Bottom sets of foresets of oblique crescentic dunes migrated southwards along the slipface of the tranverse draa ("Facies C" in Karpeta, 1990)	Site 1: 17 points

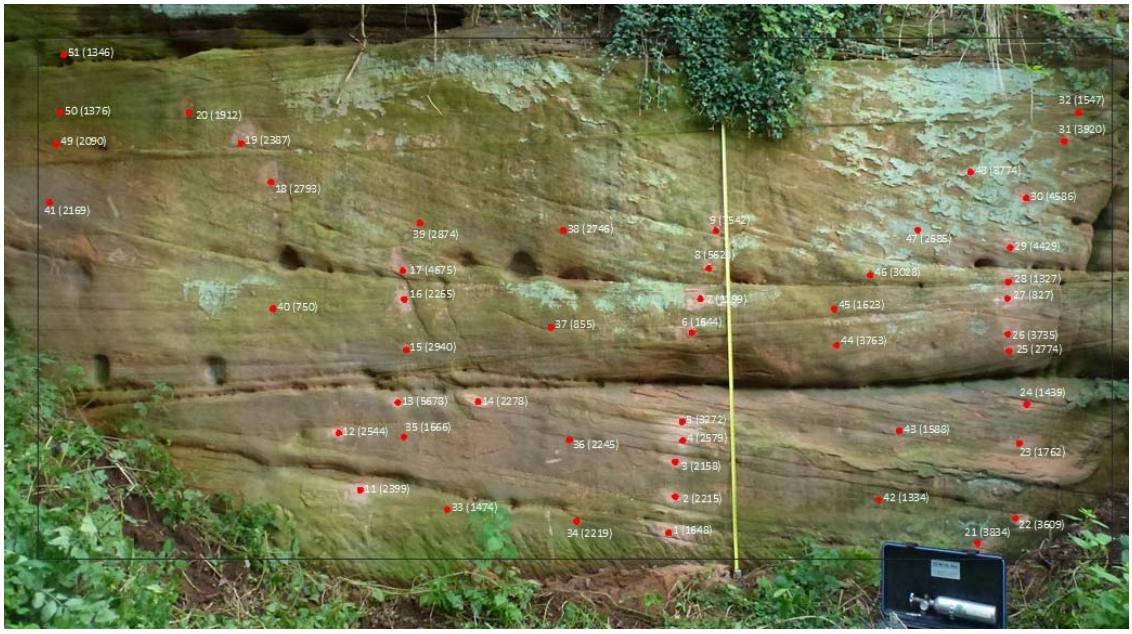

Fig.5-7. Photo of sandstone outcrop the Site 1 at the Bridgnorth Sandstone outcrop showing points (in red) of air permeability measurements and their values (in mD, in brackets). The measuring tape is 2.6 m high.

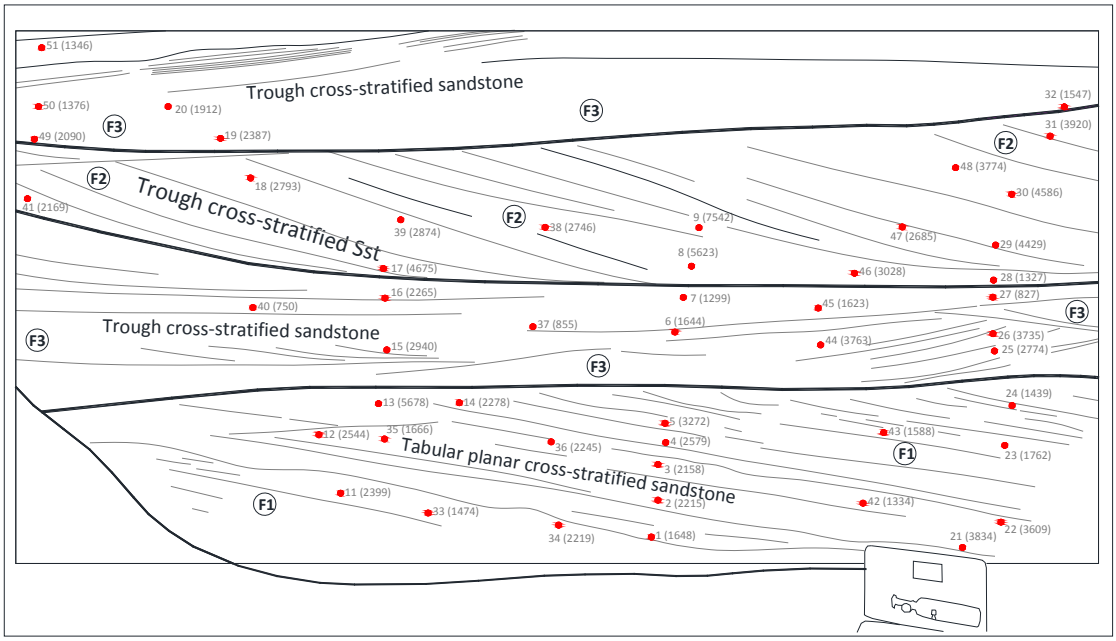

Fig.5-8. Sketch of cross-section at Site 1, showing locations for permeability measured with the air mini-permeameter and permeability values (in mD, in brackets), and sedimentary interpretations.

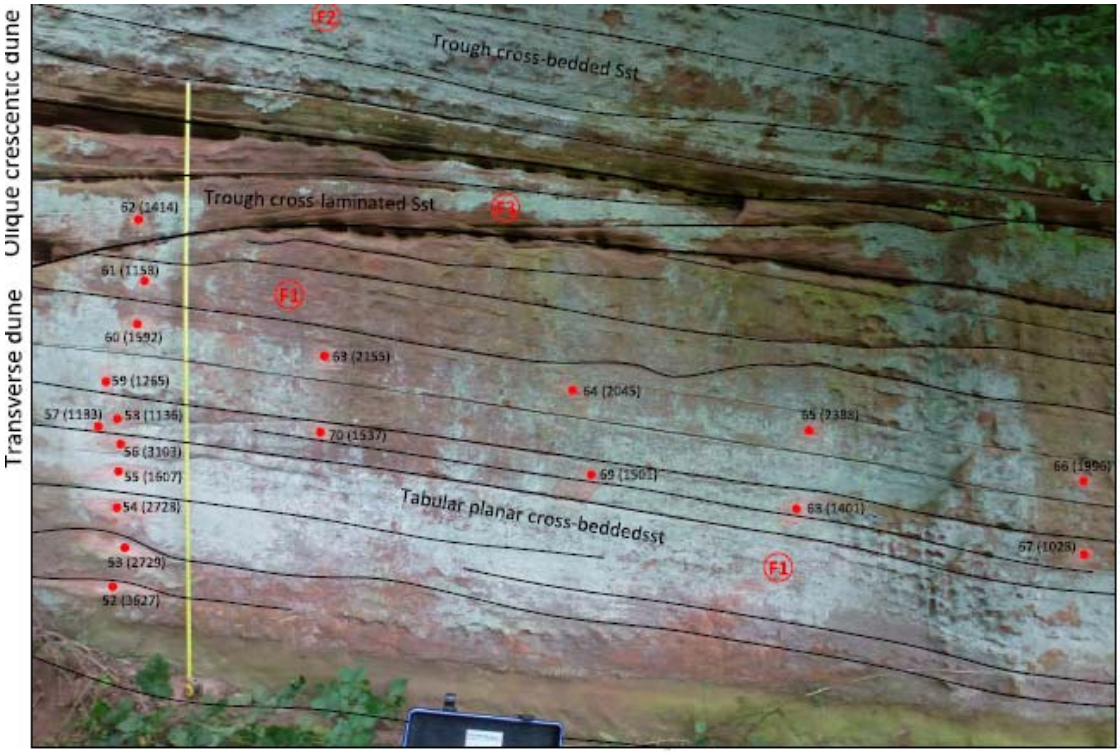

Fig.5-9. A photo of cross-section at Site 2 showing points of permeability measured with the air mini-permeameter and their values (in mD) in brackets, and interpretation of sedimentary structures. The measuring tape is 2.26 m high.

5.4.3 In situ measurement of air prmeability and geostatistical analysis of the measured permeabilities

A total of 51 measured points, with 254 measurements of permeability using the air mini-permeameter, were performed at Site 1 and 19 measured points, with 114 measurements, at Site 2. At Site 1, permeabilities were measured for all lithofacies with point locations and values shown in Fig.5-7 and Fig.5-8, whereas almost all measured permeabilities were undertaken on F1 at Site 2 as seen in Fig.5-9.

The measured permeabilities are summarized in Table 5-6 and Fig.5-10a,b. Overall, permeabilities vary over about an order of magnitude, ranging from 750 mD (equivalent to 0.62

m/d at 20ºC) to 5678 mD (4.73 m/d) with a geometric mean of 2266 mD (1.89 m/d), and interquartile range from 1606 mD (1.34 m/d) to 3150 mD (2.62 m/d). The permeabilities follow lognormal distributions. For Site 1 alone, F1 and F2 have quite similar ranges of permeability, while F3 shows a slightly narrower range.

Permeabilities measured with liquid falling head permeametry (Chapter 2) for core plug samples taken from the Bridgnorth Sandstone outcrop provided a permeability range from 0.63 m/d to 4.53 m/d, with a geometric mean of 1.74 m/d, and an interquartile range (IQR) from 1.1 to 3.6 m/d (Table 3.3 in Chapter 3), in agreement with the measurements obtained using the mini-permeameter at this site. The conductivities derived from the in situ measurement using the mini-permeameter are also broadly consistent with those reported by Allen et al. (1997) for the Bridgnorth Sandstone Formation in Shropshire with a range from 2×10^{-5} to 15 m/d, a geometric mean of 0.16 m/d, and interquartile range from 0.02 to 2.6 m/d (Chapter 3).

Box and whisker and cumulative frequency plots of logarithm base 10 of permeability (permeability in mD) as a function of lithofacies are shown in Fig.5-11 and Fig.5-12 respectively. F1 and F2 have similar maximum and minimum values. Their minimum values are roughly equal to the first quartile value (Q1) of F3. Q1 of F1 is similar to the median value (Q2) of F3. Generally, then, the permeabilities of F2 are greater than those of F1 and F3. F1 and F3 show some overlap (Fig.5-11). To test this, K-S tests were performed.

Table 5-6. Statistics of measured permeability at Site 1- the Bridgnorth outcrop.

LF code	Num.	Min mD (m/d)	Max mD (m/d)	Mean* mD (m/d)	Median mD (m/d)	Std. dev mD (m/d)	IQR mD (m/d)		Distribution
							Q1	Q3	
F1	19	1334 (1.11)	5678 (4.73)	2247 (1.87)	2219 (1.85)	1063 (0.89)	1648 (1.37)	2579 (2.15)	Log normal
F1*	18	1028 (0.86)	3627 (3.02)	1771 (1.48)	1600 (1.33)	754 (0.63)	1299 (1.08)	2330 (1.94)	Log normal
F1**	37	1028 (0.86)	5678 (4.73)	2001 (1.67)	2045 (1.70)	950 (0.79)	1488 (1.24)	2562 (2.13)	Log normal
F2	13	1327 (1.11)	5623 (4.69)	3224 (2.69)	3028 (2.52)	1189 (0.99)	2716 (2.26)	4508 (3.76)	Normal and log normal
F3	17	750 (0.62)	3763 (3.14)	1746 (1.46)	1644 (1.37)	930 (0.77)	1322 (1.10)	2580 (2.15)	Normal and log normal
All LFs**	49	750 (0.62)	5678 (4.73)	2266 (1.89)	2265 (1.89)	1188 (0.99)	1606 (1.34)	3150 (2.62)	Log normal

F1: permeability measured for lithofacies F1 at Site 2*
*F1**: combination of permeability measured for lithofacies F1 at Site 1 and Site 2*
*LFs**: Combination of permeabilities measured for all lithofacies at Site 1*
Mean: geometric mean*
Std. dev: standard deviation
Q1, Q3: first quartile (i.e. 25 %) and third quartile respectively
IQR: interquartile range (i.e. IQR = Q3 – Q1).

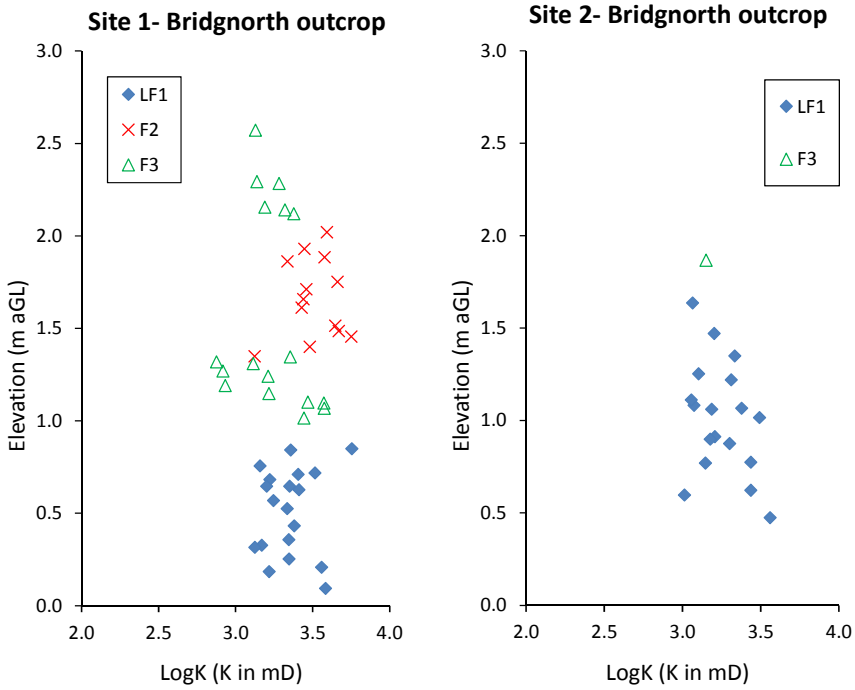

a) b)

Fig.5-10. Permeabilities (in mD) versus depths as function of lithofacies at the Bridgnorth Sandstone outcrop: a) at Site 1; and b) at Site 2.

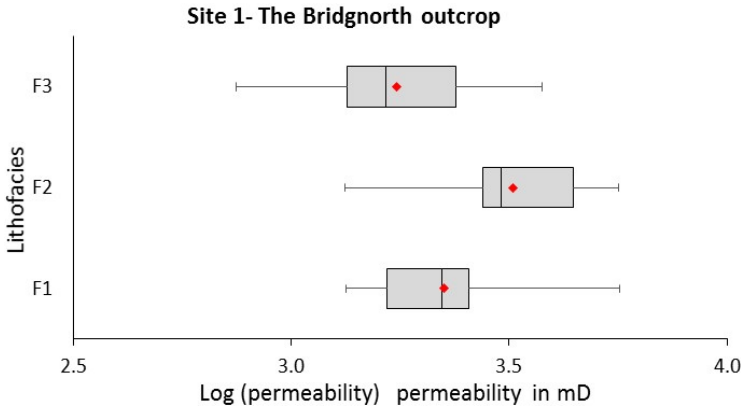

Fig.5-11. Box and whisker plot for log-transferred permeability as function of lithofacies at Site 1.

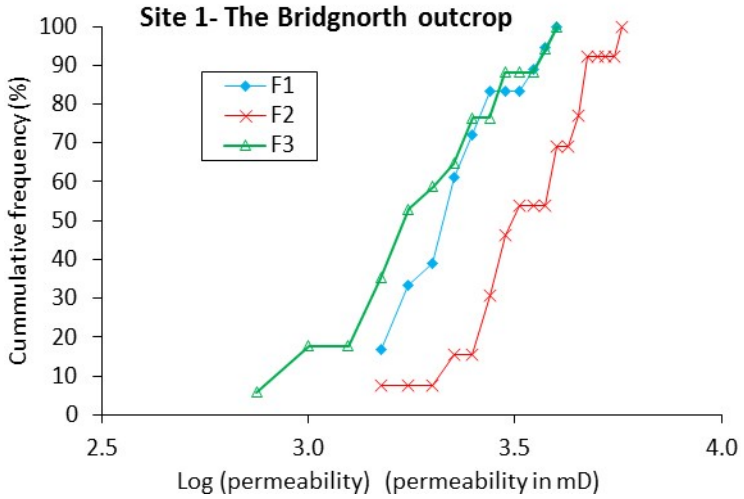

Fig.5-12. Cumulative frequency plot for log-transferred permeabilities as function of lithofacies at Site 1.

The results of these tests are given in Table 5-7. At 99% confident level, p values are small for F1 against F2: 0.002 for Site 1, and 0.000 for the combined data sets from the two sites, suggesting permeability distributions for F1 and F2 are distinct. A similar distinction is seen for F2 versus F3. However, a high p value (0.27) for F1 versus F3 for Site 1 suggests that F1 and F3 have quite similar permeability distributions. The chance that the permeability datasets

for F1 and F3 come from different populations decreases when data are combined from Site 1 and Site 2. This confirms the similarity between F1 and F3 as mentioned above.

Table 5-7. K-S test results on the permeability variation with lithofacies at Site 1.

Lithofacies code	p values				Number of measurement
	F1	F1**	F2	F3	
F1	-	-	0.002	0.265	19
F1**		-	0.000	0.744	37
F2			-	0.004	13
F3				-	17

*F1**: combination of permeability measured for lithofacies F1 at Site 1 and Site 2.*

Spatial variations of log-transformed permeability data sets were characterized at the Bridgnorth Sandstone outcrop. At Site 1, directional variograms were estimated and modelled for permeability variation in different directions: vertical (Fig.5-13a); perpendicular to the apparent lamination dip ('perpendicular'); (Fig.5-13b); horizontal (Fig.5-13c); and parallel with the apparent lamination dip ('parallel') (Fig.5-13d). Parameters for the best fit variogram models are summarized in Table 5-8. All directional variograms were fitted with spherical-type models with no nugget effect. The vertical and perpendicular directions show the shortest correlation lengths (0.2 m), whereas the horizontal and parallel directions have similar and longer correlation lengths (0.5-0.6 m). The greatest variability (0.06) is in the vertical direction, whilst the smallest variability (0.04) was calculated for the perpendicular direction.

For the vertical variogram, at lag distance of less than 0.2 m almost all pairs of measurement will be within one bed; at lag distance of 0.2-1.2m most pair will be between beds: for F1 and F2 or F1 and F3 so gamma will be high; beyond 1.2 m lag most pair will come to F1 and F3 so that gamma is low and creates a hole deep hole at 1.8 m distance. For the perpendicular variogram, it shows regular well-developed holes at distance of 0.3, 0.7, 1.5, and 2.1m. These

holes could reflect the thicknesses of the cosets of the inclined lamination (F1, F2) between reactivation surfaces (Fig.5-7). Note that the hole at 1.8 m lag almost disappears in the perpendicular data because of the change in the direction for variogram estimation. For the horizontal variogram, it shows within lithofacies estimation and seems like the range is rather greater, but the sill is slightly smaller than for the vertical variogram, and there are also well-develop holes. The parallel variogram shows relatively shallow holes. Note that the exceptional high gammas (0.08-0.09) appear in vertical, perpendicular, and parallel variogram probably from pairs between beds, but disappear in horizontal variogram where almost all pairs of measurements are within bed. The well-developed holes seen at perpendicular and horizontal data reflect the effect of the inclined lamination cosets (F1 and F2). The vertical and horizontal range reflect some parts of the continuity of the inclined laminae. The parallel and horizontal data are quite the same given the uncertainty. Though this result is expected, the continuity in even the parallel direction appears only slightly greater than in the vertical direction, probably because of the inclined lamination sets.

At Site 2, a variogram for lithofacies F1 (Fig.5-9) was calculated for the vertical direction (Fig.5-14, Table 5-8). Lack of permeability data prevented variogram estimations for other directions. The vertical variogram broadly continues to increase for greater lags (Fig.5-14). The variogram shows relatively low γ values and seems to have a correlation length of greater than 0.6 m, the greatest seen, with a nugget of 0 m, features consistent with one relatively homogeneous unit.

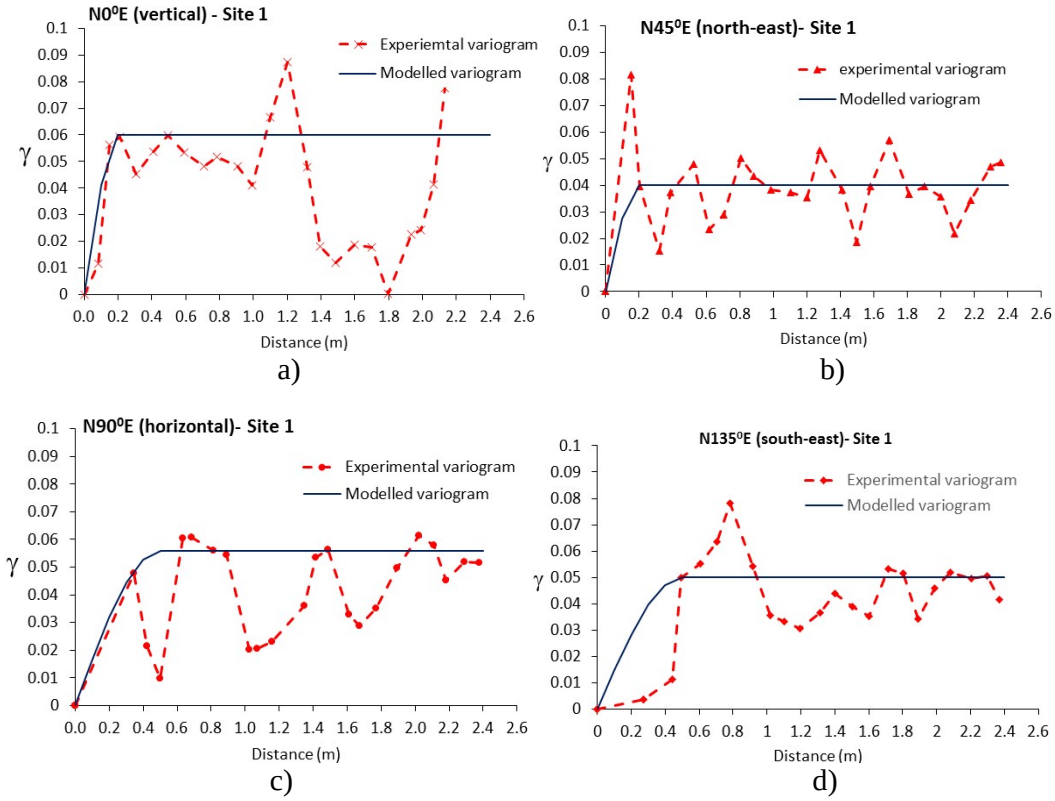

Fig.5-13. Directional experimental and best fitted variogram models of log-transformed permeabilities (permeability in mD) at Site 1: a) vertical, b) perpendicular to apparent lamination dip, c) horizontal, and d) parallel to apparent lamination dip.

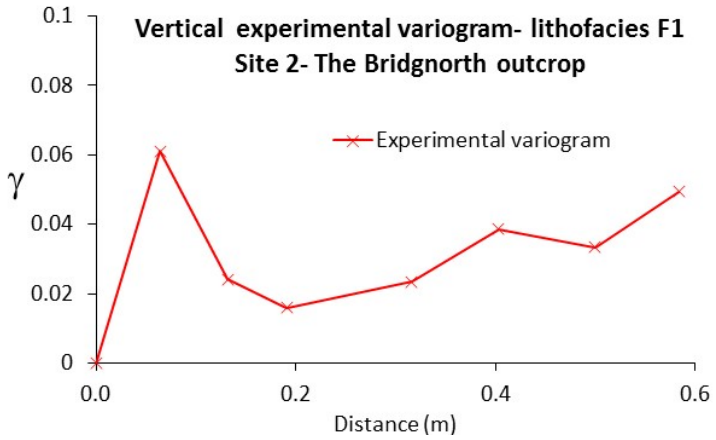

Fig.5-14. Vertical experimental variogram of log-transformed permeability (permeability in mD) at Site 2.

Table 5-8. Summary variograms for log-transferred permeability at the Site 1, Bridgnorth outcrop.

Direction	Parameters of the variogram models			
	Model type	Nugget (m)	Sill (variance)	Range (correlation length) (m)
Vertical	Spherical	0	0.06	0.2
Perpendicular	Spherical	0	0.04	0.2
Horizontal	Spherical	0	0.056	0.5
Parallel	Spherical	0	0.05	0.5

5.4.4 Conclusions and future work

The following are concluded:

Three lithofacies were mapped, and interpreted using Karpeta (1990) as the foreset of a large, solitary transverse draa (F1), the foresets of oblique crescentic dunes superimposed on the back of the transverse draa (F2), and bottom sets of foresets of oblique crescentic dunes migrating along the slip face of the transverse draa (F3).

In situ measurements of permeability with a mini-permeameter provides permeability datasets which are consistent with permeability measured by conventional method from core plug samples taken from the field and with previous published permeability values for the Bridgnorth Formation.

Statistical analysis on the measured permeabilities shows that the permeability distribution for F1 is distinct from F2, the same for F2 and F3, but the permeability distribution for F1 is weakly distinct from F3.

Variogram analysis shows the within bed and between beds variability of permeability. The hole effects reflect the repetitive features of the sets of the cross-stratified laminations. There is greatest variation and smallest ranges vertically and perpendicular to the lamination dip. However, the continuity parallel with the lamination dip is only slightly greater than that perpendicular to the lamination dip suggesting that in aeolian systems lateral continuity is limited.

At Site 2, the vertical estimation for F1 suggests relative homogenous characteristics for this unit.

5.5 Conclusions

The following conclusions can be made from the studies at the Wolverley and Bridgnorth outcrop:

The works were undertaken under non-ideal conditions as the outcrop surface were weathered and the moisture content was unknown. However, since having seen the differences that seems to be interpretable in most cases, and it suggests that these practical problems may not be dominating.

For the fluvial sandstones at the Wolverley outcrop, the lithofacies each has a distinct permeability distribution. Geostatistical analysis shows the within bed and between beds permeability structures with correlation length similar to thickness of the most and least permeable units.

For the aeolian sandstones at the Bridgnorth outcrop, the correlation between lithofacies and permeability do exist in some cases. Geostatistical analysis shows the greatest range and shortest continuity vertically and perpendicular were seen for the inclined laminated sets. Slightly different between continuity parallel and perpendicular forestest dip suggests continuity of aeolian systems is laterally limited.

It could not be guaranteed to obtain comprehensive comparison between fluvial and aeolian environment from only with these two sites, but it could be broadly seen that fluvial system is more consistent lateral continuity than aeolian system.

The result from at Wolverley outcrop is consistent with that from the study at Preston Laundry Borehole core (Chapter 4) that each sedimentary unit has a distinct, but some overlapping, permeability distribution. However, more field data on lateral variation is needed and, also for the Bridgnorth outcrop, means of cleaning and ideally drying surfaces are required to achieve best results.

CHAPTER 6

IMPLICATIONS OF SANDSTONE SEDIMENTARY AND PERMEABILITY STRUCTURES FOR SOLUTE TRANSPORT

6.1 Introduction

In previous chapters, the Permo-Triassic sandstones across England were studied (Chapter 3), and a relationship between sandstone lithofacies and permeability was found in the Preston Laundry Borehole core (Chapter 4). This chapter aims to determine the importance of the relationship for solute transport. Numerical modelling has been undertaken of solute transport in synthetic fluvial channel structures at field scale in the Permo-Triassic sandstones. The sandstone lithology and hydraulic property values used were derived from the work done for the Preston Laundry Borehole core as described in Chapter 4.

Visual Basic for Applications in Microsoft Excel (VBA) is used to build up the synthetic channel structures based on geometries from fluvial channel structures observed in the field in England (Chapter 3). Lithofacies characteristics, structures, and hydraulic properties are taken from the Preston Laundry borehole core where the correlation between sandstone lithofacies and permeability has been determined in Chapter 4. Solute transport was then modelled through the heterogeneous, isotropic channel systems using the model code Modflow (McDonald and Harbaugh, 1984), then M3TDMS (Zheng and Wang, 1999) embedded in Groundwater Vistas version 5.18 (http://esinternational.com/groundwater-vistas-2/). Different directions of solute migrating through channel structures were simulated. These outcomes were compared with each other and with equivalent homogeneous systems. The effect of contrasts between very low permeability units (e.g. mudstone) and more permeable units as a source of numerical errors has also been investigated.

6.2 Mathematical modelling

6.2.1 Flow and transport equations

Various analytical models and various numerical solution schemes have been used in this study, and this section briefly summarises some of the aspects relevant to the work undertaken. For reference, the differential equation for groundwater flow is:

$$\frac{\partial}{\partial x}(K_{xx}\frac{\partial h}{\partial x}) + \frac{\partial}{\partial y}(K_{yy}\frac{\partial h}{\partial y}) + \frac{\partial}{\partial z}(K_{zz}\frac{\partial h}{\partial z}) = S_s\frac{\partial h}{\partial t} \qquad (6\text{-}1)$$

where

x , y , z are the Cartesian coordinate coincident with the principal axis of anisotropy

S_s is the storage coefficient [L]

h is the hydraulic head [L].

The differential equation for solute transport is:

$$\frac{\partial(C)}{\partial t} = D_x\frac{\partial^2 C}{\partial x^2} + D_y\frac{\partial^2 C}{\partial y^2} + D_z\frac{\partial^2 C}{\partial z^2} - v_x\frac{\partial C}{\partial x} \qquad (6\text{-}2)$$

where

D_x is the dispersion coefficient in the x direction

$$D_x = \alpha_L v_x + D^* \qquad (6\text{-}3)$$

$$D_y = \alpha_{TH} v_x + D^* \qquad (6\text{-}4)$$

$$D_z = \alpha_{TV} v_x + D^* \qquad (6\text{-}5)$$

C is concentration [ML^{-3}]

α_L, α_{TH}, α_{TV} are longitudinal, horizontal transverse, and vertical transverse dispersion respectively [L]

v_x is groundwater velocity [LT^{-1}]

D^* is the diffusion coefficient [LT^{-2}].

6.2.2 Analytical solutions

Analytical models provide exact solutions of mathematical descriptions of physical processes. Many studies have developed analytically solutions for solute transport in groundwater (e.g. Bear, 1979; Van Genuchten and Alves, 1982; Javandel et al., 1984; Domenico and Robbins, 1985; Domenico, 1987; Wexler, 1992). Analytical solutions are inexpensive, handy, and accurate, but they are limited to relatively simple boundary and initial conditions, and also to simple physical parameter distributions. These assumptions can result in the models being far from realistic. When the groundwater and transport problems to be solved require complex boundary conditions and inhomogeneous distribution of physical parameters, analytical solution is inappropriate, and numerical solution is required.

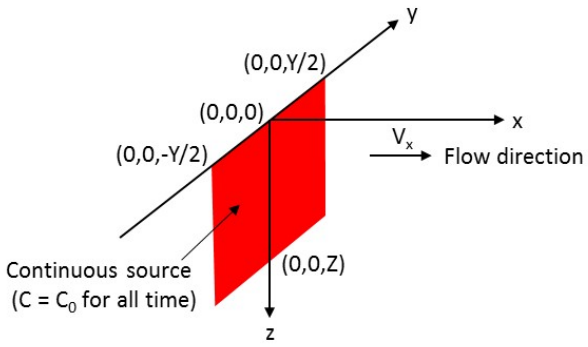

Fig.6-1. Geometry of path source with unidirectional flow (adjusted from Domenico and Robbins, 1985).

Domenico (1987) developed an approximate analytical solution for solute transport in a constant velocity field (x-direction) for a continuous source of regular geometry (Fig.6-1)

The complete Domenico (1987) solution to solve the advective-dispersive transport (Equation 6-2) is

$$C(x,y,z,t)=\frac{C_0}{8}\exp\left\{\left(\frac{xv}{2\alpha_x}\right)\left[1-\left(1+\frac{4\lambda\alpha_x}{v}\right)^{1/2}\right]\right\}erfc\left[\frac{x-vt\left(1+4\lambda\alpha_x/v\right)}{2\left(\alpha_x vt\right)^{1/2}}\right]$$

$$\left\{erf\left[\frac{y+Y/2}{2\left(\alpha_y x\right)^{1/2}}\right]-erf\left[\frac{y-Y/2}{2\left(\alpha_y x\right)^{1/2}}\right]\right\}\left\{erf\left[\frac{z+Z}{2\left(\alpha_z x\right)^{1/2}}\right]-erf\left[\frac{z-Z}{2\left(\alpha_z x\right)^{1/2}}\right]\right\} \qquad (6\text{-}6)$$

where:

C(x,y,x,t) is concentration at point (x,y,z) at time t

v is groundwater velocity in x direction

t is elapsed time

C_0: is source concentration

$\alpha_x, \alpha_y, \alpha_z$ are dispersion coefficients in *x, y*, and *z* direction respectively

Y is source width

Z is the source thickness

λ is decay constant

erf() is the error function

erfc() is the complementary error function and it is related to the error function erf() by

$$\text{erfc}(-\beta) = 1 + \text{erf}(\beta) \qquad (6\text{-}7)$$

$$\text{erfc}(\beta) = 1 - \text{erf}(\beta) \qquad (6\text{-}8)$$

$$\text{erf}(-\beta) = -\text{erf}(\beta) \qquad (6\text{-}9)$$

Values of erf() and erfc() can be found in table for the error function and complementary error function

For transport with no decay (λ = 0), Equation 6-4 reduces to Domenico and Robbins (1985) solution as follows

$$C(x,y,z,t)=\frac{C_0}{8}erfc\left[\frac{x-vt}{2(\alpha_x vt)^{1/2}}\right]$$

$$\left\{erf\left[\frac{y+Y/2}{2(\alpha_y x)^{1/2}}\right]-erf\left[\frac{y-Y/2}{2(\alpha_y x)^{1/2}}\right]\right\}\left\{erf\left[\frac{z+Z}{2(\alpha_z x)^{1/2}}\right]-erf\left[\frac{z-Z}{2(\alpha_z x)^{1/2}}\right]\right\} \quad (6\text{-}10)$$

When α_y and α_z approach zero (1D dispersion), Equation (6-4) is converted into the Ogata and Banks (1961) solution:

$$C(x,t)=\frac{C_0}{2}\exp\left\{\left(\frac{xv}{2\alpha_x}\right)\left[1-\left(1+\frac{4\lambda\alpha_x}{v}\right)^{1/2}\right]\right\}erfc\left[\frac{x-vt(1+4\lambda\alpha_x/v)}{2(\alpha_x vt)^{1/2}}\right] \quad (6\text{-}11)$$

In the present study, numerical model results for homogeneous models were compared with the analytical solution of Domenico (1987).

6.2.3 Numerical solutions

6.2.3.1 Introduction

Numerical models solve the transport equation using approximate approaches. In numerical solutions, the advection-dispersion equation has to be converted to algebraic format and to be solved digitally on a computer. The advection-dispersion equation contains first-order spatial derivatives (e.g. $\partial C/\partial x$) from advection, second-order spatial derivatives (e.g. $\partial^2 C/\partial x^2$) from dispersion and a temporal derivative ($\partial C/\partial t$). The combination of first- and second-order terms make solute transport more difficult to solve numerically than the flow equation which does not have the first-order spatial derivative.

The transport equation contains first-order spatial terms and second-order spatial terms. With a second-order spatial term only, the transport equation is referred as a 'parabolic differential equation' and can be accurately solved by Eulerian methods which require a fixed grid such as a finite difference (FD) or finite element (FE) grid. With a pure first-order spatial term, the transport equation is called a 'hyperbolic equation' and is accurately solved by Lagrangian methods that track the particles along pathlines instead of using a fixed grid. The transport equation has both an advection term (hyperbolic) and a dispersion term (parabolic), and as with its hybrid nature, neither pure Eulerian or Lagrangian methods are optimal to solve numerically the transport problem. Mixed Eulerian-Lagrangian methods which combine advantages of the Eulerian and Lagrangian methods are therefore required (Zheng and Wang, 1999). The pure Eulerian and mixed Eulerian-Lagrangian methods are briefly described below.

6.2.3.2 Summary solution techniques for solving the advection-dispersion equation

Solving the differential transport equation is more difficult than solving the differential flow equation because the advection and dispersion terms co-exist in the transport equation. There are several numerical solution techniques available to solve the differential transport equations. The numerical methods convert the form of the advection-dispersion equation to systems of algebraic equations, or simulate transport through the spread of a large number moving reference particles. A summary of numerical approaches relevant to the current study is described briefly below.

Eulerian, Lagrangian, and mixed Eulerian-Lagrangian are three main numerical approaches used to solve the advection-dispersion-reaction equations (Neuman, 1984). The Eulerian approach is mass conservative and uses a fixed grid method such as the standard finite-difference or finite-element methods. The Eulerian approach has the advantages of the

convenience of a fixed grid and solves advection-dispersion systems effectively. It is less effective at solving advection-dominated systems as it may produce excessive numerical dispersion and artificial oscillation. For applications to such systems, small grid refinement and time-steps may be required (Zheng and Wang, 1999).

The Lagrangian approach uses either a deforming grid or deforming coordinates in a fixed grid system through particle tracking to solve the advection-dispersion equation. The Lagrangian method solves effectively for advection-dominated systems with virtually no numerical dispersion. The Lagrangian method requires a fixed grid or coordinate system to avoid numerical instability and computational difficulty for non-uniform systems with complex boundary conditions and multiple sinks and sources (Yeh, 1990). Modelled concentration generally shows a "rough" appearance that requires subsequent smoothing and/or possibly interpretation (Zheng and Wang, 1999).

The mixed Eulerian-Lagrangian approach provides advantages of both the Eulerian approach and the Lagrangian approach. In the mixed Eulerian-Lagrangian approach, the advection term is solved with a Lagrangian approach (particle tracking), while the dispersion and reaction terms are solved with an Eulerian approach (finite-difference or finite-element methods). However, mass conservation may not be obtained in the mixed Eulerian-Lagrangian approach, and as with the Lagrangian approach alone, numerical errors can happen with the mixed Eulerian-Lagrangian approach. It also requires more computational sources than the purely Eulerian approach alone or the Lagrangian approach alone (Zheng and Wang, 1999).

The MT3DMS, originally MT3D, package in Groundwater Vistas has been used in the current research. It uses the standard finite-difference method, several mixed Eulerian-Lagranrian

methods, and a third-order TVD (Total-Variation-Diminishing) method to solve the differential transport equation. Brief descriptions of these methods are given below.

a. Standard finite-difference methods: This is computationally efficient more than many other methods. In the standard finite-difference method the advection component can be approximated by the concentration values at the cell interfaces. The interface concentrations are estimated using either an upstream weighting scheme or a central-in-space weighting scheme. The standard finite-difference scheme is accurate in solving the differential transport equation only for systems not dominated by advection. This limitation can be overcome by either increasing the physical dispersivity or making the grid spacing sufficient fine (Zheng and Wang, 1999).

- ***Upstream weighting scheme***: This is numerical oscillation free. In the upstream weighting scheme, the interface concentration between two adjacent nodes in a particular direction (e.g. x direction) is set equal to the concentration at the upstream node in the same direction. The upstream weighing scheme is numerical oscillation free solution, but is only accurate for first order terms, and for advection-dominated systems it leads to high numerical dispersion. This is because that the advection solution leads to truncation error that is of the same order and could be solved in the second-derivate physical dispersion term (Zheng and Bennett, 1995).
- ***Central-in-space weighting scheme***: This is numerical dispersion free. In the central-in-space weighting scheme, the interface concentration is set equal to the weighted average of the concentrations on the two sides of the interface. For regular grid spacing, the solution for advection is accurate to the second order, leading to numerical dispersion free as the dispersion solution is accurate to the second order. For advection-dominated systems, however, the central-in-space weighting scheme can lead to significantly artificial oscillation- the higher-order of truncation error (Zheng and Wang, 1999).

- ***Third-order TVD methods:*** The total-variation-diminishing (TVD) methods (Harten, 1983; 1984; Cox and Nishikawa, 1991) The third-order TVD methods are Eulerian techniques as they are higher-order finite difference (or finite volume), and are mass conservative. In this method the interface concentration is calculated through a third-order polynomial interpolation of nodal concentrations, supplemented by a universal flux to minimize unphysical oscillations which may occur if sharp concentration fronts are present. The third-order TVD method provides solutions for the advection-dispersion equation with no excessive numerical dispersion and oscillation free. The TVD methods are much more accurate in solving the advection-dominated problems than the other two, standard finite difference, methods, but the TVD methods require more computer memory to solve the advection-dispersion equation. The TVD methods are less effective in eliminating numerical dispersion than some Lagrangian or mixed Eulerian-Lagrangian methods such as the method of characteristics (MOC), but the TVD methods produce better mass conservation, and require less computer memory.

b. Mixed Eulerian-Lagrangian methods

- ***Method of characteristics (MOC)*** (Garder et al., 1964; Zheng, 1993; Konikow et al., 1996; Zheng and Bennett, 1995)**:** The MOC method employs a conventional particle-tracking technique to solve the advection term. From the start of the simulation, a set of moving particles is distributed either randomly or with a fixed pattern. Each particle is defined with its Cartesian coordinate and concentration. The particles are tracked forward through flow systems using a small time increment, and at the end of each time increment, the average intermediate concentration particular cell is calculated from the concentration of moving particles located in that cell. This intermediate concentration then is used to estimate changes in concentration caused by dispersion or other processes in that time increment. The advantage of the MOC

method is that it provides a solution free of numerical dispersion caused by spatial truncation errors. The disadvantage is a requirement for large computational resources to track a large number of moving particles, particularly in three dimensional systems. Another drawback of this method is it leads to error in mass balance if model grid is highly irregular as the discrete nature of the particle-tracking-based mixed Eulerian-Lagrangian approach fails to guarantee local mass balance at a particular time-step (Zheng and Bennett, 1995).

- ***Modified method of characteristics (MMOC)*** (Russell and Wheeler, 1983; Healy and Russell, 1993)**:** Apart from the solution for the advection term, the MMOC method is similar to the MOC method. In contrast with the MOC method, which tracks forward in time a large number of moving particles, the MMOC methods place one fictitious particle at the nodal points of the fixed grid at each new time step (n+1). The particles are tracked backward to find its position in the previous time step (n). The concentration at that position is used to approximate the intermediate concentration caused by advection during the period starting from the preceding time step. The MOC uses several particles per cell, whereas the MMOC method uses a particle for each cell. Unlike MOC methods, the MMOC method starts particles at nodal points at each new time step, which frees computer memory to store the particle formation. This reduces computational resources significantly which is a significant advantage over the MOC method. The MMOC is free of artificial oscillation for lower-order interpolation schemes such as linear interpolation; however, in lower-order interpolation schemes, the MMOC leads to significant numerical dispersion, especially for sharp front problems. This error can be eliminated with higher-order schemes: however, these are more computationally expensive and can introduce artificial dispersion for sharp front problems.

Several interpolation schemes for 1D problems have been examined by Healy and Russell (1989) who found that a mixture of linear and quadratic schemes can minimize both numerical

dispersion and artificial oscillation. However, this requires much higher computational resources, particularly in a multidimensional system, than the linear scheme: moreover, it fails to guarantee mass conservation.

For all the above reasons, the MMOC method in the M3TDMS package is operated only with a lower-order interpolation schemes and is advocated only for non- sharp front systems.

- ***Hybrid method of characteristics (HMOC)*** (Neuman, 1984; Yeh et al., 1992)**:** HMOC is a hybrid of the two methods MOC and MMOC. The HMOC will solve a sharp concentration front (advection-dominated) by the MOC technique with forward tracking of moving particles around each front. Away from such fronts, the HMOC will solve the advection term by the MMOC technique with tracking backward of fictitious particles at nodal points. The forward tracking will be stopped automatically once a front disappears as a result of dispersion or chemical reactions. The HMOC method however may sometimes not be effective as either the MOC or MMOC methods as the point at which switching between MOC and MMOC techniques occurs may not be optimal (Zheng and Wang, 1999).

6.2.3.3 Numerical models used in the study

All model systems in this study were simulated using groundwater flow and solute transport package embedded in a computer software Groundwater Vista. These packages and the software were briefly described below.

a. Groundwater flow: MODFLOW package (Modular Finite-Difference Groundwater Flow Model) (McDonald and Harbaugh, 1984)**:** This computer software code was used to model the groundwater flow systems. It solves the three-dimensional groundwater flow using a block-centred finite difference method. The model code was first published by the U.S Geological Survey in 1984 (McDonald and Harbaugh, 1984). It has been developed through several

versions: MODFLOW-88, MODFLOW-96, MODFLOW-2000 (Harbaugh et al., 2000; Hill et al., 2000), and the current version MODFLOW-2005 (Harbaugh 2005). The MOFLOW package has the advantage of being a public-domain, open-source code, and easy to understand and to operate.

b. Groundwater flow particle tracing path: MODPATH package (Pollock, 1994): this is a post-processing model code for MODFLOW to track particles. Assumpting advective transport only, this model code traces the pathlines of particles either forward or backward in time.

c. Groundwater solute transport: MT3DMS package (Modular 3-D Multi-Species Transport Model for Simulation of Advection, Dispersion, and Chemical Reactions of Contaminants in Groundwater Systems) (Zheng and Wang, 1999). The first model code is MT3D released by the U.S Environmental Protection Agency (Zheng, 1990). MT3D directly interfaces with MODFLOW for groundwater flow simulation. For solute transport simulation, MT3D requires either a pure Eulerian scheme in the finite difference approach or a mixed Eulerian-Lagrangian scheme. Each approach has its own advantages and drawbacks. MT3DMS is a development of MT3D, in which is added functions for multi-species transport (MS). MT3DMS version 5 was used (Zheng, 2006).

Ground Water Vistas

Ground Water Vistas which was employed to simulate the solute transport throughout this chapter is a sophisticated window graphics user interface for modelling 3D groundwater flow and transport. The software is developed and marketed by Environmental Simulations International (ESI) Ltd., UK (http://esinternational.com/groundwater-vistas-2/). Ground Water Vistas supports MODFLOW 2000, MODFLOW 2005, MODPATH, MT3D/MT3DMS, SEAWAT etc. The version used was Ground Water Vistas version 5.18 (ESI).

6.3 Model scenarios

6.3.1 Sedimentary fluvial cycles

Fluvial sandstones account for a major proportion of the Permo-Triassic sandstone sequence in England (Chapter 3). Fluvial sandstones dominate in west Cumbria in the St Bees Sandstone Formation (Chapter 3), at Rawhead in Cheshire (Chapter 3), at Ladram Bay in southwest England (Chapter 3), and in the Preston Laundry borehole core sequence (Chapter 4). Cyclicity within the sedimentary sequence is present from microscopic scale to megascopic scale in Permo-Triassic sandstones (e.g. Thompson, 1970; Wills, 1970; Lovelock, 1977), although the cycles are mostly incomplete. River channel migration and seasonal to millennial climate variation cause the superposition of different scale cycles of varying thickness and varying degrees of cycle completion. A fining-up in grain size is normally seen in a typical cycle that starts with at the base with a conglomerate, then passes up into sandstones to mudstones at the top; the latter is in turn overlain by the basal conglomerate of the next cycle (Lovelock, 1977).

Fluvial channel cycle thicknesses obtained from the different field sites across England mentioned in Chapter 3 are given in Table 6-1. The channel cycles range from 1.5 m to 3.0 m thick, with an arithmetic mean of 2.0 m. The cylcity of fluvial sandstones in the Preston Laundry borehole cores were statistically analysed using a Markov chain approach (Chapter 4). Most of cycles were not complete, and the most frequent vertical transition sequence was from channel lag sandstone (LF5) passing up through sandstones (LF4, LF3, LF2) of smaller grain size to mudstone (LF1) (Chapter 4) and this cycle was used to erected the bodies of the channel systems.

Table 6-1. Summary for cycle thickness of fluvial channels in the English Permo-Triassic sandstones at the locations described in Chapter 3.

Locations of outcrop/cliffs/borehole	Cycle thickness (m)
St Bees cliff, West Cumbria	1.50
Rawhead, Cheshire	2.50
Croxden Quarry, Cheshire	3.00
Ladram Bay cliff, southwest	2.50
Preston Laundry Borehole core, Lancashire	1.46
Average	2.00

6.3.2 Fluvial channel geometry

Sparse information has been reported on fluvial channel geometry of the English Permo-Triassic sandstones. At field scale, some small channel structures which have channel widths and depths ranging from cm-scale to approximate m-scale were observed in some of the locations described in Chapter 3 (e.g. in West Cumbria and Ladram Bay). Larger channel structures were observed at Raw Head (one example) and West Cumbria, with widths approximately in the range of tens of metres, though the orientation relative to the thalweg of the channels was difficult to determine. From analogue modern environments it might be expected for channels to range in widths up to hundreds metres or more in width with asymmetric curvy sides.

Two types of channel structure have been defined for the purposes of the modelling using the ratio of channel width to channel depth: 1) ‘shallow’ systems having multiple-stacked channels of channel width of about 300 m and channel depth of 0.5 m; and 2) ‘deep’ systems having multiple-stacked channels of width about 80 m and depth of 0.5 m (Fig.6-2). Although all the channels have the same depth (0.5 m), the ‘shallow’ and ‘deep’ terms here refer to the relative difference in ratio of channel depth to channel width (0.5/300 and 0.5/80). Both the shallow and deep channel systems were simplified as horizontal multi-stacked channels flowing in the same direction.

The shallow channel systems are closest to those observed in the field (Chapter 3). The deep channel system are much less common in the field works (Chapter 3), but their inclusion in the modelling work provides a useful comparison with solute transport in the shallow channel systems.

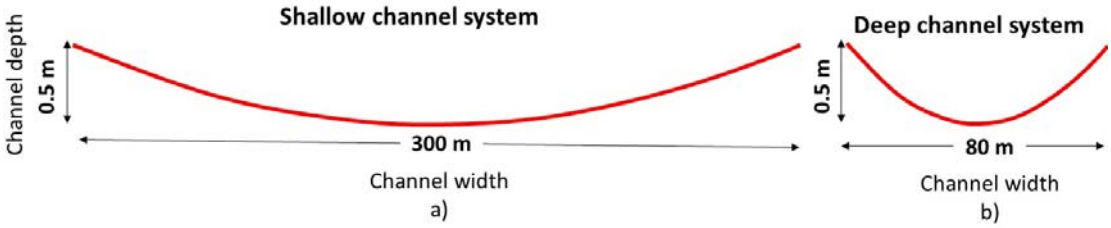

Fig.6-2. Schematic cross-sections of fluvial channel geometries modelled:
a) the shallow channel system and b) the deep channel system.

6.3.3 Model representation for the channel systems

The channel systems were simplified and conceptualized to represent solute migrating downstream in multiple-stacked channel systems with boundary conditions as specified in Fig.6-3. The model domains are 100 m long and 100 m wide with thickness of 2.7 m for shallow system and 3.2 m for the deep system. These sizes are large enough to represent solute transport in the systems and efficient for computational memory and time.

The upstream and downstream boundaries are assigned as constant head boundaries of 20 m and 19 m, creating a hydraulic gradient of 0.01. The side boundaries are set as sloping linear-head boundaries from 20 m to 19 m.

Monitoring wells were set at downstream boundaries to capture concentration at points at downstream boundary (Fig.6-3). Names of the monitoring well were set to be identical with their row number (for cross channel systems) and column number (for along channel systems). For instance, monitoring well W100 was set at row number 100th (middle of model) at the

downstream boundary (for the cross channel system) or at column number 100th at the downstream for the along channel systems.

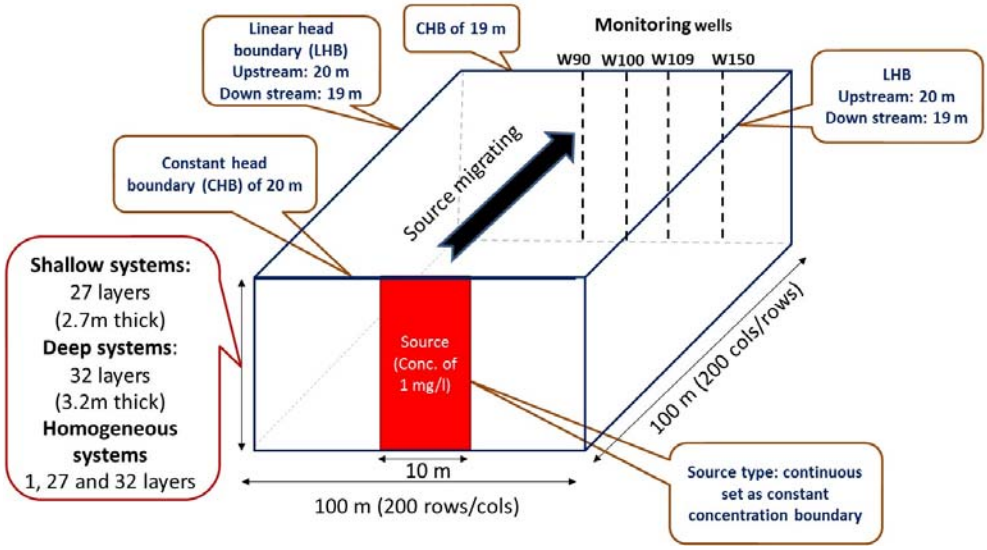

Fig.6-3. Schematic model representation for the channel systems.

The contaminant source was located at the middle of the upstream boundary and was set as a continuous, conservative source (Fig.6-3). The width of the source is 10 m and it is completely penetrating. The source has a constant concentration of 1 mg/l, and initially, zero concentration is present elsewhere. No diffusion or chemical reactions were modelled.

6.3.4 Properties

6.3.4.1 Lithology and hydraulic properties

Lithofacies and their hydraulic properties derived from the Preston Laundry Borehole core (Chapter 4) were used to build up material for the channel systems (Table 6-2). Table 6-2 summarises the palaeoenvironmental and hydraulic properties of the lithofacies. Note that the permeability values of LF4 and LF5 take into account the effects of pellets (Chapter 4).

Averaged thicknesses of the five lithofaces are also given in Table 6-2. The five lithofacies have a total thickness between 1.8 m and 2.6 m: this compares with the average cycle thickness of 2.0 m (Table 6-2). The properties listed in Table 6-2 were used randomly to create the lithofacies sequences using a VBA code in Excel. This code generates shallow or deep channel systems of complete or incomplete cycles with LF1, LF2 and LF5 each having thickness of 0.2 m, and with randomly varying thickness from 0.6 to 1.0 m for LF3 and LF4. Details of the VBA code can be found in Appendix 4.

Table 6-2. Summary lithofacies description and hydraulic properties using in the fluvial channel systems.

LF ID	Color code	Lithological characteristics				Sedimentology	Averaged thickness (m)	Hydraulic properties	
		Gain size	Mud clasts/ pebbles	Mica	Lamination			Arithmetric mean porosity	Geometric mean permeability (m/d)
1		Mudstone	Mudstone	N/A	N/A	Overbank deposit	0.2	0.35	3.6×10^{-6}
2		Very fine sandstone	No	lots	Flat to low-angle	Overbank deposit or channel fill	0.2	0.15	0.003
3		Fine to medium sandstone	Occationally	yes	Flat or gently inclined	Channel fill	0.6-1.0	0.17	0.019
4		Medium to coarse sandstone	Often	yes	Gently inclinded or steep	Channel fill	0.6-1.0	0.20	0.040
5		Medium to coarse sandstone	Lots	yes	No (massive sandstone)	Channel lag	0.2	0.19	0.074

6.3.4.2 Dispersivities

Many studies have been done on estimation of dispersivities (e.g. Scheidegger, 1961; Gelhar et al., 1992; Ballarini et al., 2012; Liu and Kitanidis, 2013). Gelhar et al. (1992) presented a critical review, including of field measurements worldwide, and assigned a level of reliability (Fig.6-4a-c). Dispersivity is a scale-dependent property. Considering the more reliable values in Fig 6-4, longitudinal dispersivities are about one order of magnitude smaller than the distances over which the tests have been run, whist horizontal transverse and vertical transverse dispersivities are two or three to four orders of magnitude smaller than test length respectively. Table 6-3 summarises the approximate relationships that might be used in estimating dispersivities based

on the analysis of Gelhar et al. (1992). In systems of horizontal stratification, for flow parallel with the stratification the value of the transverse dispersivity across the stratification may be similar to value of effective diffusion coefficient (Sudicky, 1986).

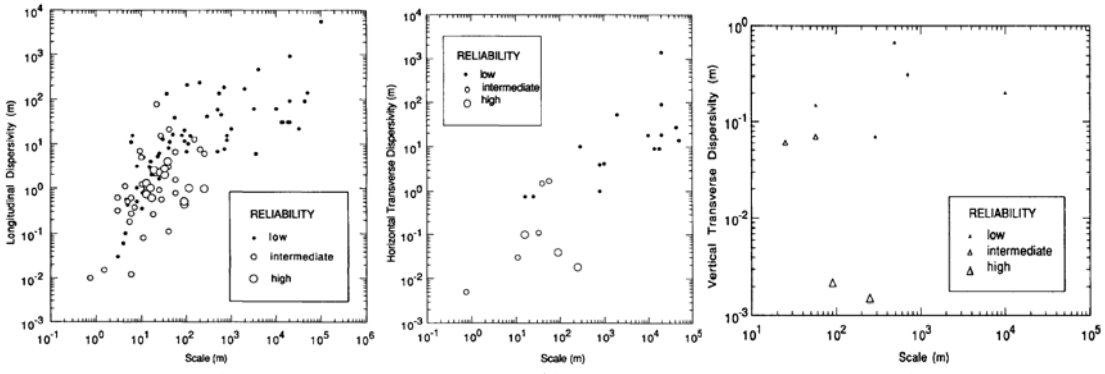

a) b) c)

Fig.6-4. Dispersivities as a function of scale: a) longitudinal dispersivity; b) horizontal transverse dispersivity; and c) vertical transverse dispersivity (from Gelhar et al., 1992).

Table 6-3. Estimation of longitudinal dispersion for macroscopic scales (Lecturer note by Mackay, 2010).

Scales of measurements	Scale of system = L	Estimated α_L (m)
Laboratory (smallest)	1 - 10 m	$(0.1L)^2$
Field (intermediate)	10 - 100 m	$0.1L$
Regional (largest)	> 100 m	$L^{1/2}$

As the channel system domain is 100 m long and 100 m wide and 2.7 m thick (for the shallow channel systems) and 3.2 m thick (for the deep channel system), the longitudinal dispersivity (α_L) is therefore assigned to be 10 m, one tenth the length of the model. Similarly, the horizontal transverse dispersivity (α_{TH}) is set to be one tenth the longitudinal dispersion length (α_{TH} = 1 m), and the vertical transverse dispersivity (α_{TV}) is equal to one tenth the horizontal transverse dispersivity (α_{TV} = 0.1 m). All the systems were simulated with no diffusion and no chemical reaction (Table 6-4).

Table 6-4. Summary model geometries and transport parameters assigned for the channel systems.

	Parameter	Values (m)
Model geometry	Model length	100.0
	Model width	100.0
	Model thickness: the shallow channel system	2.7
	Model thickness: the deep channel system	3.2
Dispersions	Longitudinal dispersivity (α_L)	10.0
	Horizontal transverse dispersivity (α_{TH})	1.0
	Vertical transverse dispersivity (α_{TV})	0.1
Diffusion: no effect of diffusion	Diffusion coefficient	0.0

6.4 Representation in models of scenarios

6.4.1 Finite-difference grid

The channel systems and related homogeneous systems were simulated for flow and solute transport with the finite-difference approach. In the finite-difference approach, a three-dimensional grid system for groundwater flow and solute transport is formed by rectangular blocks (Fig.6-5a). For a three-dimensional grid system having n rows (*nrow*), m columns (*mcol*), and u layers (*ulay*), and in an (i, j, k) coordinate system, the grid of a block (a cell) is defined by i (row number: i = 1, 2,.., *nrow*), j (column number: j = 1, 2, .., *mcol*), and k (layer number: k = 1, 2, .., *ulay*). Here, the origin of the grid system is the upper-left corner of the topmost layer (Fig.6-5a). Note that the origin of the rectangular (Cartesian) coordinate system is at the lower-left corner of the topmost layer. Lateral discretization is on rows and columns, whereas vertical discretization is on layers. The grid nodes are formulated as block-centred (Fig.6-5b), i.e. the nodes are at the centres of the blocks.

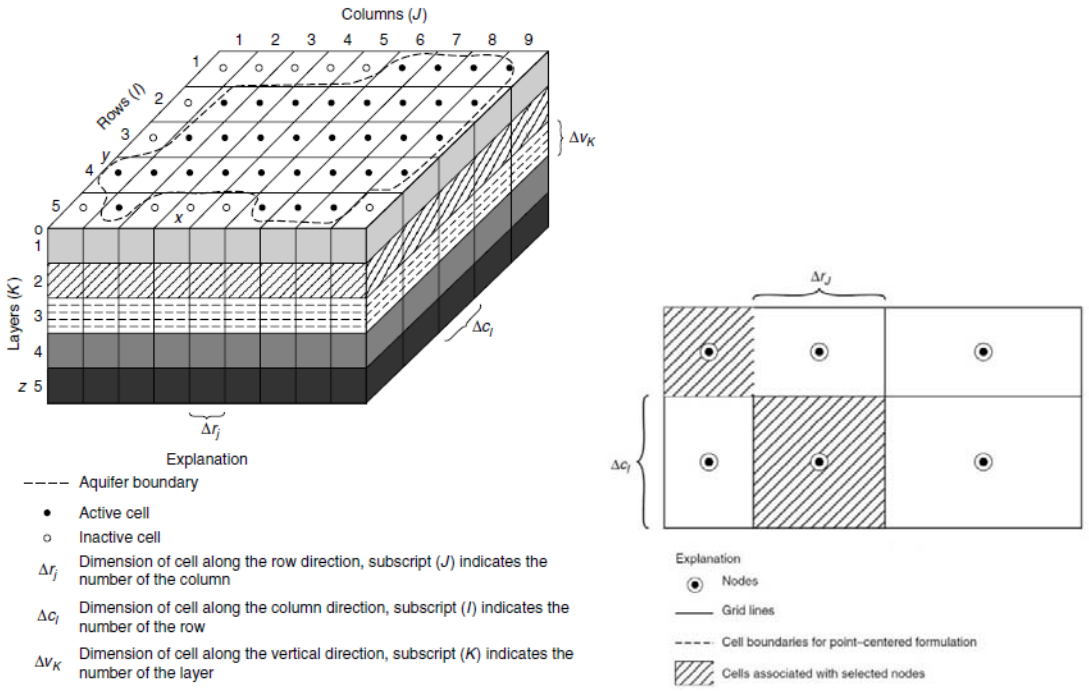

a) b)

Fig.6-5. Finite-difference grid system: a) A discretized aquifer system; b) Block-centred grid (from McDonald and Harbaugh, 1984).

6.4.2 Spatial discretisation for the channel systems

6.4.2.1 Lateral discretisation

The model can be designed with a regular or an irregular grid, depending complexity and location of interest. For regular grids, the dimension along the row (Δr_j), along the column (Δc_i), and in the vertical direction (Δv_k) are all constant, but not necessary equal (Anderson and Woessner, 1992). For irregular grids, which are commonly required to obtain accurate solutions, finer spaced nodes should be allocated for areas of point stresses where head/concentration gradients are steepest. The cell spacing should be changed gradually and the dimensions of adjacent cells should not differ by greater than a factor of 1.5 (Anderson and Woessner, 1992; Batu, 2006). When designing the grid, it is necessary that the aspect ratio (cell

length to width) should be kept as close as possible to 1 else numerical instability is more likely to occur, particularly if the aspect ratio is greater than about 5 (Anderson and Woessner, 1992). An irregular grid specification was applied for the refined grid models to deal with the numerical oscillation that occurred in the channel systems (see below).

Spatial discretization for solute transport is more restrictive than that required for flow modelling as the numerical solution for the former is more difficult than for the latter (Batu, 2006). When accounting for dispersion, numerical solutions for the solute transport equation can cause numerical errors depending on the grid dimensions (Huyakorn and Pinder, 1983; Price et al., 1966; Batu, 2006). A useful measure of numerical errors due to grid discretization is a local Peclet number (P_e) (Batu, 2006):

$$P_e = \frac{vL}{D} \tag{6-12}$$

where:

v is the average linear velocity vector [LT^{-1}]

L is characteristic length, normally taken as the grid cell width [L]

D is dispersion coefficient [L^2T^{-1}].

For a one-dimensional system, D is given by $D_L = \alpha_L v$ where α_L is longitudinal dispersivity. Thus the Peclet number can also be written as

$$P_e = \frac{L}{\alpha_L} \tag{6-13}$$

The Peclet number also characterizes the level of advection dominance in systems. Huyakorn and Pinder (1983) and Ségol (1994) suggested that the value for P_e should be ≤ 2, and Anderson

and Woessner (1992) < 4, although sometimes an acceptable solution may be achieved with a P_e as high as 10 (Huyakorn and Pinder, 1983). The value of L will be cell width in x direction for one-dimensional transport systems, and be maximum of cell widths for x and y direction for two-dimensional systems (Batu, 2006).

For lateral discretization in the channel systems (both shallow and deep channels), a regular cell spacing of 0.5 m is used, small enough to enable model grid size to meet the criteria of convergence and accuracy for model simulations (i.e. P_e as small as 0.05).

6.4.2.2 Vertical discretisation

In reality, the groundwater systems which are represented by a grid system consist of sequences of stratigraphic units which are rarely exactly horizontal, leading to some modelled cells representing two or more different materials (Batu, 2006). This makes the physical properties of the systems much more difficult to specify. A common solution for this problem is to deform the grid to enable the grid layers to coincide with the surface of the stratigraphic units (Fig.6-6) (Batu, 2006).

Another unique feature of vertical discretization for the layered-aquifer systems is that there is often very low permeability layers present. Tellam and Barker (2006) reported that groundwater flow will go around mudstones (clay) of limited lateral extent, but may pass through mudstone units having lengths of hundreds of metres.

In such layered systems (Fig.6-7a-c) the flow is almost vertical in the clay layer. Thus, to simulate the change in head across the clay accurately, many layers are required to represent it. Alternatively, no flow condition can be set for the clay. This will enable the ability to simulate the system without calculating head and concentration in clay layer (clay layer will not be

modelled) (Fig.6-7c). This alternative solution was applied to the channel model systems to resolve numerical oscillation (see below).

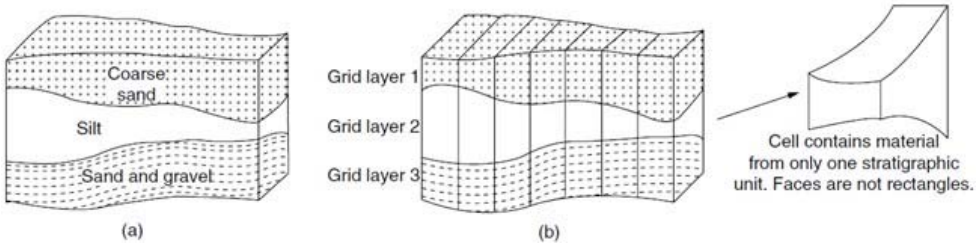

Fig.6-6. Modelling representation of a nature aquifer system: a) Cross-section of aquifer; b) Cross-section of deformation grid superimposed (from McDonald and Harbaugh, 1984).

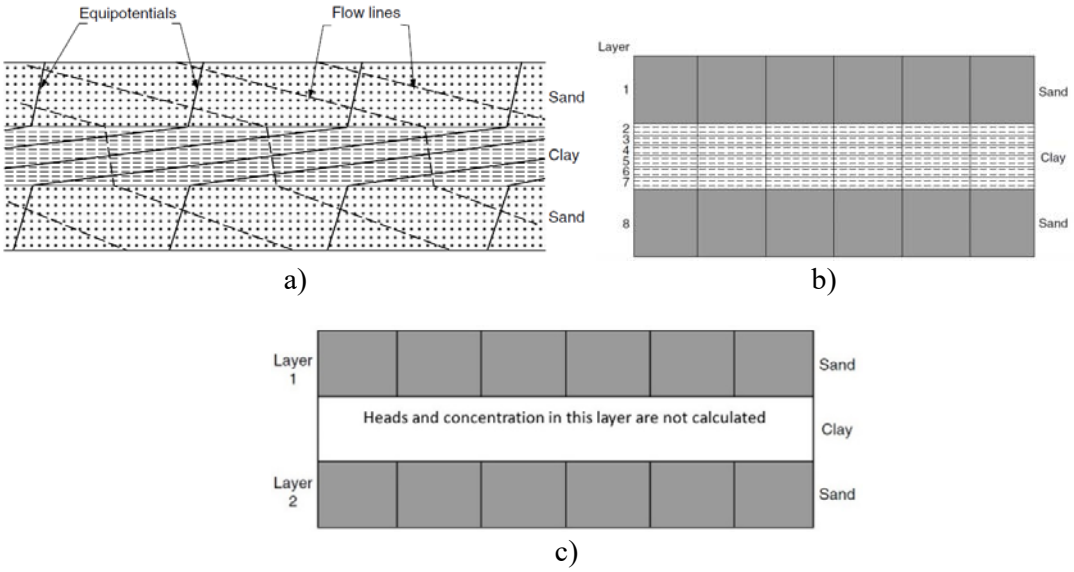

Fig.6-7. Cross-sections for aquifer consisting very low permeabilty (clay): a) cross-section of flow net in system; b) an example for vertical discretization for the system; and c) alternative soltion as a set of no-flow for clay layer (after McDonald and Harbaugh, 1984).

For vertical discretization in the channel systems (both shallow and deep channels), as the averaged thickness of the lithofacies ranges from 0.2 m to 1 m (Table 6-2), a discretisation of 0.1 m was assigned in the vertical direction. Thus, the shallow systems with a domain depth of 2.7 m will have 27 layers (Fig.6-8a,b) and the deep systems will have 32 layers (Fig.6-9a,b).

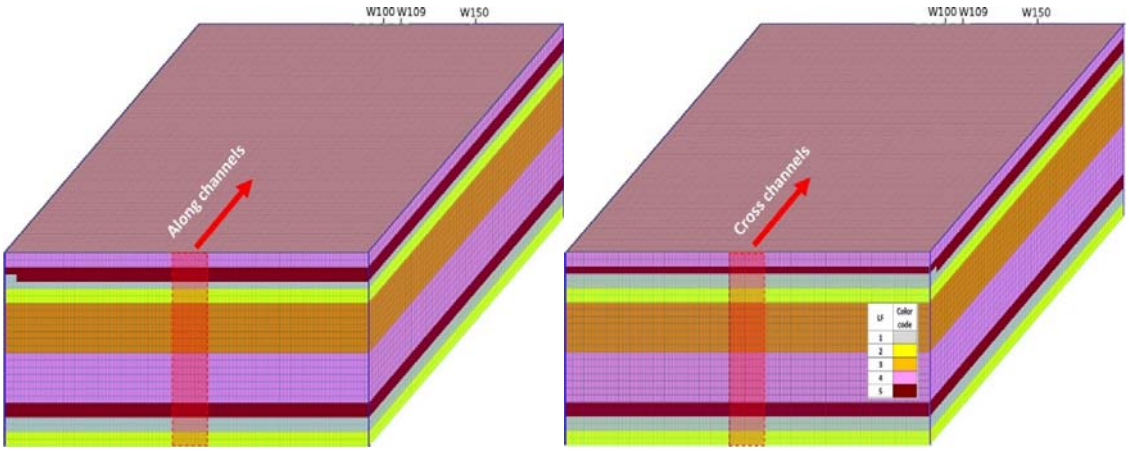

a) b)

Fig.6-8. The shallow channel systems:
a) solute migrating along the channels, and b) solute migrating across channels.

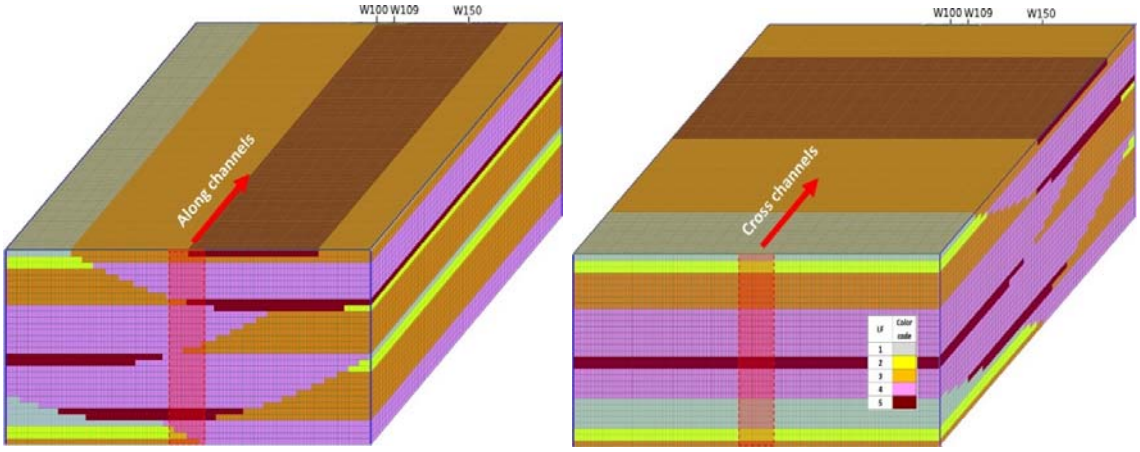

a) b)

Fig.6-9. The deep channel systems:
a) solute migrating along the channels, and b) solute migrating across channels.

6.4.3 Temporal discretization

The models are run in steady state conditions with maximum transport time step assigned to meet the Courant number (C_r) restriction:

$$C_r = \frac{v\Delta t}{\Delta x} \qquad (6\text{-}14)$$

where:

Δt is time step [T]

Δx is cell width [L]

For stability of explicit solutions, $C_r \leq 1$ (Huyakorn and Pinder, 1983; Anderson and Woessner, 1992). Thus $\Delta t \leq \Delta x / v$. This can also be expressed in words as: for a stable solution, the solute should not migrate any further than one grid block per time step. In the channel model and homogeneous systems, Δx = 0.5 m.

Table 6-5 shows the time and distance for advective transit for the channel and homogeneous systems: v was calculated either manually from Darcy's Law using the model input parameter values (Table 6-2) or by using MODPATH (Pollock, 1994). The 100 m transit time for single lithofacies increases from 70 years for LF5 to 2.7 x 10^6 years for LF1. In the shallow channel system, it takes about 183 years to travel in each direction; in the deep channel system, it takes 156 and 148 years along and across channels respectively.

Small time steps and fine model grid spacing are required for stable and accurate solutions, but this results in greater computer storage and time. Since the advective travel times are greater than 50 years, a compromise of a maximum timestep size of 100 days with a first timestep of 1 day and a timestep multiplier of 1.2 were chosen. Smaller first timestep (0.1 days) and smaller maximum timestep (10 days) (multiplier of 1.05) were selected to examine numerical stability.

A C_r of 1 was selected to run all model systems. Smaller values of Courant Number (0.5 and 0.1) were also set to run for numerical stability investigations.

Table 6-5. Advective travelling time and distance for the channel and homogeneous systems.

Homogenous systems	LF ID	LF color code	Hydraulic properties		Groundwater velocity (m/d)	Distance travel after 110 years (m)	Time to travel over 100m-long (years)
			Arithmetric mean porosity	Geometric mean permeability			
Homogeneus systems with hydraulic properties as single lithofaices	1		0.35	$3.6x10^{-6}$	$1.0x10^{-7}$	0.004	$2.7x10^{6}$
	2		0.15	0.003	$2.0x10^{-4}$	8.0	1,370
	3		0.17	0.019	$1.1x10^{-3}$	44.7	245
	4		0.20	0.040	$2.0x10^{-3}$	80.0	137
	5		0.19	0.074	$3.9x10^{-3}$	160.0	70
	Direction of solute mirgation						
Equivalent homogenous system (Shallow channel system)	Along channels		0.2	0.030	$1.5x10^{-3}$	60.0	183
	cross channels		0.2	0.030	$1.5x10^{-3}$	60.0	183
Equivalent homogenous system (Deep channel system)	Along channels		0.19	0.034	$1.8x10^{-3}$	70.1	156
	cross channels		0.19	0.036	$1.9x10^{-3}$	74.2	148

6.4.4 Equivalent homogeneous models and bulk hydraulic property estimation

The flow of water will be affected by the permeability architecture, including internal low permeability barrier units such as mudstone lenses and the distribution of lithologies of variable permeability (Wells, 1995). Orientation of the maximum directional permeability in sandstone is generally parallel with horizontal stratification or with the inclined stratification of cross-bed sets, whist orientation of the minimum permeability is normally perpendicular to sedimentary stratification (Domenico and Schwartz, 1990; Wells, 1995; Allen et al., 1997). This preferred permeable pathway is caused by the orientation and packing deposition of grains by traction currents (Miall, 1988; Domenico and Schwartz, 1990). A progressive increase or decrease in permeability can occur within a single unit as, for instance, with gradually increasing or decreasing in grain size. A layered heterogeneity will occur for systems having highly permeable units interbedded with low permeability units (Wells, 1995).

Though channel systems have complex permeability structures, solute transport is often represented using averaged-hydraulic-properties (homogeneous), so these have been

investigated too. Average hydraulic- properties were estimated from hydraulic properties of the channels (below). The homogeneous system models were otherwise identical to the (heterogeneous) channel models.

Bulk permeability estimation is dependent on stratification systems and degree of heterogeneity of sandstones. For sequences of continuous layers that can be assumed to be homogeneous and isotropic, bulk permeability parallel to the layering can be estimated using an arithmetic mean. Also for these systems, harmonic mean can be used to estimate permeability perpendicular to the layering. Otherwise, geometric mean permeability is the more appropriate measure of bulk permeability of heterogeneous systems. Generally $K_h/K_v > 1$ in many approximately horizontally bedded sedimentary sequences. The most permeable units dominate the systems for horizontal flow, whist the least permeable units dominate the system with vertical flow, as is clear from the definitions of arithmetic and harmonic means. However, in the channel systems permeability is assumed to be isotropic (i.e. $K_h/K_v = 1$) and heterogeneous.

In addition to considering the idealised layered representation using arithmetic and harmonic means, equivalent homogeneous permeabilities were estimated by modelling. For both shallow and deep channel systems, two directions were simulated for groundwater flow. The bulk permeabilities were then calculated from the model flows and Darcy's Law.

Bulk porosity values for each model system were averaged as arithmetic means with weighting the volumes of each lithofacies. The averaged porosities and permeabilities for each lithofacies are given in Table 6-2.

Bulk values of porosities and permeabilities, i.e. the assumed equivalent homogeneous, isotropic representations, for the channel systems are shown in Table 6-6. For the shallow channel systems, bulk permeability estimated by Modflow models are the same for flow along

and flow across channels (0.03 m/d) which are the same as arithmetic mean permeability (0.03 m/d). For the deep channel system, flow across channel bulk permeability (0.036 m/d) is only very slightly higher than that of flow along channels (0.034 m/d) which is the same as the arithmetic mean permeability estimated for the deep channel system.

The harmonic and geometric mean permeabilities are smaller than the arithmetic mean and modelled-derived permeability by about two to three orders of magnitude. These values are close to those of the low permeability lithofacies (LF1 and LF2), as expected, and results in no breakthrough curves for the running time frame (110 years). The Modflow-derived values were thus selected to represent the homogeneous- and isotropic- case bulk permeabilities.

Table 6-6. Hydraulic properties from lithofacies and from averaging heterogeneous systems used for homogeneous systems.

Equivalent homogenous systems with hydraulic properties derived from	Direction of solute mirgation	Porosity	Bulk permeability (m/d)			
			Arithmetic mean	Harmonic mean	Geometric mean	Estimated from Modflow model
Shallow channel systems	Along channels	0.20	0.030	3.2×10^{-5}	9.0×10^{-4}	0.030
	cross channels					0.030
Deep channel systems	Along channels	0.19	0.034	1.0×10^{-4}	5.8×10^{-4}	0.034
	cross channels					0.036

The channel (heterogeneous) and homogeneous systems were simulated for solute transport using the M3TDMS package (Zheng and Wang, 1999) with different sets of dispersion directions, including only longitudinal spreading (α_L=10 m, α_{TH}=α_{TV}=0 m), without vertical spreading (α_L=10 m, α_{TH} =1 m, and α_{TV}=0 m), and all spreading directions (α_L=10 m, α_{TH}=1 m, and α_{TV} = 0.1 m). These models were compared with each other and with the homogeneous systems with the same set of spreading directions.

All the Ground Water Vista model output files for the channel systems and equivalent homogeneous systems can be found in Appendix 5.

6.5 Numerical issues

6.5.1 Boundary resolutions and no-flow boundaries

The channel systems were represented with constant-head conditions at upstream (20 m) and downstream (19 m) boundaries (Fig.6-3). This is a special case of Type 1 specified-head boundary (Anderson and Woessner, 1992; Franke and Reilly, 1987; Franke et al., 1987) and it allows water into the system without any limitation. If the sides of the models are set with sloping linear-head boundary condition, this enables flow to cross the boundaries. The sides of the systems can alternatively set as no-flow boundaries.

For the systems having sloping linear-head boundaries at the edges, care must be taken when assigning head along the edges of the systems because small differences in head assigned at model edges can result in different concentrations (personal communication, Alan Herbert). Using Groundwater Vistas version 5.18 allows head to be imported with a maximum precision of 0.01 m: as each cell has a head drop of 0.05 m, this leads to two consecutive cells having the same head along the edge boundaries. This caused some errors for head distribution. Setting no-flow boundaries for the edge of model will constrain the systems and still cause some error.

6.5.2 Convergence criteria

6.5.2.1 Convergence criterion with flow models

As the transport model requires the velocity distribution from the flow model, precisely solving the flow model is essential. The flow model was solved using the Preconditioned Conjugate-Gradient Package (PCG2) (Hill, 1990). The PCG2 uses both head-change and residual criteria to determine convergence criteria. The PCG2 solver solves the flow term at one time step using a use a two-tier approach: inner and outer iterations.

Outer iterations are used to vary the preconditioned parameter matrix of the solution and at an outer iteration the parameters (e.g. hydraulic conductivity, storativity) of the flow model are updated in the preconditioned set of matrices. In PCG2 a maximum value of outer iterations were set at the default of 25 and proved adequate for most problems.

The inner iteration is continued until a user-defined maximum number of inner iteration is met or final convergence is achieved. In PCG2, a default value of 10 was set. The outer iteration will continue until the final converged solutions are reached on the first inner iteration after an update.

The default head change criterion for convergence is 0.001 m. A test was run of the sensitivity of mass balance errors to head change criterion values. Table 6-7 shows the properties used. A small head change criterion (1×10^{-7}m) showed significantly smaller mass balance errors for both homogeneous and heterogeneous systems, the latter being more sensitive. Accordingly a head change criterion of 1×10^{-7}m was chosen for all simulations.

Table 6-7. Summary convergence criteria for flow models.

System	Head change criterion (m)	Mass balance error for flow model (%)
LF4-homogeneous	1×10^{-3}	2.50
	1×10^{-6}	0.003
	1×10^{-7}	0.001
Heterogeneous (shallow channel system- along channels)	1×10^{-3}	4.80
	1×10^{-6}	0.005
	1×10^{-7}	0.0007

6.5.2.2 Convergence criteria for solute transport models

a. Concentration change for convergence criterion

Implicit Generalised Conjugate Gradient (GCG) solver was used to solve the non-advective term in the transport equation. The GCG solver is generally faster than the explicit finite-difference method as there are no time step constraints, but it requires more computer memory than the explicit method. The GCG uses two iteration loops. Within the inner loop, the solver continues to iterate toward the solution until the user-defined relative convergence criterion is met or the user-defined maximum number of inner iterations is reached (default value of 50). The outer iteration will be greater than 1 only for nonlinear sorption (default value of 1). The convergence criterion in terms of relative concentration is used to assess the convergence of the inner iterations of the solver.

There are three pre-conditioning options in GCG: 1) Jacobi; 2) SSOR; and 3) Modified Incomplete Cholesky (Modified Cholesky). The latter option is used throughout this work as it usually converges faster than the other options, but it requires more computer memory.

b. Time stepping criteria

The initial step size value is set as 1 day.

The time step multiplier (TTSMULT) generally has value from 1 to 2. The TTSMULT will reduce the accuracy of the solution at later times, but can reduce significantly simulation times. A maximum transport step size is required when TTSMULT is greater than 1.

The homogeneous system with hydraulic properties as of LF4 and the shallow along-channel system were used to examine convergence criteria. Mass balance calculations were obtained

from the model output (MT3DMS). The difference between the total mass in and out is calculated by MT3DMS (Zheng and Wang, 1999) for particular time as follows:

$$Mass\_error(\%) = \frac{(M_{In} - M_{out})}{0.5(M_{In} + M_{out})} 100 \qquad (6\text{-}15)$$

where

M_{In} is the total mass entering the model

M_{out} is the total mass leaving the model

Fig.6-10a,b shows mass balance errors calculated as a function of the concentration change criterion for homogeneous and heterogeneous systems respectively. Both homogeneous and heterogeneous systems show greater mass balance errors for greater concentration change criteria values. As with the flow simulation, the homogeneous systems are less sensitive. For the heterogeneous systems, the mass conservative is seen after about 50 years of simulation, followed by significant increase in error for system with relative high concentration change for convergence (Fig.6-10b). The value of 1 x 10^{-7}mg/l (concentration change for convergence) was therefore selected.

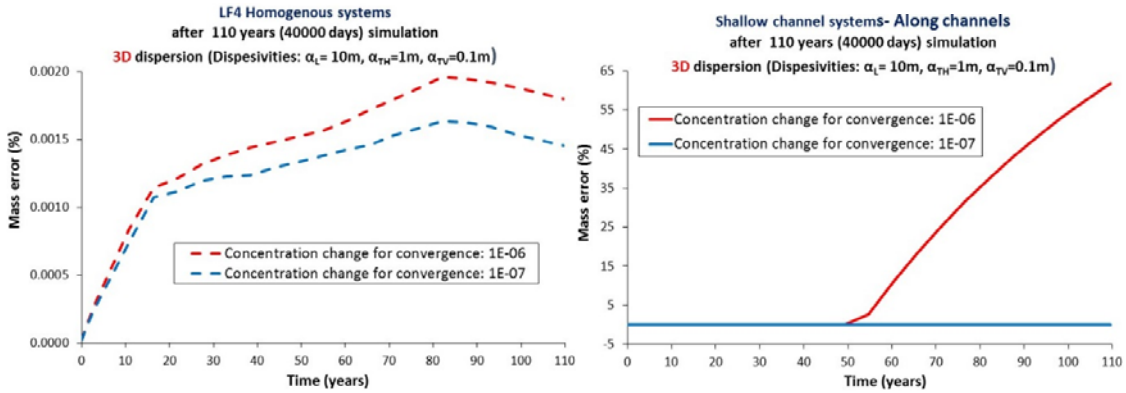

a) b)

Fig.6-10. Mass balance errors as function of convergence criterion for change in concentration (mg/l): a) homogeneous (LF4) model; b) heterogeneous (shallow channel system- along channels) model.

6.5.3 Numerical stability

The LF4-homogeneous system with no vertical transverse dispersion (2D dispersion: α_L=10m, α_{TH}=1m, α_{TV}=0m) was examined for an advection solution by several different methods: the finite difference (FD) methods with both up-stream and central-in-space weighting schemes; the finite difference upstream weighting-scheme method (FD) with small timestep (0.1 days) and small timestep multiplier (1.05); the method of characteristics (MOC) and its modified versions (MMOC and HMOC); and the total-variation-diminishing (TVD) method. Small transport timestep size (0.1 days) and small timestep multiplier (1.05) was also set to simulate the LF4-homogeneous system. These numerical solutions then were plotted in Fig.6-11. Note that in homogeneous systems with source thickness extending to full thickness of the systems (Fig.6-3), the system with 3D dispersion will numerically produce the same results as the same system with 2D dispersion (Fig.6-12b and Fig.6-12c).

Numerically, all cross profile breakthrough curves from the various methods for solving the advection-dispersion equation are identical (Fig.6-11). This is because the homogeneous channel system has a small Peclet number (P = 0.5/10 = 0.05) and the system is not advection-dominated. For computational efficiency purposes, the finite difference approach (FD) with the up-stream weighting scheme with Courant Number of 1, the first timestep size of 1 day, maximum timestep size of 100 days, and timestep multiplier of 1.2 was chosen to simulate the solute transport for all models.

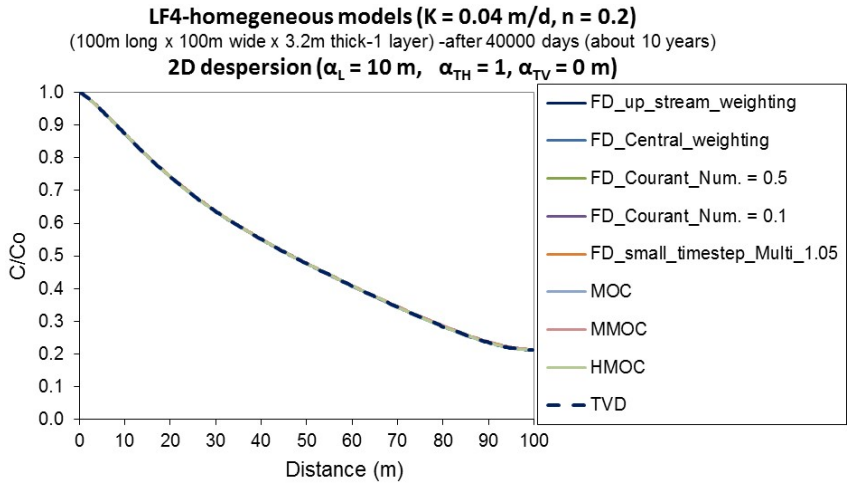

Fig.6-11. Concentration profiles for numerical solutions of the LF4-homogeneous models with longitudinal dispersivity (α_L=10 m), horizontal transverse dispersivity (α_{TH}=1 m), and vertical transverse diversisivity (α_{TV}=0 m). Advection solution by numerical models: FD upstream: finite difference solution with up-stream weighting scheme; FD central-in-space: finite difference solution with central-in-space weighting scheme; MOC: method of characteristics; MMOC: modified method of characteristics; HMOC: hybrid method of characteristics; and TVD: total variation diminishing.

6.5.4 Numerical solution versus analytical solution

The LF4-homogeneous system was set to run numerically and to compare with an analytical solution for the same system using the Domenico (1987) analytical solution. These numerical and analytical were run the same dispersivity scenarios: 1D dispersion (α_L=10m, α_{TH}=α_{TV}=0m); 2D dispersion (α_L=10m, α_{TH}=1m, α_{TV}=0m); and 3D dispersion (α_L=10m, α_{TH}=1m, α_{TV}=0.1m). Fig.6-13a-c shows concentration profiles for the numerical and analytical solutions for the LF4-homogeneous system.

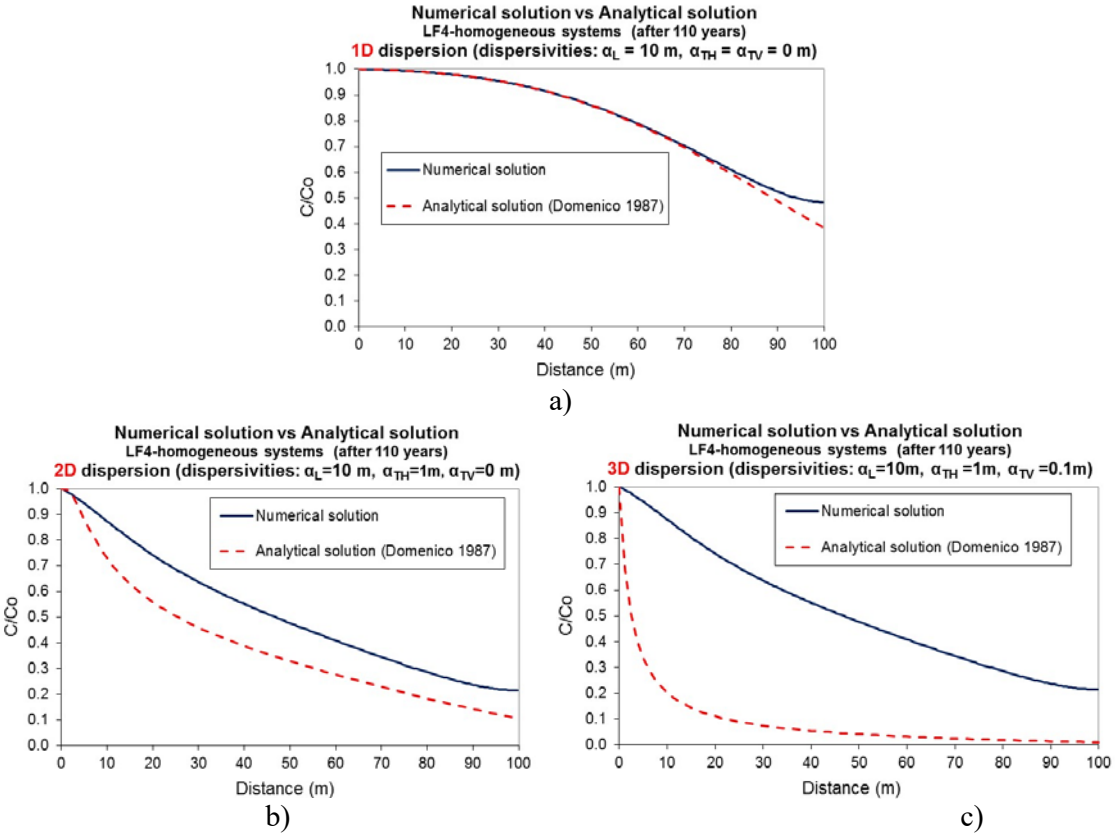

Fig.6-12. Cross profile for LF4-homogeneous models: numerical versus analytical solution, a) 1D dispersion models (α_L=10m, α_{TH}=α_{TV}=0m); b) 2D dispersion (α_L=10m, α_{TH}=1m, α_{TV}=0m); and c) 3D dispersion (α_L=10m, α_{TH}=1m, α_{TV}=0.1m).

The discrepancy between the analytical solution by Domenico (1987) and the numerical solution is greater for the cases where there is transverse dispersion, and greater for 3D than 2D dispersion. Where only longitudinal dispersion is included the differences are negligible except close to the downflow boundary (Fig.6-12a). Note that the numerical solutions for the 2D and 3D systems are identical as expected.

The difference between the numerical and analytical solutions is probably due to the differences between the boundary conditions of these two solutions. The width of the numerical model is finite (100 m), whereas the analytical solution assumes an infinite width. This will be most important when transverse dispersions are involved in the systems (Fig.6-12b,c), and almost

negletable for the systems with 1D dispersion (Fig.6-12a). For the systems with 1D dispersion, however, the numerical solution departs from the analytical solution at the downstream model boundary as the no-dispersive flux assumption of the numerical model makes the profile flat here. The systems where no transverse dispersion occurs, however, are unrealistic. Hence the results presented from the numerical model are for systems where there is no vertical dispersion to above or below the upper and lower source levels.

6.5.5 Numerical errors

6.5.5.1 Introduction

Numerical solutions for the transport equation present an approximation to the exact solution of the differential advection-dispersion equation. The first type of numerical error is numerical dispersion (Fig.6-13) which introduces a similar effect as seen with physical dispersion. The numerical dispersion is caused by truncation error, leading to the smearing of concentration fronts. Numerical dispersion can be controlled by reducing the grid spacing and time step, or adjusting the difference equation (using different or a combination of different weighting schemes).

The second type of numerical error is numerical oscillation. Numerical oscillation causes values higher (overshoot) and lower (undershoot) than the correct solution to be calculated (Fig.6-13). Overshoot can occur behind a moving front, and undershoot can occur ahead of the front and vice versa (Konikow, 2011). Undershoot can lead to calculation of negative concentrations. Overshoot, however, can introduce errors of equal magnitude which may be less easy to recognise. Numerical oscillation generally does not cause any error in mass balance, and often dampens out over time. In some cases, numerical oscillation can become unbounded, leading to an unstable solution or failure to converge. Numerical errors tend to minimize at the centre

of the front (i.e. relative concentration C/Co = 0.5). Minimizing numerical errors requires sufficiently fine grid spacing and small time steps; consequently these result in more computer storage and computational time.

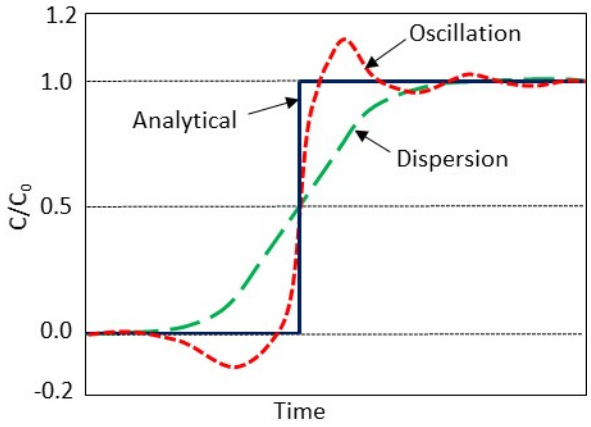

Fig.6-13. Breakthrough curves showing effects of numerical errors: numerical dispersion and oscillation.

6.5.5.2 Numerical oscillations

The upstream (backward) weighting scheme significantly reduces numerical oscillation, but does not solve the numerical dispersion problem for advection-dominated problems. The central-in-space weighting scheme can significantly reduce numerical dispersion, but cannot deal with numerical oscillation for advection dominated problems. Mixed Eulerian-Lagrangian approaches, including MOC, MMOC, and HMOC, solve the transport equation with dispersion/diffusion terms being solved by particle tracking methods and the advection term being solved by the finite difference method. The mixed Eulerian-Lagrangian methods can satisfactorily deal with advection-dominated problems, but may result in inaccurate mass balances.

The Peclet number for the channel systems being simulated so far is small (P= 0.5/10 = 0.05), indicating not advection-dominated systems and when simulated with the Finite Difference

(FD) method with an upstream weighting scheme should be free numerical oscillation. The solute transport simulations in the channel systems, however, show numerical oscillation, particularly for systems with no vertical dispersion and where flow is across the channels (Fig.6-24b,c and Fig.6-38b,c). Contaminant travelling along the channel for both the shallow and deep channel systems shows no numerical oscillation (Fig.6-23a-c and Fig.6-37a-c). The numerical oscillations were eliminating as transverse dispersions were included (Fig.6-24c vs Fig.6-24b vs Fig.6-24a for the shallow channel systems; Fig.6-38c vs Fig.6-38b vs Fig.6-38a for the deep channel systems).

These occurrences of numerical oscillation in the channel systems are caused by the presence of highly contrasting permeabilities next to each other, e.g. at the top of each sedimentary cycle. The advection-dispersion equation may be more hyperbolic in one area (or at one time) and more parabolic in another area (or at another time), leading to numerical errors, including numerical dispersion and oscillation somewhere in the model (Konikow, 2011).

In the channel systems, numerical oscillations appear around areas where there is laterally highly contrasting permeabilities (between LF1 and LF3; LF1 and LF4; LF1 and LF5) with about four orders of magnitude difference in permeabilities. These conductivity contrasts are located near the source boundary when solute is migrating across the channel. In these cases, the plumes first found it hard to travel through very low permeability zones (LF1) then immediately into relatively high permeability (LF5 in Fig.6-14a, and into LF3 or LF4 or LF5 in Fig.6-15a). The current numerical solutions with no vertical dispersion produce numerical errors (numerical oscillations) for these layers and their adjacent layers.

In the shallow channel system with flow across channel and with 2D dispersion, laterally highly contrasting permeabilities occur in in layer 4 (comprised of LF1 and LF5) that caused oscillations in this layer (undershoot) and in adjacent layers where there is no permeability

contrast as seen in layer 3 (LF5) (overshoot) and layer 5 (LF1) (undershoot and overshoot) at the same distance (about 3.5 m from the source boundary), causing numerical errors of up to 230% (Fig.6-14b). Apart from these three layers, there is no oscillation, even in very low permeability layers: layer 24 (LF1) and layer 25 (LF1) (Fig.6-14a,b).

In the deep channel system with flow across channel and with 2D dispersion, oscillations again occur at zones of highly contrasting permeability as seen at layer 1 (combination of LF1, LF3, and LF5), layer 25, layer 26, and layer 29 (combination of LF1 and LF4), layer 27 and layer 28 (combination of LF1 and LF5) (Fig.6-15a,b). These cause numerical error of up to 65% (Fig.6-15b). There is no effect of oscillations in adjacent layers to these layers as seen with layer 2 (combination of LF2 and LF3- just about an order of magnitude of permeability difference), and layer 30 (combination of LF2 and LF4- just above an order of magnitude of permeability difference), but some overshoot occurred in layer 24 located just above the layer 25 where there is highly contrasting permeability zone (LF1 and LF4) (Fig.6-15b).

The numerical oscillation completely disappears for the same channel systems, but where flow is along the channels (Fig.6-23a-c, and Fig.6-37a-c) and for all systems having vertical dispersion (Fig.6-23a, Fig.6-24a, Fig.6-37a, and Fig.6-38a). For systems with solute travelling along the channels, the plumes face layers having zones of high and low permeabilities as seen in layer 4 for the shallow channel system (Fig.6-8a and Fig.6-14a) and in layer 1 and from layer 25 to layer 29 for the deep channel system (Fig.6-9a and Fig.6-15a), and the plumes prefer spreading into the high permeability zone (LF5 and LF4 in these layers), causing no problem with numerical oscillations. For all systems having vertical dispersion (α_{TV} = 0.1 m), the plumes can spread vertically through very low permeability but relatively thin (0.1 m) layers.

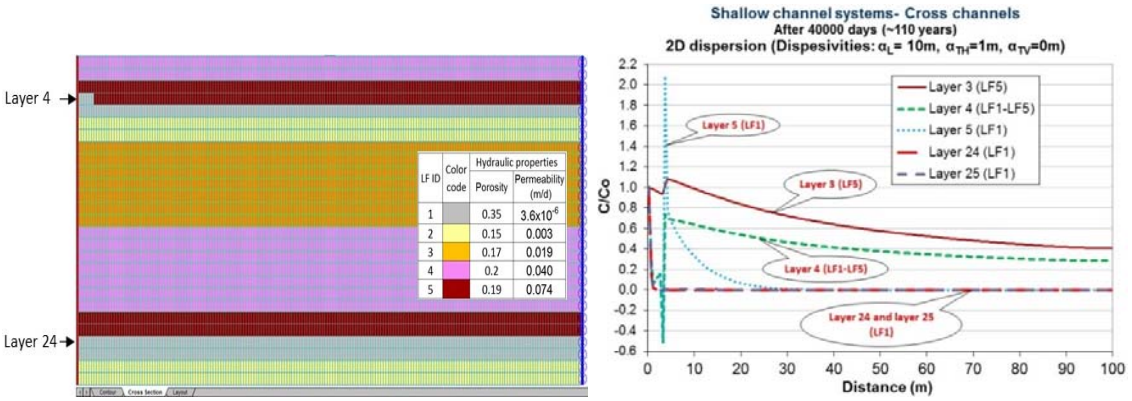

a) b)

Fig.6-14. Numerical oscillations as effect of conductivity contrast in layers in the 2D-dispersion shallow channel systems- cross channels: a) vertical cross section (flow from left to right); and b) concentration profiles.

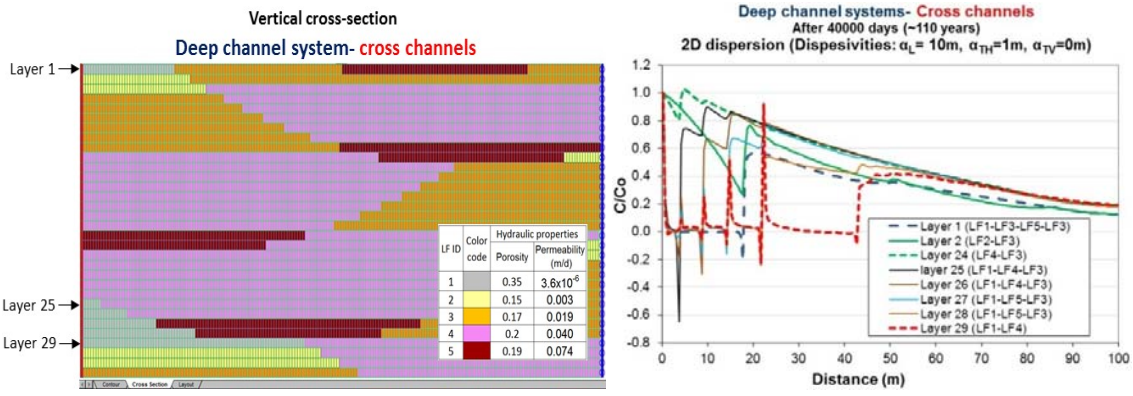

a) b)

Fig.6-15. Numerical oscillations as effect of conductivity contrast in layers in the 2D-dispersion deep channel systems- cross channels: a) vertical cross section (flow from left to right); and b) concentration profiles.

6.5.5.3 Solutions for the numerical oscillations

The numerical oscillation in the solute transport process of the channel systems is due to the highly contrasting permeability zones. To solve this numerical oscillation, the following approaches can be used

1) Adding vertical dispersion - this had already been done;

2) Using the currently used Finite Difference (FD) method, but with small Courant number, and small transport time frame, the Hybrid method of characteristics (HMOC) method, and the variation diminishing (TVD) method;

3) Refining the model grid in the very low permeability layers and where there is highly contrasting permeabilities;

4) Setting no-flow boundaries for areas occupied by the very low permeability zones; and

5) Applying problem with diffusion represented in the very low permeability (LF1) zones.

Since the same numerical errors occur in 1D and 2D dispersivity systems, only 2D systems need be examined. Methods 3 and 4 were attempted, and Method 2 was attempted but only in the case of the shallow channel system with solute migrating across channels because of computational time and computer memory limitations. Applying diffusion in the very low permeability units requires an alternative setting up of the system and it was beyond scope of this chapter. The last method, therefore, could be interesting for future work.

Since the use of the Finite Difference (FD) with upstream-weighting scheme with small Courant Number (0.5), and with transport time restriction (small first timestep size (0.1 days), small maximum timestep size (10 days)), HMOC, TVD methods are very expensive in computational time, only shallow channel system in which solute travelling across channels was examined for numerical oscillation.

Fig.6-16a-d shows plots of concentration profiles for the original model (advection portion solved by the Finite Different (FD) method with upstream-weighting scheme), FD method with upstream-weighting scheme and with small transport-time frame, TVD, and HMOC respectively. There is no improvement over the original method, and the HMOC even shows

slightly more oscillations (Fig.6-16c). This is because the channel system has a very low Peclect Number (0.05), and is therefore not an advection-dominated problem, so the use of FD method with upstream-weighting, using small timesteps, and using HMOC or TVD will not help- it is the permeability contrasts that cause the problem.

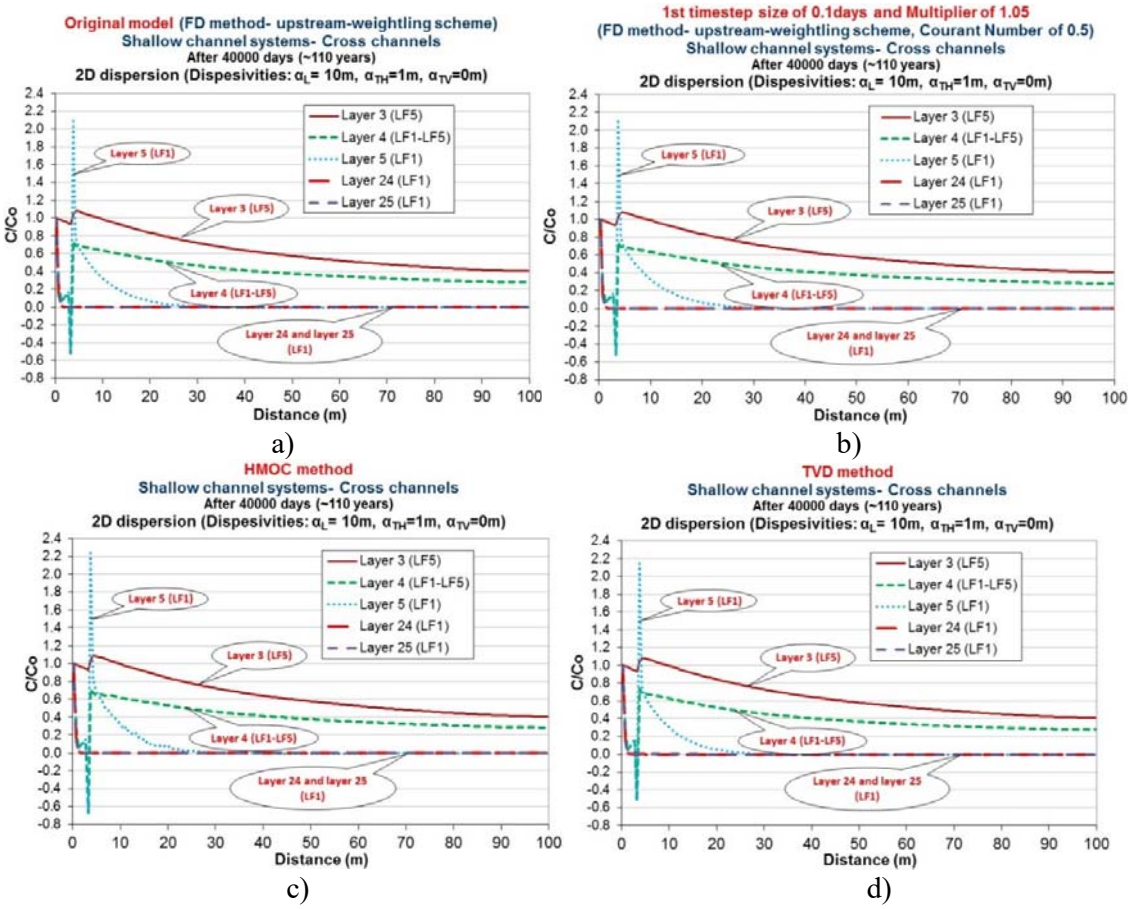

Fig.6-16. Profiles for the shallow channel system of 2D dispersion with solute migrating across channels showing numerical oscillations: a) the original model solved with FD method with upstream-weighting scheme (Courant Number of 1, first timestep size of 1 day, maximum timestep size of 100 days, and timestep multiplier of 1.2); b) FD method with upstream-weighting scheme with small Courant Number (0.5), small first timestep size (0.1 days), small maximum timestep size (10 days), and small timestep multiplier (1.05); c) the systems solved by HMOC method; and d) the system solved by TVD method.

Spatial discretization was refined laterally as shown in Fig.6-17. Grid refinements of a regular spacing of 0.1 m were set for the whole width of the source (10 m), increasing from the source to 0.5 m in distant cells.

Vertical refinements were made for the channel systems at layers where there are highly contrasting permeabilities. For the shallow channel system, layer 4 (combining of LF1 and LF5) and layer 5 (LF1) (Fig.6-18a) were each further divided into 5 layers, creating a refined model for the shallow channel system with 35 layers (Fig.6-18b). The same vertical refinements were applied for the deep channel system: layer 1 (combining LF1, LF3, LF5, and LF3), layers 25 and 26 (combining LF1 and LF4), layers 27 and 28 (combining LF1 and LF5), and layer 29 (combining LF1 and LF5) were each divided further into 5 layers, resulting in the refined grid deep channel system having 56 layers (Fig.6-19b).

This refinement created model grid sizes of 330 rows and 220 columns and 35 layers for the shallow channel system and 56 layers for the deep channel system. Consequently, more computer storage and computational time were required to run these models.

For the shallow channel system, the numerical oscillations were almost removed with no overshoot from layer 9 to layer 13 (originally layer 5 (LF1)), but still have slight overshoot in layer 3 (LF5) (Fig.6-20b). This refined-grid model reduces numerical error to about 5% (Fig.6-20b), and further refinements can address this oscillation, but can also require more computational capacity and time to simulate such models.

There is little improvement for the deep channel system. There is no overshoot in layer 51 (originally layer 29 (combination of LF1 and LF4)), but more overshoot at higher layers: layer 28 (originally layer 24 (combination of LF4 and LF3), layer 36 (originally layer 26 (combination of LF1 and LF4)), and layer 31 (originally layer 25 (combination of LF1 and LF4)) (Fig.6-21b). The refined grid reduces numerical error to about 38%, and this can be also further improved by more refinement for the layers at and adjacent to layers which present highly contrasting permeabilities, and this in turn also require more computer storage and computational time to simulate.

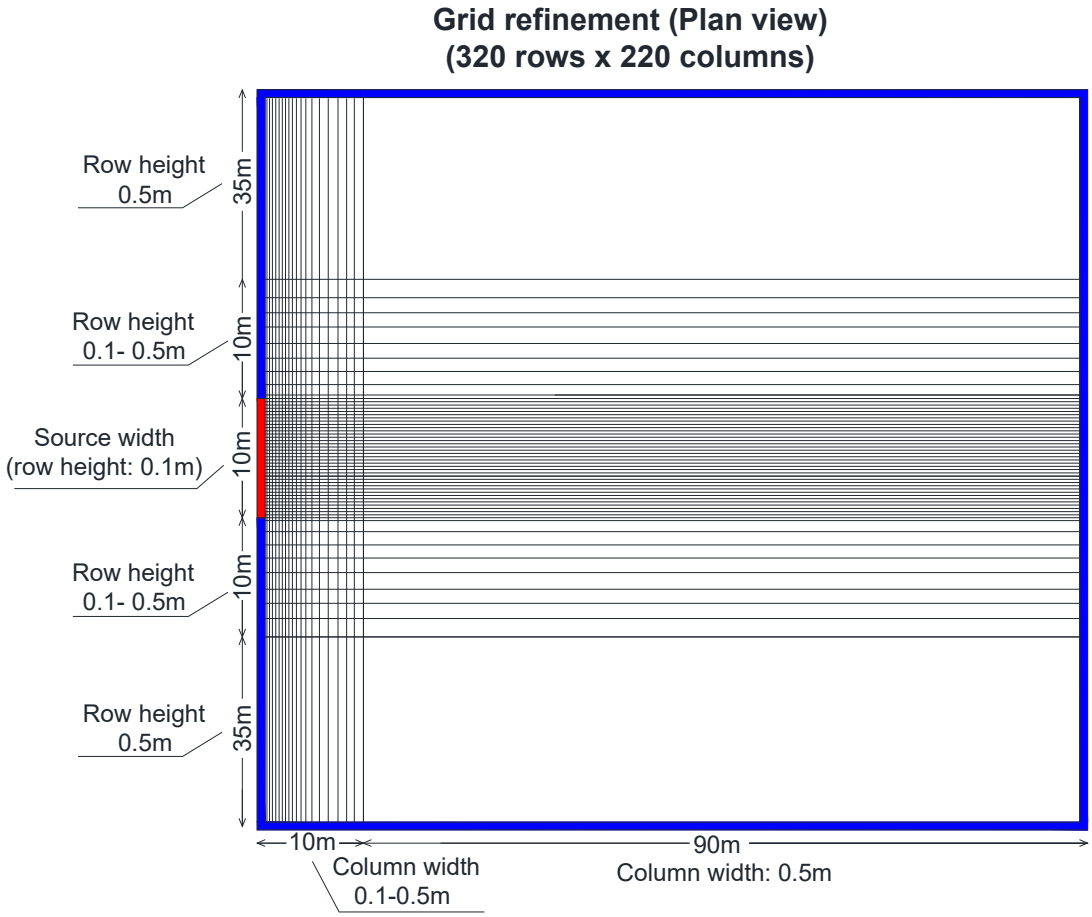

Fig.6-17. Schematic of plan view of model grid refinement as a solution for numerical oscillations effect.

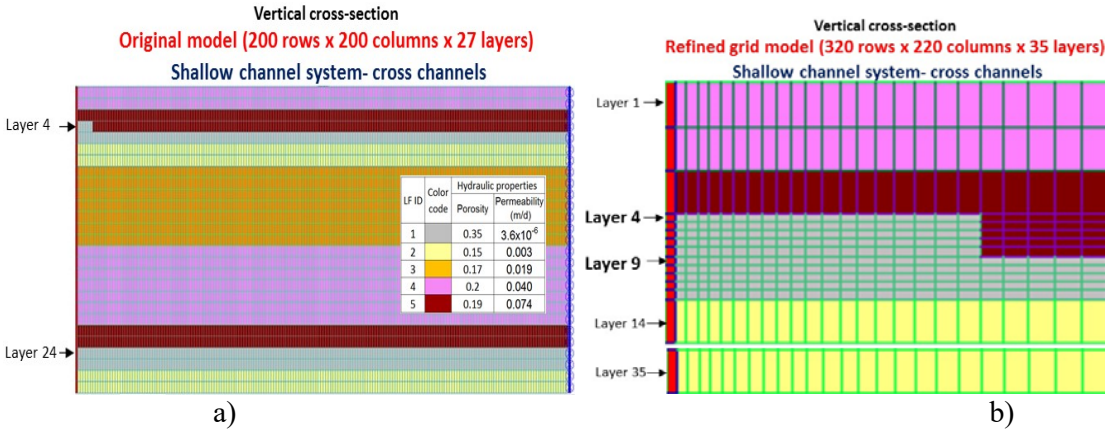

a) b)

Fig.6-18. Vertical cross-section for the shallow channel systems with solute migrating across channel (from left to right): a) original model (200rows x 200 columns x 27 layers); b) refined grid model (320 rows x 220 columns x 35 layers)- vertical refined layers for the layer 4 (combing LF1 and LF5) and layer 5 (LF5) from the original model.

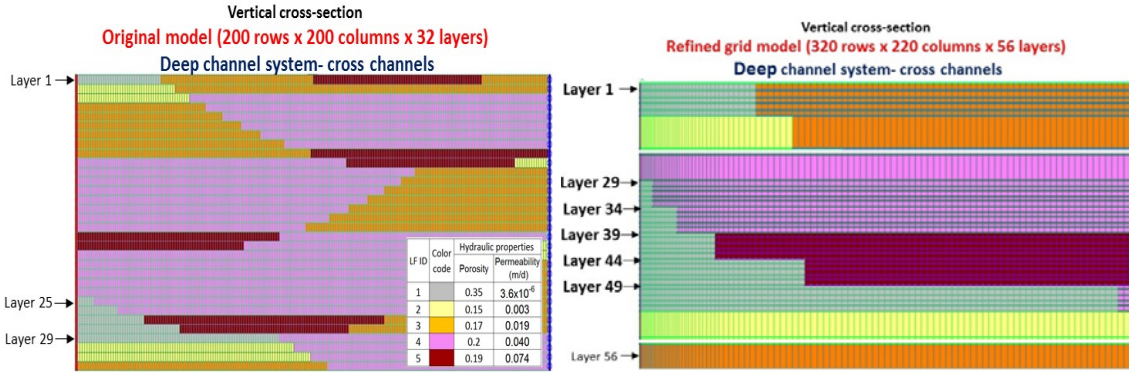

a) b)

Fig.6-19. Vertical cross-section for the deep channel systems with solute migrating across channel (from left to right): a) original model (200 rows x 200 columns x 32 layers); b) close view at the refined grid model (320 rows x 220 columns x 56 layers)- vertical refined layers for the layer 1 (LF1-LF3-LF5-LF3), layer 25 to layer 26 (LF1-LF4), layer 27 and layer 28 (LF1-LF5), and layer 29 (LF1-LF4) from the original model.

Finally, the LF1-bearing zones were modified as zones of no-flow for solute migrating across both the shallow and deep channel systems without vertical dispersivity (α_L = 10 m, α_{TH} = 1 m, and α_{TV} = 0m), while all other model parameters and boundary conditions remained unchanged. Fig.6-20c and Fig.6-21c show concentration profiles obtained. This solution is obviously efficient as it made numerical error of less than 1% with the numerical oscillations now almost all disappeared and solute transport in other parts of the models comparable to the initial models. This also suggests that the very low permeability (LF1) units do not carry any flow, and it produces very good approximations for the transport systems with numerical error of less than 1% (Fig.6-20c and Fig.6-21c).

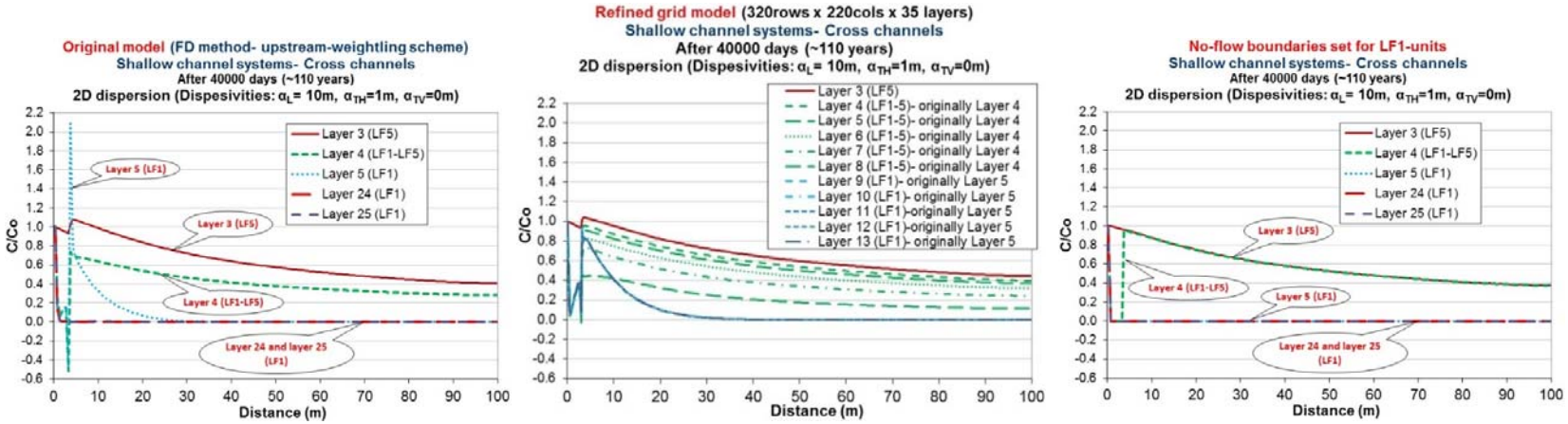

a) b) c)

Fig.6-20. Concentration profiles for the shallow channel systems- cross channels: a) original model; b) refined grid model; and c) no flow set for LF1-units model.

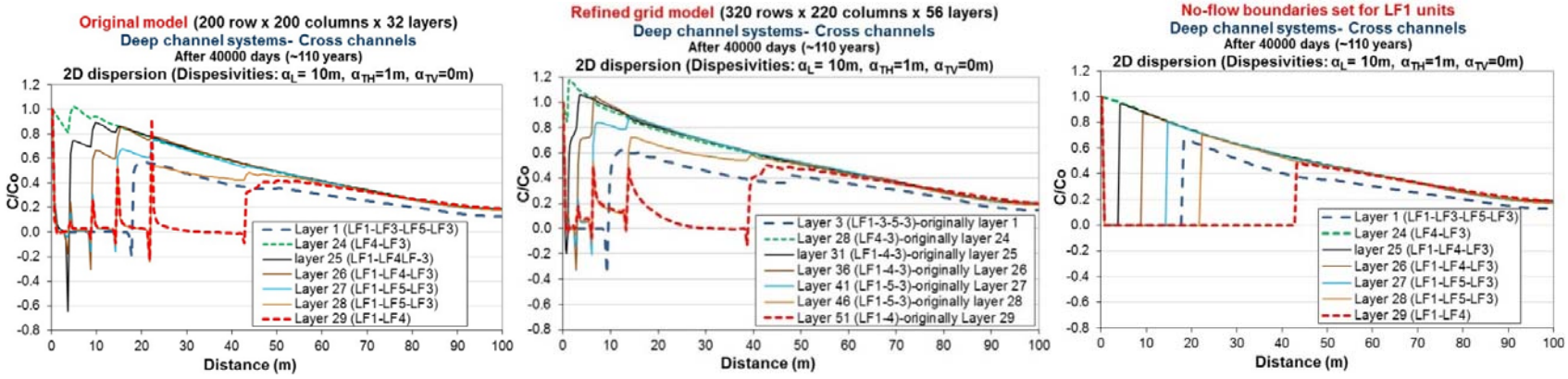

a) b) c)

Fig.6-21. Concentration profiles for the deep channel systems- cross channels: a) original model; b) refined grid model; and c) no flow set for LF1-units model.

6.5.6 Concluding remarks for the numerical issues

Given the heterogeneity of the channel structures, selecting appropriate boundary conditions is particularly important. Relatively tight convergence criteria for both flow and solute transport is critical for solving the flow and transport equations properly, and to provide reasonable mass balances.

Because of different model domains and boundary conditions, the MT3DMS numerical solution and Domenico's (1987) analytical solution did not agree for systems involving transverse dispersions. Where no transverse dispersion is represented, the numerical and analytical solutions were very similar except at the downstream boundary where again different boundary conditions become important.

Numerical oscillations caused by highly contrasting permeabilities zones were minimised by spatially refining model grids, and largely solved by representing LF1 as impermeable units.

All systems were then simulated with the initial assumption (e.g. systems of isotropic hydraulic properties without diffusion), tight convergence criteria for flow and solute transport, small Peclect Number (0.05), Courant Number ≤ 1.

In general, these investigations indicate that particular attention should be given to making assumptions, spatial and temporal discretisations, representing dispersion, and selecting methods to solve the advection and non-advection components for heterogeneous porous media, even in relatively simplified systems such have been used here.

Interesting future work would include investigation of the effects of enabling diffusion, greater spatially refining grids. These will in turn require greater computer capacity and computational time to simulate.

6.6. Results and discussion

6.6.1 Introduction

The shallow and deep channel systems and their equivalent homogeneous systems were run with sets of different dispersion directions allowed: 1D dispersion (i.e. α_L = 10m, $\alpha_{TH} = \alpha_{TV}$ = 0m); 2D dispersion (i.e. α_L = 10m, α_{TH} = 1m, α_{TV} = 0m); and 3D dispersion (i.e. α_L = 10m, α_{TH} = 1m, α_{TV} = 0.1m). For each type of channel system and each set of dispersivities, middle-plume concentration profiles, breakthrough curves at the downstream boundaries, and point breakthrough curves at the monitoring wells (Fig.6-3, Fig.6-8a,b, and Fig.6-9a,b) for solute migrating along and cross channels are plotted. Breakthough curves are plotted at the downstream boundaries for the models with refined grids with no-flow set for LF1 systems and with 2D dispersion. Breakthrough curves for different locations of the monitoring wells at downstream boundaries for the equivalent homogeneous (hydraulic property averaged) systems (Table 6-6) with bulk permeabilites estimated from flow models, and porosities) and channel systems (heterogeneous) were compared.

The LF4 homogeneous systems were set to run for systems with 1D dispersion (α_L = 10m, $\alpha_{TH} = \alpha_{TV}$ = 0m), 2D dispersion (α_L = 10m, α_{TH} = 1m, α_{TV} = 0m), and 3D dispersion (α_L = 10m, α_{TH} = 1m, α_{TV} = 0.1m). Homogeneous systems with hydraulic properties of LF2, LF3, and LF5 were run with 3D dispersion α_L = 10m, α_{TH} = 1m, α_{TV} = 0.1m).

The solute transport models, their equivalent homogeneous models, and lithofacies-homogeneous models were run for a time of 40000 days (about 110 years), which is two times the eslaped time expected for solute movement to reach breakthrough (i.e. C/C_0 = 0.5). The breakthrough curves at the downstream boundary were calculated as a relative ratio of outlet

(at downstream boundary) concentration mass (M_{out}) to inlet (at upstream boundary) conentration mass (M_{in}).

6.6.2 The shallow channel systems

6.6.2.1 Profiles and breakthrough curves

Solute migrating along and across the shallow channel systems were simulated and middle-plume concentration profiles and breakthrough curves at the downstream boundaries were plotted. Fig.6-22a-d shows general 3D views of concentration plumes for the shallow channel systems with 3D dispersion for flow along and across channels. Fig.6-23a-c and Fig.6-24a-c show concentration profiles for the shallow channel systems with various dispersivities for solute migrating along and across channels respectively. Longitudinal dispersion causes plume spreading along the flow paths, while horizontal (vertical) dispersion leads to spreading of the plume horizontally (vertically) perpendicular to the flow paths, leading to less concentration at the centre of the plumes. The channels systems where only longitudinal dispersion is present (α_L = 10m, α_{TH} = α_{TV} = 0 m) have highest concentration in centre of plumes (Fig.6-23c and Fig.6-24c). When horizontal transverse dispersion (α_{TH} = 1m) was added, the concentration in the centre of plumes reduces (Fig.6-23b and Fig.6-24b), and they are smallest if vertical dispersion is added (α_{TV} = 0.1m) (Fig.6-23a and Fig.6-24a).

There is not much difference between the profiles for the systems with 3D dispersion for the along and across channel cases (Fig.6-23a vs Fig.6-24a), but there are differences for the 1D and 2D dispersion cases (Fig.6-23b vs Fig.6-24b; Fig.6-23c vs Fig.6-24c). For the 3D dispersion cases (α_L = 10 m, α_{TH} = 1m, α_{TV} = 0.1m), with the thickesses of the systems are relative small (2.7 m and 3.2 m thick for the shallow and deep channel system respectively) compared with

system width and length (100 m wide and 100 m long), even the small vertical transverse dispersivity (α_{TV} = 0.1m) is enough for mixing vertically after 100 m downstream (Fig.6-23a and Fig.6-24a). The 1D and 2D dispersion models, however, have different profiles (Fig.6-23b,c and Fig.6-24b,c).

The profiles for the shallow channel systems with solute moving across the channels without vertically spreading both show numerical oscillation as for LF1-bearing layers. This is due to effect of the significant contrast between very low and high permeability layers (e.g. LF1 in layer 5 LF5 in layer 3 above) (Fig.6-8a,b and Fig.6-14a).

The numerical oscillation completely disappears for the same channel systems, but where flow is along the channels (Fig.6-23a-c) and for all systems having vertical dispersion (Fig.6-23a, Fig.6-24a). For systems with solute travelling along the channels, the plume abuts layers having zones of high and low permeabilities (e.g. layer 4 for the shallow channel system), but the plumes can spread into the adjacent high permeability zone (LF5), causing no problem with numerical oscillations. When vertical transverse dispersion was added in the systems (the 3D dispersion), the plumes can spread through very low permeability but thin (0.1 m) layers.

The breakthrough curves at the downstream boundaries were shown on Fig.6-25a-c and Fig.6-26a-c. Note that breakthrough concentration for travel cross channels with 2D dispersion case for the refined gird and no-flow set for LF1 systems for solving the oscillation above are plotted on Fig.6-26b. For the channel systems with 3D dispersion, additional homogeneous models of hydraulic properties (porosity and permeability) as that of LF3, LF4, LF5, and the equivalent homogeneous model of average porosity and permeability from the shallow channel system (Table 6-2 and Table 6-6: with permeabilities estimated from Modflow models) were set to run to compare with the channel systems (heteorogeneous models) (Fig.6-25a, and Fig.6-26a). For

other transport systems without vertical spreading, only homogeneous systems of porosities and permeabilities as those of LF4 and equivalent homogeneous systems of averaged porosities and permeabilities from the channel systems were compared to the channel systems (Fig.6-25b,c, and Fig.6-26b,c). The identical breakthrough cuvres seen in Fig.6-26b indicates reasonable results for the channel system compared with the refined grid and no-flow set for LF1 unit systems.

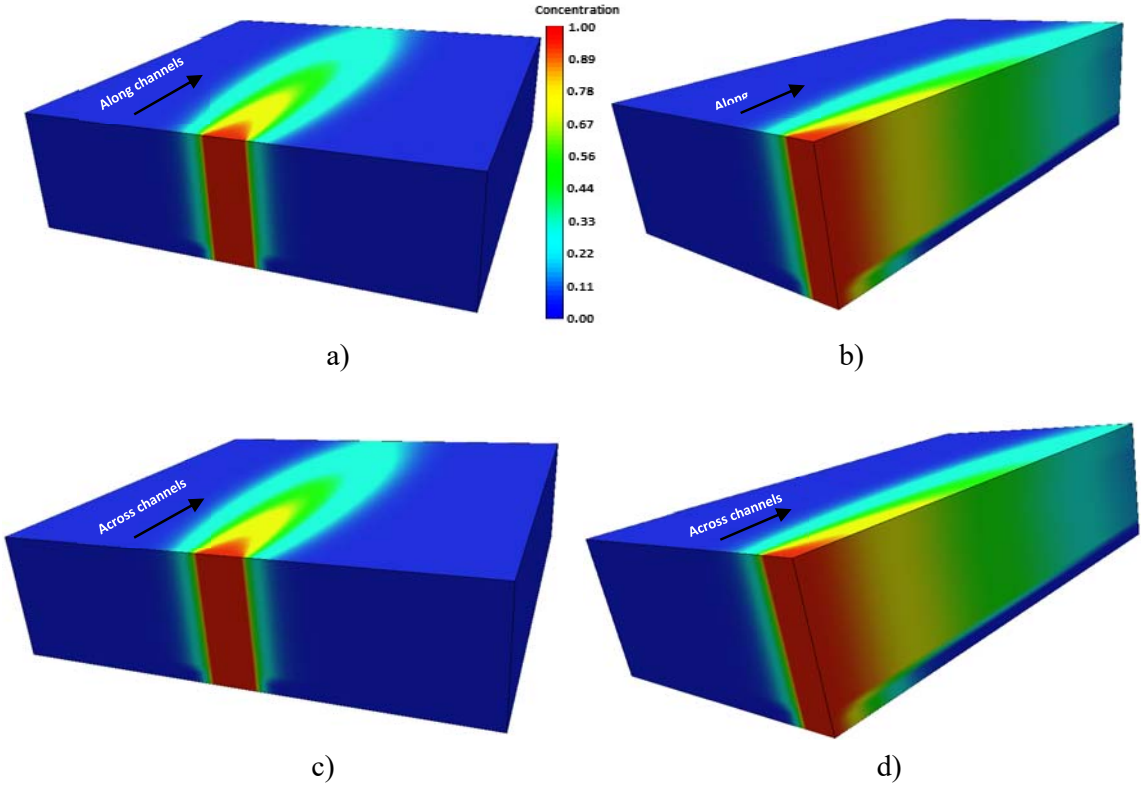

Fig.6-22. The shallow channel systems with 3D dispersion after 110 years of simulation: a) flow along channels- whole model; b) flow along- half of model; c) flow across channels- whole model; d) flow across channels- half model.

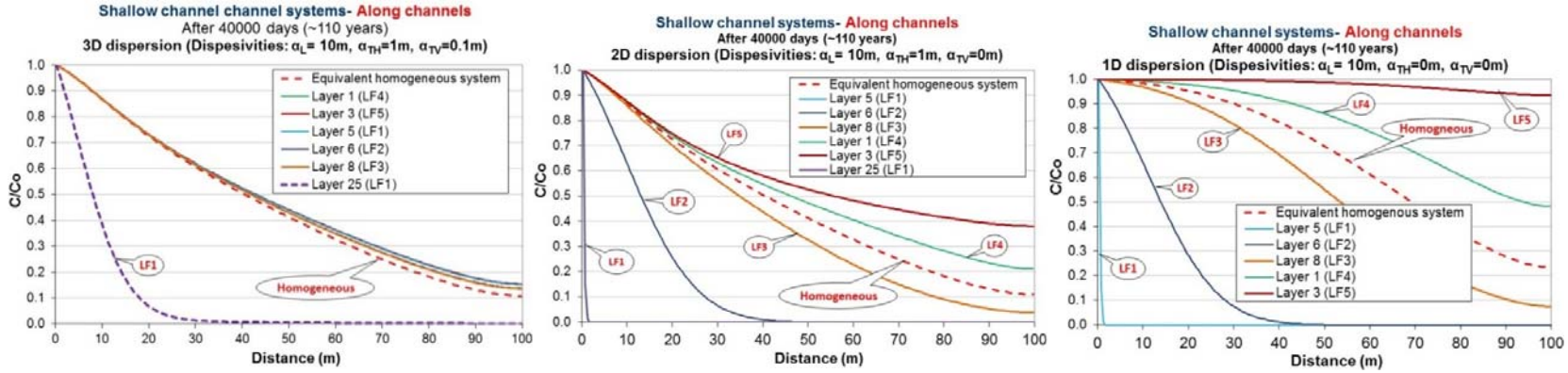

a) b) c)

Fig.6-23. Cross profiles for the shallow channel systems- solute migrating along channels:
a) 3D dispersion; b) 2D dispersion; and c) 1D dispersion.

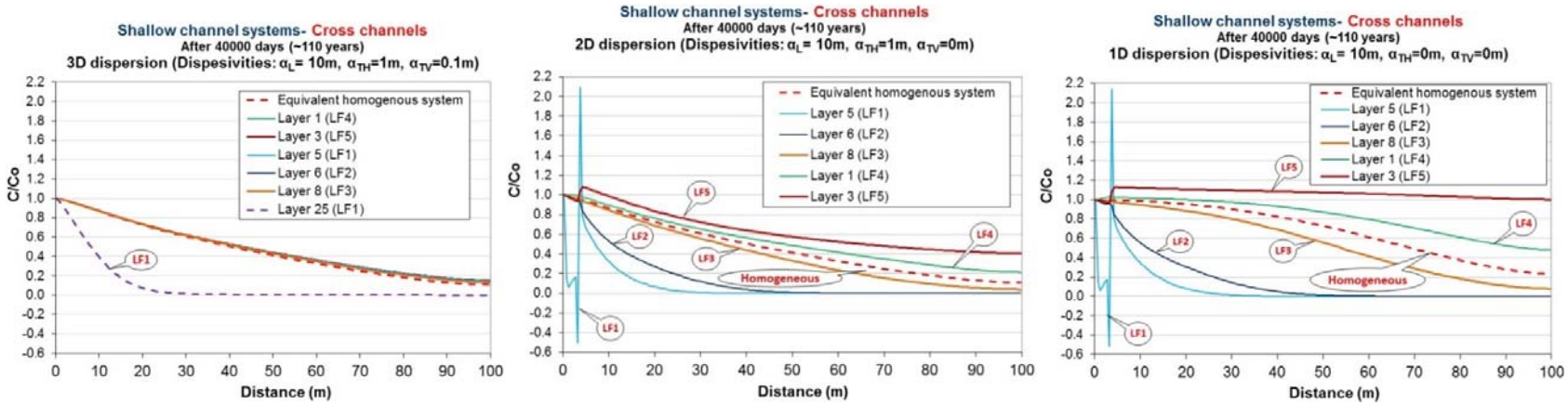

a) b) c)

Fig.6-24. Profiles for the shallow channel systems- solute migrating cross channels:
a) 3D dispersion; b) 2D dispersion; and c) 1D dispersion.

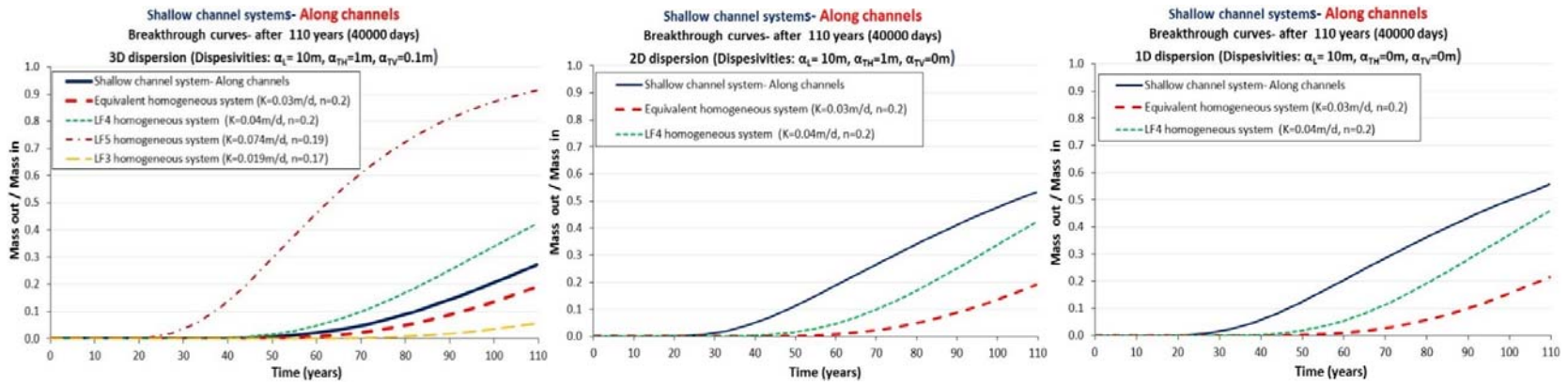

a) b) c)

Fig.6-25. Breakthrough curves at downstream boundaries for the shallow channel systems- solute migrating along channels: a) 3D dispersion; b) 2D dispersion; and c) 1D dispersion.

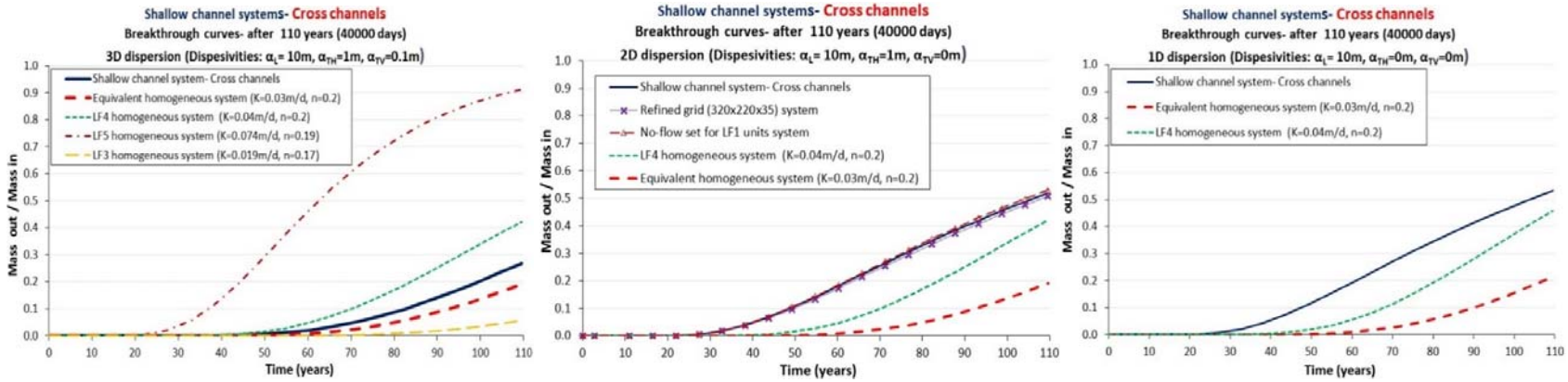

a) b) c)

Fig.6-26. Breakthrough curves at downstream boundaries for the shallow channel systems- solute migrating across channels: a) 3D dispersion; b) 2D dispersion (including the refined grid, and no-flow set for LF1 systems); and c) 1D dispersion.

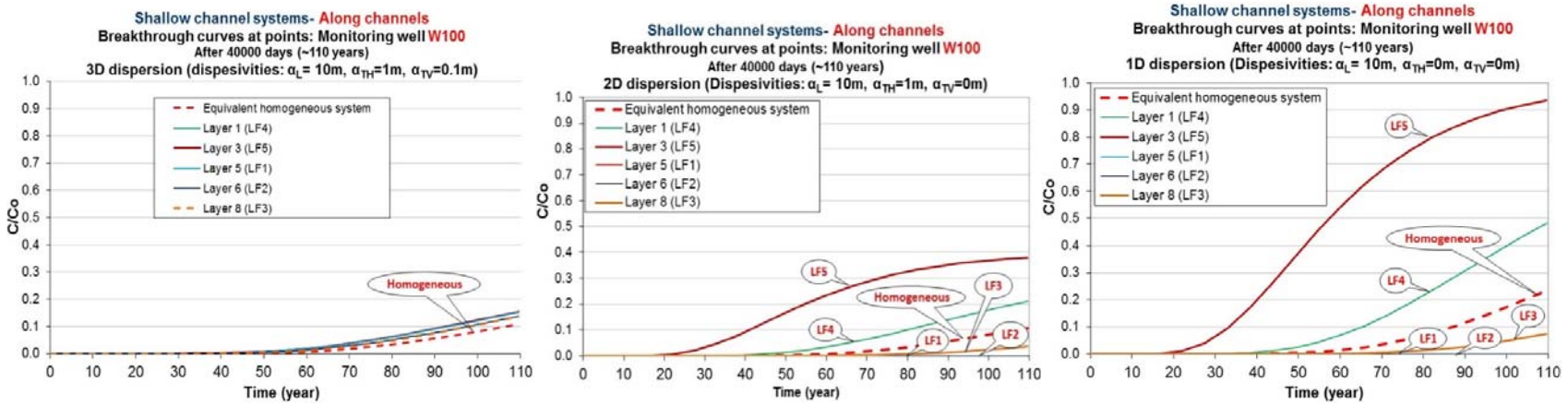

a) b) c)

Fig.6-27. Breakthrough curves at points of the monitoring well W100 for the shallow channel systems- solute migrating along channels: a) 3D dispersion; b) 2D dispersion; and c) 1D dispersion.

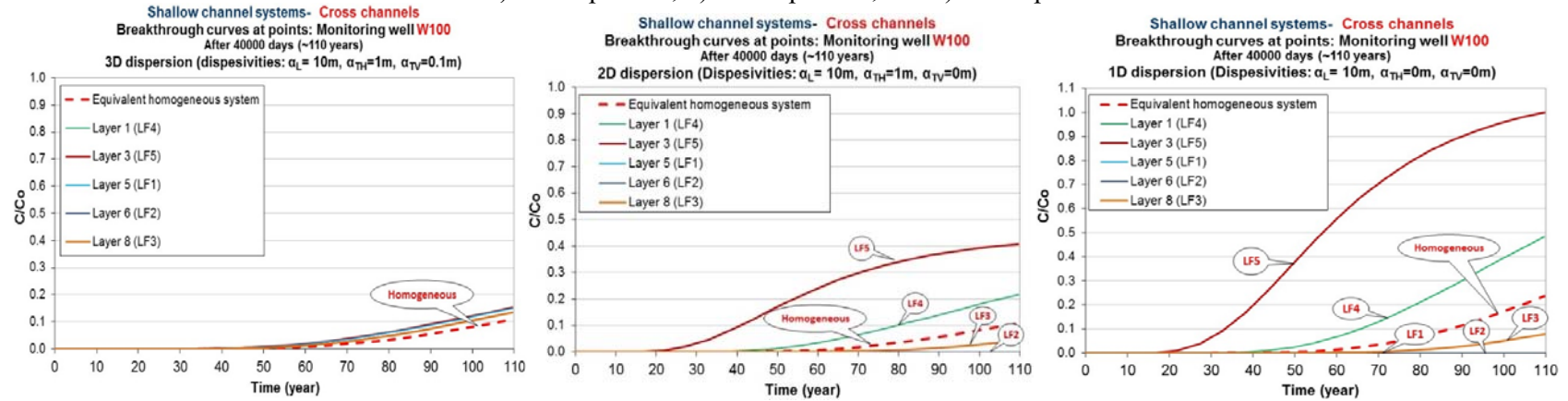

a) b) c)

Fig.6-28. Breakthrough curves at points of the monitoring well W100 for the shallow channel systems- solute migrating cross channels: a) 3D dispersion; b) 2D dispersion; and c) 1D dispersion.

In the shallow channel systems, breakthrough curves for the solute migrating along and across channels are very similar for each set of dispersivities (Fig.6-25a vs Fig6-26a, Fig.6-25b vs Fig.6-26b, and Fig.6-25c vs Fig.6-26c). This is due to the similar channel structures in the shallow channel systems with solute migrating along (Fig.6-8a) and cross (Fig.6-8b) channels. As with concentration profiles, breakthrough curves for the 3D dispersion show less concentration than those at breakthrough for the correpsonding 2D and 1D dispersion systems as in the 3D dispersion systems the plumes are most spread, then 2D dispersion systems and 1D dispersion systems having least spreading plumes. The equivalent porous medium models underestimate breakthrough concentrations for both along and across systems (Fig.6-25a-c and Fig.6-26a-c), but only just and are quite good estimates of concentrations.

Within the shallow channel systems with 1D and 2D dispersion, higher permeability layers show quicker spreading of the solute plumes. The LF5-bearing layer (the most permeable layer) causes the plume to spread most quickly, then the LF4-bearing layer, and so on; the LF1-bearing layers (very low permeable layers) have slowest movements of plumes and also cause numerical errors as already mentioned.

The breakthroughs for the shallow channel systems are probably controlled by highly permeable layers for both along- and across- flow system with all dispersion scenarios (Fig.6-25a-c, and Fig.6-26a-c), with lateral dispersion over the relatively small vertical distances being very important.

Point breakthrough curves at the monitoring well W100 (Fig.6-3 and Fig.6-8a,b), the moniroting well at the middle of the downstream boundary, at the downstream boundaries also provide similar trend for both systems of solute moving along and cross channels (Fig.6-27a-c and Fig.6-28a-c). Note that as with the middle-plume profiles and breakthrough curves at the

downstream boundaries, concentration is lower if the plume is spread. Oscillation occurs in the breakthrough curve for shallow channel 1D dispersion systems in which solute across channels (Fig.28c).

Since the sources were fully penetrating, there is no difference for middle-plume profile and breakthrough curves for the equivalent homogeneous systems of 2D and 3D dispersion, but there is a difference between the heterogeneous systems, especially in 3D dispersion as solute goes quickly in high permeability layers and then disperses vertically into low permeability layers (Fig.6-23a vs Fig.6-23b; Fig.6-24a vs Fig.6-24b; Fig.6-25a vs Fig.6-25b; Fig.6-26a vs Fig.6-26b; Fig.6-27a vs Fig.6-27b; Fig.6-28a vs Fig.6-28b).

6.6.2.2 Breakthrough curves at points for equivalent homogeneous and heterogeneous systems

Concentration cross sections at the downstream boundaries are plotted for different dispersivities for both the along-flow shallow channel model and its equivalent homogeneous (hydraulic properties averaged) model (Fig.6-29a,b; Fig.6-31a,b; and Fig.6-33a,b) after a simulation time of 110 years with 1D, 2D, and 3D dispersion. Breakthrough curves for these monitoring points are also plotted on Figs.6-30a,b; 6-32a,b; 6-34a,b.

The monitoring points in the shallow channel systems show greater concentrations than in the equivalent homogeneous systems. This supports what has been found above for the shallow channel systems, i.e. that the averaged-hydraulic-property (homogeneous) systems underestimate breakthrough concentrations, albeit slightly.

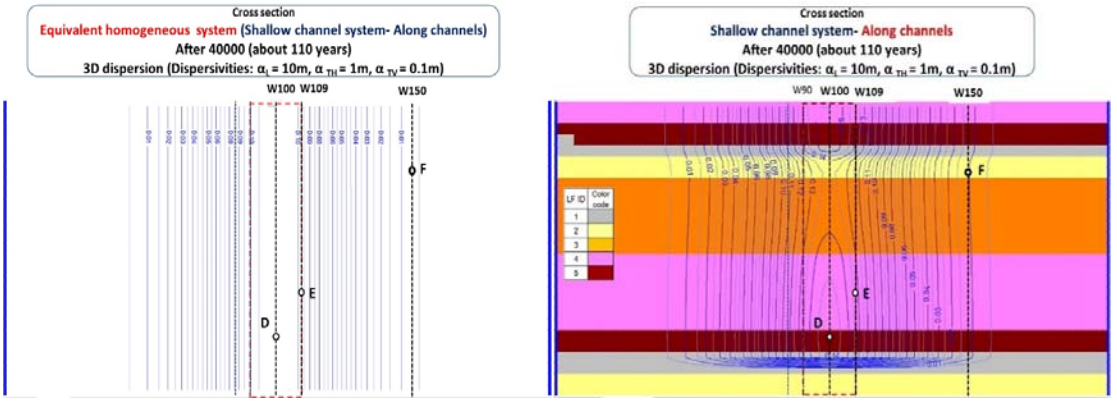

a) b)

Fig.6-29. Concentration cross sections at downstream boundaries showing points (D, E, F) at monitoring wells (W100, W109, W150) for 3D dispersion systems (α_L = 10m, α_{TH} = 1m, α_{TV} = 0.1m): a) Equivalent homogeneous system; b) the shallow channel system - along channels.

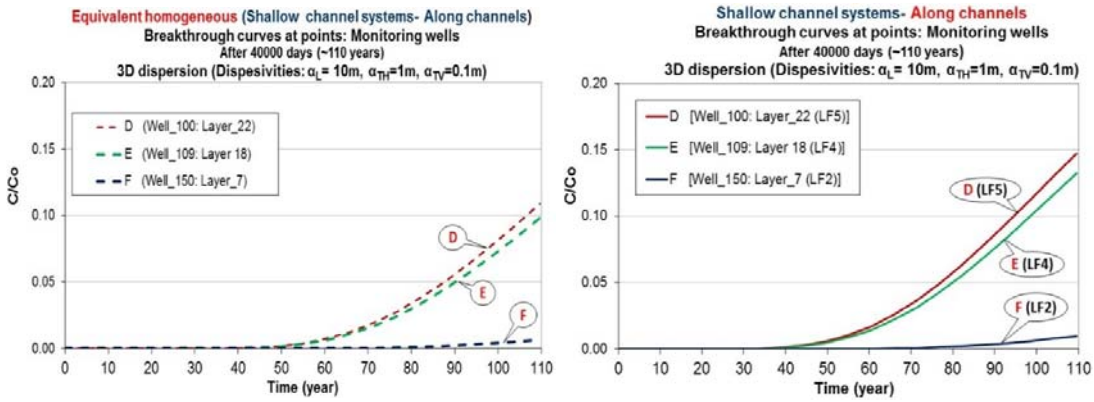

a) b)

Fig.6-30. Breakthrough curves at the points (D, E, and F) at the monitoring wells in the Fig.6-29 for a) equivalent homogeneous system; b) the shallow channel system - along channels.

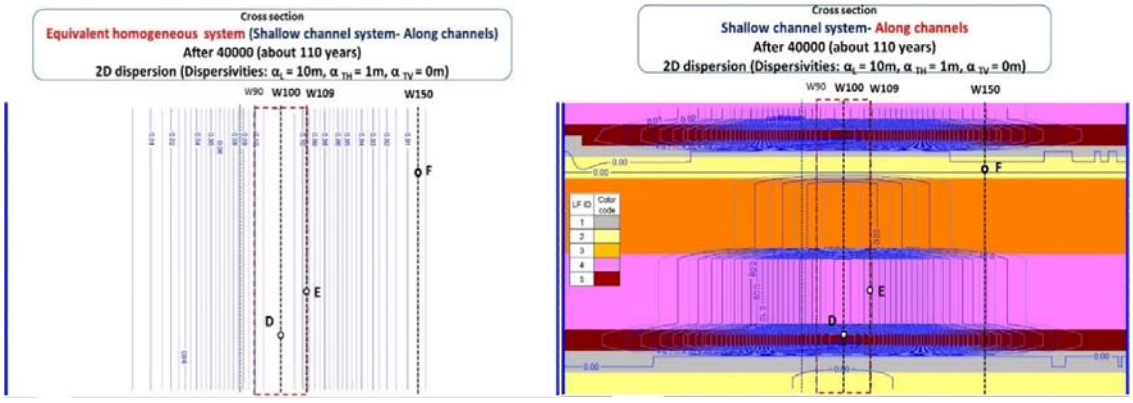

a) b)

Fig.6-31. Concentration cross sections at downstream boundaries showing points (D, E, F) at monitoring wells (W100, W109, W150) for 2D dispersion systems (α_L = 10m, α_{TH} = 1m, α_{TV} = 0m): a) equivalent homogeneous system; b) the shallow channel system - along channels.

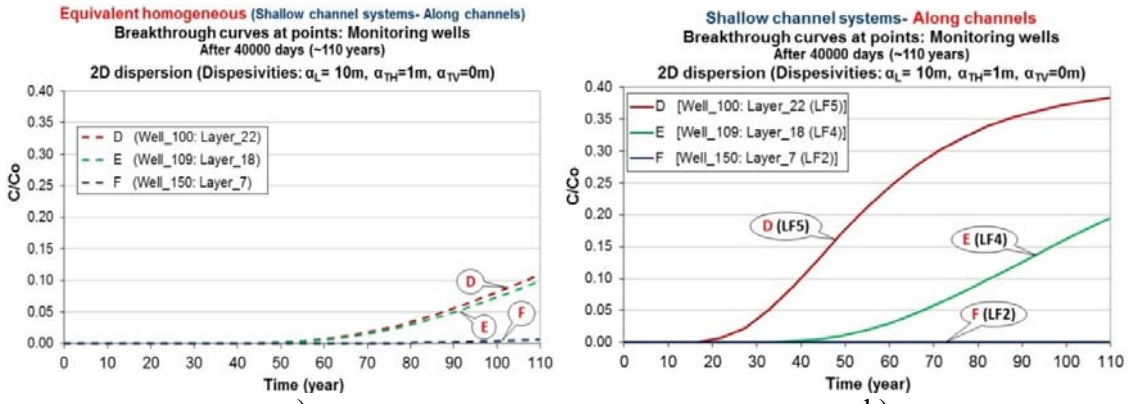

a) b)

Fig.6-32. Breakthrough curves at the points (D, E, and F) at the monitoring wells in the Fig.6-31 for: a) equivalent homogeneous system; b) the shallow channel system - along channels.

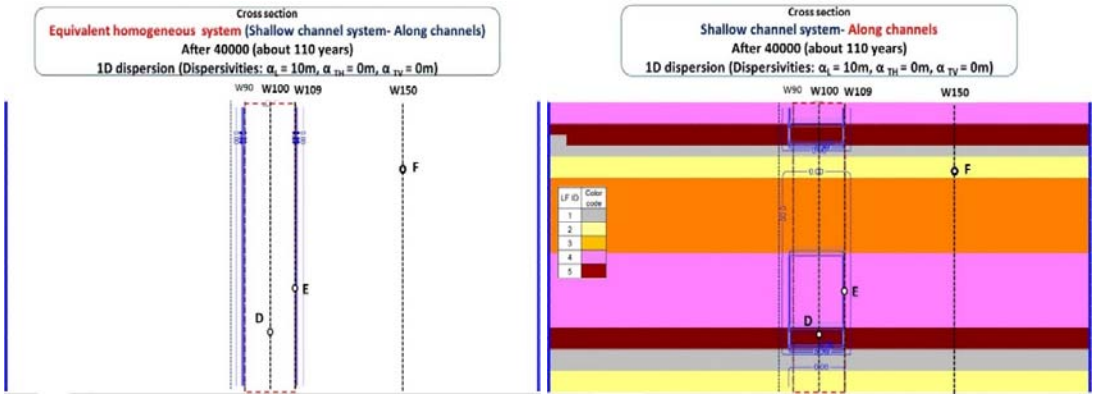

a) b)

Fig.6-33. Concentration cross sections at downstream boundaries showing points (D, E, F) at monitoring wells (W100, W109, W150) for 1D dispersion systems (α_L = 10m, α_{TH} = α_{TV} = 0m): a) equivalent homogeneous system; b) the shallow channel system - along channels.

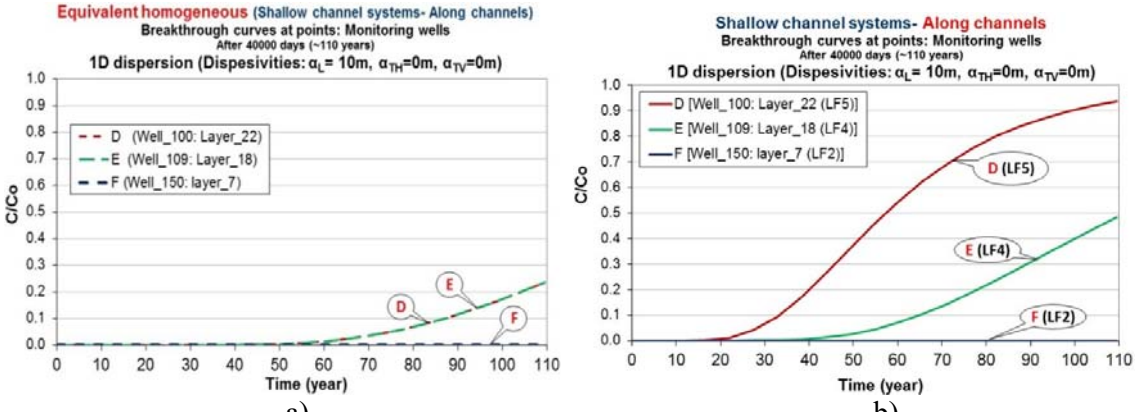

a) b)

Fig.6-34. Breakthrough curves at the points (D, E, and F) at the monitoring wells in the Fig.6-33 for a) equivalent homogeneous system; b) the shallow channel system - along channels.

6.6.3 The deep channel systems

6.6.3.1 Introduction

As with the shallow channel systems, solute migration along and across the channels with different sets of dispersivities were set up and compared with the equivalent homogeneous systems. Concentration profiles along the middle of the plumes, breakthrough curves at the downstream boundaries (M_{out}/M_{in}) and breakthrough curves from monitoring wells (Fig.6-3 and Fig.6-9a,b), and from various locations in the deep channels systems are plotted.

6.6.3.2 Concentration profiles and breakthrough curves

Fig.6-35a-d shows 3D views of the concentration plumes for the deep channel systems. Figs.6-37 and 6-38 show concentration profiles along the middle of plume with solute transport along the channel for solute travel along and across channels respectively. Corresponding breakthrough curves estimated at the downstream boundaries are presented in Figs.6-39 and 6-40. Again, point breakthrough curves in the monitoring well W100 (Fig.6-3 and Fig.6-9a,b) are presented in Figs.6-41 and 6-42.

Plume shapes, profiles and breakthrough curves for flow along the channels differ from those for flow across channels because the solute meets different channel structures when migrating along channels (Fig.6-9a) and across channels (Fig.6-9b). Adding dispersion directions leads to reducing concentration in the centre of the plumes and causes vertical mixing.

For 3D dispersion systems, the solute for the systems with flow along the channels has the same profile and the same breakthrough curve at monitoring well W100 for all layers in the model of the system (Fig.6-37a and Fig.6-41a) and similar trends were seen for the system with flow across the channels (Fig.6-38a and Fig.6-42a). This is vertical mixing is the effect of vertical

transvese dispersion as seen with the shallow channels systems and 3D dispersion. For 2D and 1D dispersion cases, in contrast, different layers consisting of different lithofacies show different profiles and breakthroughs at monitoring well W100 for the systems with flow along the channels (Fig.6-37b,c and Fig.6-41b,c) compared with the system with flow across the channels (Fig.6-38b,c and Fig.6-42b,c).

For travel along the channels, plumes spread faster than for travel across the channels (Fig.6-36a vs Fig.36b, Fig.6-39a-c vs Fig.6-40a-c; Fig.6-41a-c vs Fig.6-42a-c).

Numerical oscillation seen in Figs.6-38b-c is probably caused by the contrast between very low permeability zones (i.e. LF1) and very high permeability zones (e.g. LF4 and LF5). As with the shallow channel systems, numerical oscillations are seen in the deep channel, cross flow systems where 1D and 2D dispersion is present (Fig.6-38b-c). Also as with the shallow cross-flow channel systems, numerical oscillations increase from the 2D to 1D dispersion cases. This is due to the fact that adding more dispersion directions creates more chance for solute transporting through the very low permeability units: this is especially the case when vertical dispersion is present as it significantly increases the chance for solute to penetrate the relatively thin (0.1 m thick) low permeability layers.

In the deep channel systems, breakthrough curves (M_{out}/M_{in}) at downstream boundaries for travel along channels differ from those for travel across channels. Plume spreading is faster for travel along channels for all sets of dispersion lengths (Fig.6-39a-c vs Fig.6-40a-c). Fig.6-40b also includes the refined grid and no-flow set for LF1 systems (for solving the oscillations). Again, this difference is attributed to the difference of lithofacies structures for the two systems (Figs.6-9a and 6-9b). The solute has more chance to go through higher permeability zones/layers than vertically disperse through low permeability (LF1) layers in the along-

channel direction (Fig.6-9a), whereas solute found it difficult first to migrate through low permeability (LF1) zones/layer in the across-channel direction (Fig.6-9b).

In the systems with flow along channels, the equivalent homogeneous system underestimates the breakthrough concentrations for all dispersion conditions (Fig.6-39a-c). For the system with flow across, however, the equivalent homogeneous system slightly overestimates breakthrough concentrations for the 3D dispersion case, the most realistic case (Fig.6-40a), and slightly underestimates breakthrough concentrations when dispersions in the other transverse directions are removed (Fig.6-40b,c).

For the system with flow along channels, breakthrough concentrations are controlled mainly by LF4 layers for the 3D dispersion system (Fig.6-39a) and less for 2D and 1D dispersion systems (Fig.6-39b,c). A reverse trend is seen for the system with flow across channels: breakthrough concentrations are controlled mainly by LF4 layers for 2D and 1D dispersion systems (Fig.6-40b,c) and less for 3D dispersion system (Fig.6-40a).

As with the shallow channel system, the identical breakthrough curves seen in Fig.6-40b confirm consistent results for the deep channel systems compared with the refined grid and no-flow set for LF1 unit systems.

The breakthrough curve features mentioned above are strongly supported by breakthrough curves from the monitoring well W100 (Fig.6-41a-c and 6-42a-c) on which, as with the shallow channel systems, lower concentrations were seen with more spreading directions. Adding vertical transverse dispersion also caused effectively complete vertical mixing from about 100 m downstream (Fig.6-41a and 6-42a).

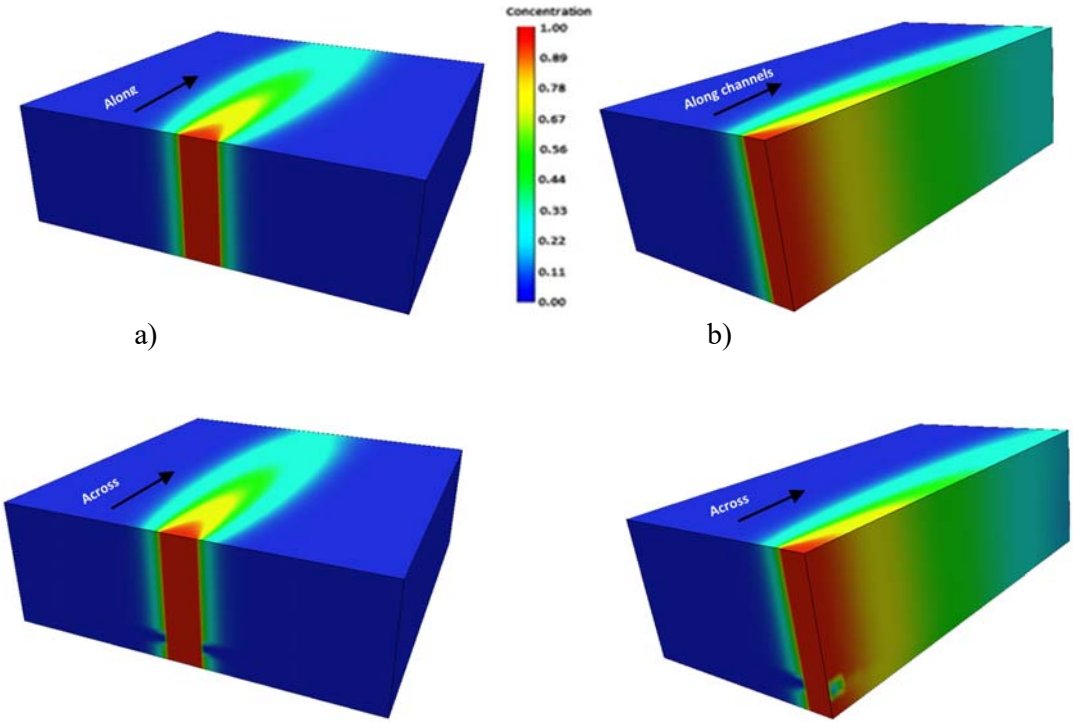

a) b)

c) d)

Fig.6-35. The deep channel systems with 3D dispersion after 110 years of simulation: a) flow along channels- whole model; b) flow along-half of model; c) flow across channels- whole model; d) flow across channels- half model.

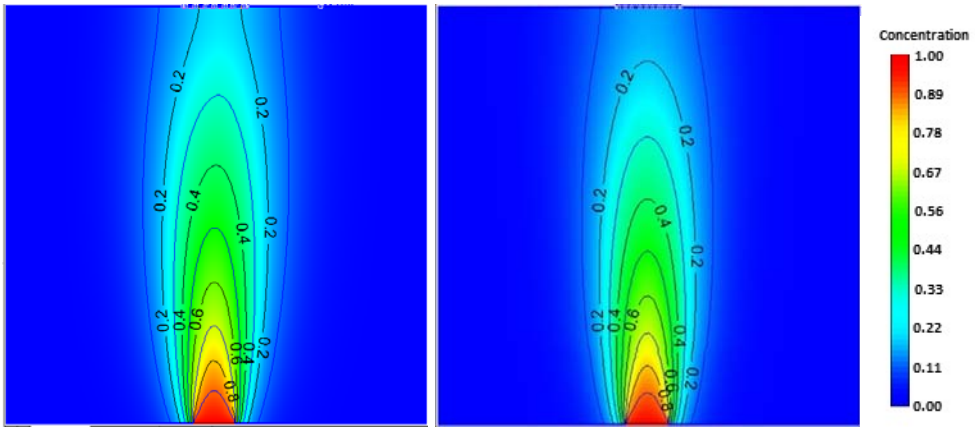

a) b)

Fig.6-36. Plumes for the deep channel systems with 3D dispersion in layer 1, simulated after 110 year (concentration colour, contours and their concentration values): a) flow along the channels; b) flow across the channels.

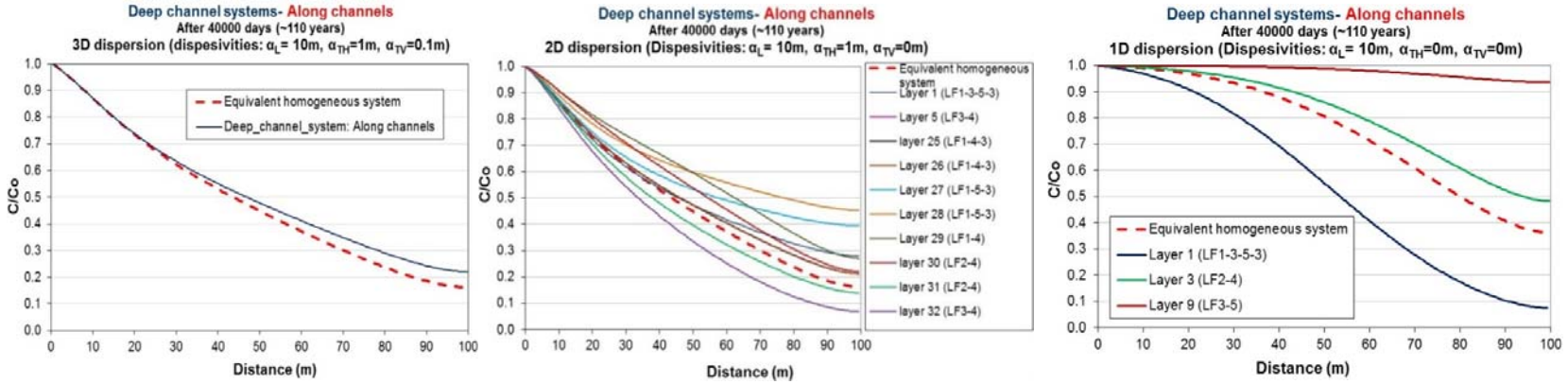

a) b) c)

Fig.6-37. Cross profiles for the deep channel systems- solute migrating along channels: a) 3D dispersion; b) 2D dispersion; and c) 1D dispersion.

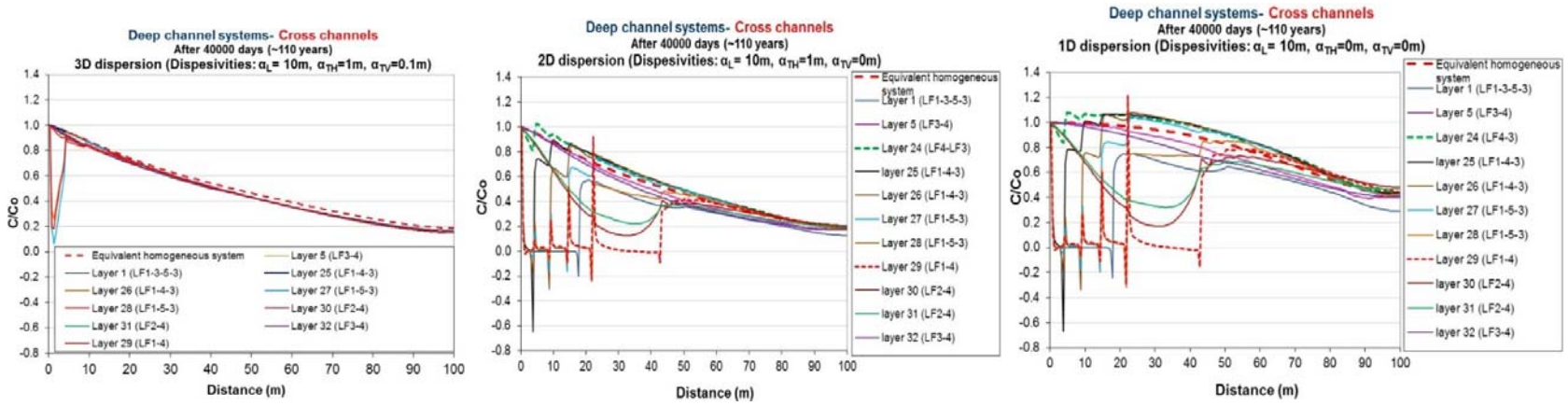

a) b) c)

Fig.6-38. Cross profiles for the deep channel systems- solute migrating cross channels: a) 3D dispersion; b) 2D dispersion; and c) 1D dispersion.

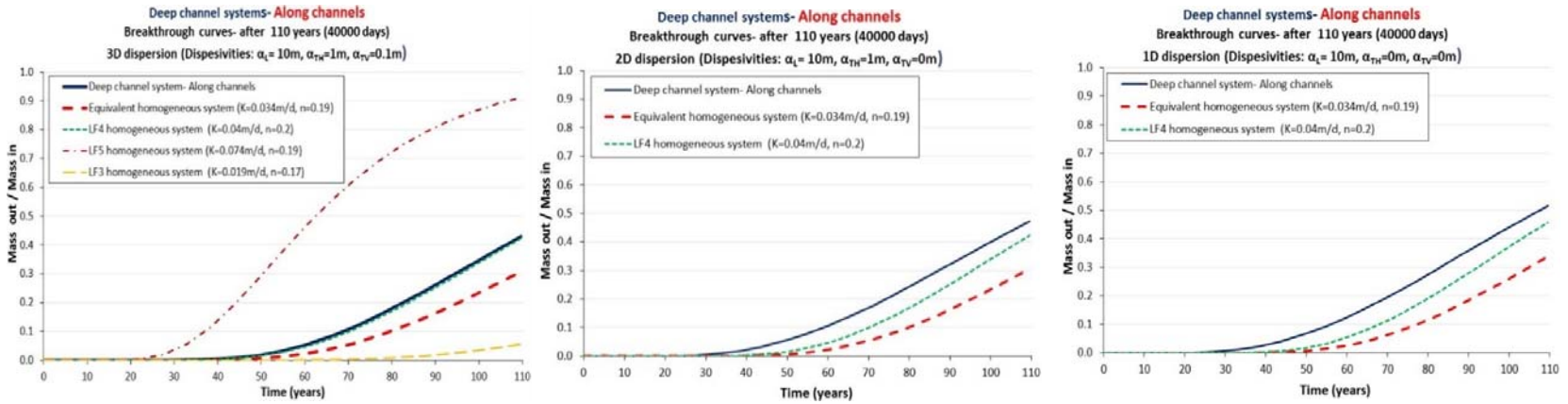

a) b) c)

Fig.6-39. Breakthrough curves at downstream boundaries for the deep channel systems- solute migrating along channels: a) 3D dispersion; b) 2D dispersion; and c) 1D dispersion.

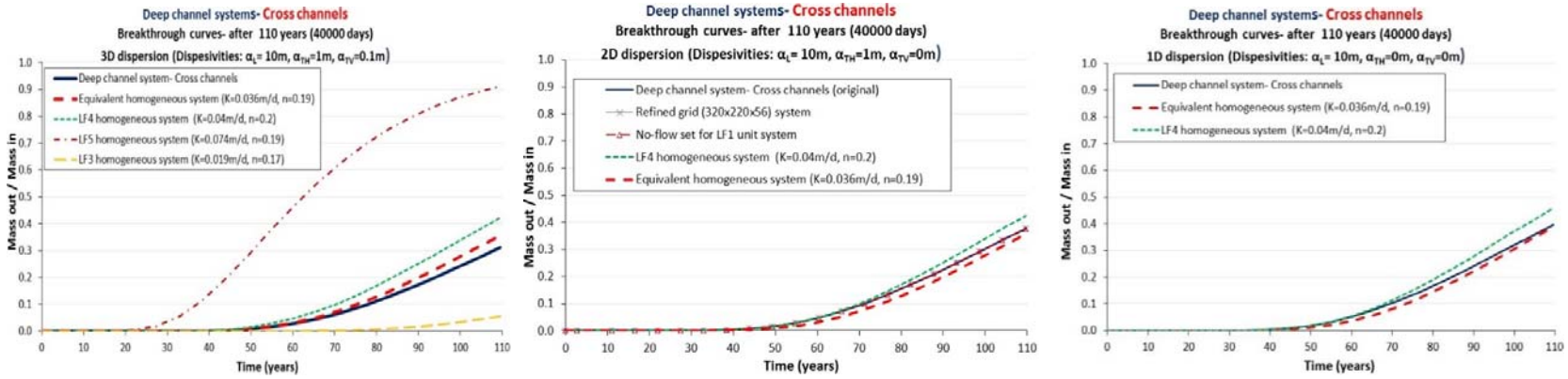

a) b) c)

Fig.6-40. Breakthrough curves at downstream boundaries for the deep channel systems- solute migrating cross channels: a) 3D dispersion; b) 2D dispersion (including the refined grid, and no-flow set for LF1 systems); and c) 1D dispersion.

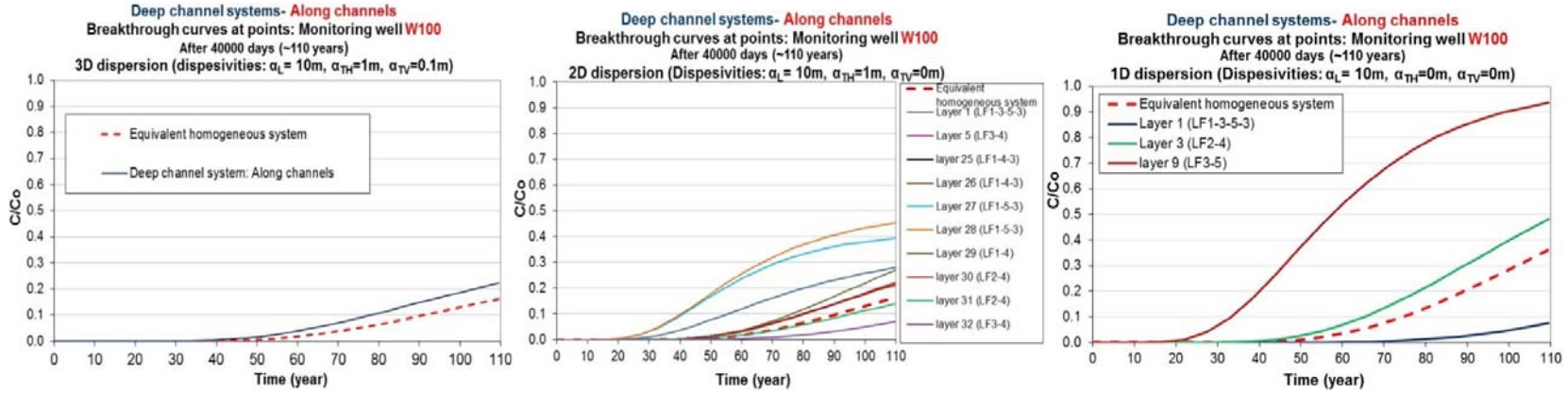

a) b) c)

Fig.6-41. Breakthrough curves at points of the monitoring well W100 for the deep channel systems- solute migrating along channels: a) 3D dispersion; b) 2D dispersion; and c) 1D dispersion.

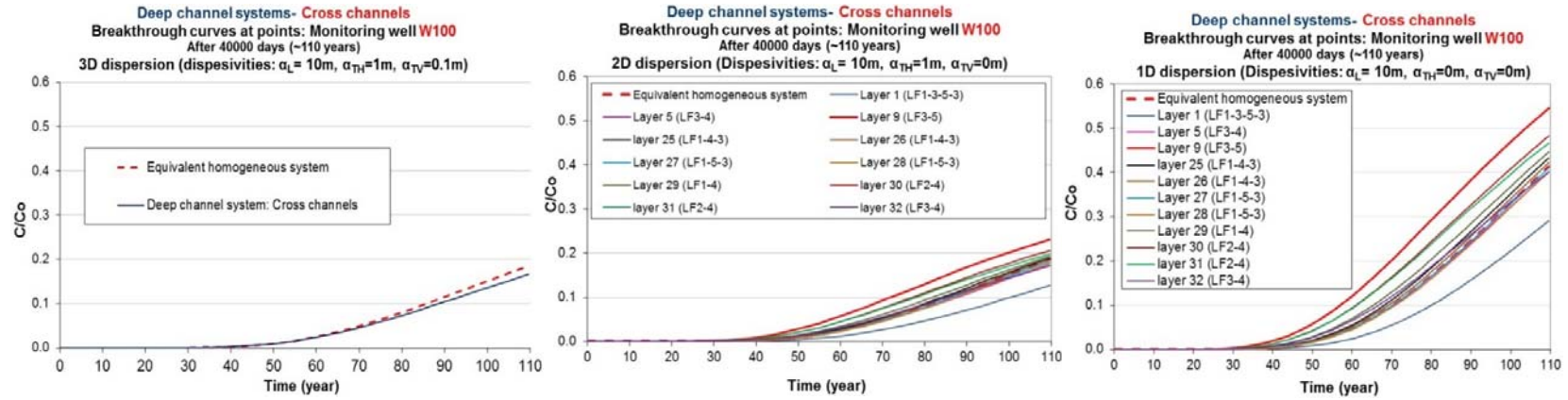

a) b) c)

Fig.6-42. Breakthrough curves at points of the monitoring well W100 for the deep channel systems- solute migrating cross channels: a) 3D dispersion; b) 2D dispersion; and c) 1D dispersion.

6.6.3.3 Breakthrough curves at points for homogeneous systems versus heterogeneous systems

Fig. 6-43a,b to Fig. 6-48a,b show the concentration distributions in space and breakthrough curves at specific points for the range of conditions investigated.

All plots consistently support the finding above that plumes spread faster and wider in higher permeability layers (LF5, LF4) (Fig.6-43b, and Fig.6-45b), and that the equivalent homogeneous systems underestimate breakthrough concentrations (Fig.6-44a,b; Fig.6-46a,b; and Fig.6-48a,b). Vertical mixing occurred as effects of vertical transverse dispersion as seen in Fig.6.43b where there is no concentration contour difference for different layers except in the the first layer and the base where LF1-units are present. This suggests the importance of transvese dispersion and low permeability (LF1) layers for solute transport.

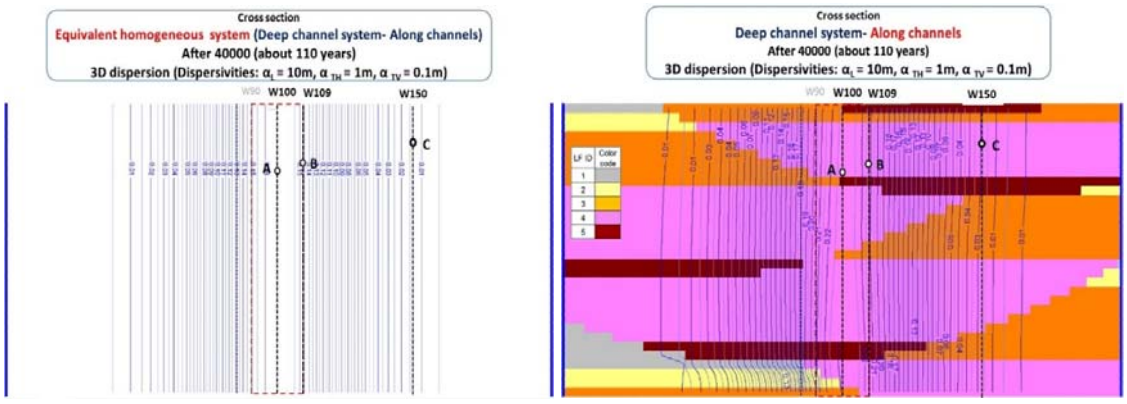

a) b)

Fig.6-43. Concentration cross sections at downstream boundaries showing points (A, B, C) at monitoring wells (W100, W109, W150) for 3D dispersion systems: a) equivalent homogeneous system; b) the shallow channel system - along channels.

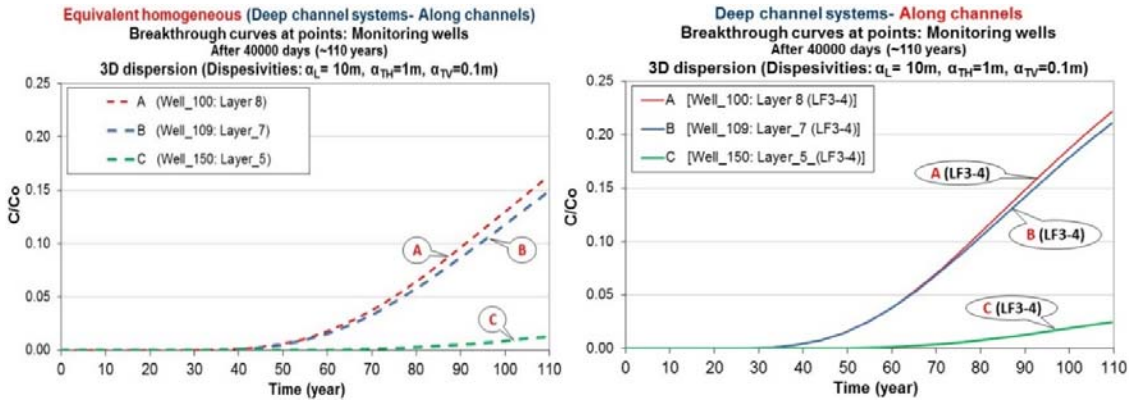

a) b)

Fig.6-44. Breakthrough curves at the points (A, B, and C) at the monitoring wells in the Fig.6-43: a) equivalent homogeneous system; b) the shallow channel system - along channels.

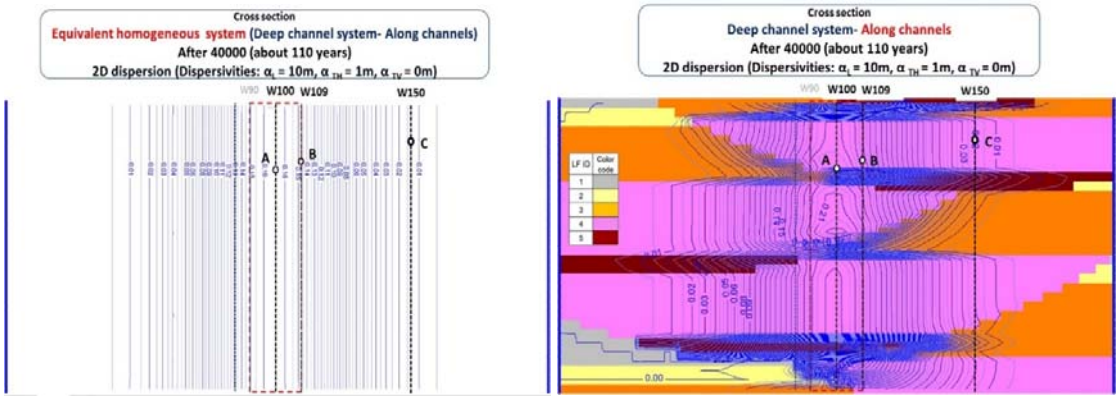

a) b)

Fig.6-45. Concentration cross sections at downstream boundaries showing points (A, B, C) at monitoring wells (W100, W109, W150) for 2D dispersion systems: a) equivalent homogeneous system; b) the shallow channel system - along channels.

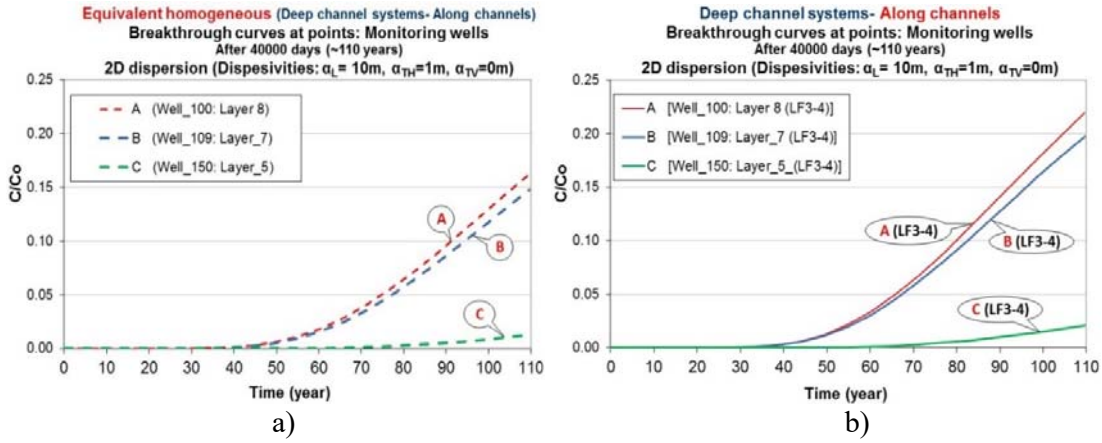

a) b)

Fig.6-46. Breakthrough curves at the points (A, B, and C) at the monitoring wells in the Fig.6-45 for a) equivalent homogeneous system; b) the shallow channel system - along channels.

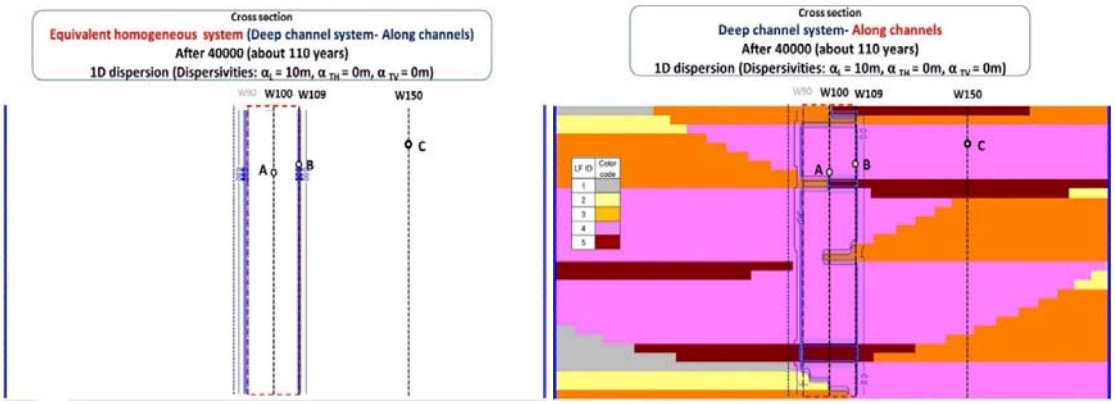

a) b)

Fig.6-47. Concentration cross sections at downstream boundaries showing points (A, B, C) at monitoring wells (W100, W109, W150) for 1D dispersion systems: a) equivalent homogeneous system; b) the shallow channel system - along channels.

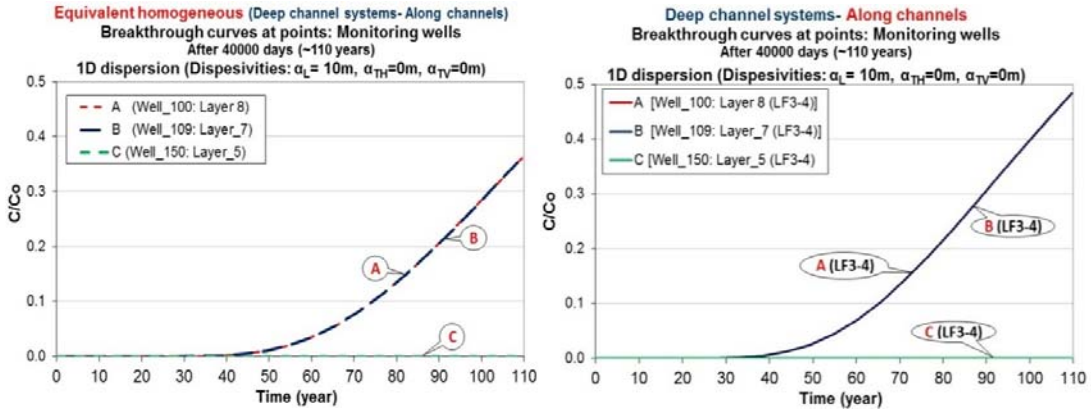

a) b)

Fig.6-48. Breakthrough curves at the points (A, B, and C) at the monitoring wells in the Fig.6-47 for a) equivalent homogeneous system; b) the shallow channel system - along channels.

6.7. Conclusion and future work

6.7.1 Introduction

In this chapter, solute transport through synthetic multilayer fluvial channel systems were simulated numerically for a range of conditions. Two channel types were considered: shallow, where the resulting sequence was effectively a set of parallel layers within the modelled domain, the edges of the channels not being seen; and deep, where the channels interdigitated with each other in a jigsaw-type arrangement. The following conclusions can be made.

6.7.2 Numerical issues

- Numerical issues include the selection of boundary conditions, head and concentration change criteria, and time step size criteria. Particularly for homogeneous media, these numerical issues are critical for numerical accuracy and stability, otherwise the simulations will fail to converge or display considerable mass balance errors. Differences in model domain and boundary conditions led to differences between the numerical solution and the analytical solution of Domenico (1987), indicating again that choice of boundary conditions is very important and would be an interesting subject for further study.
- Numerical oscillations are caused by highly contrasting conductivity variations, even with non-advection-dominated problems. Numerical oscillations appear here only with systems of solute moving across channels. Several methods were attempted to resolve the numerical solutions, including adding vertical dispersion, using other solvers for advection (such as FD method with upstream-weighting with small Courant Number and small transport time frame, HMOC, and TVD method), refining the model grids, assigning no-flow boundaries for the areas occupied by zones of very low permeability (LF1), and resetting the systems with diffusion effect dominating in the very low permeability units. Adding vertical dispersion is appropriate, as vertical dispersion occurs in the real systems, but it should not be used simply to avoid numerical problems. Using others solvers failed to improve the numerical oscillations. Model grid refinement can improve the numerical oscillation. Assigning areas occupied by the very low permeability material as impermeable units effectively solved numerical oscillation. This avoids a lot of numerical errors by recognising that the low flow unit does not carry any flow, and this approach also has the advantage of reducing computation memory and time. The last method requires an alternative setting up of the system and was beyond scope of this chapter.

- Overall, it is vital that particular attention should be given to the assumptions made, spatial and temporal discretisations, representing dispersion, and selecting methods to solve the advection-dispersion equation for heterogeneous porous media, even in relatively simplified system such as have been studied here.

6.7.3 Shallow channel systems

In the shallow 100 m long channel systems, run for 110 years, the 3D dispersion case shows no difference between concentration profiles for travel along channels and travel across channels, but reducing spreading directions results in significant differences in concentration profiles between along and across channel travel.

Breakthrough concentrations at downstream boundaries and at monitoring wells for solute migrating along and across channels are similar and are mainly controlled by high permeability layers.

In the shallow channel systems with no vertical dispersion, higher permeability layers show quicker spreading of the solute plumes. The LF5-bearing layer (the most permeable layer) causes the plume to spread most quickly, then the LF4-bearing layer, and so on; the LF1-bearing layers have slowest movements of plumes.

Numerical oscillation occurred in profiles for the system without vertical transverse dispersion and with solute migrating across channels, and also in breakthrough concentrations at a monitoring well for the system without any transverse dispersions.

Vertical mixing in profiles and breakthrough concentration occur for 3D dispersion systems.

Though if the system does mix quite well, it could still be an issue if there were different geochemical properties for different lithofacies (e.g. different retardation factor for each).

However, with the exception of the presence of mudstone pellets, Jaweesh (In preparation) did not find any correlations between lithofacies and geochemical properties.

6.7.4 Deep channel systems

In the deep channel systems, concentration profiles and breakthrough concentration for travel along channels differ from those for travel across channels with plumes moving faster for the former as expected.

For travel along channels, breakthrough concentrations are controlled mainly by LF4 layers in the 3D dispersion system and less in the 2D and 1D dispersion systems. A reverse trend is seen for travel across channels: breakthrough concentrations are controlled mainly by LF4 layers for 2D and 1D dispersion systems and less for 3D dispersion system.

Numerical oscillation occurred in the case of travel across channels and with no vertical dispersion.

As with the shallow channel system, vertical mixing occurred when systems have all spreading directions.

6.7.5 Comparison with equivalent homogeneous systems

The heterogeneous systems behave differently from the homogenous systems for 2D and 3D dispersion. There is no difference for profiles and breakthrough curves for homogeneous systems between 2D and 3D dispersion cases as the source is fully penetrating, whereas profiles and breakthrough curves are different between 2D and 3D dispersion applied to heterogeneous (channelled) systems.

In the shallow channel systems, the equivalent homogeneous systems underestimate the breakthrough concentration for both systems with solute moving along and across channels.

In the deep channel systems, the equivalent homogeneous system underestimates breakthrough concentration for the system with flow along channels. For travel across channels, the equivalent homogeneous system slightly overestimates breakthrough concentration for the 3D dispersion system, and slightly underestimates breakthrough concentrations for the 2D and 1D dispersion systems.

In general, the heterogenous medium is reasonably approximated by an equivalent homogenous medium for prediction purposes, but determining appropriate properties for the equivalent homogenous medium is challenging.

6.7.6 Effects of spreading directions in solute transport

In the shallow and deep channel systems, reducing transverse dispersion leads to different profiles and breakthrough for different layers and causes increasing numerical oscillations in profiles for flow across channels.

Adding vertical dispersion to 2D-dispersion cases results in vertical mixing for profiles and breakthrough concentrations for both shallow and deep channel systems with along- and across-channel flow directions.

These findings show the importance of transverse dispersion for solute transport in heterogeneous systems. Systems without transverse dispersion have much more heterogeneity in the breakthrough, whereas systems with transverse dispersion over long time frames show vertical mixing. The source distribution and transverse dispersion have an important role in controlling the solute distribution. Therefore, it is critical to determine transverse dispersivity in real porous media.

In this chapter, the permeabilities assigned for the lithofacies in the channel systems (Table 6-2) were geometric averages of permeabilities measured at different points within each

lithofacies (Chapter 4). All the simulations in this chapter were repeated for the same systems, but with the geometric means replaced by arithmetic means. The results were very similar and can be found in Appendix 7.

6.7.7 Future work

Considering the limitations of the simulated systems, the following interesting work should be further investigated

- Further work needed on numerical modelling to reduce numerical effects.
- Investigate effects of transverse dispersivity in greater detail with values from a real system.
- Simulate the fluvial channel systems under transient flow conditions.
- Solute transport in fluvial channel systems of anisotropic permeability should be simulated to examine the effect of spatially heterogeneous hydraulic properties on solute movement.
- Systems with diffusion processes dominating in the very low permeability units (mudstone).
- Solute transport for more complex channel structures such as asymmetry, dipping, and sinuous channels.
- Investigate the extent of vertical mixing, and at which distances the vertical mixing is effectively complete- i.e. where can use equivalent porous media approach.
- Simulate solute transport at smaller distances where it is comparable with tracer test results.
- Simulate the systems with chemical reactions, including sorption, desorption, (bio)degradation, and precipitation/dissolution.
- Apply pumping and example sampling and remediation scenarios
- Simulate channel system with fracture and granulation seams effects.
- Investigate how to determine the values needed for an equivalent porous medium.
- Solute transport for aeolian sandstone sequences.

CHAPTER 7

CONCLUSION AND FUTURE WORK

7.1 Introduction

The aims of the project were (Section 1.4.1):

1. To determine the strength of correlation between lithofacies and permeability in example English Permo-Triassic sandstone sequences, and;
2. To determine whether the permeability distributions discovered can be used to improve prediction of solute transport.

These aims have been undertaken by using the following approaches (Section 1.4.2):

1. Examine variation of some examples of sandstone lithofacies associations across England in order to determine likely architectures for later work on modelling solute transport;
2. Statistically analyse existing borehole core permeability datasets;
3. Determine petrographic and hydraulic property distributions in a borehole core and at outcrop;
4. Statistically analyse data collected in 3 to determine strength of hydraulic property / lithofacies correlations;
5. Undertake numerical modelling using the correlations between hydraulic property values and lithofacies collected in 3 and the architectural data collected in 1 to determine the effect of permeability distributions on solute transport in groundwater.

The outcomes of the research indicate that the English Permo-Triassic sandstone sequences appear with a wide range of sedimentary characteristics and hydraulic properties, varying within and between sequences, sites and regions. The aeolian sandstones generally have greater permeability (hydraulic conductivity) than the fluvial sandstones do. Correlations between English Permo-Triassic sandstone lithofacies and permeability were found in the core and outcrop studies. These correlations can be used to improve prediction of solute transport in groundwater as illustrated by the numerical simulation of solute transport carried out. The solute transport modelling also indicates the importance of transverse dispersivity in controlling solute breakthrough behaviour. It shows that a heterogeneous system can be reasonably introduced by an equivalent homogeneous system, but determining appropriate properties for the equivalent homogenous system appears to be difficult.

In the following sections, the findings of the project throughout the field investigation, in situ and laboratory measurements of hydraulic properties, data analysis and numerical modelling are further detailed and reviewed (Section 7.2 and 7.3), and further work is recommended (Section 7.4).

7.2 Aim 1: to determine the strength of correlation between lithofacies and permeability in example English Permo-Triassic sandstone sequences

A reconnaissance investigation of Permo-Triassic sandstone exposures across England was undertaken partly to gain a qualitative indication of the possibility of correlations between 'sub-'lithofacies (i.e. sub-facies within a fluvial or aeolian lithofacies) and hydraulic properties. In addition, detailed studies of a borehole core from northwest England and detailed investigations of outcrops of a fluvial deposit and an aeolian deposit were undertaken to determine quantitatively correlations between sandstone lithofacies and permeability.

From the limited set of hydraulic and lithofacies data collected during the reconnaissance field survey part of the current project combined with very limited amounts of paired hydraulic property and lithofacies data from the literature, hydraulic properties of the sandstones, particularly permeability, were found to vary within beds less than between beds. There also seems to be significant variations from one sedimentary basin to another even if the sequences in the regions involved have a similar palaeoenvironmental origin or not (e.g. St Bees Head Cumbria and Raw Head, Cheshire). There also seems to be a correlation between permeability and sedimentary characteristics such as grain sizes, sorting, sedimentary structures, and cement, though the data are too few to be able to show this statistically. Generally, the aeolian sandstones, which qualitatively appear to be, and are often cited as, having better sorted and rounded sand grains, also appear to have higher permeability than the fluvial sandstones.

The borehole core study indicates that

- Lithofacies are correlated with porosity, with permeability, and with the ratio of permeability to porosity at the 95% confidence level (99% if the effects of mudpellets on permeability are ignored).
- Mudclasts can reduce the sandstone permeability of the two coarser lithofacies by 6 and 8 % respectively, causing them to be statistically slightly more similar than if just the matrix is considered.
- Though each lithofacies has a distinctive permeability distribution, a significant overlap of the permeability ranges occurs for the three coarser lithofacies. This could be attributed to the broad classification used to describe lithofacies and to the small scale of measurement of mini-permeameters that results in the ability to resolve small

zones of both very low permeabilities and very high permeabilities, thus extending the spread of values.

The two outcrop studies show within and between bed permeability correlations and that permeability values vary greater between beds than within beds. As was found in the study of borehole core, the permeability distributions for each unit investigated, though statistically distinct at the 95% confidence level, overlap with the distributions from other units. It could be broadly seen that the fluvial system is more consistent laterally than the aeolian system as expected.

7.3 Aim 2: to determine whether the permeability distributions discovered can be used to improve prediction of solute transport

Given that hydraulic properties are correlated with lithofacies, the distributions of hydraulic properties will be determined by the distributions of the lithofacies.

Markov chain analysis of the Preston Laundry Borehole core (Chapter 4) indicates that the sequence of lithofacies is structured in terms of order of occurrence, and hence the permeability is also structured in a similar way.

The reconnaissance study of the Permo-Triassic sandstone sequences across England (Chapter 3) showed that complete fluvial channel structures are rarely preserved at outcrops, the most common macroscopic structure in fluvial systems being a sequence of layered units. Distinct large-scale cross-stratification, grainfall, grainflow, and pinstripe lamination structures of aeolian systems are often seen at the aeolian sites.

Though complete fluvial channel structures are rarely preserved rather than layered structures, when they are observed, width of channels show range from centimetres to metres (scours),

often from tens to hundreds of metres, with some stacking cycles. These fluvial sedimentary architectures along with the lithofacies/permeability correlations found from the borehole core study (Chapter 4) were used to create synthetic multilayer fluvial channel systems: shallow and deep channel systems in which steady state flow solute transport simulations were performed (Chapter 6). The following outcomes were observed:

- Despite the relatively simple geometries involved, numerical instability proved surprisingly problematic, and though methods were developed to circumvent the problems, further work on modelling solute movement will require also research on modelling methods.
- Vertical heterogeneity in solute concentrations is highly dependent on transverse dispersion, and again this would need more research before solute movement in these structured systems is properly understood.
- Despite these problems, the modelling clearly established that breakthrough patterns are dependent on lithofacies properties, geometry and flow direction. Therefore, correlations between lithofacies and permeability can be used to improve prediction for solute transport, if lithofacies geometry including orientation could be established in the field.
- In general, the heterogeneous system can be reasonably represented by an equivalent homogeneous system for prediction purposes, but determining appropriate properties for the homogeneous medium is challenging – another area for future research.

Generally, the findings of the project could be used as the first step in attempt to develop better approaches for predicting solute transport in Permo-Triassic sandstone sequences. The main properties used in the lithofacies definitions (matrix grain size, sedimentary structure types, and presence of mudclasts and pebbles) are amenable to geophysical logging techniques, especially

if optical televiewer equipment is available. The scales at which the results would be useful are considered to be:

1. At site scale, perhaps up to at most a few 100m, though this limit would be dependent on unit size and flow velocity; at this scale, fractures may also play an important role, again another area for future research (e.g. correlations with lithofacies);
2. At larger scales, where the relationship with lithofacies may allow better estimation of properties at the larger scale, including dispersive properties, but again more modelling work linking dispersivity and hydraulic properties (and flow directions) would need to be undertaken.

7.4 Recommendations for future work

7.4.1 Method developments

7.4.1.1 The use of a mini-permeameter

Further investigation of the use of the mini-permeameter in the field is required. Particular investigations should include determining how best to deal with the effects of moisture content and weathering. There are also other issues with developing better constrained geometric factors especially for anisotropic media.

7.4.1.2 Using geophysical logging to determine lithofacies distributions in the vertical

Development of interpretation methods that are aimed at identifying lithofacies. This could include the use of optical televiewer combined with standard geophysical logging methods, the latter linked together where they measure related properties (e.g. natural gamma ray logging might indicate clay percentage that might provide a better estimate of matrix conduction for interpreting resistivity logs) and interpreted in terms of typical signatures for given lithofacies

types. It would be useful if lithofacies orientation (e.g. channel axis) could be identified using logging, but this may be difficult. If so, is this a major problem to be investigated using numerical simulation.

7.4.1.3 Simulation solute transport in sandstone sequences

The following further work is recommend for numerical simulation of solute transport in sandstone aquifers

- Investigating further on numerical modelling to minimize numerical errors.
- Studying in greater detail the effects of transverse dispersion with experiments in a real system.
- Investigating the relationships between realistic sequences of structured hydraulic properties and apparent dispersivity at various scales; how can the latter be derived from the former?
- Simulating the fluvial channel systems with anisotropic permeability, and under transient conditions.
- Simulating systems diffusion as a significant process in the very low permeability units (mudstones).
- Simulating the systems with chemical reactions, (bio)degradation, and precipitation/dissolution.
- Applying pumping and example sampling and remediation scenarios.
- Simulating with more complex channel structures.
- Simulating channel systems with effects of fractures and granulation seams.
- Determining appropriate properties for an equivalent homogeneous medium.
- Simulating solute transport for aeolian sandstone sequences.

- Attempting to determine what the limit is on what might be determined in a given sequence.

7.4.2 Further developing of lithofacies understanding

1. Lithofacies definitions

   The overlapping of permeability distributions for each lithofacies may be reduced if further detailed classification of lithofacies is made (e.g. lithofacies classification is undertaken using more detailed grain size data). Alternatively, it may be more of a scale issue, as seen with results from the mini-permeameter measurement, thus it would be better either to measure at larger scale or by averaging permeability values obtained at smaller scales.

2. More investigation of the variation in permeability in the field should be undertaken at many sites, in particular investigation of the within-lithofacies lateral variation in permeability compared with the variation between lithofacies.

3. Geometry of lithofacies

   Further work should be done to determine the geometries of fluvial and aeolian systems with field studies on sandstones or their modern analogues.

7.4.3 Investigation of other effects

1. Importance of cementation on controlling permeability. These can be investigated with analysis of thin sections and basin to basin comparisons. Needs to be done quantitatively, and this may require the development of appropriate statistical (and image-analysis) approaches.

2. Fractures including granulation seams for correlation with sandstone lithofacies and for modelling.

3. Correlation between sandstone lithofacies and geochemistry, and hence geochemical and hydraulic properties (Jaweesh, In preparation).
4. Confirm numerical modelling predictions for pellets (mudclasts) in sandstones by laboratory experimentation.
5. Explore the scale of measurement issues associated with the use of the mini-permeameter
    a. Extreme permeability values being detected because of the small scale of measurement of the device
    b. Repeat the current work with larger scale of measurement, e.g. with laboratory falling head permeameter measurement
    c. The variation of apparent vertical to horizontal permeability ratios as a function of scale.

7.4.4 Confirming and exploring solute transport effects

1. Because of its apparent importance in solute movement (Chapter6), transverse dispersion needs to be further studied to develop better conceptual models and also better means of quantification.
2. Solute transport modelling and field experiments where possible in different types of structured media in different directions
    a. At various timescales to determine transverse, including diffusive, dispersion
    b. To investigate in situ the processes in the rock mass, including both fracture and intergranular flow effects.
3. Examination of bleached zones as an indicator of flow mechanisms for reactive solute transport.

REFERENCES

AHMAD, S. R., GHAZI, S., SHARIF, S., KHAN, M. S. & MEHMOOD, S. A. 2012. Cyclicity and lithofacies modelling by application of Markov chain analysis to the Warchha sandstone, Salt Range, Pakistan. *Pakistan Journal of Science*, 64, 232-241.

AIGNER, T., ASPRION, U., HORNUNG, J., JUNGHANS, W. D. & KOSTREWA, R. 1996. Integrated outcrop analogue studies for Triassic alluvial reservoirs: examples from southern Germany. Journal of Petroleum Technology, 19, 393-406. *Journal of Petroleum Technology,* 19**,** 393-406.

AKHURST, M. C., CHADWICK, R. A., HOLLIDAY, D. W., MCCORMAC, M., MILLWARD, D. & YOUNG, B. 1997. *Geology of the west Cumbria district*. Memoir of the British Geological Survey, Sheets 28, 37 and 47 (England and Wales).

AL-HINAI, S., FISHER, Q. J., AL-BUSAFI, B., GUISE, P. & GRATTONI, C. A. 2008. Laboratory measurements of the relative permeability of cataclastic fault rocks: An important consideration for production simulation modelling. *Marine and Petroleum Geology,* 25**,** 473-485.

ALLEN, D. J., BLOOMFIELD, J. P., GIBBS, B. R. & WAGSTAFF, S. J. 1998. *Fracturing and the Hydrogeology of the Permo-Triassic Sandstones in England and Wales*. British Geological Survey Technical Report WD/98/1, and Environment Agency R&D Technical Report W164.

ALLEN, D. J., BREWERTON, L. J., COLEBY, L. M., GIBBS, B. R., LEWIS, M. A., MACDONALD, A. M., WAGSTAFF, S. J. & WILLIAMS, A. T. 1997. *The Physical Properties of Major Aquifers in England and Wales*. British Geological Survey Technical Report, WDI97134. Environment Agency R&D Publication, 8.

ALLEN, J. R. L. 1964. Studies in Fluviatile Sedimentation : Six Cyclothems from the Lower Old Red Sandstone, Anglo-Welsh Basin. *Sedimentology*, 3, 163-198.

AMBROSE, K., HOUGH, E., SMITH, N. & WARRINGTON, G. 2014. Lithostratigraphy of the Sherwood Sandstone Group of England, Wales and south-west Scotland.

ANDERSON, M. P., AIKEN, J. S., WEBB, E. K. & MICKELSON, D. M. 1999. Sedimentology and hydrogeology of two braided stream deposits. *Sedimentary Geology,* 129**,** 187-199.

ANDERSON, M. P. & WOESSNER, W. W. 1992. *Applied Groundwater Modelling,* San Diego, Academic Press.

BAHAR, A. & KELKAR, M. 2000. Journey from well logs/cores to integrated geological and petrophysical properties simulation: A methodology and application. *Spe Reservoir Evaluation & Engineering,* 3**,** 444-456.

BALLARINI, E., BAUER, S., EBERHARDT, C. & BEYER, C. 2012. Evaluation of transverse dispersion effects in tank experiments by numerical modeling: parameter estimation, sensitivity analysis and revision of experimental design. *Journal of Contaminant Hydrology,* 134**,** 22-36.

BARNES, R. P., AMBROSE, K., HOLLIDAY, D. W. & JONES, N. S. 1994. Lithostratigraphical subdivision of the Triassic Sherwood Sandstone Group in west Cumbria. *Proceedings of the Yorkshire Geological Society,* 50**,** 51-60.

BASHAR, K. & TELLAM, J. H. 2006. Non-reactive solute movement through saturated laboratory samples of undisturbed stratified sandstone. *In:* BARKER, R. D. & TELLAM, J. H. (eds.) *Fluid Flow and Solute Movement in Sandstones: The Offshore UK Permo-Triassic Red Bed Sequence.* Geological Society, London, Special Publications, 263, 233-251.

BATU, V. 2006. *Applied flow and solute transport modeling in aquifers: Fundamental principles and analytical and numerical methods.* Boca Raton, FL: Taylor & Francis.

BEAR, J. 1979. *Hydraiilics of Groundwater,* New York, McGraw-Hill.

BENTON, M. J., COOKE, E. & TURNER, P. 2002. *Permian and Triassic Red Beds and the Penarth Group of Great Britain*, Geological Conservation Review Series, No. 24, Joint Nature Conservation Committee, Peterborough.

BIRMINGHAM, U. O. 1981. Saline Groundwater Investigation Phase 1 - Lower Mersey Basin. *Report to North West Water Authoruty* -Final Report and Hydrogeology Appendix.

BIRMINGHAM, U. O. 1984. Saline Groundwater Investigation Phase 2 - North Merseyside. *Report to North West Water Authoruty* - Final Report and Hydrogeology Appendix.

BLACK, J. H. & BRIGHTMAN, M. A. 1996. Conceptual model of the hydrogeology of Sellafield. *Quarterly Journal of Engineering Geology and Hydrogeology,* 29**,** S83-S93.

BLOOMFIELD, J. P., GOODDY, D. C., BRIGHT, M. I. & WILLIAMS, P. J. 2001. Pore-throat size distributions in Permo-Triassic sandstones from the United Kingdom and some implications for contaminant hydrogeology. *Hydrogeology Journal,* 9**,** 219-230.

BLOOMFIELD, J. P., MOREAU, M. F. & NEWELL, A. J. 2006. Characterization of permeability distributions in six lithofacies from the Helsby and Wilmslow sandstone formations of the Cheshire Basin, UK. *In:* BARKER, R. D. & TELLAM, J. H. (eds.) *Fluid Flow and Solute Movement in Sandstones: The Onshore UK Permo-Triassic Red Bed Sequence.* Geological Society, London, Special Publications, 263**,** 83-101.

BLOOMFIELD, J. P. & WILLIAMS, A. T. 1995. An empirical liquid permeability gas permeability correlation for use in aquifer properties studies. *Quarterly Journal of Engineering Geology,* 28**,** S143-S150.

BOUCH, J. E., HOUGH, E., KEMP, S. J., MCKERVEY, J. A., WILLIAMS, G. M. & GRESWELL, R. B. 2006. Sedimentary and diagenetic environments of the Wildmoor Sandstone Formation (UK): implications for groundwater and contaminant transport, and sand production. *In:* BARKER, R. D. & TELLAM, J. H. (eds.) *Fluid Flow and Solute Movement in Sandstones: The Onshore UK Permo-Triassic Red Bed Sequence.* Geological Society, London, Special Publications, 263**,** 129-153.

BOWDEN, R. A., BUMPUS, C. & LITTLEBOY, A. K. 1998. An overview and update of the site characterization studies at Sellafield. *Proceedings of the Yorkshire Geological Society,* 52**,** 125-137.

BRIAN, J. W. & CHRISTOPHER, D. W. 2000. Quantitative Outcrop Data for Flow Simulation. *Journal of Sedimentary Research,* 70**,** 788-802.

BÜYÜKUTKU, A. G. & BAĞCı, A. S. 2005. Clay controls on reservoir properties in sandstone of Kuzgun formation and its relevance to hydrocarbon exploration, Adana basin, Southern Turkey. *Journal of Petroleum Science and Engineering,* 47**,** 123-135.

BYRNES, A. P. 1997. Reservoir characteristics of low-permeability sandstones in the Rocky Mountains. *The Mountain Geologist,* 34**,** 37-48.

CAMPBELL, J. E. 1982. *Permeability characteristicsofthe Permo-Triassic sandstones of the Lower Mersey Basin.* MSc thesis, University of Birmingham.

CARLYLE, H. E., TELLAM, J. H. & PARKER, K. E. 2004. The use of laboratory-determined ion exchange parameters in the prediction of field-scale major cation migration over a 40 year period. *Journal of Contaminant Hydrology,* 68**,** 55-81.

CHAPLOW, R. 1996. The geology and hydrogeology of Sellafield: an overview. *Quarterly Journal of Engineering Geology and Hydrogeology,* 29**,** S1-S12.

CHENEY, C. S., COBBING, J. E., NEWELL, A. J. & CUNNINGHAM, J. E. M. 2004. *The Permo-Triassic Sandstone aquifer of the English Midlands*. British Geological Survery Internal Report, 143pp (unpublished).

COX, R. A. & NISHIKAWA, T. 1991. A new total variation diminishing scheme for the solution of advective-dominant solute transport. *Water Resources Research,* 27**,** 2645-2654.

CURIÃO, V. 2002. *The effect of Mudstones on Flow in the Triassic Sandstones (UK). Laboratory Measurement of Mudstone Permeability (Unpublished).* BSc thesis, University of Birmingham.

DAVIS, J. M. 1994. *A conceptual sedimentological-geostatistical model of aquifer heterogeneity based on outcrop studies.* PhD, New Mexico Inst. of Mining and Technology.

DAVIS, J. M., LOHMANN, R. C., PHILLIPS, F. M., WILSON, J. L. & LOVE, D. W. 1993. Architecture of the Sierra Ladrones Formation, central New Mexico: Depositional controls on the permeability correlation structure. Geological Society of America Bulletin, 105, 998-1007. *Geological Society of America Bulletin,* 105**,** 998-1007.

DAVIS, J. M., ROY, N. D., MOZLEY, P. S. & HALL, J. S. 2006. The effect of carbonate cementation on permeability heterogeneity in fluvial aquifers: An outcrop analog study. *Sedimentary Geology*, 184, 267-280.

DAVIS, J. M., WILSON, J. L. & PHILLIPS, F. M. 1994. A portable air minipermeameter for rapid in-situ field measurements. *Ground Water,* 32**,** 258–266.

DAVIS, J. M., WILSON, J. L., PHILLIPS, F. M. & GOTKOWITZ, M. B. 1997. Relationship between fluvial bounding surfaces and the permeability correlation structure. *Water Resources Research*, 33, 1843-1854.

DEUTSCH, C. V. & JOURNEL, A. G. 1998. *GSLIB: Geostatistical Software Library and User's Guide,* New York, Oxford University Press.

DINWIDDIE, C. L., MOLZ, I. F. L. & CASTLE, J. W. 2003. A new small drill hole minipermeameter probe for in situ permeability measurement: Fluid mechanics and geometrical factors. *Water resources research,* 39**,** SBH 2-1 – SBH 2-13.

DOMENICO, P. A. 1987. An analytical model for multidimensional transport of a decaying contaminant species. *Journal of Hydrology,* 91**,** 49-58.

DOMENICO, P. A. & ROBBINS, G. A. 1985. A new method of contaminant plume analysis. *Ground Water,* 23**,** 476 - 485.

DOMENICO, P. A. & SCHWARTZ, F. W. 1990. *Physical and Chemical Hydrogeology,* New York, John Wiley & Sons.

DOYLE, J. D. & SWEET, M. L. 1995. Three-Dimensional Distribution of Lithofacies, Bounding Surfaces, Porosity, and Permeability in a Fluvial Sandstone-Gypsy Sandstone of Northern Oklahoma. *The American Association of Petroleum Geologists Bulletin,* 79**,** 70-96.

DREYER, T., SCHEIE, A. & WALDERHAUG, O. 1990. Minipermeameter-based study of permeability trends in channel sand bodies. *The American Association of Petroleum Geologists Bulletin,* 74**,** 359-374.

DUFF, P. M. D., HALLAM, A. & WALTON, E. K. 1967a. *Developments in Sedimentology,* Amsterdam, New York Elsevier.

DUFF, P. M. L. D., HALLAM, A. & WALTON, E. K. 1967b. *Cyclic sedimentation*, Elsevier Science.

DYKSTRA, H. & PARSONS, R. L. 1950. The prediction of oil recovery by water flood. In: *Secondary Recovery of Oil in the United States*. *American Petroleum Institue, New York,* 2nd edn**,** 160–174.

EHRENBERG, S. N. 1997. Influence of depositional sand quality and diagenesis on porosity and permeability; examples from Brent Group reservoirs, northern North Sea. *Journal of Sedimentary research,* 67**,** 197-211.

EIJPE, R. & WEBER, K. J. 1971. Mini-permeameters for consolidated rock and unconsolidated sand. *The American Association of Petroleum Geologists Bulletin,* 55**,** 307-309.

FITCH, E. J., MILLER, J. A. & THOMPSON, D. B. 1966. The palaeogeographic significance of isotopic age determination on detrital micas from the Triassic of the Stockport-Macclesfield district, Cheshire. *Palaeogeography, Palaeoclimatology, Palaeoecology,,* 2**,** 281-312.

FRANKE, O. L. & REILLY, T. E. 1987. The effects of boundary conditions on the steady-state response of three hypothetical ground-water systems; results and implications of numerical experiments. US Government Printing Office.

FRANKE, O. L., REILLY, T. E. & BENNETT, G. D. 1987. Definition of boundary and initial conditions in the analysis of saturated ground-water flow systems; an introduction. US Government Printing Office.

GARDER, A. O. J., PEACEMAN, D. W. & POZZI, A. L. J. 1964. Numerical calculation of multidimensional miscible displacement by the method of characteristics. *Society of Petroleum Engineers Journal,* 6**,** 175-182.

GELHAR, L. W., WELTY, C. & REHFELDT, K. R. 1992. A critical review of data on field scale dispersion in aquifers. *Water Resoures Research*, 28, 1955-1974.

GIBBONS, K., HALVORSEN, C. & SIRING, E. 1993. Vertical and horizontal permeability variation within a sandstone reservoir based on minipermeameter measurements. *Marine and Petroleum Geology*, 10, 4, 325-334.

GOGGIN, D. J. 1993. Probe permeametry: is it worth the effort? *Marine and Petroleum Geology,* 10**,** 299-308.

GOGGIN, D. J., CHANDLER, M. A., KOCUREK, G. & LAKE, L. W. 1988a. Patterns of permeability in eolian deposits: Page sandstone (Jurassic), northeastern Arizona. *SPE Formation Eval.,* 3**,** 297-306.

GOGGIN, D. J., THRASHER, R. L. & LAKE, L. W. 1988b. A theoretical and experimental analysis of minipermeameter response including gas slippage and high velocity flow effects. *In Situ; (United State),* 12**,** 79–116.

GRESWELL, R. 1995. *A laboratory investigation of flow and transport processes in the Lincolnshire limestones.* PhD Thesis, University of Birmingham.

GRESWELL, R. 2010. Falling head permeameter measurement- A guidance

GRESWELL, R. B., DURAND, V., ALLER, M. F., RILEY, M. S. & TELLAM, J. H. 2014. A method for conducting simultaneous convergent tracer tests in multilayered aquifers. *Groundwater,* 52**,** 525-534.

HALLETT, M. J. 2014. *Permeability and Porosity Structures in English Permo-Triassic Sandstone Sequences*. MSci Thesis. Univeristy of Birmingham.

HALVORSEN, C. & HURST, A. 1990. Principles, practice and applications of laboratory minipermeametry In: *Advances in Core Evaluation: Accuracy and Precision in Reserves Estimation (Ed. P.F. Worthington),* (EUROCAS I) Gordon and Breach, London. 521-549.

HARBAUGH, A. W., BANTA, E. R., HILL, M. C. & MCDONALD, M. G. 2000. *MODFLOW-2000, the U.S. Geological Survey Modular Ground-Water Model—User Guide to Modularization Concepts and the Ground-Water Flow Process*. U.S. Geological Survey Open-File Report 00-92.

HARTEN, A. 1983. High resolution schemes for hyperbolic conservation laws. *Journal of Computational Physics,* 49**,** 357-93.

HARTEN, A. 1984. High resolution schemes for hyperbolic conservation laws. *Journal of Computational Physics,* 21**,** 955.

HEALY, R. W. & RUSSELL, T. F. 1989. Efficient implementation of the modified method of characteristics in finite-difference models of solute transport. Proc. 4th int. conf. on the use of models to analyze and find working solutions to groundwater problems, National Water Well Association.

HEALY, R. W. & RUSSELL, T. F. 1993. A finite-volume Eulerian-Lagrangian localized adjoint method for solution of the advection-dispersion equation. *Water Resources Research,* 29**,** 399-2413.

HEATHCOTE, J. A., JONES, M. A. & HERBERT, A. W. 1996. Modelling groundwater flow in the Sellafield area. *Quarterly Journal of Engineering Geology and Hydrogeology,* 29**,** S59-S81.

HILL, M. C. 1990. *Preconditioned conjugate-gradient 2 (PCG2), a computer program for solving ground-water flow equations*. US Geological Survey; Books and Open-File Reports Section.

HILL, M. C., BANTA, E. R., HARBAUGH, A. W. & ANDERMAN, E. R. 2000. *MODFLOW-2000, the U.S. Geological Survey Modular Ground-Water Model—User Guide to the Observation, Sensitivity, and Parameter-Estimation Processes and Three Post-Processing Programs.* US Geological Survey Open-File Report.

HOLLOWAY, S. 1985. The Permian, *In*: A. Whittaker (ed.) *Atlas of Onshore Sedimentary Basins in England and Wales: Post-Carboniferous Tectonics and Stratigraphy*. Blackie and Sons, Glasgow, 26-30.

HORNUNG, J. & AIGNER, T. 1999. Reservoir and aquifer characterization of fluvial architectural elements: Stubensandstein, Upper Triassic, southwest Germany. *Sedimentary Geology,* 129**,** 215-280.

HOUNSLOW, M. W. & RUFFELL, A. H. 2006. Triassic: seasonal rivers, dusty deserts and saline lakes. *In:* BRENCHLEY, P. J. & RAWSON, P. F. (eds.) *The Geology of England and Wales*. Geological Society, London, 295-324.

HUYAKORN, P. S. & PINDER, G. F. 1983. *Computational Methods in Subsurface Flow,* New York, Academic Press.

HUYSMANS, M., PEETERS, L., MOERMANS, G. & DASSARGUES, A. 2008. Relating small-scale sedimentary structures and permeability in a cross-bedded aquifer. *Journal of Hydrology,* 361**,** 41-51.

IAN WEST. 2008. *Dawlish Warren Sand Spit and Langstone Rock, Devon. Geology of the Wessex Coast of Southern England.* http://www.southampton.ac.uk/~imw/Dawlish-Warren.htm. *(*Accessed throughout from January 2012 to January 2016).

JACOBSEN, T. & RENDALL, H. 1990. Permeability patterns in some fluvial sandstones: An outcrop study from Yorkshire, north east England. *Reservoir Characterization II***,** 315-338.

JAVANDEL, I., DOUGHTY, D. & TSANG, C.-F. 1984. *Groundwater Transport. Handbook of Mathematical Models*, American Geophysical Union, Water Resources Monograph 10.

JAWEESH, M. In preparation. *The importance of correlation between lithofacies, within sandstone sequences, and hydraulic and geochemical properties in groundwater contaminant transport.* PhD Thesis, University of Birmingham.

JENSEN, J. L., CORBETT, P. W. M., PICKUP, G. E. & RINGROSE, P. S. 1996. Permeability semivariograms, geological structure, and flow performance. *Mathematical Geology,* 28**,** 419-435.

JENSEN, J. L., GLASBEY, C. A. & CORBETT, P. W. M. 1994. On the interaction of geology, measurement and statistical analysis of small-scale permeability measurements. *Terra Nova,* 6**,** 397–403.

JONES, N. S. & AMBROSE, K. 1994. Triassic sandy braidplain and aeolian sedimentation in the Sherwood Sandstone Group of the Sellafield area, west Cumbria. *Proceedings of the Yorkshire Geological Society,* 50**,** 61-76.

JONES, S. C. 1992. The profile permeameter: A new, fast, accurate minipermeameter. SPE 24757, 4–7.

JUSSEL, P. 1989. Stochastic description of typical inhomogeneities of hydraulic conductivity in fluvial deposits. In: Kobus & Kinzelbach (eds.). *Contaminant Transport in Groundwater,* 221-228.

KARPETA, W. P. 1990. The Morphology of Permian Palaeodunes: A Reinterpretation of the Bridgnorth Sandstone Around Bridgnorth, England, in the Light of Modern Dune Studies. *Sedimentary Geology,* 69**,** 59-75.

KIRKMAN, T. 1996. Statistics to use. http://www.physics.csbsju.edu/stats/. (Accessed throughout from January 2012 to January 2016).

KITTRIDGE, M. G., LAKE, L. W., LUCIA, F. J. & FOGG, G. E. 1990. Outcrop/subsurface comparisons of heterogeneity in the San Andres Formation. *SPE Formation Evaluation,* 5**,** 233–240.

KLINKENBERG, L. J. 1941. The permeability of porous media to liquids and gases. *API Drilling and Production Practice* New York: American Petroleum Institute.

KONIKOW, L. F. 2011. The secret to successful solute-transport modeling. *Ground Water,* 49**,** 144-59.

KONIKOW, L. F., GOODE, D. J. & HORNBERGER, G. Z. 1996. *A threedimensional method-of-characteristics solute-transport model (MOC3D).* U.S. Geological Survey Water-Resources Investigations Report, 96-4267.

KRUMBEIWN, C. & DACEYM, F. 1969. Markov chains and embedded chains in geology. *Journal of International Association for Mathematical Geology.* 1, 79-96.

KUPFERSBERGER, H. & DEUTSCH, C. V. 1999. Methodology for Integrating Analog Geologic Data in 3-D Variogram Modeling. *The American Association of Petroleum Geologists Bulletin,* 83**,** 1262-1278.

LAMBERT, M. R., COLE, R. D. & MOZLEY, P. S. 1997. Controls on permeability heterogeneity in the Tocito Sandstone (Upper Cretaceous), northwest New Mexico. Mesozoic geology and paleontology of the Four Corners Region, edited by: Anderson, OJ, Kues, BS and Lucas, SG, Guidebook, 48th Field Conference, Geological Society, New Mexico, 217-228.

LAMING, D. J. C. 1966. Imbrication, paleocurrents and other sedimentary features in the lower New Red Sandstone, Devonshire, England. *Journal of Sedimentary Research,* 36**,** 940-959

LAMING, D. J. C. 1982. The New Red Sandstone. *In*: E.M. Durrance and D.J.C. Laming (eds) *The Geology of Devon.* University of Exeter, Exeter, 148-178.

LITTLEBOY, A. 1996. The geology and hydrogeology of the Sellafield area: development of the way forward. *Quarterly Journal of Engineering Geology and Hydrogeology,* 29**,** S95-S104.

LIU, Y. & KITANIDIS, P. K. 2013. A mathematical and computational study of the dispersivity tensor in anisotropic porous media. *Advances in Water Resources,* 62**,** 303-316.

LOVELOCK, P. E. R. 1977. Aquifer Properties of the Permo-Triassic Sandstones in the United Kingdom. *Bulletin of the Geological Survey of Great Britain,* 56.

MACCHI, L. & MEADOWS, N. S. 1987. The Permo-Triassic of Cheshire and Cumbria. *Poroerm Excursion Guide, Proroperm-Geochem Limited, Chester,* 12**,** 140.

MADER, D. & YARDLEY, J. M. 1985. Migration, modification and merging in aeolian systems and the significance of the depositional mechanisms in Permian and Triassic dune sands of Europe and North America. *Sedimentary Geology,* 43, 85-218.

MCDONALD, M. G. & HARBAUGH, A. W. 1984. *Modular Three-Dimensional Finite-Difference Ground water Flow Model*, Open File Report 83–875, U.S. Geological Survey, National Center, Reston, Virginia, 1984.

MCKIE, T., AGGETT, J. & HOGG, A. J. C. 1998. Reservoir architecture of the upper Sherwood Sandstone, Wytch Farm field, southern England. *Development, Evolution and Petroleum Geology of the Wessex Basin,* 133**,** 399-406.

MCKINLEY, J. M., ATKINSON, P. M., LLOYD, C. D., RUFFELL, A. H. & WORDEN, R. H. 2011. How Porosity and Permeability Vary Spatially With Grain Size, Sorting, Cement Volume, and Mineral Dissolution In Fluvial Triassic Sandstones: The Value of Geostatistics and Local Regression. *Journal of Sedimentary Research,* 81, 844-858.

MCKINLEY, J. M., LLOYD, C. D. & RUFFELL, A. H. 2004. Use of variography in permeability characterization of visually homogeneous sandstone reservoirs with examples from outcrop studies. *Mathematical Geology,* 36**,** 761-779.

MIALL, A. D. 1973. Markov chain analysis applied to an ancient alluvial plain succession *Sedimentology,* 20**,** 347-364.

MIALL, A. D. 1985. Architectural Elements and bounding Surfaces: A new method of facies analysis applied to fluvial deposits. *Earth-Science Reviews*, 22, 261-308.

MIALL, A. D. 1988. Reservoir heterogeneities in fluvial sandstones: lessons from outcrop studies. *The American Association of Petroleum Geologists Bulletin,* 72**,** 682-697.

MICHIE, U. 1996. The geological framework of the Sellafield area and its relationship to hydrogeology. *Quarterly Journal of Engineering Geology and Hydrogeology*, 29**,** S13-S27.

MILODOWSKI, A. E., GILLESPIE, M. R., NADEN, J., FORTEY, N. J., SHEPHERD, T. J., PEARCE, J. M. & METCALFE, R. 1998. The petrology and paragenesis of fracture mineralization in the Sellafield area, west Cumbria. *Proceedings of the Yorkshire Geological Society,* 52**,** 215-241.

MONICARD, R. P. 1980a. *Properties of reservoir rocks: core analysis.* Editions Technip. Paris. 168 pp (Trans. By O. Berley, dist. By Granham and Trotman Ltd., London).

MONICARD, R. P. 1980b. *Properties of Reservoir Rocks: Core Analysis,* Editions Technip, Paris.

MOORE, J. 1996. *Upscalling the Triassic Sandston.* MSc Thesis, University of Birmingham.

MORAN, N. 2008. *Lithofacies/K correlations: Developing a New Approach for Solute Transport in Sandstone Systems.* MSc thesis, University of Birmingham.

MOULD, A. 2007. *Lithofacies and hydraulic conductivity correlations in the Permo-Triassic Sandstones of the UK: implications for fluid and solute migration.* MSc thesis, University of Birmingham.

NEUMAN, S. P. 1984. Adaptive Eulerian-Lagrangian finite element method for advection-dispersion. *International Journal for Numerical Methods in Engineering,* 20**,** 321-337.

NEWELL, A. J. 1992. *Sedimentological Controls on Vertebate Taphonomy in Triassic Fluvial Environment*. PhD Thesis, Queen's University of Belfast.

NEWELL, A. J. 2001. Bounding surfaces in a mixed aeolian-fluvial system (Rotliegend, Wessex Basin, SWUK). *Marine and Petroleum Geology,* 18**,** 339-347.

NEWELL, A. J. 2006. Calcrete as a source of heterogeneity in Triassic fluvial sandstone aquifers (Otter Sandstone Formation, SW England). *In:* BARKER, R. D. & TELLAM, J. H. (eds.) *Fluid Flow and Solute Movement in Sandstones: The Onshore UK Permo-Triassic Red Bed Sequence.* Geological Society, London, Special Publications, 263, 119-127.

NIREX. 1993. *RE: The The Geology and Hydrogeology of the Sellafield Area: Interim Assessment.* Report 524, UK Nirex Ltd*.*

OGATA, A. & BANKS, R. B. 1961. *A solution of the differential equation of longitudinal dispersion in porous media*. US Government Printing Office.

POCOCK, R. W. & WRAY, D. A. 1925. T*he geology of the country around Wem*. Mem. Geological Survey, Great Britian, 138p.

POLLOCK, D. W. 1994. *User's Guide for MODPATH/MODPATH-PLOT, Version 3: A Particle Tracking Post-Processing Package for MODFLOW, the U.S. Geological Survey Finite-Difference Ground-Water Flow Model*. US Geological Survey Open-File Report, 6, 94-464.

POSSEMIERS, M., HUYSMANS, M., PEETERS, L., BATELAAN, O. & DASSARGUES, A. 2012. Relationship between sedimentary features and permeability at different scales in the Brussels Sands. *Geologica Belgica*, 15, 156-164.

PRICE, H. S., VARGA, R. S. & WARREN, J. E. 1966. Application of oscillation matrices to diffusion-convection equations. *Journal of Mathematical Physics,* 45**,** 301–311.

PRICE, M., MORRIS, B. & ROBERTSON, A. 1982. A study of permeability variations in Chalk and Permean aquifers using double packer injection testing. *Journal of Hydrology,* 54**,** 401-423.

PURVIS, K. & WRIGHT, P. 1991. Calcretes Related to Phreatophytic Vegetation from the Middle Triassic Otter Sandstone of South West England. *Sedimentary Geology,* 38**,** 539-551.

RAMINGWONG, T. 1974. *Hydrogeology of the Keuper sandstone in the Droitwich syncline area - Worcestershire*. PhD thesis, University of Birmingham.

READING, H. G. 1996. *Sedimentary environments: processes, facies, and stratigraphy,* Cambridge, Mass, Blackwell Science.

RITZI, R. W., DAI, Z. X., DOMINIC, D. F. & RUBIN, Y. N. 2004. Spatial correlation of permeability in cross-stratified sediment with hierarchical architecture. *Water Resources Research,* 40, 1-14.

ROGERS, P. J., PIPER, D. P. & CHARSLEY, T. J. 1981. *The conglomerate resources of the Sherwood Sandstone Group of the country around Cheadle, Staffordshire. Description of part 1: 25 000 Sheet Sk 04. Miner. Assess. Rep. Inst. Geol. Sci.,* No.57.

RUFFELL, A. H., HOLLIDAY, D. W. & SMITH, D. B. 2006. Permian: arid basins and hypersaline seas. In BRENCHLEY, P J, and RAWSON, P F (eds) *The Geology of England and Wales.* Geological Society, London, 269-293.

RUSSELL, T. F. & WHEELER, M. F. 1983. Finite element and finite difference methods for continuous flows in porous media. *The mathematics of reservoir simulation,* 1**,** 35-106.

SCHEIDEGGER, A. E. 1961. General Theory of Dispersion in Porous Media. *Journal of Geophysical Research*, 66**,** 3273-3278.

SÉGOL, G. 1994. *Classic Groundwater Simulations: Proving and Improving Numerical Models*, PTR Prentice Hall, Englewood Cliffs.

SELLEY, R. C. 1969. Studies of sequence in sediments using a simple mathematical device. *Quarterly Journal of the Geological Society,* 125**,** 557-581.

SELLEY, R. C. 1988. *Applied sedimentology,* London, Academic Press.

SELWOOD, E. B., EDWARD, R. A., SIMPSON, S. & CHESTER, J. A. 1984. *Geology of the Country Around Newton Abbot. Memoirs of British Geological Survey*, British Geological Survey.

SHOTTON, F. M. 1956. Some aspects of the New Red desert in Britain. *Liverpool and Manchester Geological Journal,* 1**,** 450-465.

SHOTTON, F. W. 1937. The Lower Bunter Sandstones of North Worcestershire and East Shropshire. *Geological Magazine,* 74**,** 534-553.

SMEDLEY, P. L., NEUMANN, I. & BROWN, S. 2005. Baseline Report Series 20: The Permo-Triassic Sandstone Aquifer of Shropshire. British Geological Survey Commissioned Report No. CR/05/061N.

SMITH, D. B., BRUNSTROM, R. G. W., MANNING, P. I., SIMPSON, S. & SHOTTON, F. W. 1974. *A Correlation of Permian Rocks in the British Isles*. Geological Society, Lodon.

STEEL, R. J. & THOMPSON, D. B. 1983. Structures and textures in Triassic braided stream conglomerates ('Bunter' Pebble Beds) in the Sherwood Sandstone Group, North Staffordshire, England. *Sedimentology,* 30**,** 341–367.

STREETLY, H., HAMILTON, C. A. L., BETRS, C., TELLAM, J. H. & HERBBERT, A. W. 2002. Reconnaissance tracer tests in the Triassic Sandstone aquifer north of Liverpool, UK. *Quarterly Journal of Engineering Geology and Hydrogeology,* 35**,** 167-178.

STRONG, G. E. 1993. Diagenesis of the Triasic Sherwood Sandstone Group Rocks, Preston, Lancashire, UK: a possible evaporitic cement precursor to secondary porosity? In: NORTH, C.P. & PROSSER, D.J. (eds) *Characterization of Fluvial and Aeolian Reserviors*. Geological Society, London, Special Publications, 37, 279-289.

STRONG, G. E. & MILODOWSKI, A. E. 1987. Aspects of the diagenesis of the Sherwood Sandstones of the Wessex Basin and their influence on reservoir characteristics. In: MARSHAL, J.D. (ed.) *Diagenesis of Sedimentary Sequences*. Geological Society, London, Special Publications, 36, 325-337.

STRONG, G. E., MILODOWSKI, A. E., PEARCE, J. M., KEMP, S. J., PRIOR, S. V. & MORTON, A. C. 1994. The petrology and diagenesis of Permo-Triassic rocks of the Sellafield area, Cumbria. *Proceedings of the Yorkshire Geological Society,* 50**,** 77-89.

SUDICKY, E. A. 1986. A natural gradient experiment on solute transport in a sand aquifer: Spatial variability of hydraulic conductivity and its role in the dispersion process. *Water Resources Res,* 22**,** 2069-2082.

SUTHERLAND, W. J., HALVORSEN, C., HURST, A., MCPHEE, C. A., ROBERTSON, G., WHATTLER, P. R. & WORTHINGTON, P. F. 1993. Recommended practice for probe permeametry *Marine and Petroleum Geology,* 10**,** 309-317.

TELLAM, J. H. & BARKER, R. D. 2006. Towards prediction of saturated-zone pollutant movement in groundwaters in fractured permeable-matrix aquifers: the case of the UK Permo-Triassic sandstones. *In:* BARKER, R. D. & TELLAM, J. H. (eds.) *Fluid Flow and Solute Movement in Sandstones: The Onshore UK Permo-Triassic Red Bed Sequence.* Geological Society, London, Special Publications, 263, 1- 48.

TELLAM, J. H. & LLOYD, J. W. 1981. A review of the hydrogeology of British onshore non-carbonate mudrocks. *Quarterly Journal of Engineering Geology and Hydrogeology,* 14**,** 347-355.

THOMPSON, D. B. 1970. Sedimentation of the Triassic (Scythian) red pebbly sandstones in the Cheshire Basin and its margins. *Geological Journal*, 7, 183-216.

TOGHILL, P. 1990. *Geology in Shropshire.* The Swan Hill Press.

TYE, R. S. & HICKEY, J. J. 2001. Permeability characterization of distributary mouth bar sandstones in Prudhoe Bay field, Alaska: How horizontal cores reduce risk in developing deltaic reservoirs. *The American Association of Petroleum Geologists Bulletin,* 85**,** 459-475.

TYLER-WHITTLE, R., BROWN, S. & SHAND, P. 2002. *Baseline Report Series 3: The Permo-Triassic Sandstones of South Staffordshire and North Worcestershire*. British Geological Survey Commissioned Report No. CR/02/119N.

VAN GENUCHTEN, M. T. & ALVES, W. J. 1982. *Analytical Solutions of the One-Dimensional Convective-Dispersive Solute-Transport Equation* (No 157268). United States Department of Agriculture, Economic Research Service.

WARD, R. S., WILLIAMS, A. T., BARKER, J. A., BREWERTON, L. J. & GALE, I. N. 1998. *Groundwater Tracer Tests: A Review and Guidelines for Their Use in British Aquifers*, British Geological Survey London.

WARRINGTON, G., AUDLEY-CHARLES, M. G., ELLIOT, R. E., EVANS, W. B., IVIMEY-COOK, H. C., KENT, P. E., ROBINSON, P. L., SHOTTON, F. M. & TAYLOR, F. M. 1980. *A correlation of Triassic rocks in the British Isles,* Oxford, Geological Society of London Special Report 13.

WARRINGTON, G. & SCRIVENER, R. C. 1990. The Permian of Devon, England. *Review of Palaeobotany and Palynology,* 66**,** 263-272.

WELLS, R. M. 1995. *An investigation of solute transport mechanisms in the Permo-Triassic sandstones, England.* MSc Thesis, Univeristy of Birmingham.

WEXLER, E. J. 1992. *Analytical Solutions for One-, Two-, and Three-Dimensional Solute Transport in Ground-Water Systems with Uniform Flow.* US Government Printing Office.

WILLIS, B. J. & WHITE, C. D. 2000. Quantitative outcrop data for flow simulation. *Journal of Sedimentary Research,* 70**,** 788-802.

WILLS, L. J. 1970. The Triassic succession in the central Midlands in its regional setting. *Quarterly Journal of the Geological Society,* 126**,** 225-283.

WILLS, L. J. 1976. The Trias of Worcestershire and Warwickshire. Institute of Geological Sciences, Report No. 7612.

WOODCOCK, N. & STRACHAN, R. 2000. *Geological history of Britain and Ireland,* Oxford, Balckwell.

YEH, G. T. 1990. A Lagrangian-Eulerian method with zoomable hidden finemesh approach to solving advection-dispersion equations. *Water Resoures,* 26**,** 1133-1144.

YEH, G. T., CHANG, J. R. & SHORT, T. E. 1992. An exact peak capturing and oscillation-free scheme to solve advection-dispersion transport equations. *Water Resources Research,* 28**,** 2937-2951.

ZHENG, C. 1990. *MT3D, A modular three-dimensional transport model for simulation of advection, dispersion and chemical reactions of contaminants in groundwater systems*. Report to the U.S. Environmental Protection Agency, Robert S. Kerr Environmental Research Laboratory, Ada, OK.

ZHENG, C. 1993. Extension of the method of characteristics for simulation of solute transport in three dimensions. *Ground Water,* 31**,** 456-465.

ZHENG, C. 2006. *MT3DMS v5.2 Supplemental User's Guide*, Technical Report to the U.S. Army Engineer Research and Development Center, Department of Geological Sciences, University of Alabama.

ZHENG, C. & BENNETT, G. D. 1995. *Applied contaminant transport modeling: Theory and practice,*, New York, John Wiley and Sons.

ZHENG, C. & WANG, P. P. 1999. *MT3DMS, A Modular Three-Dimensional Multi-Species Transport Model for Simulation of Advection, Dispersion and Chemical Reactions of Contaminants in Groundwater Systems; Documentation and User's Guide.* U.S. Army Engineer Research and Development Center Contract Report SERDP-99-1, Vicksburg, MS.

APPENDICES

A CD attached to the thesis includes the Appendices for the thesis are as follows:

Appendix 1. Hydraulic property measurements

1.1 Porosities and moisture contents for Preston Laundry Borehole core

1.2 Porosities and hydraulic conductivities of samples at St Bees Head, west Cumbria

1.3 Porosities and hydraulic conductivities of samples at Bridgnorth Hermitage

1.4 Porosities and hydraulic conductivities of samples at Croxden Quarry

1.5 Porosities and hydraulic conductivities of samples at Lamdram Bay

1.6 Porosities and hydraulic conductivities of samples at Sidmouth

Appendix 2. Mini-permeameter measurements

2.1 Preston Laundry Borehole core

2.1.1 Whole borehole core

2.2.3 Drying conditions

2.2.2 Core plugs

2.2 Wolverley sandstone outcrop

2.3 Bridgnorth sandstone outcrop

Appendix 3. Kolmogorov-Smirnov test results

3.1 Porosity and permeability data for Preston Laundry Borehole core

3.2 Permeability data for the Wolverley sandstone outcrop

3.3 Permeability data for the Bridgnorth sandstone outcrop

Appendix 4. Microsoft Excel spreadsheets having VBA codes for creating

4.1 Mudpellet matrix

4.2 Fluvial multiple channel structures

Appendix 5. Groundwater Vista modelling output files for solute transport in the synthetic channel systems

Appendix 6. The English Permo-Triassic sandstone sequences (All geological descriptions).

Appendix 7. The implication of sandstone sedimentary and lithofacies and permeability structures for solute transport in groundwater with lithofacies having permeability from geometric mean (Chapter 6) replaced by arithmetic means.